Climatic Impacts and Transport of Martian Atmospheric Dust from Assimilation of Spacecraft Observations

Thesis

Climatic impacts and transport of martian atmospheric dust from assimilation of spacecraft observations

Paul Michael Streeter

MSci (Hons) Physics & Philosophy

School of Physical Sciences

The Open University

This dissertation is submitted for the degree of

Doctor of Philosophy

June 2020

On the subject of what was to happen among the celestial bodies, I could stop making new bets and wait calmly to pocket my winnings from (k)yK as my predictions gradually came true. But my passion for gambling led me, from every possible event, to foresee the interminable series of events that followed, even down to the most marginal and aleatory ones. I began to combine predictions of the most immediately and easily calculated events with others that required extremely complicated operations. "Hurry, look at the way the planets are condensing: now tell me, which is the one where an atmosphere is going to be formed? Mercury? Venus? Earth? Mars? Come on: make up your mind!..."

Italo Calvino, *How Much Shall We Bet?*

Declaration

I hereby declare that except where specific reference is made to the work of others, the contents of this dissertation are original and have not been submitted in whole or in part for consideration for any other degree or qualification in this, or any other university. This dissertation is my own work and contains nothing which is the outcome of work done in collaboration with others, except as specified in the text and Acknowledgements. This dissertation contains fewer than 100,000 words including appendices, bibliography, footnotes, tables and equations.

Paul Michael Streeter

MSci (Hons) Physics & Philosophy

June 2020

Acknowledgements

First of all I would like to sincerely thank my supervisors, Stephen and Manish, for the opportunity to be able to spend my time researching such a fascinating topic as the climate of Mars. I am indebted to them, and to my unofficial supervisor James, for all their support, time, and constructive guidance throughout my pursuit of this degree. With their support I was also able to learn about the red planet and atmospheric science generally, understand some of the secrets of the GCM, and to travel widely and meet other scientists while presenting my own work. And most recently, I am grateful for all the time and energy spent on poring over successive iterations of this thesis, particularly during the stresses of a global pandemic. I owe you all a drink (or two).

I am also grateful to the scientists I have interacted with who have helped me in various ways throughout my degree. Thanks to David Kass for contributing to my first paper and generally helping with MCS data, and (along with the rest of the MCS team) for the interesting trip to JPL. Thanks to Claire Newman and Jim Murphy for their rigorous and helpful reviews of my paper, which helped improve it substantially. Thanks to Armin Kleinböhl, Luca Montabone, François Forget, Ehouarn Millour, Steven Greybush, Leslie Tamppari, Alex Valeanu, Nick Heavens, Aymeric Spiga, and others for interesting conversations at various conferences. Thanks to Liam Steele for helping me with the GCM in my first year. And thank you to my examiners, Mike Wolff and Neil Edwards, for their time and effort in examining this thesis and for an interesting and insightful viva.

I'd like to give deep personal thanks for all the people I've met at the OU during this degree, some of whom have helped me directly with my research but all of whom have helped me to stay (somewhat) sane and to enjoy my time here. Thanks to all my various officemates: Rhian, Alex, Pegg, Chris, Candice, Rachael, Zoe, Jack, Frances, Laura, Melissa, Robert, Ben, Bea, and Joe, and to those outside the office: Andrew, Stacy, Megan, Narissa, Leanne, Slade, Hannah, Peter, and Carrie, among others, for helping me when I needed it, providing good company, and making Milton Keynes a worthwhile place to be (and for our well-deserved cricket victory). Thanks also to my housemates Jimmy and Rae for being so considerate and for watching bad action films and good pirate TV (respectively) with me. I'd also like to thank the ExoMars team at the OU for interesting conversations, good advice, and fun outings and voyages to the Continent and beyond. Special thanks to Megan for daring to read large parts of this thesis and providing excellent handwritten feedback.

I'm also grateful for my friends outside the OU. Thanks to AJ for supporting me as I applied and in that first year, and to Aleef and Rachel for some fun breaks from my routine. Thanks to Akshay and Vinu for many fun days and nights spent indoors, outdoors, in various cities, and more recently online for pandemic-related reasons; good luck with your further adventures and I hope we have many more in store together.

Finally, my deepest personal thanks to my family in the UK, Ecuador, and elsewhere. Thank you Luis Antonio for the memes, the shallow and deep conversations, and the excellent company to various gigs. I'm very proud of you. Thank you Dad for raising me, supporting me, and always having faith in me. Gracias mamá, por todo su amor y ayuda en mi vida, y su fe en todos mis esfuerzos. Le quiero mucho. Esta tesis es dedicada a usted.

Abstract

Mars' dust cycle and the radiative-dynamical impacts of atmospheric dust were investigated by assimilating Mars Climate Sounder (MCS) temperature and dust observations into a martian global climate model. Dust plays a key role in Mars' climate by interacting with solar and infrared radiation, thereby modifying atmospheric dynamics and winds, which themselves lift and transport dust. The 2018 Global Dust Storm (GDS) provided an opportunity to investigate how dust affects martian surface temperatures, polar dynamics, and the dust cycle.

The 2018 GDS was found to warm the martian surface by 0.9 K. The effects were highly spatially heterogeneous, with net warming from enhanced backscattering of surface infrared emission at low thermal inertia regions, while elsewhere blocked incident solar radiation caused net cooling. Comparisons with the 2001 GDS and free-running simulations show that GDS geographical structure is key in determining the surface temperature impact.

Martian dust lifting and deposition were shown to have a consistent interannual pattern, except during planetary-scale dust storms. Dust lifting patterns correspond to regular dynamical features including baroclinic waves, low-level jets, and CO_2 sublimation flow. Regional dust storms affect southern seasonal cap-edge dust lifting by enhancing the meridional circulation, causing increased sublimation. The 2018 GDS increased dust lifting over high-topography regions like Tharsis, but inhibited northern wave-related dust lifting. Southern high-latitude winds were found to be highly sensitive to the precise thermal structure in MCS temperature observations, with direct impacts on dust lifting.

The 2018 GDS was found to alter the elliptical structure of Mars' polar vortices via the GDS' effect on stationary topographic planetary waves, proving the link between these waves and vortex morphology. Enhanced GDS heating also significantly accelerated the destruction of the southern vortex. These results show the asymmetrical effects of an equinoctial GDS on the polar vortices, which govern tracer transport into polar regions.

Table of contents

List of figures

List of tables

Chapter 1

Introduction

I confirmed this definitely in 1909 by direct observation of the Martian continents, as I found that these more or less transparent yellow or reddish veils – less red than the continents, incidentally – were very frequent; even more so than the white clouds. I found moreover that they were most often seen near perihelion, when the solar heat, half as great again as at aphelion, produced stronger winds, so that the yellow particles and the lighter sand and dust would be more easily picked up from the Martian deserts.

Antoniadi (1975)

The planet Mars and its atmosphere have long been the subjects of fascination and scientific research. The English astronomer William Herschel first deduced both Mars' axial obliquity and, by the observation that the stars next to the planet showed no change in brightness as they passed its outer disc, the fact that its atmosphere must be thinner than our own (Herschel, 1784). As telescopic resolving power improved, subsequent astronomers noted the appearance and disappearance of yellow clouds on Mars' surface, correctly interpreted by French astronomer Eugène Antoniadi as sand and mineral dust lofted from the surface (Antoniadi, 1975). The advent of the space age and missions to Mars by the United States and the Soviet Union dramatically improved human understanding of the planet and its atmosphere, and it can now be stated that Mars is, after our own, the single planet most

studied by human beings, with multiple past and ongoing missions from various countries and organisations dedicated to exploring it.

As our knowledge of the martian atmosphere has improved, so has our appreciation for the importance of mineral dust in its meteorology. Given the planet's aridity, dust plays a central role akin to that of water in our own atmosphere: on the one hand, it is a substance with a cycle, able to be lofted from the surface via various lifting mechanisms, transported around the globe by winds, and redeposited by gravity and scavenging by ice clouds. On the other, it is also a radiatively active element, affecting Mars' temperature structure and consequently its atmospheric dynamics. Martian storms are not water vapour clouds and rain; they are dust storms which can range in size from the smallest terrestrial nations to the largest, and can encircle the planet in a deep cloud of dust for months at a time with enormous effects on the atmospheric system. In many ways Mars' atmospheric dynamics would be very recognisable to Earth meteorologists, and yet martian weather can largely be related to how much dust there is in the sky. Mars' similarities to our own planet, from its similar axial obliquity to its roughly similar size and distance from the Sun, together with its deep differences, from its utter aridity to its much sparser atmosphere and alien CO_2-related processes, make it an ideal natural laboratory for the study of meteorology as the field moves beyond its birthplace on Earth. Mars' well-preserved surface – free of the effects of tectonic activity – offers us insights into the deep past of its climate, and its current state can enhance our understanding of how planetary and atmospheric systems work outside the familiar context of our own planet, including specifically the kinds of impacts atmospheric aerosols can have on planetary atmospheres. And not least, the study of the martian atmosphere and the role of dust has eminent practical uses as humanity continues its robotic and possible future human exploration of our closest neighbour.

Our understanding of the martian atmosphere and the role of mineral dust within it has been facilitated by two basic tools: observations and numerical models. The former

offer insights into the actual state of the atmosphere, while the latter provide explanatory and predictive power by symbolic representation of the atmosphere using mathematics. Observations from Mars orbit and the martian surface have revealed the significant radiative effects of suspended atmospheric dust (e.g. Gierasch and Goody, 1972; Hanel et al., 1972; McCleese et al., 2010; Smith, 2004; Zurek et al., 1992), helped characterise the seasonal variations in dust loading reflective of the dust cycle (e.g. Fenton et al., 1997; Lemmon et al., 2015; Martin, 1986; Martin and Richardson, 1993; McCleese et al., 2010; Smith, 2004), and improved understanding of the behaviour, distribution, and atmospheric effects of dust storms (e.g. Cantor et al., 2001; Guzewich et al., 2019; Kass et al., 2016; Leovy and Zurek, 1979; Martin, 1984; Szwast et al., 2006; Wang and Richardson, 2015; Zurek and Martin, 1993), among many other insights. In parallel, numerical modelling of the martian atmosphere, including with Mars global climate models (MGCMs) has (for example) led to greater understanding of the radiative-dynamical impacts of dust (e.g. Haberle et al., 1993; Medvedev et al., 2011; Read et al., 2016; Wilson, 1997; Zurek and Haberle, 1988), replicated and helped explain the observed seasonal dust cycle (e.g. Kahre et al., 2005; Mulholland et al., 2015; Murphy et al., 1995; Newman et al., 2002a), and provided insight into the evolution and broader impacts of dust storms (e.g. Barnes et al., 1993; Basu et al., 2006; Murphy et al., 1990).

As well as using observations and numerical modelling by themselves, it is also possible to combine the two with the use of a method known as data assimilation. This method is described in detail in Chapter 3 of this thesis, but in short it is a way to integrate observational data into a numerical model to obtain the best fit between the two. Data assimilation is a standard technique in terrestrial meteorology for both research and forecasting. As a method, data assimilation has numerous advantages, among which are the ability to fill in the gaps of sparse observational data using a realistic numerical model rather than interpolation, and the representation of a more realistic atmospheric state than in models without assimilation.

Applied to the martian atmosphere, data assimilation has helped to characterise the dynamical effects of dust loading, including from Global Dust Storms (GDS) (e.g. Lewis and Barker, 2005; Montabone et al., 2005; Mulholland et al., 2016), analyse the structure of Mars' polar vortices (e.g. Mitchell et al., 2015; Waugh et al., 2016), and investigate dynamical features more generally including thermal tides and planetary waves (e.g. Battalio et al., 2016; Greybush et al., 2019; Lewis et al., 2016). Given the high sensitivity of the martian atmospheric state to the dust distribution and the current inability of models to predict specific dust events, data assimilation is therefore a highly useful tool to investigate specifically the dust cycle, the radiative-dynamical impacts of dust, and the interplay between the two.

This thesis uses data assimilation in a numerical model of Mars' atmosphere to investigate the martian dust cycle and the radiative and dynamical impacts of suspended dust. Observations from the Mars Climate Sounder provide data for six consecutive full martian years, including a year containing the 2018 Global Dust Storm. Assimilation of these observations therefore provides an excellent opportunity to identify interannual similarities and differences in the dust cycle, and to investigate the effects of a real Global Dust Storm on planetary dynamics and surface processes. The research questions addressed in this thesis are discussed below.

1.1 Research questions

This thesis addresses three main research questions:

RQ1. How do Global Dust Storms affect Mars' surface and near-surface temperature environment?

RQ2. Where and when does dust lifting and deposition occur on the martian surface, how does this vary between martian years and during a Global Dust Storm, and what dynamical processes are responsible?

RQ3. How do Global Dust Storms affect Mars' polar vortices?

These research questions are outlined in greater detail in the following parts of this section. Previous literature is discussed and the specific hypotheses pertaining to the work presented in this thesis are set out.

1.1.1 RQ1. How do Global Dust Storms affect Mars' surface and near-surface temperature environment?

The hypothesis leading into the work in this thesis was that the 2018 GDS would be shown to cause net surface cooling, due to the reduction in radiative flux reaching the surface. Famously, early orbital observations of a martian Global Dust Storm helped inspire the concept of nuclear winter, which postulated that massive aerosol loading from a global nuclear conflict on Earth would cause dramatic cooling at the surface and in the lower atmosphere (Turco et al., 1983). Previous observations of the planet's surface during Global Dust Storms have indicated that these events cause temperatures to cool during the day and warm during the night (e.g. Gurwell et al., 2005; Guzewich et al., 2019; Hanel et al., 1972; Ryan and Henry, 1979; Smith, 2004), due to the blocking of incident solar radiation and enhanced backscattering of surface infrared emissions respectively. For the 2001 GDS the globally-averaged surface temperatures from the Thermal Emission Spectrometer, which were all measured at two local times due to the spacecraft's orbit, show an average surface cooling (Smith, 2004). Modelling assuming the scenario of Global Dust Storm-scale dust loading has predicted a significant decrease in net incident surface radiation (e.g. Read et al., 2016), implying overall cooling. The work described in Chapter 4 uses an assimilated MGCM, with temperature and dust observations from the Mars Climate Sounder, to investigate the daytime, nighttime, and diurnally averaged effects of the 2018 Global Dust Storm on surface and near-surface temperatures by comparison to a relatively clear martian year. The surface temperature difference maps, globally-averaged values, and values at specific locations are

compared to observational data including from the Mars Climate Sounder. The results are interpreted in terms of dust optical properties as used in the MGCM, martian surface properties, Global Dust Storm structure, and the effects of true diurnal averaging (as opposed to diurnal averages using primarily two local times).

1.1.2 RQ2. Where and when does dust lifting and deposition occur on the martian surface, how does this vary between martian years and during a Global Dust Storm, and what dynamical processes are responsible?

For the work on this RQ, the hypothesis was that both regional and global-scale dust storms would have a significant impact on dust lifting and deposition in the martian atmosphere, increasing both due to enhanced near-surface wind speeds and atmospheric dust loading respectively; meanwhile, the high interannual similarity of martian atmospheric dynamics would result in high interannual similarity in dust lifting and deposition. Investigations of the dust cycle, and dust lifting processes in particular, have long been a staple of martian atmospheric research. Previous work has used free-running MGCMs and revealed the seasonal variation of dust lifting by near-surface winds (e.g. Basu et al., 2004; Kahre et al., 2006, 2005; Newman et al., 2002a,b) and its high geographical heterogeneity (e.g. Chapman, 2018; Montabone et al., 2005; Mulholland et al., 2013, 2015). Free-running simulations have also identified specific dynamical features thought to be related to dust lifting via high near-surface wind speeds, such as subtropical zonal jets linked to the Hadley circulation (Joshi et al., 1997), the western boundary current (Joshi et al., 1995), enhanced wind speeds during a Global Dust Storm (Montabone et al., 2005, using an assimilated MGCM), and baroclinic wave activity at mid-high latitudes and around the seasonal CO_2 ice caps (e.g. Hinson et al., 2012; Wang et al., 2013; Xiao et al., 2019). Baroclinic wave activity has

been corroborated by observations of frequent dust storm activity at both polar cap edges throughout the martian year (e.g. Cantor et al., 2002; Guzewich et al., 2015, 2017; Hinson and Wang, 2010; Hollingsworth et al., 1997; James et al., 1999; Wang, 2007; Wang and Fisher, 2009; Wang et al., 2005), which may also be linked to sublimation flow activity (Chow et al., 2019). The work presented here is the first use of a multi-year assimilated MGCM dataset to identify dust lifting and the less-often discussed deposition patterns; the use of six years of observations allows investigation of interannual variability in these processes, and for the identification of seasonal and geographical lifting and deposition patterns across martian years. It also allows study of how the 2018 Global Dust Storm affected lifting and deposition, as well as the smaller regional storms which occur regularly during the perihelion season (Kass et al., 2016). This study compares the identified lifting patterns to patterns in dynamical phenomena, including baroclinic wave activity, thermal tides, zonal and meridional jets, and the dynamical effects of dust storms, to attempt to provide the fullest picture yet of how specific dynamical phenomena are related to modelled dust lifting. The multi-annual record of modelled lifting and deposition is compared to a temporally overlapping dataset of observed dust storm activity, and similarities and differences in the two are interpreted. Later in this thesis, specific high near-surface wind features at southern high latitudes are investigated in further detail, due to their divergence from previous modelling work. These features are characterised and compared to existing observational data and modelling work. The possible causes of these features and the likelihood of their being physically real phenomena are discussed, along with a broader discussion on the effects of processing temperature data prioir to assimilation on the modelling of southern cap-edge wind speeds.

1.1.3 RQ3. How do Global Dust Storms affect Mars' polar vortices?

The starting hypothesis for this work was that the 2018 GDS would cause significant disruption to both of Mars' northern and southern polar vortices via diabatic and dynamical heating. Like Earth, Mars has coherent polar vortices: areas of colder air around the poles, strongest during winter and circumscribed by powerful zonal jets. These high winds can act as a barrier for atmospheric tracers and be modulated by planetary waves, making the polar vortices arguably the dominant dynamical feature in the polar regions. The last few years have witnessed an increase in investigation of these features, primarily through the analysis of free-running (e.g. Guzewich et al., 2016; Rostami et al., 2018; Seviour et al., 2017; Toigo et al., 2017) and assimilated (e.g. Mitchell et al., 2015; Waugh et al., 2016) models. Particularly of interest has been the distinct morphology of the polar vortices as compared to their terrestrial counterparts, with much discussion of their elliptical shape (e.g. Rostami et al., 2018; Waugh et al., 2016) and their annular structure (e.g. Mitchell et al., 2015; Rostami et al., 2018; Seviour et al., 2017; Toigo et al., 2017; Waugh et al., 2016). This latter characteristic, which should be dynamically unstable (Seviour et al., 2017), has been attributed to the effect of latent heating over the poles from the condensation of atmospheric CO_2 (Rostami et al., 2018; Toigo et al., 2017). The elliptical shape has been speculated to be linked to topography and/or inhomogenous deposition of CO_2 ice (Rostami et al., 2018). The effects of dust on the polar vortices has also been investigated: a regional-scale storm was found to significantly shift the northern vortex off the pole (Mitchell et al., 2015), while a simulated high dust loading meant to resemble a northern winter solsticial (L_S=270°) Global Dust Storm appeared to disrupt the northern vortex for a period of tens of sols (Guzewich et al., 2016). Meanwhile, Mars Climate Sounder observations during the 2018 Global Dust Storm show the southern vortex completely displaced onto the nightside of the planet (Kleinböhl et al., 2020). The work in this thesis used an assimilated MGCM to study the effects of the specific 2018 event to investigate the effects of an equinoctial Global Dust Storm

on polar dynamics, which has not been previously done. Both the southern and northern polar vortices are investigated, and both diurnally-averaged and diurnal results are presented. The use of assimilation allows the incorporation of both temperature and dust observational data, making it an especially valuable tool for studying the polar atmosphere; this is the first dedicated study of martian polar vortex dynamics assimilating Mars Climate Sounder data. The storm also acted as a form of natural laboratory allowing investigation of causes behind the elliptical shape of the vortices, and a hypothesis explaining this shape is presented.

1.2 Thesis outline

This thesis is structured as follows. Chapter 2 introduces basic concepts relevant to the study of Mars, including timekeeping and the martian calendar, the geographical structure of Mars, and the composition and basic properties of the atmosphere. It then discusses the relevant aspects of the atmosphere including the thermal structure and dynamics. The crucial role of suspended mineral dust is described: the cycle of lifting by winds and deposition, and the effects of dust on atmospheric temperatures and dynamical processes. Lastly, Mars' dust storms are discussed, including the uniquely martian phenomenon of the Global Dust Storm and the impacts of these events on the entirety of the martian weather and climate.

Chapter 3 lays out the tools used in this thesis to investigate the research questions. First, the Mars Global Climate Model (MGCM) is described: its basic dynamics, its parametrizations of martian atmospheric processes, and its structure. The concept of data assimilation is then introduced and discussed in detail, and the assimilation scheme used in this thesis is explained. The observations from the Mars Climate Sounder which were assimilated for this work are introduced and described. Lastly, the experiments performed for the work in this thesis are outlined.

Chapter 4 addresses RQ1 by discussing the 2018 Global Dust Storm and its effects on martian surface temperatures, using results from the assimilation. The surface and near-

surface air temperatures from the year of the storm and a relatively clear year are compared to ascertain the temperature impacts of the storm. The direct effects of the high dust loading and the impact of surface properties are discussed in the context of the results. The assimilated MGCM results are then compared to assimilated MGCM results from the 2001 Global Dust Storm, which had a similar geographical and seasonal extent to the 2018 event. These results are then compared to surface temperature observations from orbital spacecraft, ground-based telescopes, and *in situ* landers and rovers for the 2018 event and earlier Global Dust Storms in order to assess the veracity of the assimilated MGCM results. This chapter addresses RQ1.

Chapter 5 takes a multi-annual look at how dust is lifted from and deposited at the surface in both the Global Dust Storm case and in non-storm years. Predicted dust lifting and deposition in the assimilated MGCM are calculated using MGCM variables. Patterns in geographical and seasonal dust lifting and deposition are examined over six martian years, including the year of the 2018 Global Dust Storm. Dynamical mechanisms linked to the high wind speeds necessary for lifting in the MGCM are identified, including thermal tides, baroclinic planetary waves, and zonal and meridional wind features. This climatology of lifting and deposition is compared to an observational record of martian dust storms. This chapter addresses RQ2.

Chapter 6 focusses on dynamics at the martian poles, and is divided into two sections. The first section examines how the 2018 Global Dust Storm affected the martian polar vortices in both hemispheres. The structure of the vortices during the storm and in a clear year in the assimilated MGCM are compared to analyse what the impacts were, and are related to the meridional circulation and planetary wave activity. The modelled annular morphology of the vortices during clear years is explained in terms of these mechanisms. This section addresses RQ3. The second section focusses on a dust lifting feature around the southern seasonal polar cap identified in Chapter 5, linked to modelled high near-surface wind speeds. These wind speed features are characterised and possible explanations for their presence in

the assimilated MGCM are presented, tied to a broader discussion about the effects of how best to process polar temperature data before assimilation and the effects on modelled polar near-surface dynamics. This section addresses RQ2.

Lastly, Chapter 7 presents a summary and some conclusions on the thesis work as a whole. The results presented in Chapters 4-6 are discussed in the context of the research questions posed in this chapter. Themes running throughout the work are expressed and directions for possible future work are outlined.

Chapter 2

Dust in the martian atmosphere

This chapter presents an introduction to the most important aspects of the martian atmosphere and the role of atmospheric dust. The fundamentals of Mars' atmospheric composition and orbital parameters, the martian atmosphere's basic thermal structure and atmospheric dynamics, spacecraft observations of the planet, the atmospheric dust cycle, and the phenomena of dust storms and global dust storms are all discussed. This chapter is intended as a background for the work later presented in this thesis, and more specific and detailed discussions of previous research in the context of the results in this thesis are discussed in the introductions of Chapters 4, 5, and 6.

2.1 Background

Mars is often referred to as a sibling of Earth and indeed, the two share many similarities, as shown in Table 2.1. Both are rocky planets of comparable sizes (Mars has roughly half the radius of Earth), at comparable distances from the Sun, with very similar rotation rates and axial tilts. Water is present on both, though in vastly different column abundances. Both have atmospheres with recognisable features; for example, winds, seasonal variations, and clouds (seen on Mars in Fig. 2.1). Mars has a comparable thermal Rossby number (representing the

balance between the inertial force of the thermal wind and the Coriolis force) and Ekman number (representing the atmospheric "friction"), allowing for similar large-scale dynamical features like the presence of baroclinic wave activity (e.g. Read et al., 2017, and references therein).

Table 2.1 Comparison of planetary and atmospheric parameters of Mars and Earth. Numbers are from the NSSCA NASA Goddard Planetary Fact Sheets unless otherwise specified.

PLANETARY	**Mars**	**Earth**
Equatorial radius (km)	3396.2	6378.1
Semimajor axis (AU)	1.524	1
Rotation period (hrs)	24.6229	23.9345
Axial obliquity (deg)	25.19	23.44
Orbital eccentricity	0.0935	0.0167
Orbital period (days)	686.98	365.256
Surface gravity (m/s^2)	3.72	9.81
ATMOSPHERIC	**Mars**	**Earth**
Avg. surf. temp. (K/C)	∼210/-63	288/15
Surface pressure (Pa)	∼610	101400
Composition		
CO_2	95%	Trace
Nitrogen	3%	78%
Oxygen	Trace	21%
H_2O col. abundance	∼10-100 g	∼40 kg (Smith et al., 2002)

However, there are also marked differences. Mars is a cold, dry, desert planet with no vegetation, no oceans, and no liquid water. Fig. 2.2 demonstrates that liquid water is unstable at typical martian surface pressures (∼610 Pa) and temperatures (average ∼210 K, or -63° C). Mars also has a much thinner atmosphere than our own, with an average surface pressure a mere 0.6% the value of Earth's. These two factors contribute to the low thermal inertia of the martian atmosphere, with a radiative relaxation timescale of ∼1 sol (Read and Lewis, 2004). This timescale represents the characteristic time needed for the temperature to be brought back to equilibrium by radiative means only, meaning that on Mars radiative effects are very

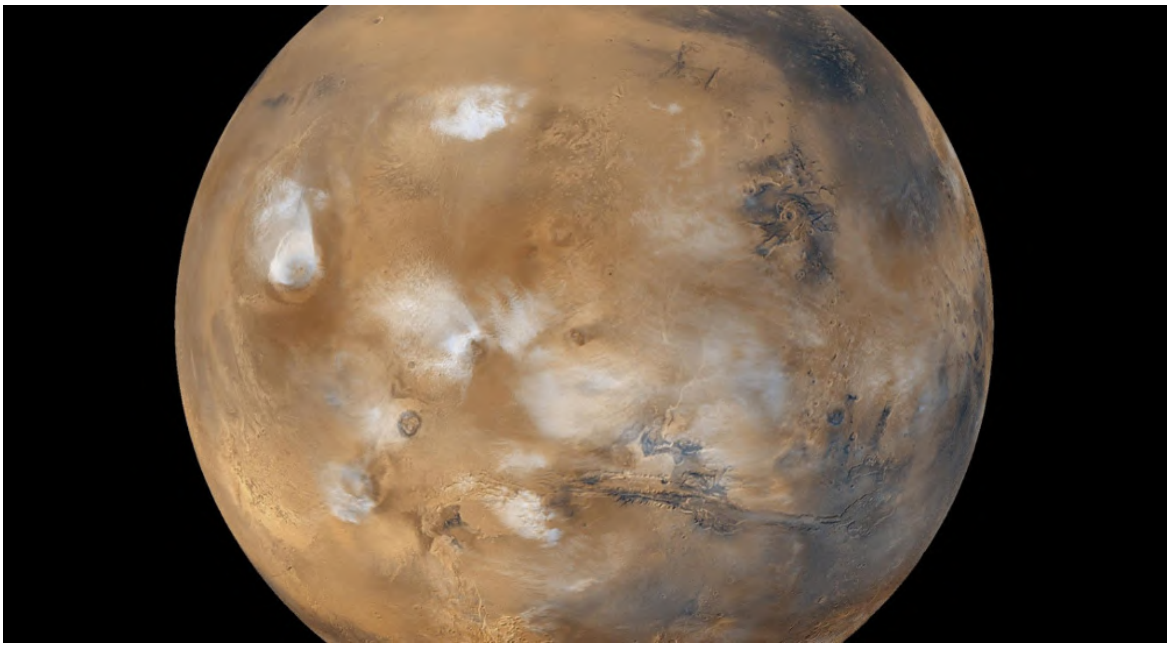

Fig. 2.1 Mars as imaged from the Mars Global Surveyor orbiter. Credit: NASA/JPL.

important even over short time periods. This is in contrast to a terrestrial tropospheric radiative timescale of $\sim$10 days, an order of magnitude greater than the characteristic timescale of air motion in the troposphere (Salby, 2011); that is, the time needed to restore equilibrium by dynamical means. This renders the effects of air motion much more significant in Earth's troposphere, as temperature changes will be brought to equilibrium by circulatory changes (ie. wind) far more efficiently than by radiative effects.

2.2 Composition, element cycles, and seasonality

Mars' atmosphere has a composition marked by very different chemical abundances to that of our own. Earth's atmosphere is composed of predominantly nitrogen and oxygen (together 99%), with carbon dioxide (CO_2) present in trace amounts. On Mars, CO_2 constitutes 95% of the atmosphere, with the remainder consisting of nitrogen (3%) and other gases in trace amounts. However, Mars contains even more CO_2 than that which is present in the atmosphere, much of it locked up in the form of ice. Atmospheric CO_2 seasonally condenses

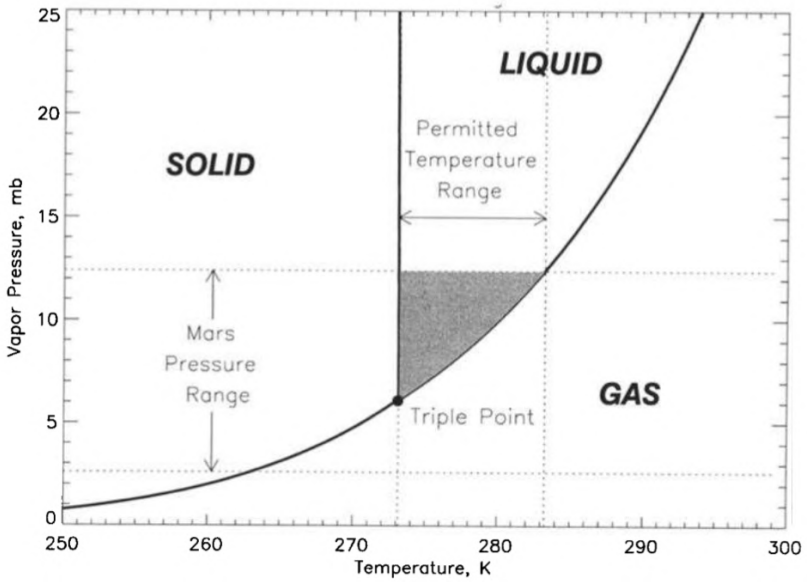

Fig. 2.2 Pressure-temperature diagram showing the triple point of water and the approximate surface pressures and temperatures on Mars. Reprinted with permission from Haberle et al. (2001).

onto the surface, mostly around the poles (Leighton and Murray, 1966), leading to variations of up to tens of percent of the atmosphere on a regular, repeatable basis (Kahre and Haberle, 2010).

Mars' atmosphere contains far less H_2O than Earth, and the surface holds no liquid water, but it still possesses a water cycle involving vapour and ice. Despite its dryness, the martian atmosphere does possess trace amounts of water vapour, with greater amounts in the northern hemisphere due to the sublimation of the northern CO_2 ice cap (Smith, 2004). Water-ice clouds are also present, while being far thinner than their Earth counterparts, and are present in an equatorial belt during the aphelion season (the "aphelion cloud belt") and over the poles during their respective autumn/winter seasons (the "polar hood clouds") (Montmessin et al., 2004). Atmospheric dust can act as nuclei for cloud formation; for example, the southern pole experiences more polar hood cloud activity than the north due to the dusty southern summer preceding it (Cantor et al., 2010). Most of the water on Mars, however, is probably locked up in the form of ice in the polar caps and in the martian subsurface. The polar caps

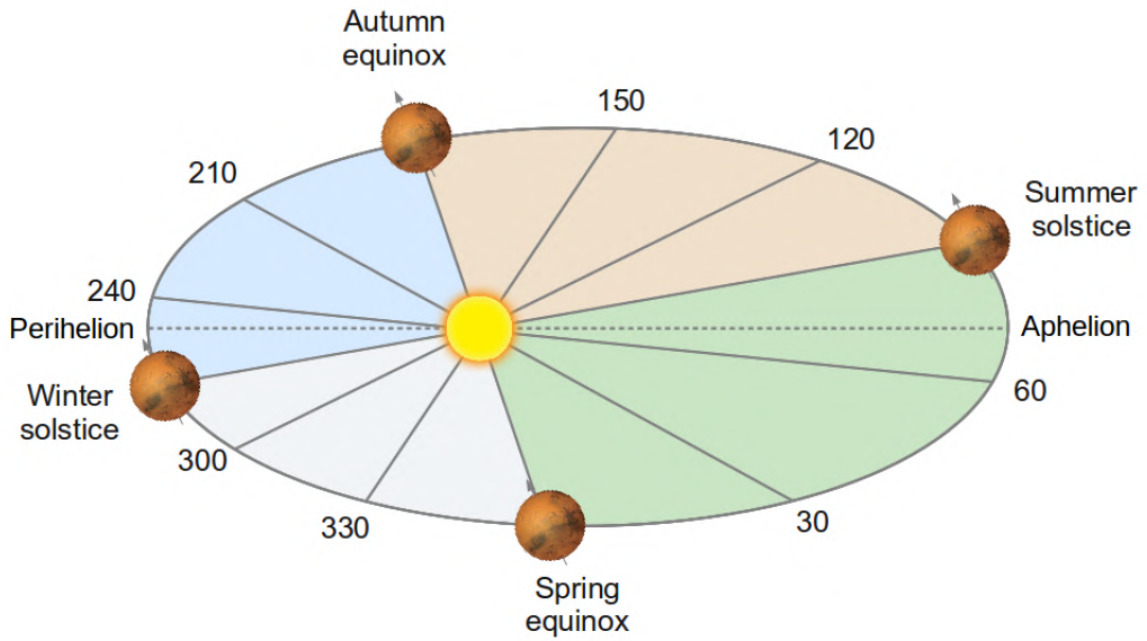

Fig. 2.3 The martian calendar, represented in terms of areocentric longitude (L_S). Reprinted with permission from Steele (2014).

consist of both CO_2 and water ice and have both a permanent and a seasonal component, with the latter subliming during local summer (Smith et al., 2001). Subsurface ice appears to be present throughout the planet (Mitrofanov et al. 2004), but its exact abundances and distribution remain poorly known.

While Mars experiences seasonal variations and has a similar axial tilt to that of Earth, the greater eccentricity of its orbit makes these seasonal effects more extreme. Mars dates are usually expressed in terms of areocentric longitude (L_S), and one Mars year is a complete cycle between L_S=0 and L_S=360°, equivalent to 668.6 martian sols or 687 terrestrial days (almost two terrestrial years). This eccentric orbital cycle can be seen in Fig. 2.3. The Mars Year (MY) notation is commonly used, with L_S=0 of MY 1 beginning on April 11, 1955 (Clancy et al., 2000). The aphelion season (L_S∼0-180°) corresponds to northern hemisphere spring-autumn, and is characterised by relatively dust-free skies and low storm activity; the perihelion season (L_S∼180-360°) corresponds to northern hemisphere autumn-spring, and is relatively dustier with greater dust storm activity (Smith, 2004).

2.3 Thermal structure, circulation, and dynamics

Mars experiences differential solar insolation due to its axial obliquity, with the equator receiving more heat than the poles. At equinox Mars has a roughly symmetrical zonally-averaged temperature profile. This consists of a warmer equatorial atmosphere sloping smoothly down into colder poles (Smith et al., 2001), as seen in Fig. 2.4.a. The central plateau visible in Fig. 2.4.a represents a barotropic region of the atmosphere, where contours of constant pressure and constant temperature are parallel. This makes the equatorial region relatively stable to disturbances and thus quiet in the sense of weather and wave activity, with an absence of vertical shear in wind speed (Salby, 2011). For the rest of the year, however, Mars' axial tilt and eccentric orbit cause this symmetry to be broken, with the most pronounced asymmetry present at the solstices. This asymmetry is especially extreme around the northern winter solstice L_S=270°, when the planet is closest to the sun (see Fig. 2.3). At solstice, maximum temperatures can be found extending from the summer pole to mid-latitudes, with temperatures decreasing smoothly towards the winter pole, as visible in Fig. 2.4.b.

The asymmetric heating experienced by Mars, with the equator/summer pole receiving the most solar insolation, gives rise to a meridional circulation which acts to transport heat towards the poles/winter pole, as described theoretically by Held and Hou (1980). On Earth this meridional circulation takes the form of Hadley cells, two roughly symmetrical thermally direct circulatory cells which transport heat from the equator to $\sim$30° poleward (Salby, 2011), a situation which roughly occurs on Mars as well around the equinoctial period (Fig. 2.5.a). However, the solsticial asymmetry in insolation results in a solsticial circulation consisting of a dominant cross-equatorial Hadley cell extending from the summer mid-latitudes to the winter mid-latitudes, with a significantly weaker Hadley cell also present at high latitudes (Fig. 2.5.b). A major difference is that Mars' lack of strong atmospheric stratification allows the meridional cells to extend far higher in the atmosphere than they do on Earth (Read et al.,

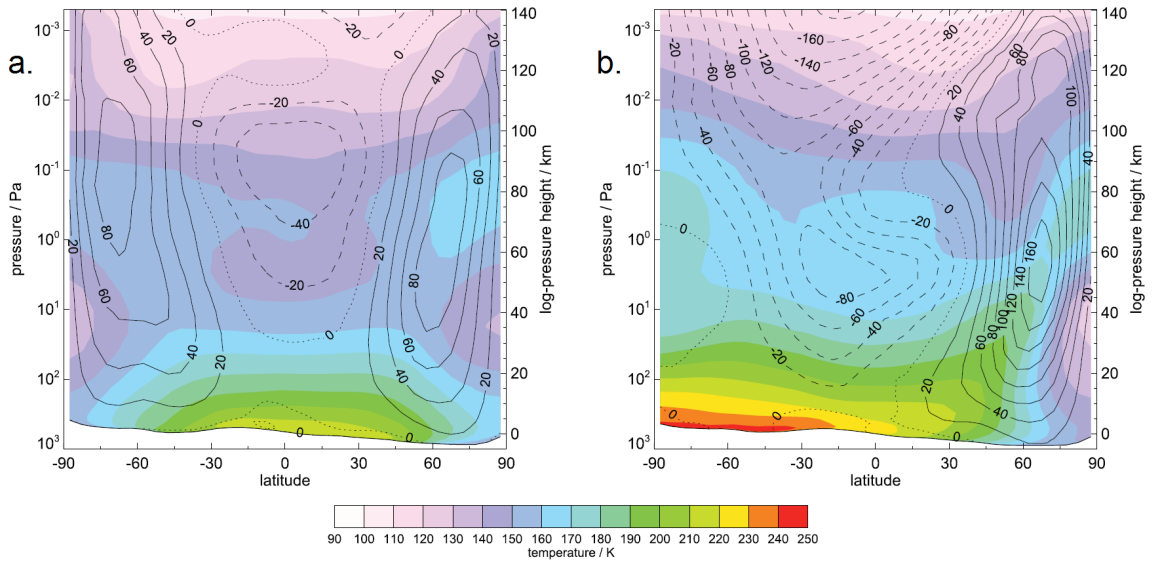

Fig. 2.4 Zonally averaged temperatures and zonal winds in a Mars GCM at (left) northern spring equinox (L_S=0) and (right) northern winter solstice (L_S=270°), with a logarithmic vertical axis representing pressure and log-pressure height. The contours at the bottom represent zonal-mean surface pressure. Reprinted with permission from Read et al. (2015).

2015). It is this depth of circulation that helps explain observed warming of the atmosphere above the winter pole, as visible in Fig. 2.4.b. The high asymmetry in thermal forcing at the winter solstice, enhanced by increased dust loading in the southern hemisphere and together with thermal tide effects, allow for the formation of a pole to pole Hadley cell able to transport heat above the north pole around northern winter solstice (Wilson, 1997). Despite the lower global dust loading around southern winter solstice, however, the magnitude of polar warming over the southern pole is comparable (McDunn et al., 2013).

Many key large-scale dynamical features can be derived from consideration of the gross thermal structure of the martian atmosphere and meridional circulation. Air masses originating near the equator rotate more rapidly than those at higher latitudes; therefore, the conservation of angular momentum implies that air masses moving poleward from the equator travel faster in the direction of planetary rotation (relative to the surface) at higher latitudes, causing the zonal jets visible in Fig. 2.4 (Read and Lewis, 2004). The sloping of the temperature structure at mid-high latitudes results in intersecting pressure and temperature

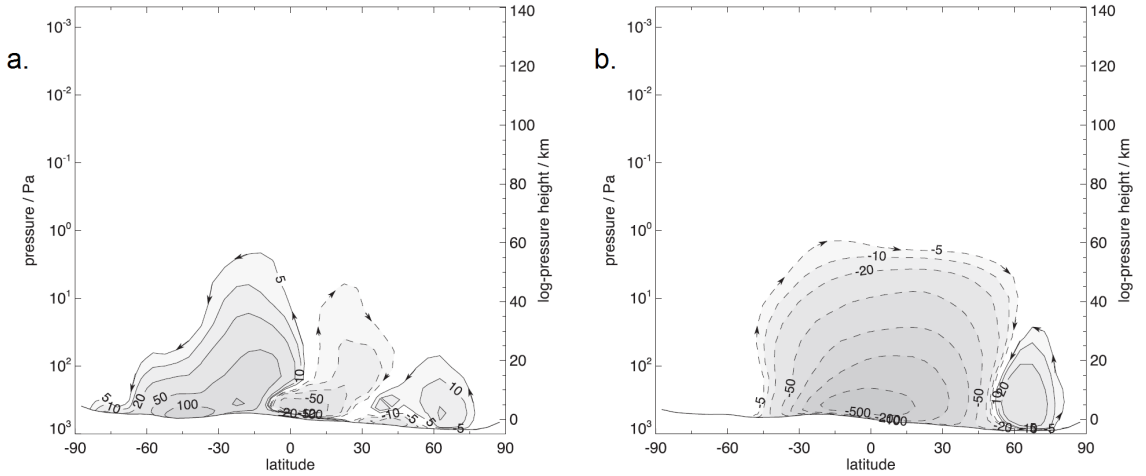

Fig. 2.5 The mean meridional circulation at (left) northern spring equinox (L_S=0) and (right) northern winter solstice (L_S=270°), with a logarithmic vertical axis representing pressure and log-pressure height. The contours at the bottom represent zonal-mean surface pressure. Reprinted with permission from Read et al. (2015).

contours, unlike in the equatorial regions. There, for example, a hot air mass displaced upwards into a colder region also experiences a reduction in pressure, thus bringing it into equilibrium; this is a barotropic region, such as the equatorial atmosphere during equinox in Fig. 2.4.a. When pressure and temperature contours intersect, however, disturbances can propagate; a hot air mass can move into a colder region without experiencing a change in pressure, allowing it to continue propagating. This is because a temperature gradient is present on a given surface of constant atmospheric pressure, thus enabling meridional heat transport in the form of waves, analogous to convection (this behaviour is therefore sometimes referred to as “sloping convection"). This condition of intersecting temperature and pressure contours is known as baroclinicity, and these propagating waves are called baroclinic instabilities (Holton, 2004e). In practice, they constitute much of what on Earth is considered “weather” in the mid-high latitudes. On Mars, such instabilities also occur, as visible in pressure data from the Viking landers (Collins et al., 1996) and have important effects on the circulation (Read et al., 2015); for example, they are associated with a certain type of“frontal” dust storm found at high latitudes (e.g. Wang et al., 2005). Evidence of such

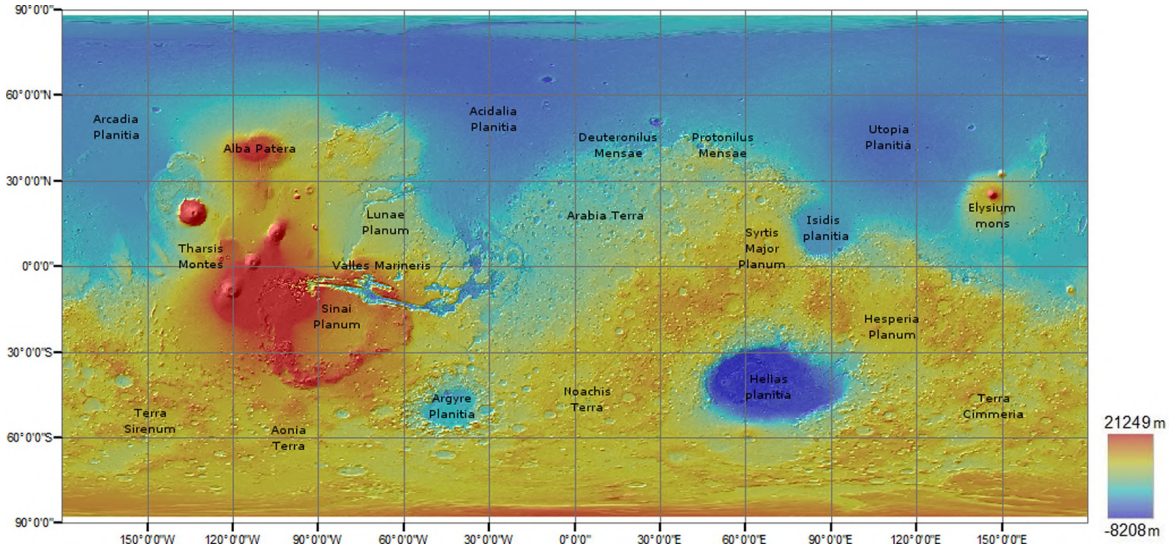

Fig. 2.6 Labelled topographic map of Mars using data from the Mars Orbiter Laser Altimeter (MOLA). Altitudes are relative to the areoid. Reprinted with permission from Souness and Hubbard (2012).

weather systems crossing the equator has been seen in pressure data from the Mars Science Laboratory (MSL) (Haberle et al., 2018), and high-resolution pressure measurements from the Insight lander will likely lead to greater understanding of these and other atmospheric phenomena (Banfield et al., 2020). Also modelled and observed via their effects on polar hood clouds are stationary (non-travelling) waves, forced by Mars' extreme topographic variations and therefore especially strong at northern mid-high latitudes, where as Fig. 2.6 shows there is huge longitudinal variation in elevation (e.g. Haberle et al., 2019; Pollack et al., 1981).

Mars' poles show distinctive dynamical and radiative features, related to the unique phenomenon of a CO_2 atmosphere that undergoes seasonal collapse and reinflation due to the cold temperatures of the planet. This seasonal pattern can be identified in surface pressure data, such as from the Viking landers (e.g. Hourdin et al., 1993). As mentioned above, Mars' poles show the presence of seasonal CO_2 ice coverage; this has been observed to demonstrate a high degree of interannual repeatability in latitudinal extent throughout the orbital cycle, though with longitudinal variability in structure as it grows or recesses (Calvin et al., 2017;

Piqueux et al., 2015). As CO_2 sublimation or condensation occur, there are associated dynamical features. The condensation flow at both caps has been modelled to be very weak, while the sublimation flow is much stronger particularly at the southern cap (where insolation is stronger during cap recession due to Mars' orbital eccentricity), reaching up to 10 m/s (Chow et al., 2019). There is observational evidence for this near-surface flow in the streaks left behind by subsurface jets which rupture the surface as the ice cover sublimes (Aye et al., 2019). Higher up in the atmosphere, Mars also displays strikingly distinct polar phenomena. Like Earth, Mars has polar vortices, areas of cold isolated air at the winter pole circumscribed by a strong zonal jet. Fig. 2.7 shows the potential vorticity structure of the terrestrial and martian polar atmospheres. Potential vorticity is a variable related to the rotation and static stability of the atmosphere, and is conserved under adiabatic processes, making it a useful diagnostic for polar dynamics; a greater magnitude of polar vorticity indicates a stronger polar vortex. Fig. 2.7 shows that Mars' polar vortices present a very different structure to their terrestrial equivalents, with a characteristic annular morphology and a notable ellipticity in the northern vortex (Mitchell et al., 2015). This shape is not instantaneously coherent however, but the averaged result of smaller coherent regions which show high variability on the timescale of a sol (Waugh et al., 2016). This distinctive annular shape is thought to be due to the uniquely martian phenomenon of condensing CO_2 ice at the poles, which releases latent heat thereby disrupting the vortices over the poles themselves (Rostami et al., 2018; Toigo et al., 2017) thus allowing the seasonal persistence of this otherwise barotropically unstable structure (Seviour et al., 2017).

2.4 Orbital observations

Satellites have been in orbit around Mars since the 1970s, with the Mars Global Surveyor (MGS) (1997-2007) and the Mars Reconnaissance Orbiter (MRO) (2006-present) being the most relevant to modern martian atmospheric research and this thesis. They have recently

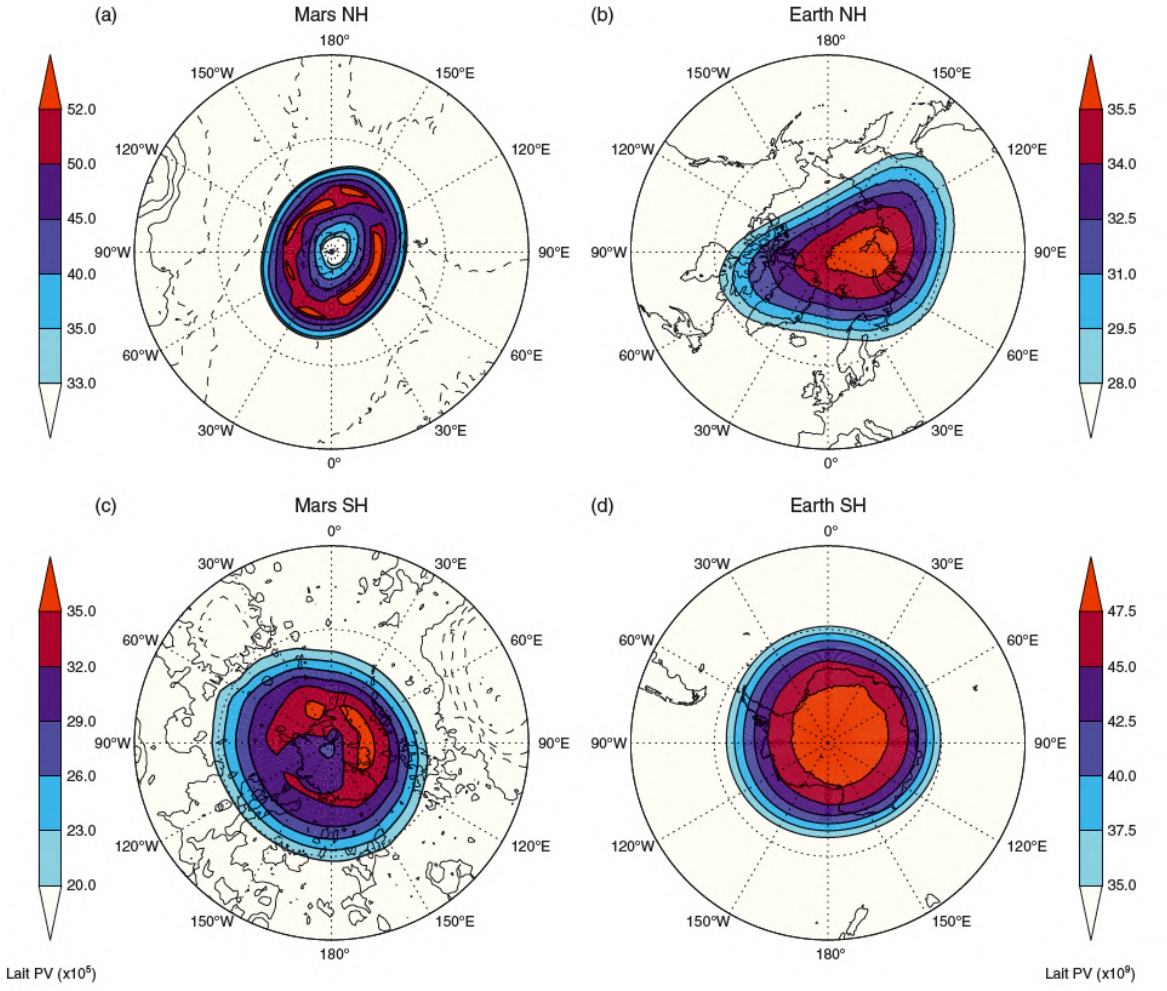

Fig. 2.7 Polar stereographic plots of winter-averaged Lait potential vorticity for (left) Mars on the 350 K isentropic surface (∼40 km) and (right) Earth on the 850 K isentropic surface (∼30 km) for (top) the northern hemisphere and (bottom) the southern hemisphere. Note the difference in scales. Contours represent topography. Reprinted with permission from Mitchell et al. (2015).

been joined by the ExoMars Trace Gas Orbiter (TGO) which, has been collecting data since 2018 with its NOMAD (Patel et al., 2017; Vandaele et al., 2015) and ACS (Korablev et al., 2017, 2015) spectrometers; TGO's orbit means it can measure over a range of local times, which should enhance future understanding of diurnal variability in the martian atmosphere. From Mars orbit, satellite instruments are able to retrieve useful quantities including atmospheric temperature, aerosol content, and chemical species (e.g. Urban et al., 2005). This section concentrates on the Thermal Emission Spectrometer (TES) aboard MGS and the Mars Climate Sounder (MCS) aboard MRO, as both have mature data products which were available throughout the writing of this thesis. MCS data, which was assimilated for the results presented in this thesis, is discussed in greater detail in Chapter 3.

2.4.1 MGS/TES

MGS is in a sun-synchronous orbit, meaning that observations are taken at two martian local times, roughly 02:00 and 14:00 (Smith, 2008). The TES instrument provided close to continuous global nadir coverage of the martian atmosphere for 6 years, or 3 martian years. Its main product was atmospheric temperature profiles with a vertical resolution of approximately 10 km from the surface to an altitude of 35 km, and a horizontal resolution of 9-20 km (Smith, 2004). Significantly less frequent limb observations also allowed for the extension of temperature profiles to approximately 65 km above the surface (Smith, 2004). Retrieval of temperature profiles allowed for calculations of the zonal temperature structure and the general circulation of Mars (Conrath et al., 2000).

Nadir observations from TES also allowed for the retrieval of atmospheric aerosols, specifically dust (Smith, 2004; Smith et al., 1999b). This was in the form of column-integrated dust opacity, with a well-mixed assumption for the retrievals, offering no information on the vertical distribution of the dust (Smith, 2004). The coverage of aerosol opacity was not as extensive as for temperature, due to the retrieval algorithm requiring a minimum

surface-atmosphere thermal contrast, resulting in a lack of coverage in regions with a surface temperature below 220 K (Smith, 2004). This resulted in a solar-latitude varying dust opacity coverage, visible in MYs 24-26 and part of MY 27 in Fig. 2.8. TES column integrated dust opacities are available for 3 MYs.

2.4.2 MRO/MCS

Like MGS, MRO is in a sun-synchronous orbit, making limb observations at 03:00 and 15:00 local time (Kleinböhl et al., 2009). The MCS instrument has been providing limb profiles of the martian atmosphere for over 5 martian years, including of temperature, water ice, dust, and condensates (McCleese et al., 2007). MCS limb observations can be used to retrieve temperature profiles up to 80 km above the surface, with a vertical resolution of 5 km and a horizontal resolution of approximately 5 degrees in longitude and latitude, roughly the resolution of most martian GCM grids (McCleese et al., 2010).

In addition to temperature, MCS profiles allow retrieval of pressure and vertical profiles of dust opacity and water ice opacity (Kleinböhl et al., 2009). Dust in particular can be retrieved with a vertical resolution of 5 km, from approximately 8 km to 40-50 km above the surface (Kleinböhl et al., 2009), giving a significant dataset of vertical dust profiles to be used for analysis and data assimilation (the latter concept is described in Chapter 3). Fig. 2.8 shows that despite some gaps in coverage (due to technical problems), dust opacity coverage in the MCS years (starting in MY 28) is generally near-continuous and global. A newer retrieval algorithm since the original retrievals outlined in (Kleinböhl et al., 2009) has been developed recently, in order to improve on the previous retrieval's assumption of spherical symmetry. These new 2D retrievals have significantly improved retrievals in the polar regions, where the spherical symmetry assumption falls down (Kleinböhl et al., 2017).

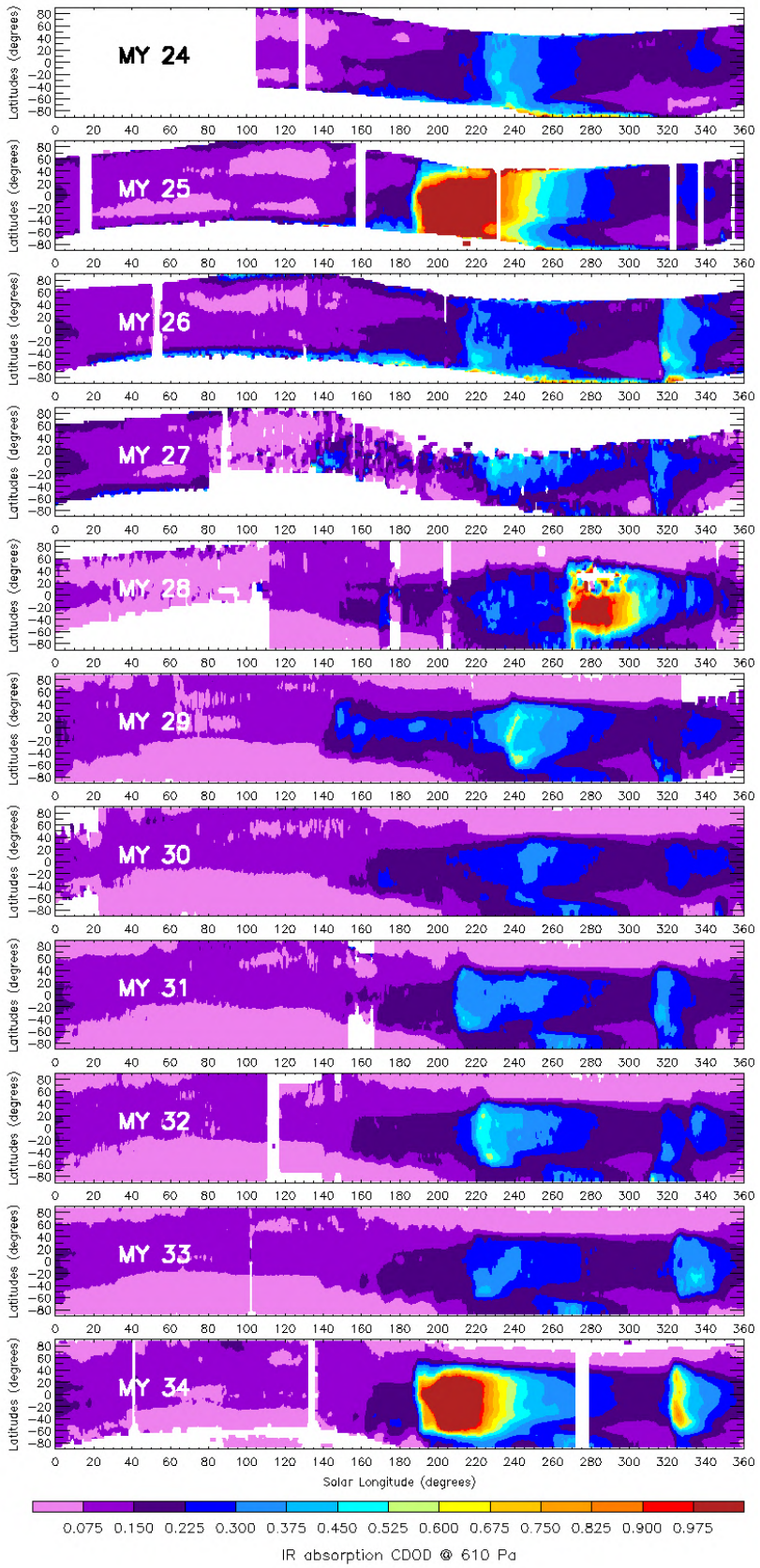

Fig. 2.8 Zonally averaged pressure-normalised infrared dust optical depths from Martian Years 24 to 34, using data from TES, Mars Odyssey's Thermal Emission Imaging System (THEMIS), and MCS. Reproduced with permission from Montabone et al., Multiannual Climatology of the Martian Atmospheric Column Dust Optical Depth, Mars Climate Database (http://www-mars.lmd.jussieu.fr/mars/dust_climatology/index.html.)

2.5 Atmospheric dust

The key radiative element in the martian lower and middle atmosphere is mineral dust. Mars' aridity contributes to an environment rich in dust, with a background visible atmospheric aerosol optical depth (OD) of 0.1-0.2 even during clear conditions which can increase up to 5 during periods of heavy dust loading (e.g. Fenton et al., 1997; Martin, 1986; Martin and Richardson, 1993). Mars has been estimated to have a dust-settling rate of approximately 20,000 $\mathrm{kg\,km^{-2}}$ per year, implying significant loading to replenish it (Pollack et al., 1979). On Earth, with exceptions, aerosol does not tend to vary significantly beyond a background level of <0.1 OD, with large increases often attributable to either moist air or the burning of biomass (Holben et al., 2001). Dust interacts with solar (0.3-4 μm) and thermal (4-25 μm) radiation in important ways, through scattering and absorption. Scattering of solar radiation cools the surface under large dust events (e.g. Sagan et al., 1973), but also acts to warm the atmosphere at night by scattering thermal radiation emitted from the surface (Read and Lewis, 2004). Significantly for the atmospheric temperature structure, dust absorbs solar radiation and re-emits in the infrared, causing local atmospheric warming (Gierasch and Goody, 1972). Mars' short radiative timescale means that these thermal forcing effects are extremely significant for the general circulation, and the dust distribution therefore represents the main source of uncertainty and interannual variability in the martian atmosphere.

2.5.1 Properties

Given the crucial radiative role played by atmospheric dust in the martian atmosphere, it is important to understand its radiative properties. These properties are determined by the physical characteristics of the mineral dust, its size distribution, and its atmospheric distribution, and while our knowledge of these characteristics has improved since the first Mars missions, they are often still poorly constrained. The physical characteristics in particular often have a high degree of wavelength-dependency, making retrieval a difficult

and ill-constrained problem to solve. The current best estimates used in the Open University's Mars climate model (discussed in Chapter 3) are from Wolff et al. (2006) and Wolff et al. (2009). Using combined rover and orbiter observations, they found that the mean effective dust particle radius ranged from 1.3 to 1.8 μm, though with spatial and vertical variability apparent. According to Mie scattering theory, this implies the strongest interaction occurs with wavelengths of ∼1-2 μm, ie. solar radiation.

Wolff et al. (2006) and Wolff et al. (2009) also extracted scattering properties over a range of wavelengths, visible in Fig. 3.1, where Q_{ext} is the efficiency of the dust in extinguishing the light beam, ω represents how much the particles scatter light, and g is a measure of the asymmetry of the scattering. It can be seen that all three depend strongly on the incident wavelength. At the same time, even minor differences in these values as used in climate models can have an enormous effect on radiative heating rates; for example, g affects the degree of backscattering of radiation and thus the amount of solar radiation which enters the atmosphere (see Madeleine et al., 2011, for further discussion).

The main metric used to measure dust in the atmosphere is column dust optical depth (CDOD), which consists of the sum of the scattering and absorption optical depths, and is usually measured in the infrared due to the lower scattering rates (see Fig. 3.1). This provides a representation of the total amount of dust in a column of the atmosphere, from the top to the surface. Another commonly used metric is density-scaled opacity (DSO), which is the opacity (optical depth) divided by the atmospheric density. This metric has the value of being proportional to the dust mass mixing ratio (the ratio of dust mass to atmospheric mass) (McCleese et al., 2010).

2.5.2 Distribution

Detailed observations from the TES instrument have revealed the seasonal patterns of dust opacity in the atmosphere, roughly divisible into two distinct seasons: a "clear" season

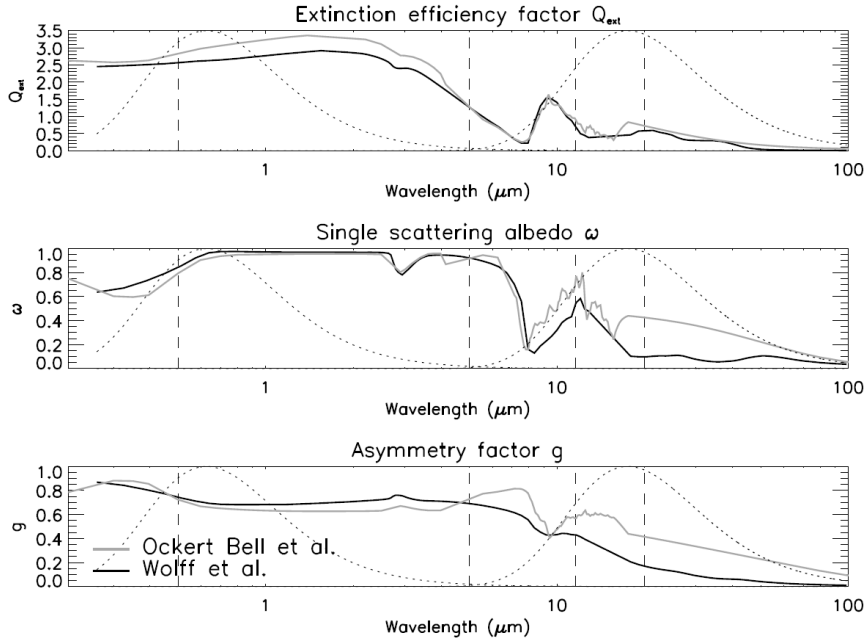

Fig. 2.9 Dust scattering parameters at solar wavelengths from Ockert-Bell et al. (1997) and at infrared wavelengths from Forget (1998) (grey line), and at all wavelengths from Wolff et al. (2006) (black line). Background dashed curves represent normalised black body spectra for (left, solar) 5870 K and (right, Mars) 210 K. Reprinted with permission from Madeleine et al. (2011).

between L_S=0-180°, and a "dusty" season between L_S=180-360°, when most dust storm activity occurs (Smith, 2004). This regular pattern is visible in observations from the martian surface such as from the Viking landers (Colburn et al., 1989) and the Mars Exploration Rovers (Lemmon et al., 2015; Smith et al., 2006), and from orbit as seen in the column dust opacity measurements in Fig. 2.10; this pattern has also been replicated in modelling work (e.g. Kahre et al., 2006; Newman et al., 2002a). The presence of this pattern can be ascribed to the orbital obliquity of Mars, discussed previously: the period of increased dust opacity corresponds to Mars' warmer perihelion season, when solar insolation is greatest, intensifying the circulation and increasing dust lifting activity. However, amid this regular pattern there is also an interannual variability in dust optical depth, most pronounced in the dusty season (Smith, 2004). A lot of this variability can be ascribed to the variable activity of local and regional dust storms (Kass et al., 2016). The source of the greatest interannual variability however, visible in the extremely high dust opacities between L_S=180-270° of MY 25 in Fig. 2.10, is the global dust storm (GDS). Spatially, the dust opacity remains fairly constant during the clear aphelion season but experiences significant variability due to dust storms in the dusty season. However, recent observations from MCS indicate a more complex picture around the poles, with apparent exclusion of dust inside the polar vortex, especially at the south pole (McCleese et al., 2017). This is despite the presence of water ice high above the pole, which implies transport by the mean meridional circulation.

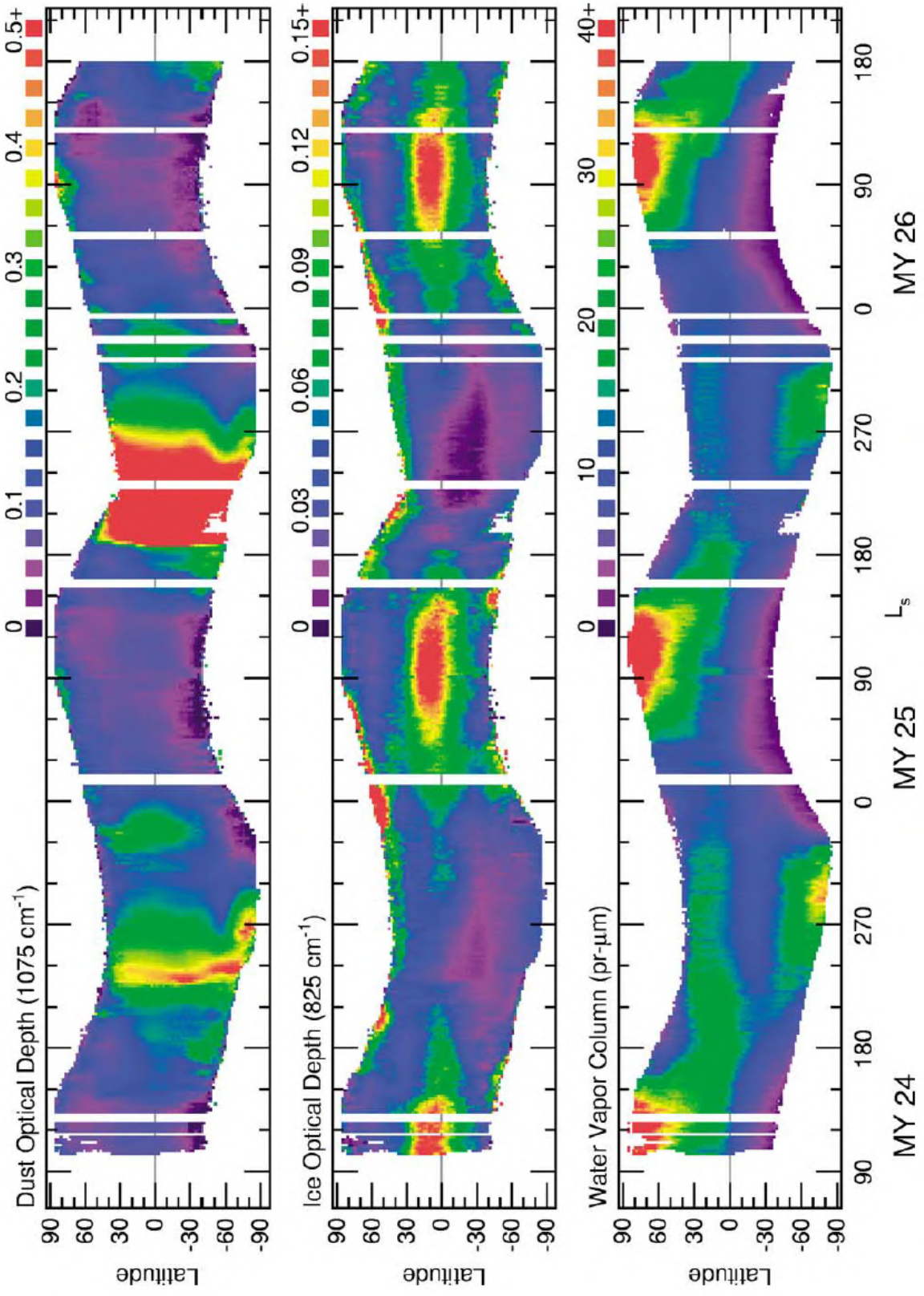

Fig. 2.10 Zonally averaged dayside measurements from TES over three MYs of, from top to bottom: column dust optical depth, ice optical depth, and water vapour column abundance. Data is binned in L_S bins of $\sim 5°$. Reprinted with permission from Smith (2004).

The vertical distribution of Mars' atmospheric dust remained for a long time unobserved from orbit, until measurements from the MCS instrument revealed a more complex vertical structure than previously assumed. Conrath (1975)'s observations of the 1971 GDS led him to develop an analytical vertical profile based on a theoretical treatment of the predominant vertical transport mechanisms affecting dust: gravitational sedimentation and vertical eddy mixing. This profile assumed a "well-mixed" region of constant dust opacity, typically extending up to $\sim$10-20 km, followed by a monotonic decrease in dust opacity with height. Profiles based on this assumption have subsequently been the standard for Mars climate models, as discussed in Chapter 3. However, the MCS instrument revealed the surprising existence of "detached dust layers" (DDLs), persistent regions of local dust opacity maxima located high above the surface (McCleese et al., 2010) and visible in Fig. 2.11, particularly in the plots corresponding to northern spring/summer. These layers have been seen at heights of 15-25 km in the tropics, contradicting the well-mixed assumption and indicating the presence of physical processes unaccounted for in the Conrath theory. The existence of DDLs was subsequently confirmed using limb observations from the TES instrument, spotting the tropical DDLs at heights of 20-30 km as well an even more elevated "upper dust maximum" at 45-65 km altitude (Guzewich et al., 2013a), and by the Compact Reconnaissance Imaging Spectrometer for Mars (CRISM) aboard MRO (Smith et al., 2013). The behaviour of these layers has also been examined, showing high diurnal variability (Heavens et al., 2011b) which cannot be reproduced by current modelling (Navarro, 2016; Navarro et al., 2014). This diurnal variation is also not geographically fixed, suggesting that variable mechanisms are at work (Heavens et al., 2014). While DDLs are found throughout the martian year, they are most commonly found in the tropics during Mars' aphelion season, when dust storm activity is at a minimum (Heavens et al., 2014).

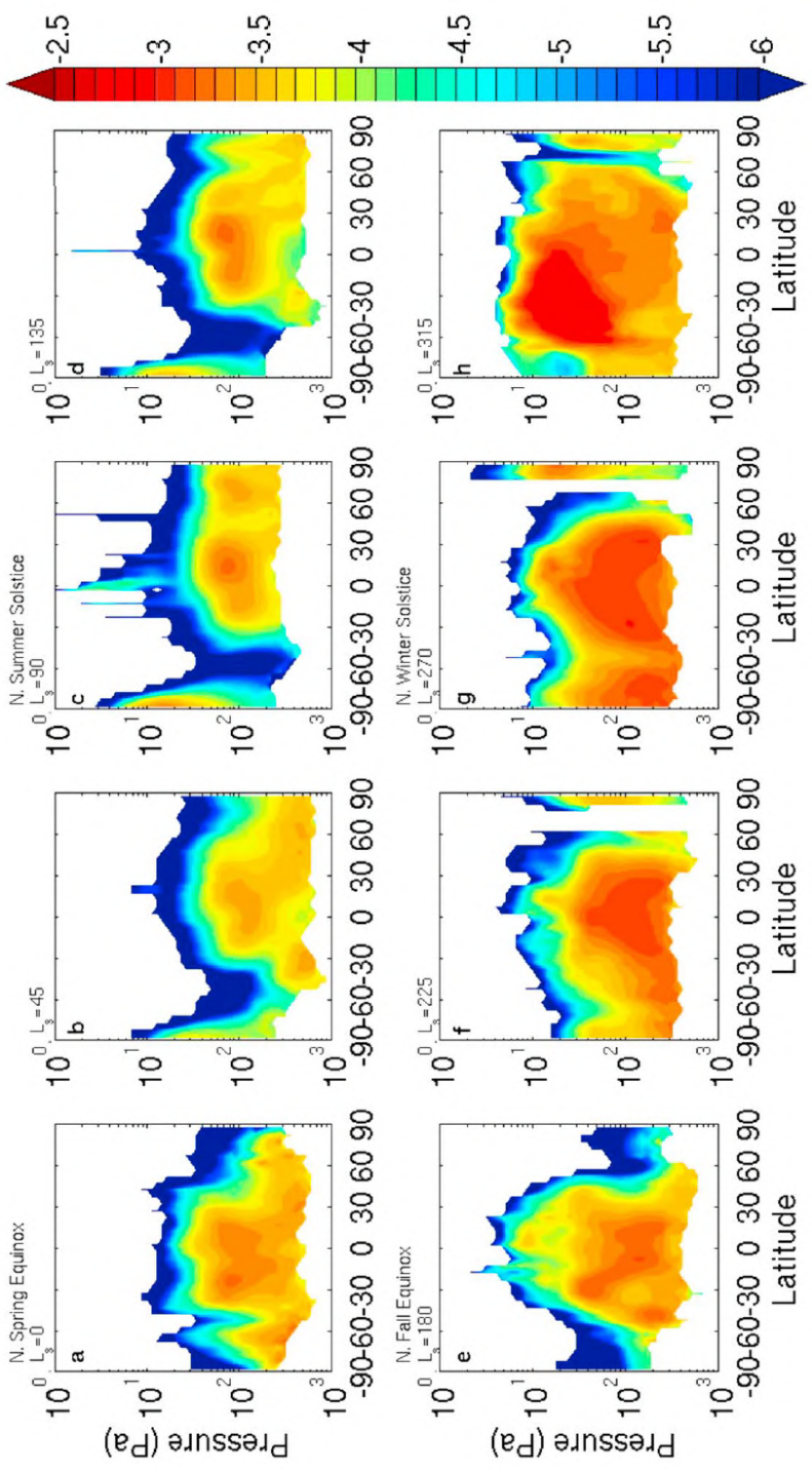

Fig. 2.11 Log_{10} zonally-averaged nightside density-scaled dust opacities from MCS for MY 29. Reprinted with permission from McCleese et al. (2010).

2.5.3 The dust cycle

Mars has a dynamic dust cycle consisting of lifting processes, transport processes, and removal processes. The various dust lifting processes which occur are parametrized in martian GCMs via two general mechanisms: near-surface wind stress (NSWS) and dust devils. NSWS acts to either directly lift particles for suspension in the atmosphere or to suspend them through the process of saltation, where heavy particles are briefly carried and dropped to cause lifting of finer particles (Kok et al., 2012), as illustrated in Fig. 2.12. Saltation in particular helps to explain the presence of the fine ie. $\sim$1.5 micron particles in the atmosphere, as the presence of inter-particle attractive forces makes such fine particles harder to directly lift than larger particles which rapidly fall out of suspension (Read et al., 2015). Indeed, numerical studies have suggested that the typical particle size found in the atmosphere would be unable to be lifted by typical martian wind speeds, emphasising the importance of saltation (Shao and Lu, 2000). NSWS lifting appears from modelling of radiatively active dust to have a positive feedback relationship with the circulation, with increased NSWS lifting causing atmospheric warming and intensifying the circulation, leading to further lifting (Murphy et al., 1995; Newman et al., 2002b). NSWS lifting is associated with dust storm activity, both from modelling work (e.g. Basu et al., 2004; Kahre et al., 2006; Newman et al., 2002a,b) and from observations that dust storms are far more prevalent during Mars' perihelion season, when the increased solar insolation intensifies the circulation (e.g. Smith, 2004; Wang, 2007; Wang and Richardson, 2015, see 2.5.4 below for more detail). Dust devils, by contrast, appear to be linked more to the constant background haze of dust on Mars (e.g. Kahre et al., 2006).

Dust is transported throughout the atmosphere by several known mechanisms. Spatially, the martian circulation determines where lifted dust is taken, with the mean meridional circulation transporting dust horizontally and vertically. On a more spatiotemporally local scale, most NSWS lifting is associated with dust storms, and so lifted dust travels with the

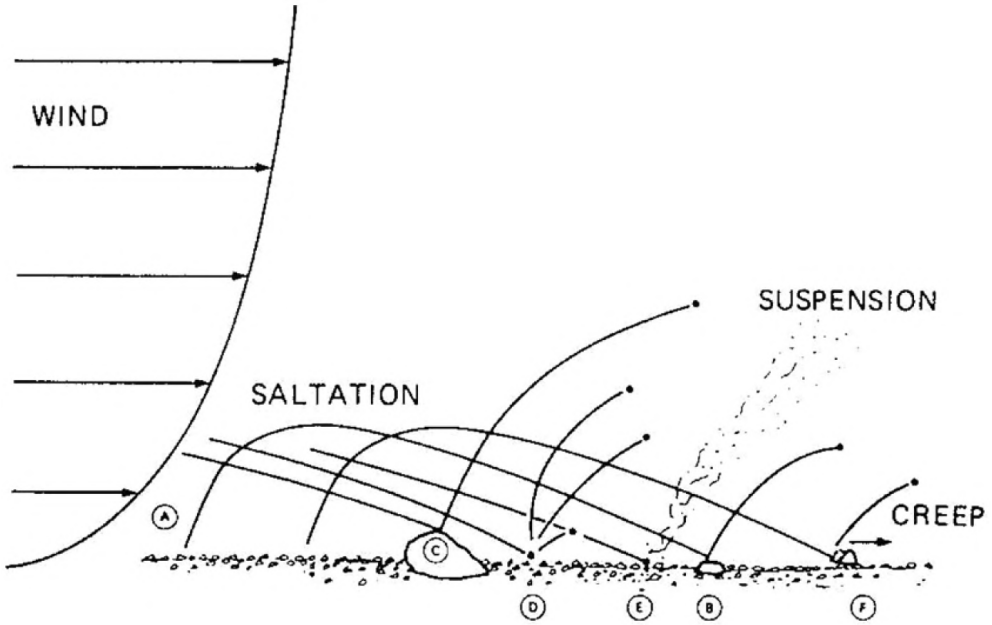

Fig. 2.12 Illustration of saltation causing suspension of particles. Reprinted with permission from Read et al. (2015), after Greeley and Iversen (1985); refer to those for further explanation of labels.

storm, with several known "storm tracks" existing (Colaprete et al., 2005); regional and global dust storms are also capable of great vertical transport of dust (Clancy et al., 2010). Dust devil lifting often takes place within the planetary boundary layer (PBL), allowing entrained dust to avoid the higher wind shears above the PBL and contributing to the martian haze. Vertically, convective eddy mixing in the PBL allows lifted dust to move upwards and enter the free atmosphere above the PBL. Topographic winds from volcanoes have also been predicted to play a role in vertical dust transport, based on the observation and reproduction by model of a spiral dust cloud over Arsia Mons (Rafkin et al., 2002). Modelling of non-radiative dust tracer transport has suggested a balance between vertical mixing forces and the mean meridional circulation, with the latter gaining dominance at solstice and the former at equinox (Barnes et al., 1996).

More recently, the discovery of DDLs has spurred investigation of further possible transport mechanisms. One widely proposed mechanism is the buoyancy caused by solar heating

of already suspended dust; this warming of the dust produces a concurrent local atmospheric warming, lifting the dust higher into the atmosphere. This self-lifting phenomenon has been observed as a mechanism of vertical aerosol transport on Earth, but the first to propose its presence on Mars was Fuerstenau (2006), as an explanation for the great height of martian dust devils. Subsequently, it has been invoked as a mechanism for the formation of DDLs in theoretical work by Rafkin (2012) and modelling work by Spiga et al. (2013) and Daerden et al. (2015). Rafkin (2012) proposed that self-lifting could cause a form of non-local deep dust transport, with dust rapidly rising in discrete updrafts in contrast to the slower, diffuse process of turbulent mixing in the PBL. While the modelling work differs slightly in the proximate cause of the suspended dust, it shares a fundamental idea that self-lifting of suspended dust allows discrete dust clumps to penetrate the top of the PBL, where they are then subjected to wind shear thus forming the observed dust "layers". However, these proposed mechanisms have not been observationally verified as of yet.

2.5.4 Dust storms

Dust storm activity is correlated with the perihelion season, which sees a greater number and size of dust storms than the aphelion season, as visible in Fig. 2.14. Dust storms can range greatly in size, from local ($\sim 10^5$ km^2) through regional ($\sim 10^6$ km^2) (e.g. Fig. 2.13) to global storms able to significantly impact the circulation of the whole planet (Martin and Zurek, 1993). While the annual occurrence of the dusty season is itself regular, it experiences significant interannual variability when it comes to the actual locations, size, and timing of the storms (Kass et al., 2016). However, some regularities have been discerned. Kass et al. (2016) identified three recurring species of regional dust storm during the dusty season. "A" storms occur early in the season and encircle the southern hemisphere; "B" storms occur near the south pole and last through L_S=270°; and "C" storms occur late in the season, some time after the end of the "B" storm, and show the most interannual variability. The "A" and

"C" type storms appear to originate in northern midlatitudes, consistent with observed lifting and storm creation by baroclinic eddies in this region (e.g. Wang et al., 2013, 2005), before crossing the equator and growing to their full scale in the southern hemisphere. "B" storms, on the other hand, originate from dust lifting near the polar cap edge, where the temperature contrast produces greater winds for dust lifting (Guzewich et al., 2017). Regional storms have been observed to contribute to the redistribution of dust throughout the martian surface (Cantor, 2007). Analysis of optical imagery of regional storms has estimated a dust loading of between 173 and 1200 $\mathrm{kg\,km^{-2}}$ per sol (Cantor et al., 2001). Interestingly, there appear to be spatial and temporal thresholds on the radiative and dynamical impacts of non-global dust storms, with local storms causing little perturbation to the background atmosphere and regional storms only having significant impacts if the storm has a duration of 10 sols or greater (Toigo et al., 2018). A regional "C" storm in an assimilated model of TES temperature and dust retrievals for MY 26 (the MACDA dataset (Montabone et al., 2014)) appeared to have significant dynamical impacts, shifting the northern polar vortex equatorward by 10° (Mitchell et al., 2015).

Each regional storm type has a chance to become a global dust storm (GDS) (visible in Fig. 2.15), but the necessary and sufficient conditions to take place are an open topic of debate. They occur infrequently, approximately every 3 or 4 martian years in recent times, last months, develop rapidly, and are capable of lifting dust to heights of 60-80 km (Clancy et al., 2010). Their presence can raise the global dust from a background dusty season average visible optical depth of 0.6-1 to 3-4 (Smith et al., 2002). Proposed mechanisms for their formation include a feedback between southern dust loading and the suppression of northern baroclinic activity (Haberle, 1986), the presence of an activation threshold for high dust lifting which is only sometimes met (Basu et al., 2006), the redistribution of surface dust to create varying lifting thresholds throughout the planet (Mulholland et al., 2013), and

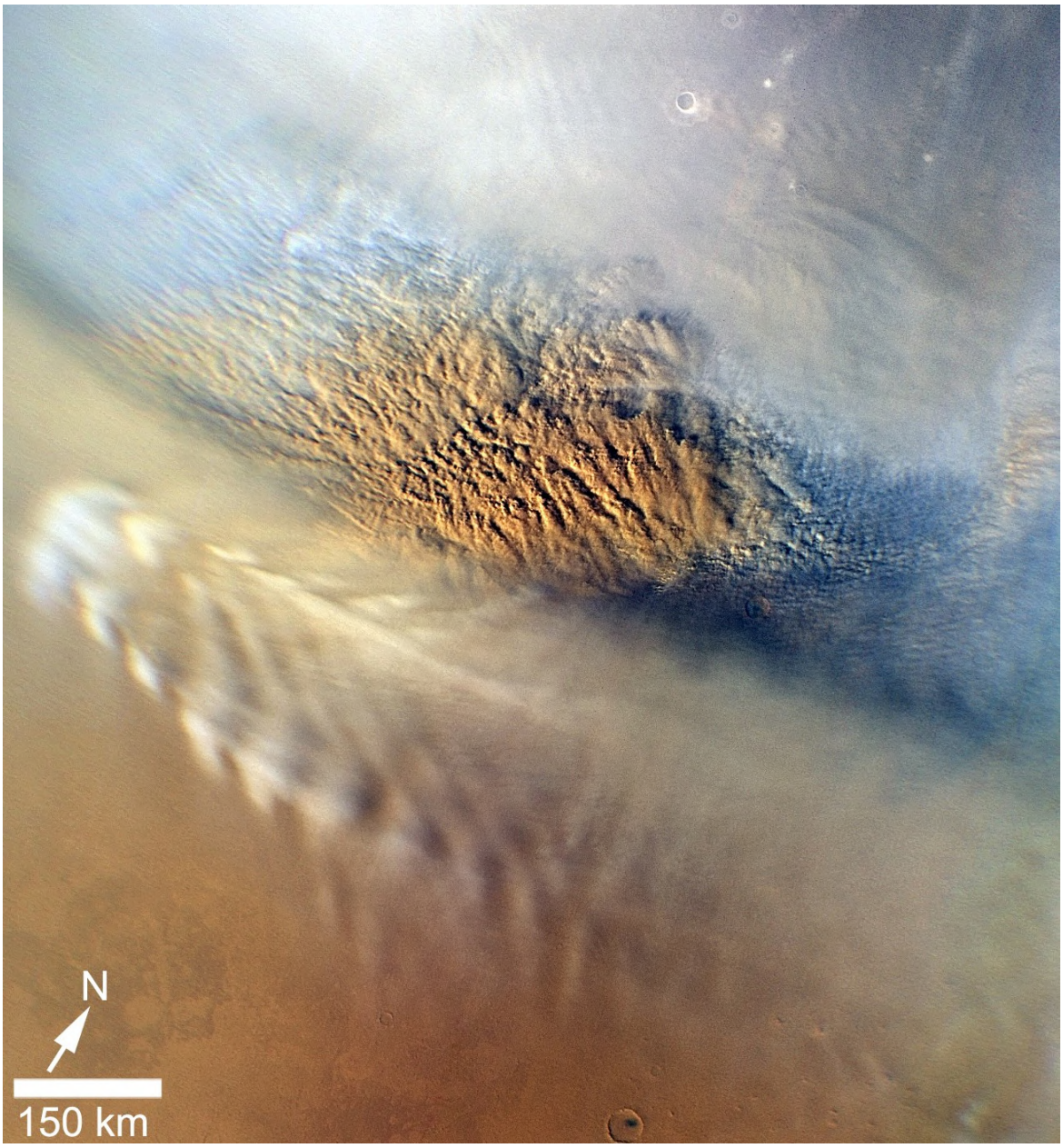

Fig. 2.13 Close-up of a small regional-scale dust storm as observed by the Mars Reconnaissance Orbiter's Mars Color Imager (MARCI) over Utopia Planitia at 53.6° N, 147.9° E during late northern winter. Orographic water ice clouds are also visible in the bottom of the image. Credit: NASA/JPL-Caltech/MSSS.

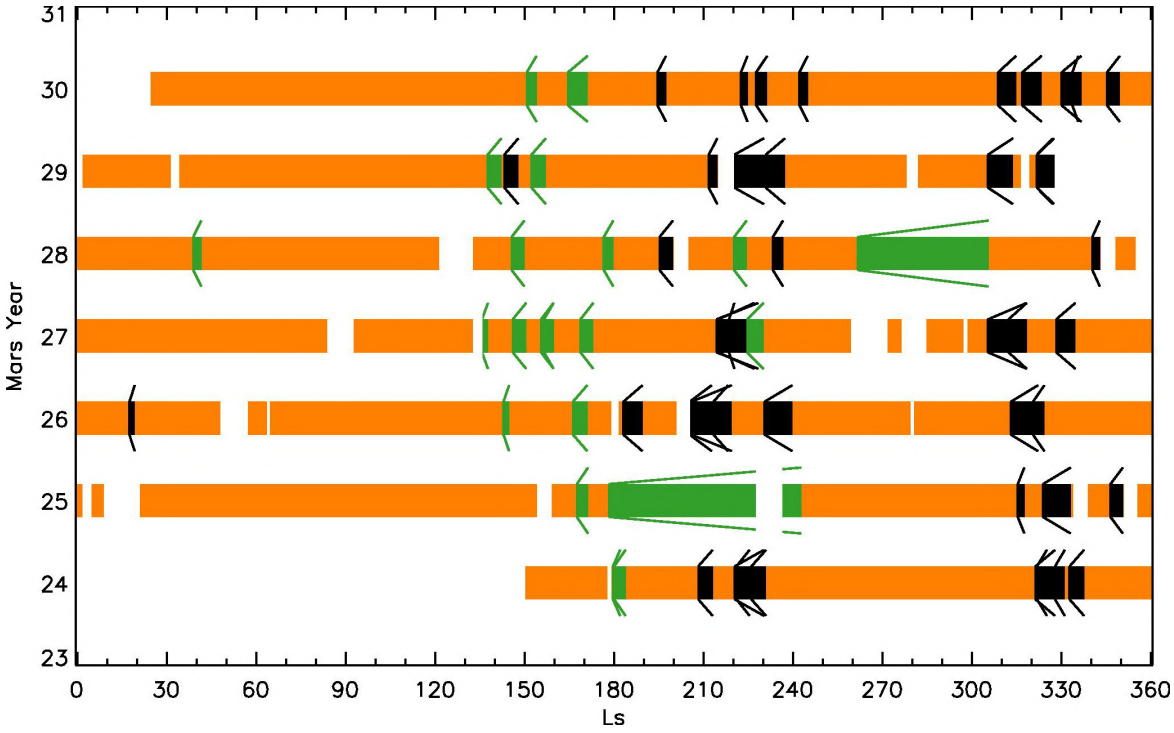

Fig. 2.14 Large (regional-scale) dust storms observed by the Mars Global Surveyor's Mars Orbiter Camera (MOC) (MY 24-28) and MARCI (MY 28-30) from MY 24 to 30. Orange indicates no storms seen, black indicates a northern hemisphere originating storm, and green a southern hemisphere originating storm. Brackets indicate the beginning and duration of each storm, while gaps indicate gaps in coverage. Reprinted with permission from Wang and Richardson (2015).

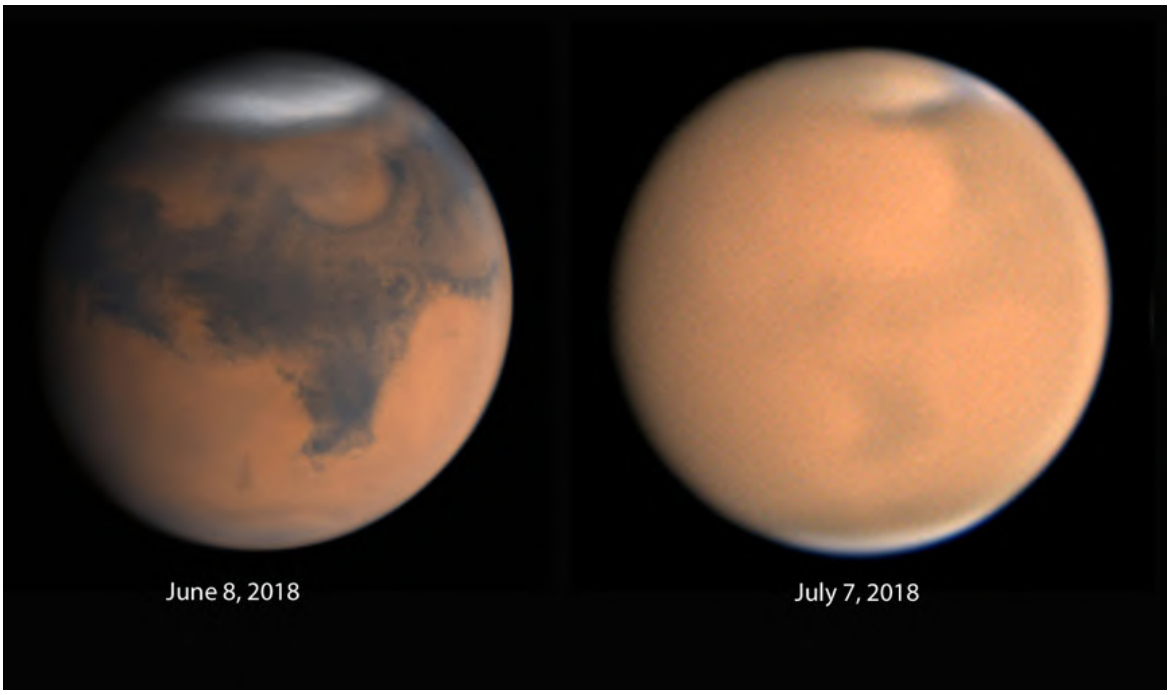

Fig. 2.15 Amateur ground-based telescope images of Mars (left) early into and (right) at the peak of the 2018/MY 34 global dust storm. Credit: Damian Peach/Chilescope team (left), Christophe Pellier (right).

intrinsic chaotic interactions in the martian climate system (Ingersoll and Lyons, 1993), to name a few.

The radiative effects of regional and global dust storms are significant. The first global dust storm to be observed in detail by an orbiter was the 2001 (MY 25) GDS, which was seen by the TES instrument to cause daytime atmospheric temperature rises of over 40 K in the southern hemisphere and an increased amplitude of the thermal tides (Smith et al., 2002), while decreasing the surface temperature by 20 K at the storm's peak by cutting off solar insolation (Gurwell et al., 2005). The specific effects on the thermal tide and wave activity have been found to be highly dependent on the exact zonal dust distribution, which is as important as the global dust optical depth for the purpose of understanding the dynamical effects of global dust storms (Guzewich et al., 2014). Other effects have been modelled for equivalently high dust loadings, such as the intensification of the mean meridional circulation (e.g. Barnes et al., 1993; Wilson, 1997), the enhancement of the solsticial pause in (mostly

northern hemisphere) baroclinic wave activity (Lewis et al., 2016; Mulholland et al., 2016), atmospheric superrotation (Lewis and Read, 2003), and disruption of the northern polar vortex (Guzewich et al., 2016). Near surface wind speeds from an assimilated model of the MY 25 GDS were found to be consistently higher than climatological values (Montabone et al., 2005). TES observations during the MY 25 GDS showed enhanced thermal tide activity, particularly in the wavenumber 1 and 2 modes (Guzewich et al., 2014), as well as accelerated recession of the southern seasonal CO_2 cap (Piqueux et al., 2015) and visible alteration in surface thermal inertia and albedo implying large-scale dust redistribution (Szwast et al., 2006). MCS observations during the 2007 (MY 28) GDS showed enhanced polar warming over the northern winter pole (McDunn et al., 2013), as well as evidence of enhanced hydrogen escape from the dust heating (Heavens et al., 2018).

The more recent 2018 (MY 34) GDS was the most-observed such event in history, with numerous orbiters and rovers able to measure its various effects. It thus represents an unprecedented opportunity to better understand the behaviour and impact of such phenomena. MCS observations of the MY 34 GDS show it lasting from approximately L_S=186°to sometime between L_S=270-281°, with a peak atmospheric temperature of 238 K at L_S=207° (Kass et al., 2019), and covering approximately 75° S to 45° N at its greatest latitudinal extent, as seen in Fig. 2.16. The MY 34 GDS was noted as having a remarkably similar spatiotemporal structure to the MY 25 GDS with similar effects on the temperature structure (Kass et al., 2019), as well as significantly enhanced dynamical heating at high latitudes of both hemispheres (Shirley et al., 2019). The spatiotemporal extent and surface effects of the MY 34 GDS are discussed in more detail in Chapter 4. MCS observations of this event and the MY 28 GDS also showed a significant role for episodic and spatially heterogeneous dusty deep convection and large plumes in the initial growth and spread of the GDS (Heavens et al., 2019). For the MY 34 event, MCS observations also showed a southern polar vortex shifted completely onto the nightside of the planet (Kleinböhl et al., 2020), confirmed by Mars

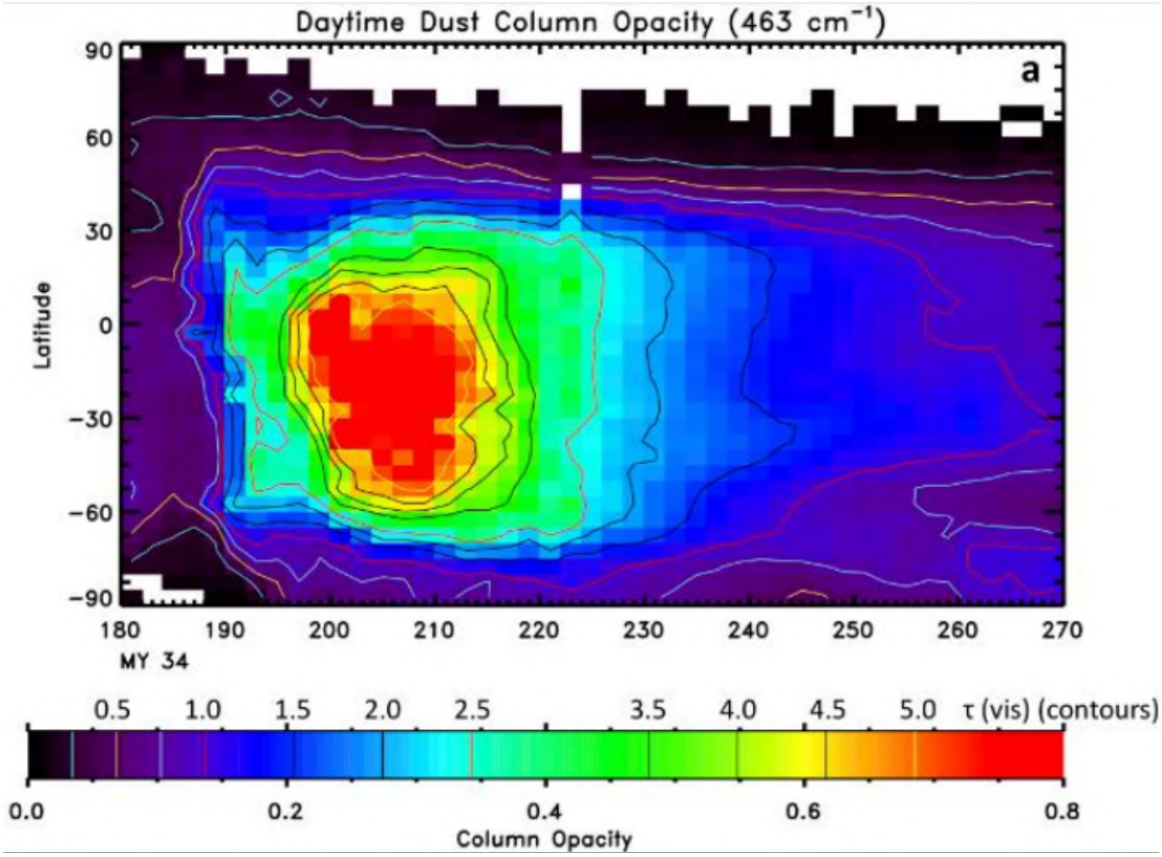

Fig. 2.16 L_S-latitude plot of daytime infrared and visible CDOD as derived from MCS observations for the 2018/MY 34 GDS. Reprinted with permission from Kass et al. (2019).

Express (Hernández-Bernal et al., 2019), indicating a substantially strengthened meridional circulation. On the ground, MSL measured significant changes in ground and air temperatures (Guzewich et al., 2019), unprecedented lofted dust particle sizes of up to 4 µm (Lemmon et al., 2019), and persistent post-GDS surface pressure changes possibly indicating changes to the northern and southern seasonal CO_2 ice caps (Juarez et al., 2019). Observations from the ExoMars Trace Gas Orbiter's NOMAD (Aoki et al., 2019) and ACS (Fedorova et al., 2020) instruments, coupled with modelling (Neary et al., 2020), suggest that the GDS heating induced much higher water vapour transport than in years without a GDS, lending support to the idea that GDS enhance escape of hydrogen from the atmosphere into space.

2.6 Summary

This chapter has introduced the most pertinent features of the martian atmosphere and the role of dust aerosol within it. Suspended mineral dust is the key radiative component in Mars' arid, thin atmosphere, and has significant impacts on dynamics and the global energy budget. By absorbing and scattering electromagnetic radiation at solar and infrared wavelengths, dust helps determine the thermal and wind structure of Mars' atmosphere. Periods of high dust loading, such as those induced by Global Dust Storms, therefore have major effects on almost every other aspect of the atmosphere; from surface and atmospheric temperatures to global dynamical processes, including at the poles, to the distribution of other elements such as water vapour. As well as being an important radiative component, dust is also governed in its distribution and behaviour by the very dynamical processes it can affect: it can be lifted by near-surface winds and transported around the planet by the global circulation before sedimenting back onto the surface, altering surface properties such as albedo and thermal inertia as it does so. This interdependence between the spatiotemporal dust distribution and atmospheric dynamics makes understanding their relationship a nonlinear problem, ripe with feedbacks. Observations have been able to better constrain the dust distribution and its effect on atmospheric temperatures, including that of regional and global-scale storms. Numerical modelling has provided insight into the mechanisms behind the observed distribution, such as dust lifting and its link to the seasonal cycle of observed opacity, and has been able to provide understanding of the dynamical changes which result from dust's radiative impacts.

The results presented in this thesis aim to combine the power of these two investigative techniques through the method of data assimilation, described in detail in the next chapter. Incorporating actual dust and temperature data into a numerical model of the atmosphere enables investigations into how the real martian atmosphere behaves under the high dust loading caused by the 2018 Global Dust Storm. Chapter 4 investigates how this event affected surface and near-surface air temperatures across the planet, with comparisons to observational

data from various sources; Chapter 5 broadens this investigation to near-surface wind speeds and associated wave activity; and Chapter 6 focusses on how the storm affected dynamics over both poles. Data assimilation also allows study of how the dust cycle itself, via lifting and deposition, is linked to the large-scale atmospheric dynamics. Chapter 5 examines dust lifting and deposition over multiple martian years, including that of the 2018 Global Dust Storm; and Chapter 6 narrows this focus to potential lifting mechanisms around the southern seasonal ice cap.

Chapter 3

Methodology: modelling and data assimilation

This chapter discusses the methodology employed in this thesis. First, the utilised numerical model of the martian atmosphere is described, with special attention paid to the parametrization and treatment of atmospheric dust aerosol: its radiative properties, implementation as a tracer, and spatiotemporal distribution. Next, the concept of data assimilation is introduced and the specific data assimilation scheme used for this thesis is described in detail. Lastly, the orbital data from the Mars Climate Sounder used in the data assimilation scheme is described, and the experiments conducted in this thesis are introduced.

3.1 The Mars Global Climate Model (MGCM)

An invaluable tool for studying the atmosphere on Earth emerged during the twentieth century in the form of "global climate models" (GCMs), four-dimensional numerical models of the atmosphere. Leovy and Mintz (1969) first adapted the UCLA terrestrial GCM to Mars conditions, and further work on Mars GCMs was conducted at NASA Ames (Haberle et al., 1993; Pollack et al., 1981). Later, the Laboratoire de Météorologie Dynamique (LMD) in

France developed their own Mars GCM (Hourdin, 1992; Hourdin et al., 1993), a joint effort between the Universities of Oxford (Joshi et al., 1994; Lewis and Read, 1995) and Reading (Collins et al., 1995, 1997) in the UK developed a GCM for Mars with a spectral dynamical core, and the GFDL in Princeton, USA developed their own Mars GCM, sharing physics with the NASA Ames model (Wilson and Hamilton, 1996). A joint effort between the University of Oxford and the LMD resulted in a Mars GCM (Forget et al., 1999) subsequently adopted and adapted by the Open University. The model used in this project is the version of this joint model with a spectral rather than a grid-point dynamical core, as opposed to most other Mars GCMs; this model, also known as the UK version of the LMD Mars GCM, will be subsequently referred to in this thesis as "the MGCM".

The MGCM is a four-dimensional numerical model of the martian atmosphere consisting of a dynamical core, which solves the primitive equations of fluid dynamics in the atmosphere, and physical parameterisations of processes such as radiative effects, CO_2 condensation, dust lifting, gravity waves, and more. The model grid itself is described in greater detail in Section 3.1.3.

3.1.1 Dynamics

The dynamical core of the MGCM consists of a spectral solver of the "primitive equations" of large-scale atmospheric motion using truncated series of spherical harmonics, based on a model developed at the University of Reading by Hoskins and Simmons (1975). It uses σ-coordinates to represent vertical height, where σ is the quotient of pressure at a given model layer and the pressure at the surface, $\sigma = p/p_s$. This allows the vertical layers to track the planet's topography.

What follows is a brief overview of the primitive equations of atmospheric motion, following Holton (2004b,c). There are three fundamental conservation principles to consider in formulating the primitive equations.

The first conservation principle is the conservation of momentum. Newton's second law of motion can be recast for motion in a rotating coordinate frame, such as a roughly spherical planet. Assuming that the only "real" forces (ie. not "pseudo-forces" due to the rotating reference frame, like the centrifugal and Coriolis forces) acting on the atmosphere are the gravitational force, frictional forces, and the pressure gradient force leads to the formulation

$$\frac{D\mathbf{U}}{Dt} = -2\Omega \times \mathbf{U} - \frac{\mathbf{1}}{\rho}\nabla_p + \mathbf{g} + \mathbf{F}_r \tag{3.1}$$

where $\mathbf{U}$ is the vector of velocity relative to the planet's rotation, Ω is the velocity vector of the planet's rotation, ρ is the atmospheric density, p is the atmospheric pressure, $\mathbf{g}$ is the effective gravitational acceleration vector (including the centrifugal pseudo-force), and $\mathbf{F}_r$ is the vector representing frictional acceleration. In other words, the acceleration of an air parcel is equal to the sum of the planet's rotational force, the pressure gradient force, the effective gravity force, and frictional forces (Holton, 2004b).

While it is possible to formulate the full momentum equation in the vertical dimension, the MGCM is a hydrostatic model, meaning that its primitive equations are formulated under the assumption of hydrostatic equilibrium,

$$\frac{\partial p}{\partial z} = -\rho g \tag{3.2}$$

where z is altitude. Analysis of the full equations of vertical momentum and consideration of the fact that pressure drops exponentially with height allows a scale analysis to be performed. A scale analysis in this context means that the pressure gradient term can be scaled by a constant factor composed of the surface pressure and the height at which the atmospheric pressure halves; this analysis reveals that for large-scale air motions modelled by a GCM, vertical pressure perturbations are neglible and so the vertical pressure gradient can be represented by Equation 3.2 as simply decreasing with atmospheric density. In other words, the air pressure at any point in the atmosphere is determined by the weight of the column of

air above it (Holton, 2004b). This allows further simplification of the momentum equation 3.1, as the vertical momentum component can be replaced with equation 3.2. As an aside, this assumption means that vertical velocity (w) cannot be directly calculated in the MGCM; there are however other ways to indirectly diagnose vertical velocity, such as from the thermodynamic energy equation. Note that non-hydrostatic formulations of the primitive equations are also possible and used in some GCMs, though not currently for Mars.

The second conservation principle is conservation of mass. For a fluid like an atmosphere, the equation that expresses this is called the continuity equation. This relationship can be expressed in either an Eulerian sense (from a fixed reference frame where air masses move through) or a Lagrangian sense (following the air masses themselves). The MGCM, like most GCMs, uses the former, so the Eulerian equation will be presented. For a fixed volume, the net mass flux into the volume from all directions must equal the rate of mass increase per unit volume (Holton, 2004b). This is formulated mathematically as

$$\frac{1}{\rho}\frac{D\rho}{Dt} + \nabla \cdot \mathbf{U} = 0 \tag{3.3}$$

The third conservation principle is conservation of energy. The first law of thermodynamics states that the total energy of an isolated system is constant, but can be transformed between heat and mechanical work. From this simple consideration and incorporating the continuity equation 3.3, the thermodynamic energy equation can be derived:

$$c_v \frac{DT}{Dt} - \frac{p}{\rho^2}\frac{D\rho}{Dt} = Q \tag{3.4}$$

where c_v is the specific heat at constant volume, T is temperature, and Q represents the rate of heating per unit mass from radiation, conduction, and latent heat (Holton, 2004b). Here, $c_v \frac{DT}{Dt}$ represents the change in energy of the air mass, and $\frac{p}{\rho^2}\frac{D\rho}{Dt}$ represents conversion between heat and mechanical energy.

It is also assumed that the atmosphere is spherical (allowing the neglect of certain curvature terms in equation 3.1); that it is shallow relative to the radius of the planet ie. $h \ll a$ where h is the height of the atmosphere and a is the radius of the planet, allowing resolved vertical motions to be considered as negligible compared to resolved horizontal motion; and that the atmosphere is composed of an ideal gas which follows the relation

$$p = \rho RT \tag{3.5}$$

where R is the gas constant per unit mass. The equations 3.1, 3.3, and 3.4 together constitute the primitive equations of meteorology for an atmosphere on a rotating planet; together with the other assumptions mentioned, they enable the numerical modelling of a hydrostatic, shallow, spherical atmosphere composed of an ideal gas, as used in the MGCM.

As mentioned above, the MGCM uses a "spectral" dynamical core to solve the primitive equations in the horizontal dimensions in spectral space, via a series of spherical harmonics, rather than on a finite-difference spatial grid. One major advantage of this method is that it avoids the problem faced by finite-difference models of grid lines converging at the poles, which can create instabilities in the polar regions. There are ways of avoiding this on finite-difference models, such as shifting the poles to locations where instabilities will cause fewer issues, or creating alternative model grid shapes; for a spectral model, however, these problems are entirely avoided. The MGCM dynamical core solves an alternative formulation of the primitive equations stated above, with four variables: vorticity (a measure of rotation), divergence (a measure of velocity), temperature, and the logarithm of surface pressure (Hoskins and Simmons, 1975). These values are calculated in spectral space for each timestep before being transformed into the real space of the physical grid, where physical tendencies of zonal and meridional winds (u,v), temperatures, and surface pressures are applied. If data assimilation is also being performed (see Section 3.3 below), this subsequently takes place.

Lastly, a Robert filter is applied to dampen non-physical oscillations that can appear when timestepping, and grow explosively if not filtered (Robert, 1966).

The dynamical core uses a finite difference grid in the vertical dimension, with variably spaced σ-layers which follow the MGCM topography. The model grids are described in greater detail later in Section 3.1.3.

3.1.2 Parametrizations

As well as resolved atmospheric dynamics, the MGCM also has a number of routines to represent various important physical processes related to the Mars atmosphere, from radiative processes to dynamical phenomena which are not resolved by the coarse MGCM grid and therefore have to be "parametrized" - represented by simpler, often empirically-based routines which interact with the large-scale flow. Certain routines are essential for the proper operation of the MGCM as a reasonable simulacrum of the martian atmosphere, such as the basic diabatic heating sources of solar insolation, dust, and atmospheric CO_2, the seasonal cycle of solar insolation, the sublimation and condensation of atmospheric CO_2 onto the seasonal ice caps, and basic representations of convection from the surface. Other routines can be adjusted or turned off for certain purposes when running the MGCM, such as Mars' water cycle and various chemical and photochemical processes. For this thesis, "essential" is meant in the sense of providing a reasonable state for the large-scale atmospheric flow on Mars. While radiatively-active water ice clouds can have an impact on atmospheric dynamics (Steele et al., 2014a) for example, many of the basic dynamical phenomena associated with Mars can be replicated without a water cycle, such as the polar warming above the winter pole (Wilson, 1997) and the basic morphology of the mean meridional circulation (Haberle et al., 1993). In addition, data assimilation of temperature measurements from orbiters can allow the MGCM to better represent the temperature structure of the real martian atmosphere - which is known to include water-ice clouds - without the need for a water cycle in the MGCM. For this reason

and to better isolate the effects of atmospheric dust, the simulations discussed in this thesis are all conducted without a water cycle.

Radiative transfer

The MGCM's radiative transfer schemes model how electromagnetic radiation interacts with the atmosphere. The most important components affecting radiative transfer in the martian atmosphere are atmospheric CO_2, dust, water ice, and CO_2 ice, with neglible contributions from water vapour and chemical species such as ozone (Forget et al., 1999). While the MGCM contains parametrizations for CO_2 surface sublimation/condensation and snowfall (see Forget, 1998), it does not currently contain radiatively active CO_2 ice clouds. This section therefore focusses on CO_2 gas and mineral dust.

Radiative transfer in the MGCM is calculated in five bands, which can be divided into two categories: shortwave (SW) and longwave (LW). The former accounts for solar wavelengths in the wavelength bands 0.1-0.5 µm and 0.5-5 µm. The latter accounts for thermal wavelengths in the wavelength bands 5-11.6 µm, 11.6-20 µm, and 20-220 µm.

The 11.6-20 µm wavelength band is especially important given the composition of the martian atmosphere, which is overwhelmingly CO_2 gas; this band is therefore further subdivided into a central peak, where CO_2 absorption is greatest between 14.2-15.7 µm, and two less absorbing wings on either side of the central peak (Hourdin, 1992). In addition, non-local thermal equilibrium (NLTE) effects are taken into account for high altitudes above 0.1 Pa (Lopéz-Valverde and López-Puertas, 2001).

After gaseous CO_2, atmospheric mineral dust is the key radiative component in the martian atmosphere, absorbing and scattering both SW and LW radiation. Atmospheric dust is also notoriously difficult to characterise radiatively from orbit, given its broad spectral response and uncertain composition and shape. While there is evidence of non-spherical dust particles (e.g. Petrova, 1999; Smith and Wolff, 2014), the MGCM assumes sphericity

both for computational ease and in order to make use of the best available datasets of dust radiative properties, which assume sphericity (e.g. Wolff et al., 2006).

The dust radiative properties in the MGCM at each of the five wavelength bands are determined by the particle effective radius, r_{eff}. This is related to the dust opacity in a given model layer, as described later in Section 3.2, and therefore can vary with time and spatial location (including altitude). The r_{eff} value in each model gridbox at each timestep is used to look up the specific radiative properties at each wavelength band, from values calculated by Wolff et al. (2006) and Wolff et al. (2009). These radiative properties determine the dust-related radiative transfer for that gridbox at that timestep.

The three key properties (the "single-scattering parameters" approximated from the full phase function) needed to characterise radiative response for an aerosol in a two-stream approximation radiative transfer model (as used in the MGCM) for a particular wavelength λ are the extinction efficiency factor (Q_{ext}), single scattering albedo (ω), and asymmetry factor (g). Briefly, $Q_{ext}(\lambda)$ defines how efficient the aerosol is at absorbing and scattering radiation at wavelength λ; $\omega(\lambda)$ is the ratio of scattered to extinguished radiation at wavelength λ (higher ω means a "brighter" aerosol, with more incident radiation being scattered); and $g(\lambda)$ indicates the degree to which the aerosol forward or backscatters incident radiation at wavelength λ, with positive values indicating forward scattering, negative values backscattering, and 0 completely isotropic scattering. The values of these three parameters with wavelength at various r_{eff} are shown in Fig. 3.1 (Madeleine et al., 2011), together with the values calculated by Wolff et al. (2006) assuming r_{eff}=1.5 μm.

With the radiative properties calculated at each gridbox for the relevant timestep, SW and LW heating rates can then be calculated. The MGCM uses a two-stream approximation for radiative transfer, meaning that radiative fluxes are only computed in two directions: above and below the gridbox. This is a standard assumption for GCMs to minimise the complexity of the equations and to reduce the computational cost of radiative transfer calculations. The

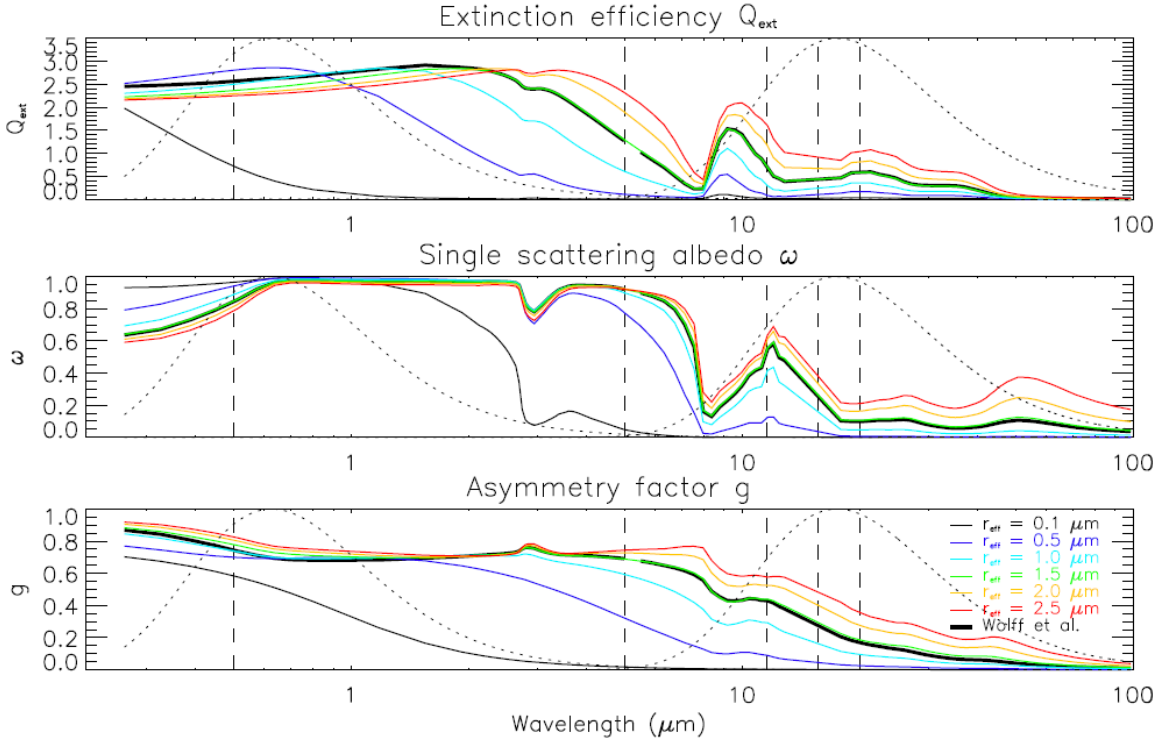

Fig. 3.1 Single-scattering parameters Q_{ext}, ω, and g for different r_{eff} values of mineral dust, including values for $r_{\text{eff}} = 1.5m$ from Wolff et al. (2006), from Madeleine et al. (2011). Dotted lines represent the normalised blackbody emission spectra for (left peak) the Sun (5870 K) and (right peak) Mars' (210 K) emission temperature. The vertical dashes represent the midpoints of the five wavelength bands used in the MGCM's radiative transfer scheme.

MGCM specifically uses the generalised radiative transfer scheme described by Toon et al. (1989), which is generally accurate to within 10% and robust up to very high aerosol loadings of $\tau \geq 10$ (Toon et al., 1989) (where τ is column optical depth at solar wavelengths), an important feature for Mars given the phenomena of Global Dust Storms.

Tracer transport

Atmospheric tracers are discrete elements or collections of elements that are transported within the atmosphere, and can include CO_2 gas, dust, water vapour and ice, and chemical species. Radiatively active tracers can influence the atmosphere through radiative heating and cooling, whereas passive tracers are simply transported by the circulation and do not radiatively affect their surroundings. For the purposes of this thesis, the most important tracer is dust, which is set to be radiatively active in every simulation considered.

Tracer advection in the MGCM is performed by a semi-Lagrangian transport scheme which uses MGCM winds at each physical timestep, as implemented by Newman et al. (2002a). This kind of scheme is widely used in numerical weather prediction; as it does not necessarily ensure mass conservation, the method described by Priestley (1993) is also implemented to ensure mass conservation at the end of each timestep.

Gravitational sedimentation of tracers is also included in the MGCM, through a conservative 1D advection scheme (Hourdin and Armengaud, 1999). Sedimentation velocities are calculated through balance of the downward gravitational force and the upward frictional drag, the latter given by Stokes' Law as modified for Mars' thin atmosphere (Rossow, 1978).

The transport of dust tracers specifically involves transport of a dust particle size distribution, with effective radii r_{eff} determined by layer opacity, mass mixing ratio, and number density; the latter two are the variables transported in the two-moment scheme used by the MGCM. This distribution and the two-moment scheme are described in greater detail in Section 3.2.

Convection

Dry convection in the lower layers of the atmosphere is parametrized in a simple way through a process called convective adjustment. Mars' thin atmosphere means that the surface and near-surface atmosphere frequently become warmer than the atmosphere above. This is an unstable situation, and leads to convection, where heat is rapidly transported upwards by turbulent mixing. Formally, an unstable atmosphere is defined in the MGCM where $\frac{\partial \theta}{\partial z} < 0$, where θ is the potential temperature:

$$\theta = T \left(\frac{p_0}{p} \right)^{R/c_p} \tag{3.6}$$

where R is the gas constant per unit mass and c_p is the specific heat at fixed pressure. When this criterion is met in the atmosphere, the convective adjustment parametrization mixes the relevant unstable layers (including any relevant tracers), and imposes a new temperature profile satisfying the adiabatic lapse rate.

The version of the MGCM used in this thesis also contains a more recent parametrization which incorporates convective thermal plumes (Colaïtis et al., 2013). These plumes have been shown to occur in high resolution large eddy simulations of the martian atmosphere, but are not capable of being resolved at standard GCM resolutions. The parametrization therefore models the effects of updrafts and downdrafts on transport within Mars' planetary boundary layer (PBL), allowing for rapid transport of heat, momentum, and tracers to the top of the PBL (Colaïtis et al., 2013). The parametrization does this by explicitly modelling the organised turbulent structures which occur in the PBL and can transport mass and energy, as opposed to the convective adjustment scheme which simply represents the mixing effects of an unstable temperature profile. This is done by representing each MGCM column within the PBL as the sum of three component columns: an environment column representing the background state, an updraft column, and a downdraft column. The values for mass flux at each layer in each column are then calculated using empirical values derived from large

eddy simulations. For updrafts, vertical velocities are calculated to determine the strength of the updraft, highest where buoyancy is strongest (ie. where there is a strongly unstable layer near the surface due to a higher surface temperature than the near-surface atmospheric temperature), and mass fluxes are calculated accordingly. Downdrafts are more difficult to parametrize directly from buoyancy, and so a prescribed ratio of updraft to downdraft mass fluxes (0.8, based on large eddy simulations) is used to calculate downdraft mass flux, and a potential temperature profile (again based on large eddy simulations) is set to reproduce a reasonable profile for turbulent transport in the PBL (Colaïtis et al., 2013). Because of this simplified downdraft model, only updraft tracer transport is calculated by the parametrization. Fig. 3.2 shows wind speeds in the MGCM with and without this parametrization; it can be seen that its inclusion can increase globally-averaged near-surface wind speeds by up to 2 m/s.

Moist convection from latent heating of H_2O, an important process for cloud formation on Earth, is neglected in the MGCM due to the aridity of Mars' atmosphere (see Chapter 2).

CO_2 sublimation and condensation

The seasonal condensation and sublimation of CO_2 ice on the martian surface is an important process with no terrestrial equivalent. The MGCM contains a parametrization for this process based on atmospheric and surface temperatures. When the temperature of either the surface or the atmosphere falls below the relevant CO_2 condensation temperature (T_{CO_2}), condensation occurs and CO_2 ice is formed. CO_2 ice created in the atmosphere can fall through the layers below under the force of gravity (snowfall); if it passes through a layer where $T > T_{CO_2}$, it can sublimate into gas again. If it doesn't sublimate before reaching the surface, CO_2 ice is deposited onto the surface. Likewise, surface CO_2 ice can sublimate when $T > T_{CO_2}$. The MGCM also calculates the corresponding pressure changes at the surface from CO_2 condensation, which reduces surface pressure, and sublimation, which increases it. The

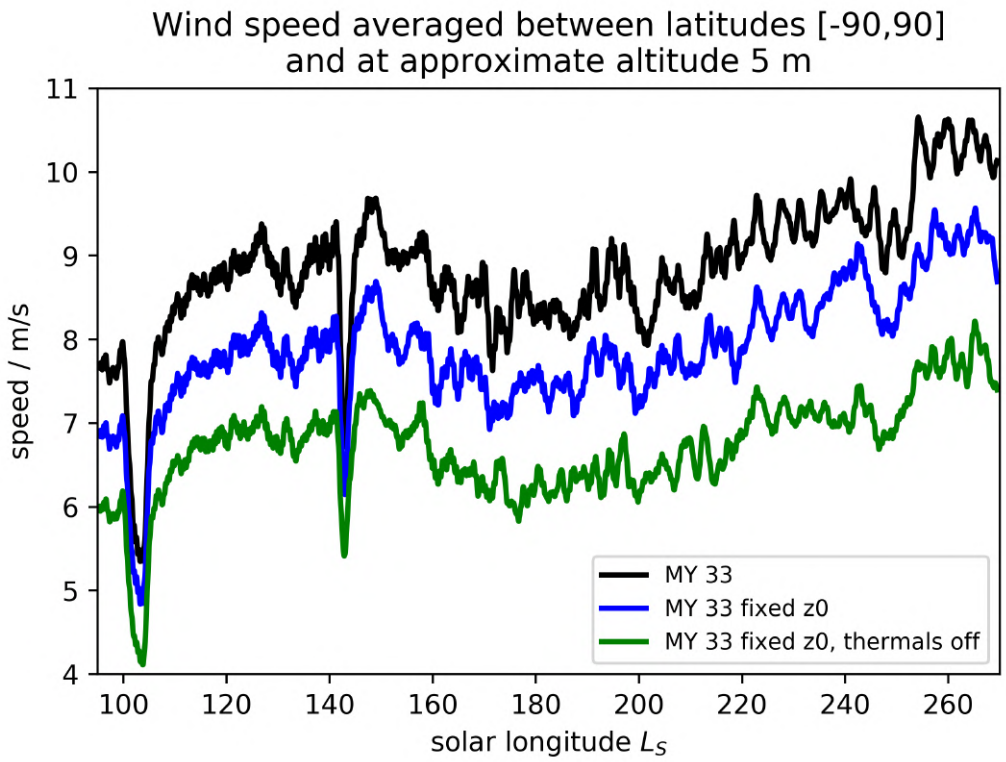

Fig. 3.2 Globally-averaged near-surface wind speeds in a reanalysis of MY 33 for the MGCM (black) with both a realistic surface roughness map and the Colaïtis et al. (2013) thermal plume scheme; (blue) with a uniform surface roughness map and the Colaïtis et al. (2013) thermal plume scheme; (green) with a uniform surface roughness map and without the Colaïtis et al. (2013) thermal plume scheme.

presence of surface CO_2 ice alters the surface albedo and emissivity in the MGCM. Further details of the parametrization can be found in Forget et al. (1998).

Other physical processes

Surface roughness The version of the MGCM used in this thesis (v6) includes realistic surface roughness maps, based on orbital rock abundance data as measured by the Thermal Emission Spectrometer (Hébrard et al., 2012). Surface roughness is effectively a measure of the drag on near-surface winds, and inclusion of a realistic map therefore has a significant impact on near-surface wind speeds compared to a model with a uniform surface roughness. This can be seen in Fig. 3.2, where its inclusion leads to an increase in globally-averaged near-surface wind speeds of up to 1 m/s. See Chapter 5 for more details.

Surface thermal inertia and albedo The MGCM includes detailed thermal inertia and albedo maps derived from orbital measurements from the Thermal Emission Spectrometer (Putzig et al., 2005).

Resolved and subgrid topography The MGCM uses topographic data from the Mars Orbiter Laser Altimeter (MOLA) instrument, which provides topography down to a spatial resolution of $\sim$4 km (Kreslavsky and Head, 2000), and a vertical resolution of 13 m (Smith et al., 1999a). This extremely high resolution dataset is then filtered to match the coarser resolution of the MGCM grid. However, subgrid-scale information about the topography is also included via its effect on gravity wave drag, using the parametrization of Lott and Miller (1997).

Gravity waves Mars' extreme topography forces gravity waves: changes in buoyancy which can propagate to high altitudes in the atmosphere and have a significant effect on dynamics via their vertical transfer of momentum (e.g. Medvedev et al., 2011). These are

parametrized in the MGCM via their drag on modelled lower atmosphere winds (see above), and via higher-up momentum transfer through gravity wave breaking (Baines and Palmer, 1990; Miller et al., 1989). Full details of the gravity wave parametrization in the GCM are described in Collins et al. (1997). There have also been observations of the possible effects of non-orographic gravity wave activity, such as from large dust events and PBL activity (e.g. Heavens et al., 2020); these are not parametrized in the MGCM however, as it is challenging to constrain their phase from currently available observations.

Boundary layer diffusion Mars' PBL undergoes extreme diurnal variation in depth and strength, making a good parametrization important for accurately representing dynamics and transport in the bottom of the atmosphere. Similar to most terrestrial GCMs, PBL dynamics in the MGCM are parametrized with a turbulent mixing scheme mathematically represented as

$$\frac{\partial a}{\partial t} = \frac{1}{\rho}\frac{\partial}{\partial z}K\rho\frac{\partial a}{\partial z} \tag{3.7}$$

where a is a variable to be mixed (e.g. θ, u, v), and K is a modelling-derived value different for each variable a. See Forget et al. (1999) for further details of the implementation.

Soil model The MGCM contains an 18-layer soil model which assumes vertically homogenous soil (Hourdin et al., 1993). Together with the surface albedo and thermal inertia maps, these soil properties determine the surface temperature through their mediation of radiative flux.

3.1.3 The model grid

The MGCM uses two different spatial grids and one vertical grid. The spatial dynamics, as described previously, are calculated in spectral space but are transformed to two different

spatial grids, one finer and one coarser. The finer grid is needed for the calculation of nonlinear terms in the primitive equations, in order to avoid the problem of aliasing during the spectral-spatial transformations (Hoskins and Simmons, 1975). The coarser grid is to calculate the (linear) physical tendencies of surface pressure, zonal and meridional winds, and temperature, which interact with the MGCM physics, before being converted back into spectral space to provide tendencies for the dynamics. The finer grid is defined in terms of a truncation of a spherical harmonic series; the higher the wavenumber at which the truncation occurs, the higher the resolution of the grid. The simulations considered in this thesis were all run at spectral resolution T42, which corresponds to a spatial dynamics grid of 64 latitudes by 128 longitudes, or an approximate resolution at the equator of 2.8°. Some of the variables used in this thesis are derived directly from this finer grid: specifically, the zonally- and diurnally-averaged mean meridional circulation (MMC), vertical velocities, and potential vorticity (PV).

The coarser spatial grid (the "physics grid") deals with linear physical variables, and standard model variables are output to this grid. For a spectral resolution of T42, this grid has a resolution of 48 latitudes by 96 longitudes, or approximately 3.75° at the equator. This grid is shown in Fig. 3.3. Due to the equal spacing of the grid at all latitudes, higher latitude gridboxes represent a smaller area of the martian surface than lower latitude gridboxes. Where relevant, area weighting is applied to model variables to ensure consistency.

Finally, the dynamics and physics share a common vertical grid which uses σ coordinates, as described above. The advantage of σ coordinates is that they inherently follow topography. This is especially important on Mars, where topographic variations across the planet are enormous. The coordinate system is calculated relative to a standard defined surface reference pressure of 610 Pa, which is the surface pressure of the Mars geoid or "areoid". From this, approximate altitudes above the areoid can be calculated with the relation

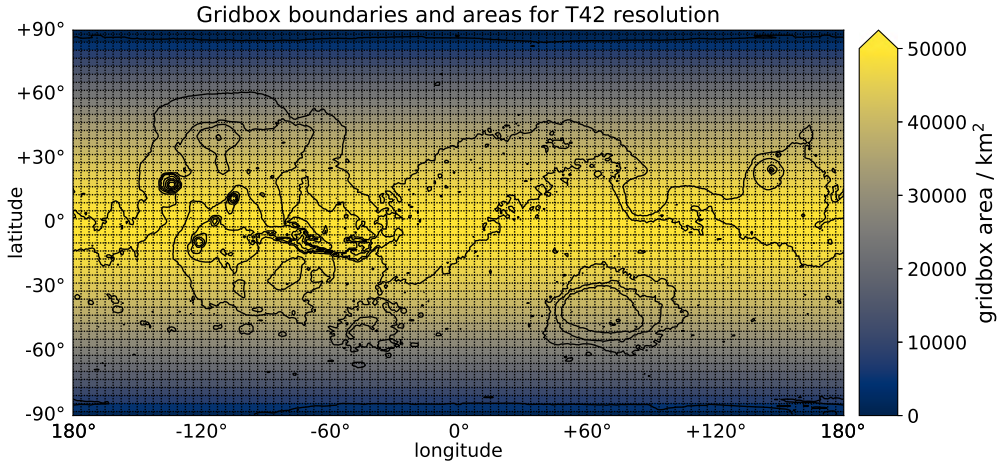

Fig. 3.3 Gridbox boundaries and areas for the MGCM physics grid at spectral resolution T42. Black contours represent topography, and are used throughout this thesis. All longitudes are east longitudes, and this is maintained throughout the rest of this thesis.

$$z = -H \ln(\sigma) \tag{3.8}$$

where H is the scale height of the martian atmosphere, the height at which the surface pressure drops by a factor of the natural log base e (approximately 10 km). For this thesis, the MGCM was run with a vertical resolution of 50 vertical layers ("L50"). As mentioned, these are unevenly spaced in altitude in order to ensure better representation of the lower atmosphere, where the surface interacts with the atmosphere and there is greater variation in height of factors of interest such as heat/momentum/tracer transport. Fig. 3.4 shows the location of the model layers in an L50 run of the MGCM. Note that the upper three layers of the MGCMs are "sponge layers"; these damp vertically propagating waves in order to reduce unphysical temperature and pressure perturbations due to reflection from the model top, as would be the case with a non-damping upper boundary.

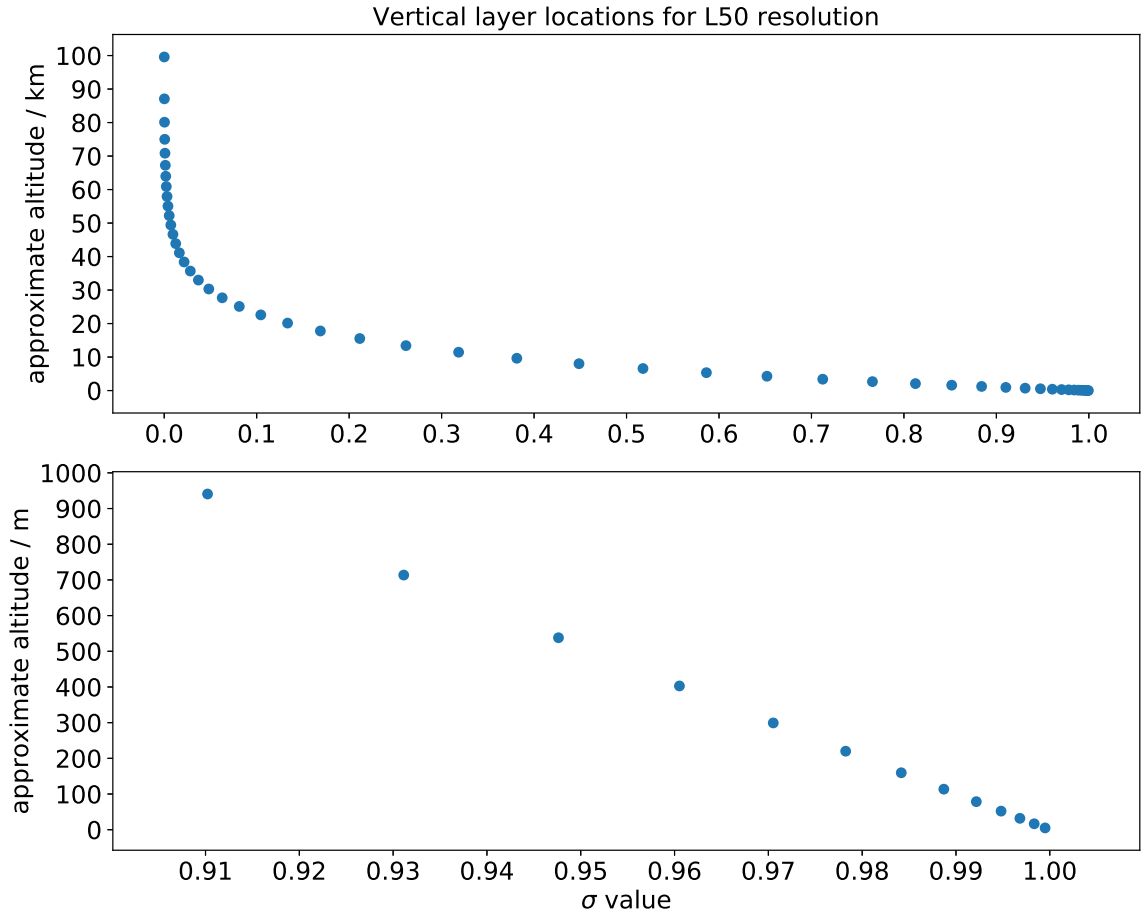

Fig. 3.4 Vertical layer approximate altitudes and σ values for the MGCM with 50 vertical layers. The bottom plot presents a close-up of the bottom kilometre of the atmosphere.

3.2 Representing dust in the MGCM

This section provides an overview of how atmospheric dust is represented in the MGCM. First, the size distribution of dust particles within the model is described, and terms for describing opacity are defined. Next, the various ways of representing the spatial distribution of dust in the MGCM are discussed. Finally, the vertical distribution of dust, and different methods for representing this, are described and shown.

3.2.1 Size distribution and opacity

As mentioned above, dust is transported in the MGCM in the form of two tracers: mass mixing ratio (q) and number density (N). It is also possible to have a static dust distribution which is not transported by model winds; some examples of fixed spatial and vertical distributions are discussed in Sections 3.2.2 and 3.2.3 respectively, but for the purposes of this thesis radiatively active, freely-transported dust was present in every considered simulation, and this case is the setup that will be described in this section.

The dust distribution in the MGCM is assumed to follow a lognormal distribution, with the dust mass mixing ratio q given by

$$q = \frac{4}{3}\pi\,\rho_p\,N\,\left(r_{\text{eff}}/(1+v_{\text{eff}})\right)^3 \tag{3.9}$$

where ρ_p is the density of the dust particle, assumed to be 2500 kg m^{-3}, characteristic of basaltic minerals (Philpotts and Ague, 2009) which are believed to be a significant part of the mineral composition of martian dust (e.g. Toon et al., 1977); N is the dust number density; r_{eff} is the effective particle radius (as observed from spectroscopy); and v_{eff} is the variance of r_{eff}, set as a constant 0.5. The size distribution of the dust population can be predicted in any gridbox at any model time with just the two tracers q and N. This can then be related to

the effective radius r_{eff}, which is the actual value used in the radiative calculations, by the following:

$$r_{\text{eff}} = \left(\frac{3}{4}\frac{q}{\pi\rho_p N}\right)^{1/3}(1+\nu_{\text{eff}}) \tag{3.10}$$

which is a rearrangement of equation 3.9. Therefore, through the transport of the two tracers q and N, the dust particle size distribution can be calculated at each gridbox and timestep and fed to the MGCM's radiative transfer scheme.

In the MGCM run with radiatively active dust transport, as with the simulations presented in this thesis, the dust opacity at each model layer is not prescribed but instead defined in terms of the tracer q with the relation

$$d\tau = \frac{3}{4}\frac{Q_{ext,vis}q}{g\rho_p r_{\text{eff}}}dp \tag{3.11}$$

where $d\tau$ is the dust extinction at 600 nm, $Q_{ext,vis}$ is the extinction efficiency of dust at 600 nm according to the look-up tables used by the radiative transfer scheme (see above), and dp is the relevant pressure layer. For clarity, $d\tau$ is henceforth referred to as "dust opacity".

In this version of the MGCM, the vertical sum of $d\tau$ in each atmospheric column is finally scaled to match a given spatial column dust optical depth distribution; this is described in Section 3.2.2. For further details of the two-moment tracer transport scheme in the MGCM, the reader is referred to Madeleine et al. (2011).

In this way, dust in the MGCM is both able to be transported by the model winds and also affect the atmosphere radiatively, making it a more accurate representation of real martian atmospheric dust than when using prescribed particle sizes and dust opacities. The vertical distribution which results from this freely-transported radiatively active dust is discussed further in Section 3.2.3, and compared to other ways of representing the dust population.

3.2.2 Spatial distribution

This version of the MGCM (v6) requires the input of spatial map of column dust optical depth (CDOD) - the extinction opacity of a column of dust in the atmosphere at 600 nm. Specifically, the MGCM uses CDOD as normalised to the surface reference pressure of 610 Pa; this allows for comparison of dust loading across Mars' extreme variations in topography. There are several different ways of representing this, the main methods being with an analytically prescribed function; with an observationally-derived time-varying map; and by data assimilation of orbital observations of CDOD.

Before the advent of high-volume orbital dust observations with the TES instrument aboard Mars Global Surveyor (see Chapter 2), measurements of dust in the martian atmosphere were relatively sparse and piecemeal. Observations came from varied sources including orbital spacecraft (e.g. Fenton et al., 1997; Gierasch, 1974; Hanel et al., 1972; Toon et al., 1977), *in situ* landers (e.g. Colburn et al., 1989; Tomasko et al., 1999), and ground-based telescopes (e.g. Clancy et al., 2000; James et al., 1999; McKim, 1996; Zurek and Martin, 1993). The radiative and dynamical importance of atmospheric dust was apparent even from early orbital data (e.g. Pollack et al., 1979), and so its inclusion in some form in early MGCMs was necessary. Early MGCMs therefore often used analytically prescribed distributions to describe the spatial dust distribution. These distributions were simple and generic enough to be easy to incorporate into the model without making possibly spurious assumptions about the real spatial distribution, while still reproducing observed aspects of the large-scale circulation, much like early cloud models in terrestrial GCMs. One example is the "Viking scenario", based on measurements from the Viking orbiters, which prescribed CDOD with the relation

$$\tau = 0.7 + 0.3\cos(L_S + 80^\circ) \tag{3.12}$$

where τ is the CDOD at 700 Pa (a reference pressure used for the dust distribution in previous versions of the MGCM) (Lewis et al., 1999). While τ is a column integrated property, a prescribed reference pressure (commonly the planet's mean surface pressure) is often used to normalise τ within the MGCM in order to enable easy comparison of the spatial dust distribution across Mars' extreme topographic variations. A more recent and complicated example is the "MGS scenario", an analytical prescribed scenario based on the first full year of observations by TES. This scenario prescribes CDOD variation with both L_S and latitude, with the northern hemisphere remaining relatively dust-clear even as the southern hemisphere experiences its seasonal increase in CDOD during southern summer (Lewis et al., 2001), and has been used in a number of modelling studies (e.g. Acker et al., 2002; Bingham et al., 2004; Newman et al., 2003; Toigo et al., 2012).

With the advent of high volume CDOD measurements from TES and the Mars Climate Sounder (MCS), a new form of representing the spatiotemporal CDOD distribution emerged: dust maps for specific martian years. The maps which can be used in runs of the MGCM are based on observations from TES, MCS, and the Thermal Emission Imaging System (THEMIS) instrument aboard Mars Odyssey, which are filtered and then spatially krigged to fill in the spatiotemporal gaps in observations (Montabone et al., 2015, 2020). These maps have been frequently used in modelling studies (e.g. Chapman et al., 2017; Holmes et al., 2015; Neary and Daerden, 2018; Spiga et al., 2017; Steele et al., 2014b) as they provide a far more realistic CDOD distribution than the older prescribed functions, particularly when investigating specific time periods in the martian atmosphere as opposed to more general climatological studies.

Finally, it is also possible with the MGCM to directly read in the CDOD retrievals from TES and MCS and assimilate them (Lewis et al., 2007). The technique by which this is performed is described in detail in Section 3.3. The advantages of this technique are that it allows coupling of the MGCM dust fields to observations, and it is also frequently performed

together with assimilation of temperature observations, resulting in more realistic dust and temperature structures. Various modelling studies have either directly used this technique in the MGCM (e.g. Lewis et al., 2016, 2007; Montabone et al., 2005; Mulholland et al., 2016) or used the Mars Analysis Correction Data Assimilation (MACDA) dataset, a run of the MGCM with CDOD and temperature assimilation (Montabone et al., 2014) for various purposes (e.g. Battalio et al., 2016; Mitchell et al., 2015; Read et al., 2016; Tabataba-Vakili et al., 2015; Waugh et al., 2016).

Fig. 3.5 compares CDOD at 610 Pa as averaged between L_S=120-150° for the MGS scenario, the MY 34 CDOD map (Montabone et al., 2020), and an assimilation of MCS CDOD in MY 34. There is evidently far better agreement between the map and the assimilation than there is between either with the MGS scenario, which appears to underestimate CDOD. Note also the unphysically precise latitudinal banding in the MGS scenario. There are some differences between the map and the assimilation, though, especially at southern high latitudes where the assimilation seems to show a clearer atmosphere. There was a lack of southern high-latitude observations from MCS at this period in MY 34; in the map, this gap was filled with spatially krigged values from lower latitudes, while in the assimilation this was not assumed to be the case.

3.2.3 Vertical distribution

The vertical dust distribution in the martian atmosphere can have noticeable effects on the modelled circulation (e.g. Guzewich et al., 2013b). The MGCM allows for both prescribed vertical distributions and for freely-transported dust.

Up until relatively recently, there was a paucity of observations of Mars' vertical atmospheric dust structure. MGCMs therefore had to assume a prescribed distribution to include within their dust representations. The most commonly used throughout MGCMs is the Conrath distribution, based on temperature observations made by Mariner 9 during the 1971

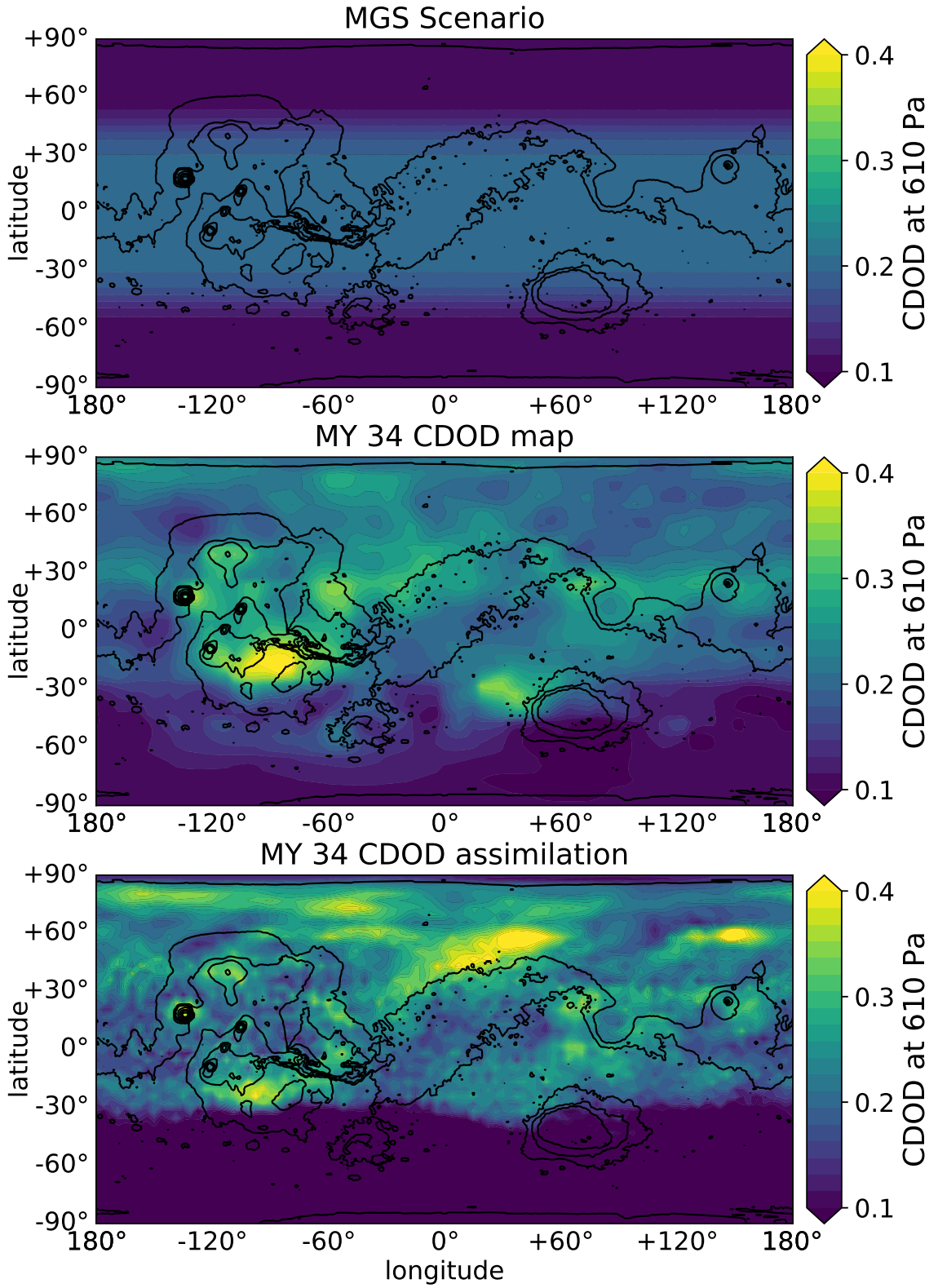

Fig. 3.5 CDOD at 610 Pa as averaged between L_S=120-130° for (top) the MGS scenario, (middle) the MY 34 CDOD map of Montabone et al. (2020), and (bottom) an assimilation of MCS CDOD in MY 34.

Global Dust Storm and consideration of the sedimentation rate of dust particles (Conrath, 1975). This distribution takes the basic form

$$q = q_0 \exp\left(\nu\left(1 - \frac{p_0}{p}\right)\right) \tag{3.13}$$

where q is the dust mass mixing ratio at a given pressure level p, and q_0 is the dust mass mixing ratio at a standard pressure level p_0 (commonly 700 Pa). ν is a parameter which describes the relative importance of dust diffusion and gravitational sedimentation, and thus controls the shape of the dust profile: namely how rapidly the dust mass mixing ratio decreases with altitude (Conrath, 1975; Lewis et al., 2001). The actual formulation implemented in the MGCM is a modified version of equation 3.13, which allows a desired cutoff altitude to be set; this modified distribution resembles the Conrath distribution for high cutoffs, but is designed to more closely resemble Viking observations for lower cutoffs (see Lewis et al., 1999). Various versions of the Conrath distribution have been used for many modelling and assimilation studies (e.g. Haberle et al., 2003; Kuroda et al., 2005; Medvedev and Hartogh, 2007; Pollack et al., 1990; Steele et al., 2014b; Toigo et al., 2012).

A parallel development has been the use of models with dust transport, where the vertical dust distribution is determined by model dynamics rather than prescribed *a priori* (e.g. Basu et al., 2004; Kahre et al., 2006; Murphy et al., 1990; Newman et al., 2005; Pankine and Ingersoll, 2002; Wilson, 1997). The advantage of such methods is that they don't make assumptions about the dust distribution, and can allow for radiative feedback effects as dust is both transported and radiatively active, making them especially useful for studies of the dust cycle. However, purely free-running models still have some issues accurately reproducing the observed temporal and spatial distribution of dust in the atmosphere, in particular the interannual variability of specific dust events including Global Dust Storms (Kahre et al., 2017). The MGCM allows dust transport, as described above, while also scaling CDOD to match a desired spatial dust distribution. This enables a freely-transported vertical dust

distribution together with spatio-temporal CDOD distributions that agree with observations. This mode is the one that was used for the simulations considered in this thesis.

Finally, recent observations along Mars' atmospheric limb from MCS (Heavens et al., 2011a) and TES (Guzewich et al., 2013a) have revealed a far more complex vertical profile than previously assumed, particularly during the aphelion "clear" season. So-called "detached dust layers" have been discovered at high altitudes, indicating a vertical dust distribution with two maxima (near the surface and at the location of the detached dust layers) rather than a monotonically decreasing profile as assumed by Conrath-type functions. Representing this in MGCMs is an area of ongoing research. Some modelling studies have incorporated new analytically prescribed profiles based on these observations (e.g. Guzewich et al., 2013b). Other efforts have attempted to parametrize the convective transport processes that are thought to be responsible for creating detached dust layers (e.g. Vals et al., 2019; Wang et al., 2018). And lastly, there are also ongoing efforts to incorporate realistic vertical dust distributions via assimilation (e.g. Navarro, 2016; Ruan, 2015), including by the author (Streeter et al., 2018). For the work in this thesis, however, the more mature method described in the previous paragraph is used.

Fig. 3.6 compares dust density-scaled opacity (DSO) for the cases of a Conrath-type prescribed dust profile, a freely-transported vertical dust distribution, and assimilated MCS dust profiles. DSO normalises actual dust opacities relative to the atmospheric pressure, allowing better investigation of elevated dust features (Heavens et al., 2011b). The freely-transported and profile assimilation cases agree with each other better than with the Conrath-type profile, both spatially and vertically. However the presence of detached dust layering is clearly visible in the profile assimilation at 20-30 km above the tropics, and not in the freely-transported case, showing that current MGCM parametrizations are not able to reproduce this phenomenon.

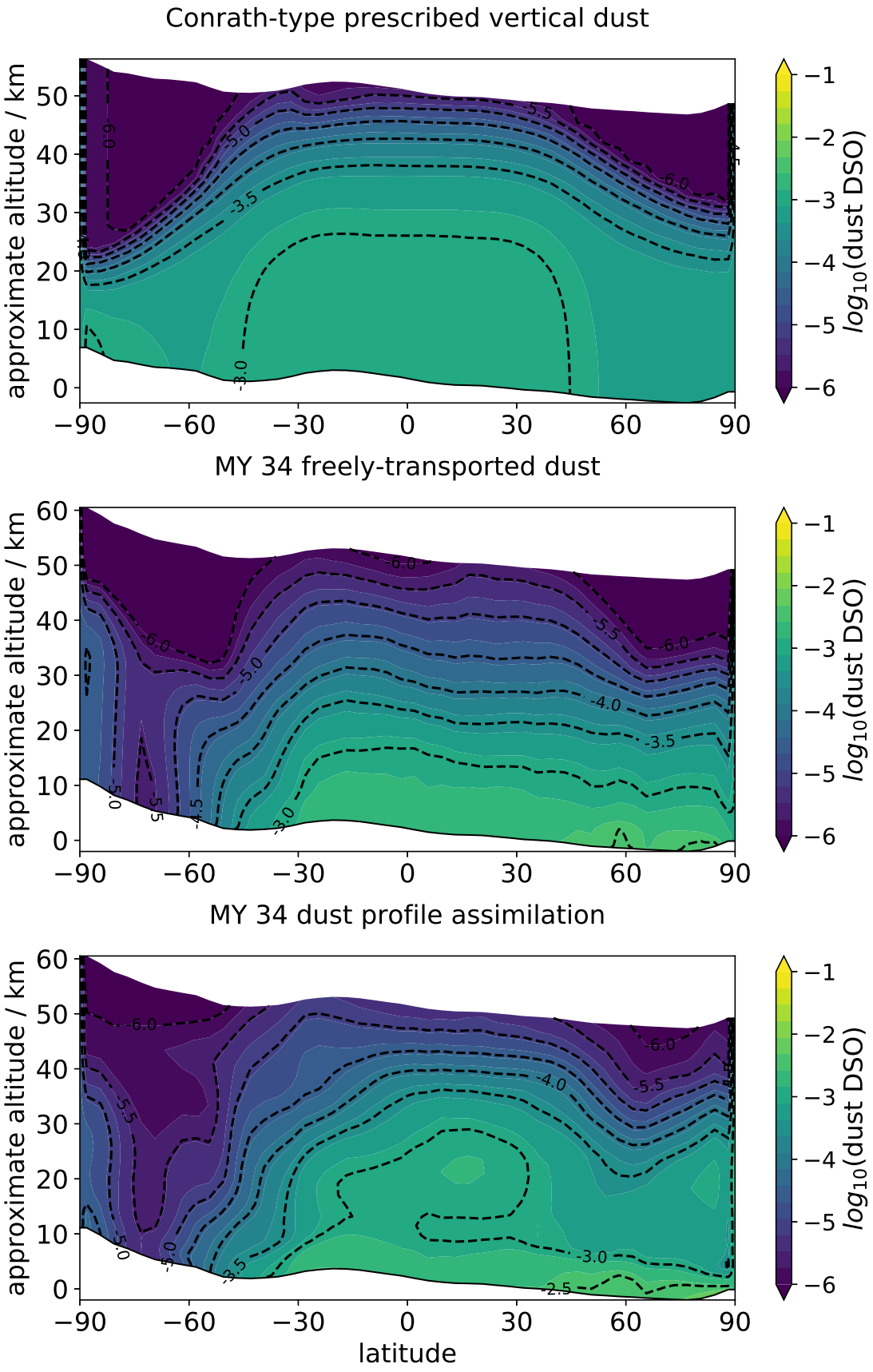

Fig. 3.6 Zonally-averaged dust DSO as averaged between L_S=120-130° for (top) a Conrath-type prescribed vertical dust distribution (dust top 55 km), (middle) MY 34 freely-transported dust, and (bottom) assimilated MY 34 MCS dust profiles.

3.2.4 Dust lifting

An "online" dust lifting calculation, where lifted dust mass is calculated as a routine in the MGCM itself and can determine the model spatiotemporal dust distribution, is available in some previous versions of the MGCM (e.g. v5) but not in the version used in this thesis (v6), which assumes a constant vertical diffusion of dust from the surface at all points not covered by CO_2 ice. An "offline" derivation of lifted dust is also possible, meaning using standard MGCM outputs to calculate lifted dust mass after the fact, and was used for some of this work. See Chapter 5 for more details.

3.3 Data assimilation

Data assimilation is a statistical technique for combining data about a system and a numerical model of the system to produce the best possible estimate of the system's state (e.g. Kalnay, 2012; Lahoz et al., 2010; Talagrand, 1997). As such, it is a technique which has evident applications in the fields of meteorology and climate science, which increasingly rely on complex GCMs for operations and research. Data assimilation, particularly for use in providing a "best estimate" initial atmospheric state for terrestrial weather forecasting, has been an area of active meteorological research since the 1950s/60s (Bergthörsson and Döös, 1955; Gandin, 1963). For other planets however, such as Mars, the major use of data assimilation is the ability to reconstruct a "best estimate" atmospheric state and its four-dimensional evolution for further study. This reconstruction of the past meteorology is called a "reanalysis".

Until relatively recently, only Earth had the volume of atmospheric data required for data assimilation; this has changed with the increasing number of orbiters observing Mars (Lewis, 2010). Lewis and Read (1995) and Banfield et al. (1995) were the first to propose the idea of assimilating satellite data into Mars atmospheric models, in anticipation of observations

from the ultimately unsuccessful Mars Observer mission. While both recognised the possible advantages of data assimilation in reconstructing atmospheric states from sparse data, these studies took different technical approaches. One main branch following Lewis and Read (1995) uses the "analysis correction" (AC) scheme of Lorenc et al. (1991), a form of variational data assimilation based on the "successive corrections" scheme developed by Bergthörsson and Döös (1955), Cressman (1959), and Barnes (1964). By contrast Banfield et al. (1995) used a simplified form of Kalman filtering, a form of sequential data assimilation. More recent sequential approaches have instead opted for a technique known as ensemble Kalman filtering (Evensen, 1994), developed from ensemble-based approaches to the problem of dynamic prediction and error (e.g. Hoffman and Kalnay, 1983).

3.3.1 The value of data assimilation

Aside from assimilation, one option for dealing with large atmospheric datasets is through simple binning and mapping of the data. This technique is valuable for obtaining information on seasonal or annual scale atmospheric features, such as via zonal-mean temperature profiles (e.g. Smith, 2004) and aerosol profiles (e.g. McCleese et al., 2010). Some valuable outputs from this include the presence of a "clear" and a "dusty" season each martian year, and the asymmetric zonal temperature profiles resulting from Mars' eccentric orbit. Simple binning combined with basic statistical interpolation has also been used for the construction of a continuous, global column dust opacity climatology from orbiter data for over eight martian years (Montabone et al., 2015).

This binning and mapping approach is very useful for examining long-scale meteorological trends in the martian atmosphere. However, it is less useful for examining short-scale (spatial and temporal) and transient dynamical phenomena of the kind which can be examined in a GCM; for example, dust storms, dust lifting activity in general, wave activity, and diurnal variability. The main reason for this is the spatial and temporal separation between the

discrete observational measurements. The MGS and MRO spacecraft are in polar orbits rather than areostationary (the martian equivalent of geostationary) orbits; this allows greater coverage of the globe, but also means that no area on Mars has continuous orbital coverage. Therefore, variables such as dust opacity at a given location may change significantly between observations. This makes it difficult to capture the details of transient processes like dust storm evolution and wave activity from just orbital observations. Another reason for this difficulty is the fact that only a few variables are currently retrieved from Mars orbit, most commonly temperature, aerosol opacity, and chemical abundances. A key variable which isn't currently retrieved from orbit is wind speed, a variable critical for understanding dust lifting and transport in the martian atmosphere and which can be output from an MGCM.

For the study of change in the martian atmosphere, therefore, assimilation has a strong advantage over the use of observations alone. By allowing the accuracy of observations to be integrated with the four-dimensional, self-consistent atmospheric representation of the MGCM, data assimilation allows for the study of phenomena that cannot be easily examined from spatiotemporally sparse observations, while providing a more realistic and accurate representation than running the model by itself. As noted by Lewis and Read (1995), assimilation can fill in the gaps to allow the investigation of transient, dynamical systems, and especially so in the context of sparser martian orbital data sets. Assimilation allows not only the incorporation of observations, but a way to combine observations of different variables (e.g. dust and temperature Lewis et al., 2007), different types (e.g. landers and orbiters Lewis et al., 1996), and from different instruments (e.g. MCS and the Compact Reconnaissance Imaging Spectrometer for Mars (CRISM) Holmes et al., 2019b). Another strength is the ability to investigate the atmosphere as a whole; for example, to assess predictability and as a way of diagnosing problems in the model (Newman et al., 2004; Rogberg et al., 2010). Crucially, the process of "filling in the gaps" does not mean that only times and locations with valid observations are affected by assimilation; the assimilation process propagates

changes throughout the simulation in both time and space, meaning that even spatiotemporal locations without valid observations can be impacted by nearby (in both time and space) observations. Changes to variables by the assimilation scheme can propagate via their effects, such as altered winds, resulting in a simulated atmospheric state different from that simulated without the use of data assimilation.

3.3.2 The Analysis Correction (AC) scheme

Overview

Lewis and Read (1995)'s work in assimilating simulated orbiter and lander data was based on the UK Met Office's analysis correction (AC) data assimilation scheme, the operational scheme used by the UK Met Office at the time (see Lorenc et al., 1991). The AC scheme is a form of "successive correction" data assimilation, where the value of the atmospheric field at a given point is successively updated by the value of observations within a spatiotemporal radius of the point, resulting in a compromise between the model's prediction and the observations (Kalnay, 2012). This radius can be tuned empirically to give the best performance in terms of error compared to observations, as can the relative weighting given to the observations and the model field values.

The proof of concept work for using the AC scheme on Mars was further developed by Lewis et al. (1996) and Lewis et al. (1997). The former tested the AC on a simplified Martian GCM, with data scarcity in mind, and obtained robust results. They also noted that the AC scheme has the advantages of being computationally inexpensive, relatively simple to implement and adjust for different observation types, and designed to handle scarcity of data. This last advantage comes from the fact that observations in the scheme have a spatiotemporal "window" of validity around their actual time and location, with their weight in the assimilation decreasing with spatiotemporal distance from their actual point of validity. This allows for the extraction of as much information as possible from each single

observation. Lewis et al. (1997) extended the study to use the full MGCM, and suggested a way to recreate the atmospheric state from temperature profiles.

After the failures of the Mars Observer and Mars Climate Orbiter missions, the successful insertion of the MGS and its TES instrument finally represented an opportunity to exploit datasets large enough to be useful for assimilation. Lewis et al. (2007) assimilated TES observations during the aerobraking phase specifically (as opposed to the scientific mapping phase), but provides a detailed overview of the assimilation process as applied to TES mapping data as well. The authors assimilated TES temperature profiles and vertically-integrated atmospheric dust opacities, and obtained robust results even with often patchy dust observations.

A high level summary of the AC process in the MGCM will be given here. Further details can be found later in Section 3.3.2 and in Lewis et al. (2007). Fig. 3.7 shows the flow of the assimilation process in the model. The AC scheme iterates between every dynamical timestep in the model; this constant updating is due to the scheme's computational inexpensiveness. Each iteration tries to minimise the difference between the MGCM's best guess of the atmospheric state and the observational values. Observations are inserted repeatedly, in order for the MGCM to get the full update and to allow related fields, such as winds, to balance. Inserted observations have a radius of validity in time and space: specifically, they are valid for 5 hours before their actual observation time and 1 hour after, and are given a weighting dependent on their temporal distance of their actual observation time and the current model time. Concurrently, the "correlation scale" function in space gives a larger footprint to the lower weighted observations further from the valid time, and focusses this footprint on a smaller area as the valid time approaches. These functions and their relation with δt, the time difference between the model time and the valid observation time, can be seen in Fig. 3.8. This ensures that the greatest possible amount of information can be extracted from

sparse observations, such as data from a single orbiter. These parameters can also be tuned to minimise error.

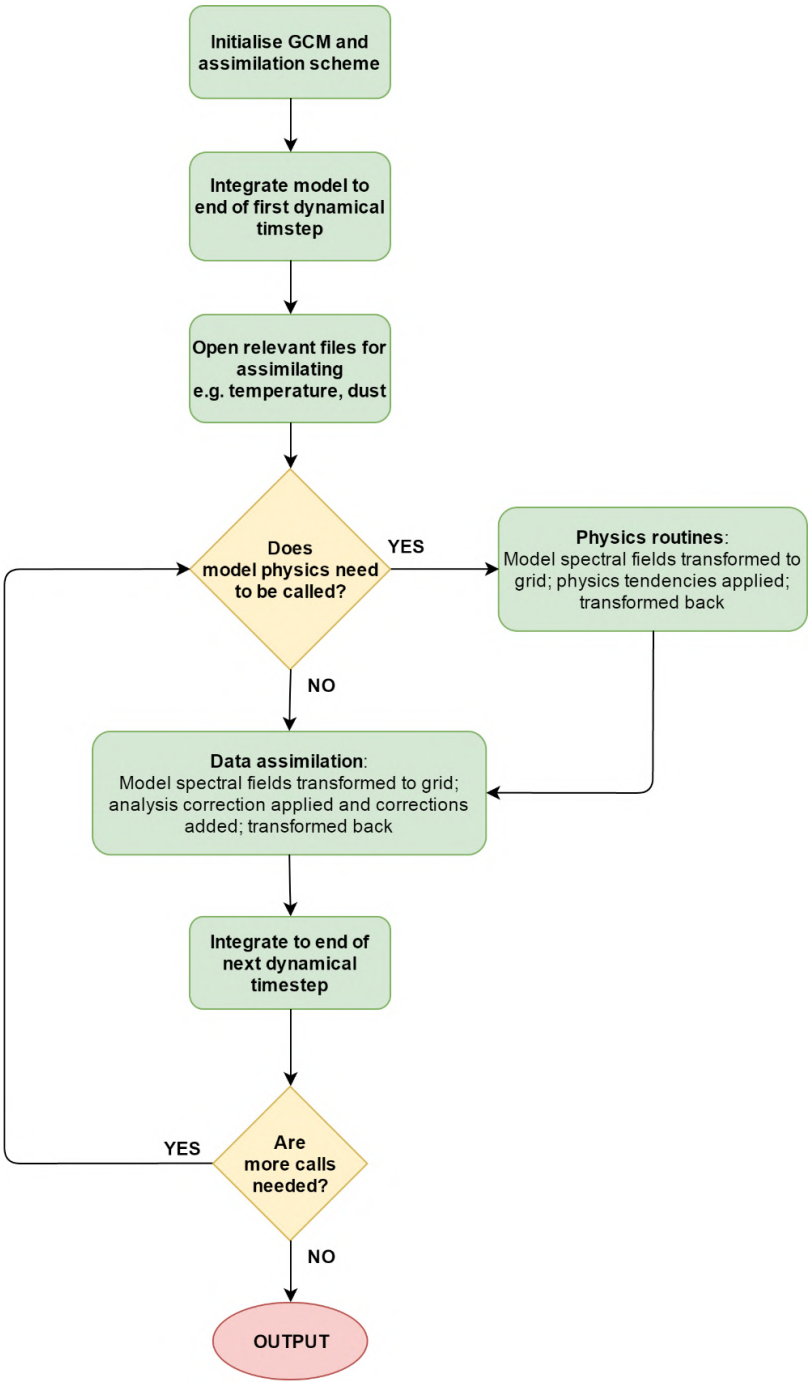

Fig. 3.7 Flowchart representing the flow of the MGCM together with the analysis correction assimilation scheme.

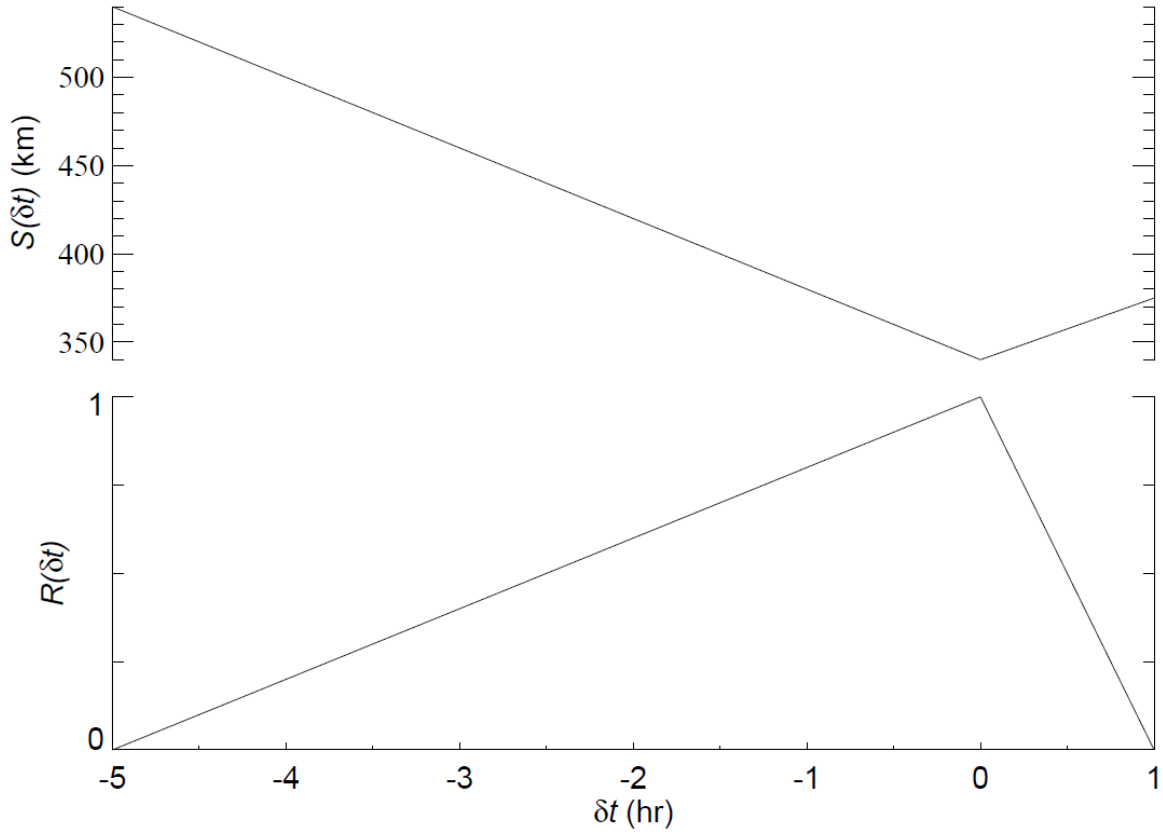

Fig. 3.8 Plot representing the relative value of the correlation scale, S, and the time weighting function, R, as functions of the time difference between the model time and the valid observation time, δt. Reproduced from Lewis et al. (2007) under the STM permissions guidelines.

Basic theory

The aim of every assimilation scheme is to minimise the errors between the assimilated model state, the nominal/"background" model state, and the observations; for variational assimilation schemes, such as the Analysis Correction scheme used in this thesis, this is done via minimisation of the "cost function", mathematically denoted with J (Kalnay, 2012). This cost function is a measure of the disagreement between the background model state $\mathbf{x}_\mathrm{b}$, the observations $\mathbf{y}_\mathrm{o}$, and the "analysis" $\mathbf{x}_\mathrm{a}$. This analysis is the assimilated model state, and is the variable to be solved for such that $\partial J/\partial \mathbf{x} = 0$ (or as close to 0 as possible), in order to get the closest agreement with the true state of the atmosphere $\mathbf{x}_\mathrm{t}$, which is unknown. The full expression of the cost function is

$$\begin{aligned} J(\mathbf{x}) &= \frac{1}{2}\left(\mathbf{x}_\mathrm{b}-\mathbf{x}\right)^\mathrm{T}\mathbf{B}^{-1}\left(\mathbf{x}_\mathrm{b}-\mathbf{x}\right)+\frac{1}{2}\left(\mathbf{y}_\mathrm{o}-\mathrm{H}(\mathbf{x})\right)^\mathrm{T}\mathbf{R}^{-1}\left(\mathbf{y}_\mathrm{o}-\mathrm{H}(\mathbf{x})\right) \\ &= J_\mathrm{b}+J_\mathrm{o} \end{aligned} \tag{3.14}$$

where J_b and J_o are the cost functions for the model background state and the observations respectively; $\mathbf{B}$ and $\mathbf{R}$ are the background error covariances for the background model state and the observations respectively; and H is the operator which transforms the observations $\mathbf{y}_\mathrm{o}$ from "real" space onto the grid of the background model state. The analysis state is therefore defined as

$$\mathbf{x}_\mathrm{a} = \operatorname{argmin} J(\mathbf{x}) \tag{3.15}$$

ie. the points at which the cost function is at its minimum. The formulation of the cost function presented in equation 3.14 relies on several simplifying assumptions. For example, it is assumed that the errors in both the model background and the observations are unbiased and uncorrelated with each other, and that the relevant model processes which are altered

behave linearly within the limit of small spatial and temporal perturbations. With the cost function specified, it must then be solved by the assimilation scheme. This is described below for the Analysis Correction scheme.

The AC assimilation process

As stated in Section 3.3.2, the basic job of the assimilation scheme is to solve the cost function so as to minimise it, thereby producing the analysis. The AC scheme uses an iterative algorithm to solve equation 3.14 for $\mathbf{x}$ by perturbing state $\mathbf{x}$ by $\delta\mathbf{x}$ at each iteration. This perturbation can be expressed solely in terms of the observations $\mathbf{y}_o$, by assuming that the difference between the model background state $\mathbf{x}_b$ and the iterated $\mathbf{x}$ is small enough to be neglected at any particular iteration; ie. $(\mathbf{x}_b - \mathbf{x}) = \mathbf{0}$, allowing the iterative solver to be formulated in terms of $\mathbf{y}_o$ alone, ignoring terms containing $(\mathbf{x}_b - \mathbf{x})$. This allows the iterative analysis equation to be expressed at iteration $n+1$ as

$$\mathbf{x}_{n+1} = \mathbf{x}_n + \mathbf{W}\widetilde{\mathbf{Q}}(\mathbf{y}_o - H(\mathbf{x}_n)) \tag{3.16}$$

where $\mathbf{W}$ is a weighting matrix incorporating the background model error covariances $\mathbf{B}$, the observation error covariances $\mathbf{R}$, and the linearised observation operator $\mathbf{H}$; and $\widetilde{\mathbf{Q}}$ is a normalisation matrix incorporating $\mathbf{W}$ and $\mathbf{H}$. For each iteration, the AC scheme calculates the raw increments between observation and model state $\mathbf{y}_o - H(\mathbf{x}_n)$; these are then normalised to the model grid by $\widetilde{\mathbf{Q}}$, this process being one of taking into account the density of observations by ensuring that co-located observations have the effect of one observation with a correspondingly lower error; and finally spread to the model points with the weightings contained in $\mathbf{W}$ (Lorenc et al., 1991). The errors in model ($\mathbf{B}$) and observation ($\mathbf{R}$) are included within the calculation of $\mathbf{W}$ (see below), and are represented by the ratio of observational to model error ε^2 for each observation. This value is user defined, and allows tuning by the user of the relative weights of the observations and the model background state,

with higher ε^2 indicating more trust in the observations than the model and vice versa. For this thesis, a value of $\varepsilon^2 = 1$ was used for all observations, indicating equal weighting for both observations and model background.

Each model variable is analysed at each run of the AC scheme following a set sequence: surface pressure, temperature, velocity, and aerosols/chemical species (e.g. dust, water ice, water vapour). After temperature is analysed, the perturbed temperature field is balanced by increments to the thermal wind, in order to avoid sudden gravity wave activity which would rapidly restore the temperature field to its pre-analysis state (Lewis et al., 2007).

Due to the size and complexity of the model background error covariance matrix **B**, the analysis process is divided into vertical and horizontal steps, with the former performed first. The relevant vertical variable (for the purposes of this thesis, temperature) is first re-gridded to a standard set of pressure levels. The placing of these levels is adjusted to match the effective vertical resolution of the retrievals (for MCS temperatures, approximately 5 km) in order to avoid the analysis from spuriously affecting features smaller than the observational resolution (Lewis et al., 2007). Ideally, the scheme would assimilate instrument radiances directly to avoid the re-gridding processes and the effects of first retrieving observations with a different model than the MGCM used for assimilation, as has been done in terrestrial contexts (e.g. Qi and Sun, 2006). This has been shown to be possible for short periods for the martian atmosphere, but is still significantly complicated due to the need for an accurate forward model for each instrument to be included in the assimilation (Lee et al., 2011); by assimilating retrieved quantities, this process is left to be performed by retrievals experts.

The horizontal analysis is then performed for the relevant variables (for the purposes of this thesis, temperature and CDOD) with a version of equation 3.16. Here, the weighting matrix **W** is composed the ratio of observational to model error ε^2, and functions for both spreading of observational increments both in space $\mu(S(\delta t))$ and weighting of observational increments time $R(\delta t)$. As can be seen in Fig. 3.8, these functions are prescribed such that

observations have their greatest weighting at the actual observed time, with the weighting declining to nothing five hours after and one hour before the observed time. This allows future observations to inform the analysis as the spacecraft moves along its orbit. Spatially, the spreading is at its lowest at the valid observed time and increases away from it. The form of these functions is based on the terrestrial AC scheme, with the specific values used tuned according to Mars-specific experiments (Lewis et al., 1997, 1996).

3.3.3 Other approaches

Aside from the AC scheme, other techniques have been proposed for martian data assimilation. Houben (1999) assimilated TES aerobraking data in a highly simplified Mars GCM using the computationally expensive 4D-Var scheme to give a good statistical fit. However, the simplicity of the model necessary for the scheme to function does not lend itself to the kind of uses provided by martian GCMs, our most advanced models for representing the martian atmosphere. In contrast, while the AC scheme provides a marginally less perfect statistical fit, it is simple enough to be easily used with an MGCM rather than requiring a highly idealised, non-representative model.

The most popular alternative to AC has been the ensemble Kalman Filter. Roughly, this approach considers all the data over a given time window, and calculates the best "path" through them, before repeating the process (Lahoz et al., 2010). In practice, this approach is almost intractable without certain simplifying assumptions. Both Kass (1999) and Zhang et al. (2001) used a steady-state Kalman Filter, effectively equivalent to the optimal interpolation approach to assimilate TES observations, showing small but limited improvements over the free-running model. Zhang et al. (2001) concluded that dust opacity was the key factor in determining the temperature field, and that therefore more realistic dust opacities and vertical profiles were essential to obtain significant improvements from assimilation. A form of this technique has been used on real TES observations by Greybush et al. (2012), yielding a

robust assimilation with outputs including comparisons to MCS thermal tide observations (Kleinböhl et al., 2013) and polar vortex analysis (Waugh et al., 2016). This assimilation has recently been extended to include MCS observations (Greybush et al., 2019, 2017). This ensemble technique has also been used for temperature assimilation recently by Navarro (2016) and Navarro et al. (2017). One issue with this ensemble approach is that Mars' short radiative timescale causes ensembles to rapidly converge due to solar thermal forcing. A way to tackle this is through the use of "adaptive inflation", in which perturbations are added to ensemble members to force divergence (described in Greybush et al., 2012).

3.3.4 Mars Climate Sounder observations

For the work presented in this thesis (with the exception of the example presented in Fig. 3.6), the assimilated observations were exclusively Mars Climate Sounder (MCS) temperature retrievals and CDOD products. The MCS retrievals are described in general below, before the temperature and CDOD observations are discussed in greater detail. Lastly, the processing and filtering procedures applied to the data before assimilation are described. The MCS data used for the work in this thesis was v5.2, unless otherwise specified, and except for the period of the 2018 Global Dust Storm (see below) which was v5.3.2 due to differences in channels used for dust sensing.

Overview

MCS is a multi-channel limb sounder aboard the Mars Reconnaissance Orbiter (MRO), optimised to study the vertical structure of martian atmospheric temperature and aerosols (McCleese et al., 2010, 2007). MCS has eight infrared channels between the wavelength bands 0.3-50 μm, and one broadband visible channel, with an effective vertical resolution for retrieved profiles of around 5 km (Kleinböhl et al., 2009). MCS has provided near-continuous observations of the Mars atmosphere from MRO's orbital insertion in September 2006 to the

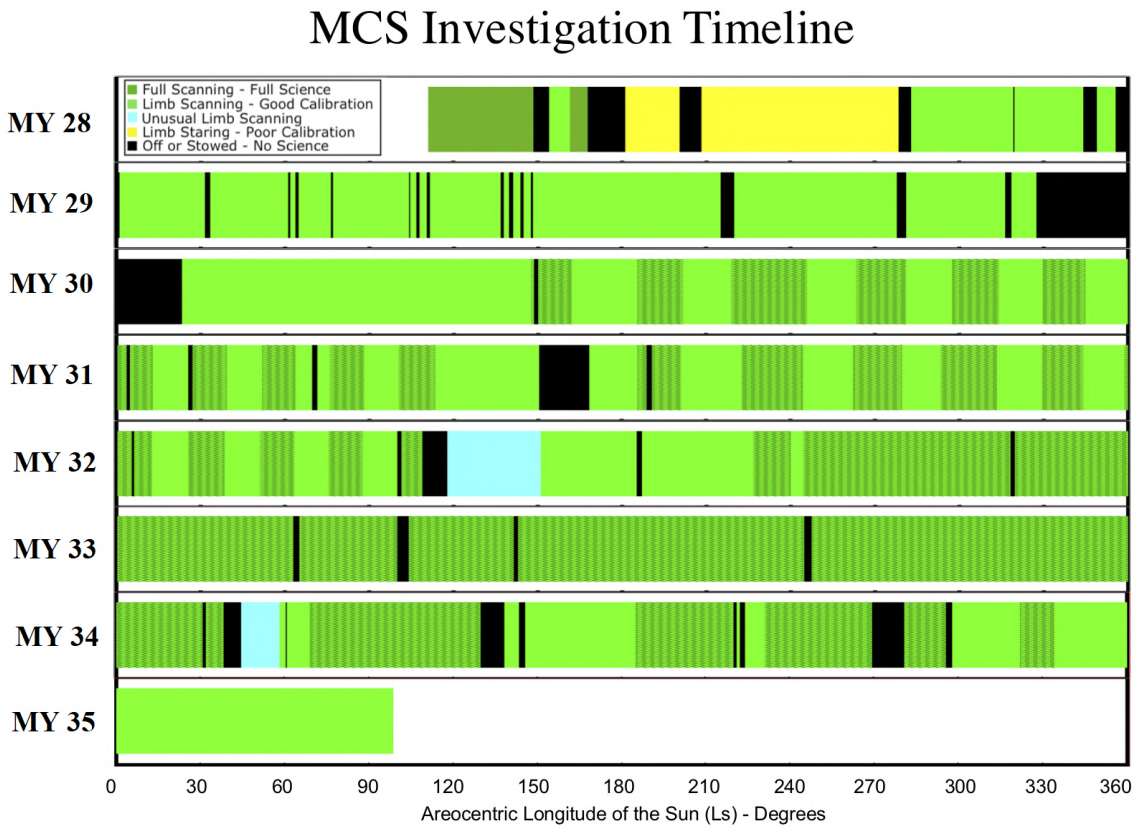

Fig. 3.9 Plot showing MCS coverage and data quality for the entire mission from the beginning of science observations in MY 28 to partway through MY 35. Credit: the MCS Team (personal communication). Lightly adapted by the author.

present day, covering six full martian years (MYs 29-34), part of MY 28, and all of MY 35 to date. There are some gaps in coverage due to various technical issues with the instrument and/or spacecraft, as seen in the blacked out sections in Fig. 3.9; in particular, MY 28 has long periods of "limb-staring" profiles with reduced data quality due to pointing issues with MRO (McCleese et al., 2010). The meteorological variables which have had continuous coverage throughout are temperature, dust opacity, and water ice, along with derived products such as CDOD and surface temperature. This multi-annual dataset therefore offers a wealth of information for assimilation in particular.

The MRO spacecraft is located in a sun-synchronous polar orbit, with full revolutions of the planet occurring 13 times per sol. The nature of the sun-synchronous orbit means

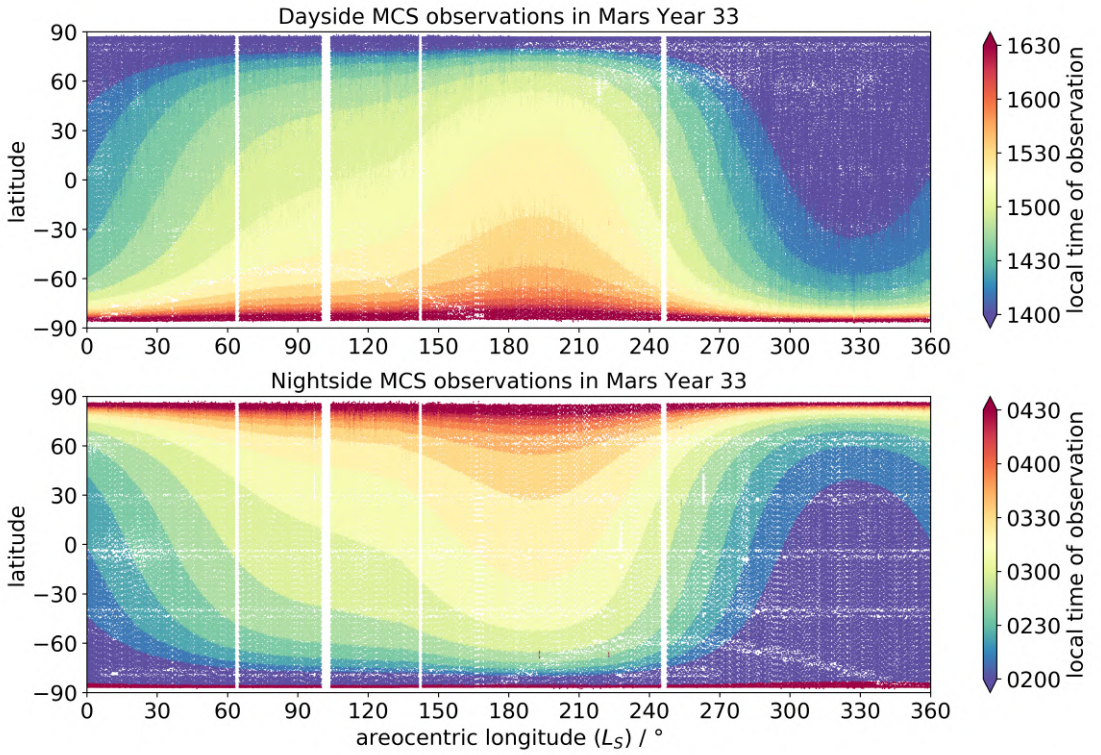

Fig. 3.10 Plot of dayside and nightside MCS observation locations and local times for MY 33.

that MCS measures at two fixed local times: approximately 03:00 and 15:00, resulting in 13 dayside passes and 13 nightside passes per sol. The exact local time varies seasonally and latitudinally, as can be seen in Fig. 3.10 which shows MCS observations in MY 33. The gaps in coverage in certain L_S intervals show times when MCS was not measuring. The latitude bands which show fewer observations, visible on the nightside at (for example) 5° S and 40° S, are due to MCS taking blackbody calibration spectra. Similarly the curved bands of fewer observations at southern high latitudes (L_S=10-170° on the dayside, L_S=180-340° on the nightside) are due to MCS taking solar calibrations when the illumination is most favourable. As well as the standard along-track observations, MCS also takes a small proportion of cross-track observations which measure perpendicular to the orbital trajectory; these are incorporated into the reanalysis used in this thesis, and provide a greater degree of local time coverage.

Temperature retrievals

MCS retrieves martian atmospheric temperature profiles through its measurement of infrared emission on the martian limb. Retrieved temperature profiles have an effective vertical resolution of 4-6 km with a precision of 0.5-2 K, over a typical altitude range of between 5-10 km and 80-90 km; they are reported on retrieved pressure levels measured to a 1-2% precision (Kleinböhl et al., 2009). Recent improvements in the retrieval algorithm to account for horizontal temperature gradients have resulted in a newer "2D" dataset which drops the previous assumption of spherical symmetry; this leads to differences in retrieved along-track polar temperatures of up to 10 K in polar winter (Kleinböhl et al., 2017). Details of the exact retrieval procedure and algorithms used can be found in Kleinböhl et al. (2009), Kleinböhl et al. (2011), and Kleinböhl et al. (2017).

Derived CDOD products

As a limb-sounding instrument, MCS cannot directly retrieve CDOD. MCS retrieves dust opacity profiles with an effective vertical resolution of around 5 km from a channel centred at wavenumber 463 cm^{-1}, which is close to a dust absorption feature at $\sim$22 μm (Kleinböhl et al., 2009). Dust single-scattering is taken into account in the retrieval (Kleinböhl et al., 2011). Dust opacities are reported, like temperatures, over a typical altitude range of between 5-10 km and 80-90 km; however, they usually cut off at lower altitudes of around 40-50 km. The extreme dust loading of a Global Dust Storm can raise the altitude of the reported profile (Montabone et al., 2020). As with temperatures, the newer 2D retrievals show different results than previous MCS retrievals. In particular, the southern winter pole shows reduced dust presence (Kleinböhl et al., 2017).

Using the measured dust opacity profiles, MCS also provides derived CDOD products. Unfortunately the MCS geometry and the rapid saturation of the relevant channels near the surface means that the dusty near-surface region of the atmosphere cannot be measured.

Therefore the measured profile is extrapolated both upwards and downwards to the surface, under the assumption of a well-mixed dust distribution beyond the lowest and highest reported profile opacities. Given the high opacities present in the planetary boundary layer, this means that there is likely systematic error in the MCS CDOD products. With this caveat in mind, they still represent an important source of information about CDOD on Mars, especially given the lack of high-volume nadir dust measurements since the end of TES operations. In seasonal comparisons, MCS CDOD values generally compare favourably with directly measured TES CDOD (Montabone et al., 2015). It should also be noted that surface temperature constraints on TES CDOD retrievals (Smith, 2004) mean that MCS effectively has greater dust coverage over the winter poles, making it a valuable data source for polar studies.

Processing

MCS temperature profiles undergo little processing before being assimilated. Unless otherwise stated, MCS temperatures are not filtered before assimilation in the simulations considered in this thesis. This is in contrast to TES temperature profiles, which extend down to the surface and are therefore generally filtered in assimilations to remove those values which fall below the CO_2 condensation temperature (e.g. Greybush et al., 2019; Lewis et al., 2007). Chapter 6 contains a detailed discussion on the effects of filtering temperatures below the CO_2 condensation temperature on modelled dynamics.

CDOD products undergo greater processing and filtering before they are assimilated into the MGCM. Equatorial daytime MCS dust profiles generally have higher cutoffs than others, meaning that extrapolation to the surface under the well-mixed assumption can cause spuriously high CDOD values; the presence of water ice clouds in the tropics can also have this effect (Montabone et al., 2015). For these reasons, daytime equatorial MCS CDOD values are generally excluded from assimilation. The exception is during the 2018/MY 34

Global Dust Storm: the well-mixed assumption generally holds better during situations of high dust loading, and the lack of water ice clouds in the lower atmosphere enabled the MCS team to add dust profile information from a channel generally use for water ice retrievals (Montabone et al., 2020); this dataset is formally labelled v5.3.2. This should lead to more reliable daytime CDOD values. Therefore, for the period of the storm (L_S=180-240°) the filtering of equatorial daytime MCS CDOD was suspended.

MCS dust retrievals and CDOD values are reported in the infrared (21.6 µm), while the MGCM uses visible opacities (600 nm) for its dust radiative transfer calculations. This requires CDOD values to be converted from the infrared to the visible before assimilation, via a scaling factor. Reported CDOD values are therefore multiplied by a standard factor of 7.3 prior to assimilation (Kleinböhl et al., 2011).

3.4 Analysis period and MGCM resolution used

The work presented in this thesis is based on one multi-annual reanalysis of six martian years, running from the beginning of Mars Year (MY) 29 to the end of MY 34. This run is henceforth referred to as "the reanalysis". MY 28 data was excluded as for a large part of the year MCS was in "limb-staring" mode, leading to a drop in the quality of retrievals (McCleese et al., 2010). The MGCM was run at a spectral resolution of T42, with 50 model levels (T42xL50). In order to focus on the effects and behaviour of dust specifically, the MGCM was run without a water cycle. This also helped enable the computationally expensive and data intensive process of running and storing a six martian year reanalysis. In order to ensure a stable atmospheric state, the MGCM was first spun up for one martian year, before being run continuously for six martian years. The observations assimilated into the MGCM were MCS temperature retrievals and CDOD products, after the processing described above. The retrievals used were v5.2, retrieved using non-spherical geometry as described in Kleinböhl et al. (2017), except for during the MY 34 Global Dust Storm when

v5.3.2 was used (Montabone et al., 2020). The following three chapters describe the core results of this thesis, with further additional experiments introduced as relevant for the work done in each chapter.

Chapter 4

Surface warming during the 2018/Mars Year 34 Global Dust Storm

This chapter uses the multi-year reanalysis described in Chapter 3 to examine the effect of the MY 34 GDS on martian surface and near-surface air temperatures. First, previous observations and modelling work on how surface temperatures are affected by high dust loading are discussed. The key factors which control martian surface temperatures are presented: CDOD and surface thermal inertia. For the former, specific optical properties of dust have been shown to be critical in determining dust radiative impacts. The results from the reanalysis are then shown, and compared against various forms of surface, orbital, and telescopic observations. The results are finally discussed in the context of previous martian literature, potential caveats are stated, and conclusions are drawn regarding the role of various factors in controlling surface temperatures and the importance of GDS spatial structure in determining globally-averaged effects on temperature.

Some of the results presented in this chapter were published in the journal *Geophysical Research Letters* (Streeter, P. M., Lewis, S. R., Patel, M. R., Holmes, J. A., & Kass, D. M. (2020). **Surface warming during the 2018/Mars Year 34 Global Dust Storm.** Geophysical Research Letters, 47, DOI: 10.1029/2019GL083936). The results presented are all based

on simulations and analysis performed solely by the author, with advice and input from coauthors and reviewers. Use of some material from the journal article (including figures) in this thesis is permitted under the terms of the Creation Commons Attribution license (CC-BY 4.0). Throughout this chapter, advice on interpretation, phrasing and structure was provided by supervisors (S.R. Lewis and M.R. Patel) and J. A. Holmes. Advice on interpretation and use of the MCS surface temperature retrievals, as well as the justification for the mask over the seasonal caps used in presenting these retrievals, was provided by an external coauthor (D.M. Kass). Finally, advice on clarifying interpretations and phrasing, additional citations to include, and additional observations to compare against was provided by journal article reviewers (Claire E. Newman and Jim Murphy). The main text, numerical experiments and comparisons against observations, and interpretations and discussion were the author's work.

4.1 Introduction

As discussed in Chapter 2, dust aerosol is a critical component of Mars' atmosphere, and has long been known to have significant radiative and dynamical effects through scattering and absorption of radiation (e.g. Gierasch and Goody, 1972; Pollack et al., 1979). Global dust storms (GDS) are a spectacular example of dust-related phenomena on Mars, occurring every few martian years and covering swathes of the planet with a deep dust cloud for months at a time (e.g. Haberle, 1986; Leovy et al., 1973; Zurek, 1982; Zurek and Martin, 1993). The high atmospheric dust loading induced by these storms has been modelled to have substantial effects on the circulation (e.g. Bougher et al., 1997; Böttger et al., 2004; Haberle et al., 1982; Lewis and Read, 2003) and radiative balance (e.g. Read et al., 2016) of the atmosphere. This chapter focusses on the radiative effects of GDS at the martian surface.

The usual way to describe the degree of dust loading in the atmosphere is using optical depth (CDOD), defined as the log of the ratio of incident to transmitted intensity of a beam at a certain wavelength (Petty, 2006) and described in Chapter 3. The actual radiative effects of

atmospheric aerosols also depend on particle radius and the specific scattering and absorption properties of the aerosol. For example, mineral dust generally has a greater scattering effect on incident solar radiation than smoke, which is compositionally different and, on Earth, generally smaller (Friedlander, 2000). Smoke primarily absorbs at visible wavelengths, lending it its characteristic dark colour; it therefore has a greater "anti-greenhouse effect", meaning that rather than trapping infrared radiation from the surface and thereby causing net warming (like CO_2 gas) it absorbs incident sunlight, causing net cooling below the smoke layer. It has been famously theorised that a global-scale cloud of soot and smoke on Earth, such as that which might be caused by global nuclear warfare, would result in drastic surface cooling or "nuclear winter" (Turco et al., 1984). The key parameter describing this tendency to either scatter or absorb at particular wavelengths is the single-scattering albedo ω, described in Chapter 3; this is the ratio of scattering to extinction of incident radiation at a particular wavelength. An example of the single-scattering albedo used for soot/smoke in nuclear winter simulations is 0.64 at solar wavelengths (Robock et al., 2007), meaning that 36% of incident sunlight is absorbed by the aerosol. Mineral dust has been shown to have surface radiative effects which are highly dependent on the specific ω used, with a higher ω of 0.97 causing a lesser reduction in shortwave flux at the surface than a lower ω of 0.84 (Shell and Somerville, 2007). Recent work on the properties of martian atmospheric dust, based on observations of the 2007 GDS, estimates an ω of 0.94 (Wolff et al., 2009); significantly greater than that of terrestrial soot/smoke, making it a "brighter" aerosol. This is the value used in the MGCM. Previous estimates of dust ω were around 0.89; revising this to 0.94, a change of $\sim$5%, was modelled to cause $\sim$45% decreased absorption of sunlight and corresponding increases in surface temperature of 4-5 K at high opacities (Wolff et al., 2009). Aerosol properties are therefore critical for determining aerosol radiative effects, and ω in particular has a large impact on shortwave radiative flux at the surface.

As well as the dust optical properties, the degree of dust loading itself also has significant impacts on the surface energy budget. High CDOD in a Mars GCM has been shown to decrease surface shortwave flux while increasing longwave emission to the surface, with a net reduction in surface flux of $\sim$70 W m^{-2} as averaged over a martian year for the scenario of a CDOD 5 dust cloud covering the planet for a whole orbital cycle (Read et al., 2016), though it should be noted that observed GDS have tended to encircle all longitudes of Mars but not reach all latitudes (e.g. Montabone et al., 2015, 2020), and have not been observed to last for entire martian years, making these unrealistic assumptions. *In situ* observations of the 2018 GDS from the Mars Science Laboratory (MSL) in Gale Crater showed substantial dayside surface and near-surface air cooling due to the reduction in shortwave flux, but also a nightside warming effect (Guzewich et al., 2019); this latter was due to enhanced longwave emission and backscattering as a result of the increased aerosol, which consequently led to higher atmospheric temperatures (Martínez et al., 2017). Orbital measurements confirm this; for example, TES surface temperature retrievals during the 2001 GDS showed peak nightside surface warming and dayside surface cooling of $\sim$20 K in both cases (Smith, 2004). These and other observations are discussed in greater detail in Section 4.3.

In addition to atmospheric dust, surface properties have also been shown to be key in controlling surface temperatures and near-surface air temperatures (henceforth "air temperatures" in this chapter). The surface thermal inertia describes the temperature response of the surface to incident energy flux, and is especially important on Mars given the low atmospheric density (and hence low atmospheric thermal inertia) and lack of oceans to act as heat reservoirs. Materials with low thermal inertia, such as loosely aggregated dust, heat and cool rapidly, while materials with high thermal inertia (like bedrock) stay relatively warm at night and cool in the day. Ground temperatures at the MSL site, for example, are driven mostly by the local thermal inertia, with lower thermal inertia regions resulting in more extreme minimum and maximum ground temperatures and vice-versa (Martínez et al., 2017).

These lower nightside and higher dayside temperatures at low thermal inertia regions are due to increased radiative heating on the dayside and rapid radiative cooling on the nightside, as infrared radiation is emitted back into space.

This chapter uses the reanalysis described in Chapter 3 to investigate how the 2018 (MY 34) GDS affected surface and air temperatures, via its modification of the radiative budget. As stated above, previous modelling work on the surface energy budget during GDS events has used unrealistic dust loading assumptions and not investigated surface temperatures themselves. Observations from orbital and *in situ* instruments, meanwhile, indicate that nightside warming caused by GDS can be close to or as great as dayside cooling. However, orbital retrievals to date have been limited in their local time coverage (TES only observed at two martian local times), while in situ instruments give full local time coverage but only at a very specific location but not global coverage. The reanalysis therefore provides an opportunity to combine MCS observations of the 2018 GDS, themselves limited in local time coverage but with global extent, with an MGCM able to provide output at any local time required. With this method, true diurnal average changes can be reported, and any spatial heterogeneity in surface and air temperature changes can be investigated.

The results in this chapter focus on the specific period L_S=200-220° of MY 34, the height of the MY 34 GDS, and compare this with the same period in MY 30, a relatively quiet year in terms of dust loading. As well as the multi-year reanalysis used for all the work in this thesis, this chapter also contains comparisons with additional MGCM runs. One was a pre-existing reanalysis of TES data for MY 25, over the period of the MY 25 GDS (Holmes et al., 2019a); again, the period L_S=200-220° was used as there was a remarkable similarity in the temporal and spatial structure of the MY 25 and MY 34 GDS (Kass et al., 2019). The others were free-running MGCM simulations with prescribed temporally and spatially uniform CDOD distributions covering the approximate temporal and spatial extent of the MY 34 GDS (L_S=185-230°, 60° S - 40° N). 15 of these free-running simulations were performed,

each with a different uniform CDOD distribution ranging from 1-15 (as normalised to 610 Pa).

4.2 Results

Throughout this chapter, dayside/daytime refers to a local time of 15:00, while nightside/nighttime refers to a local time of 03:00; these local times were chosen to match MCS observations. Differences henceforth are in relation to MY 30 of the reanalysis, so that "cooling" means cooling relative to the same period in MY 30. "Global averages", when they are used, are weighted according to area (see Chapter 3).

Mars' dayside surface underwent cooling up to 39 K, with a global average cooling of 14 K, due to dust-induced blocking of incident solar radiation. The areas with the greatest cooling included Chryse, northern Hellas, Argyre, Isidis, and Amazonis (Fig. 4.1.b). These are all low elevation regions, and corresponded to locations of high CDOD (Fig. 4.2.a) relative to the non-GDS case (Fig. 4.2.f). There was a statistically significant anti-correlation of $r = -0.54$ between CDOD and dayside surface temperature difference in the reanalysis. Mars' extreme topographic variation means topographic lows have a greater column opacity at the surface than highs, pressure-normalised opacities (CDOD at 610 Pa) being equal. Low topography regions therefore tend to have higher CDOD. During the GDS this therefore resulted in greater cooling over low topography, of up to 39 K, and less cooling over high topography, such as the southern highlands and the Tharsis plateau, of 5 K and below. Note that maximum warming/cooling values are likely to be functions of MGCM resolution, as higher resolutions enable expression of greater and lower surface thermal inertia values and surface topography. For example, a coarse model grid square with a certain thermal inertia may at a higher resolution consist of several grid squares with higher and/or lower thermal inertia values than the value of the coarse grid square; at coarser resolutions, such local variabilities are averaged out.

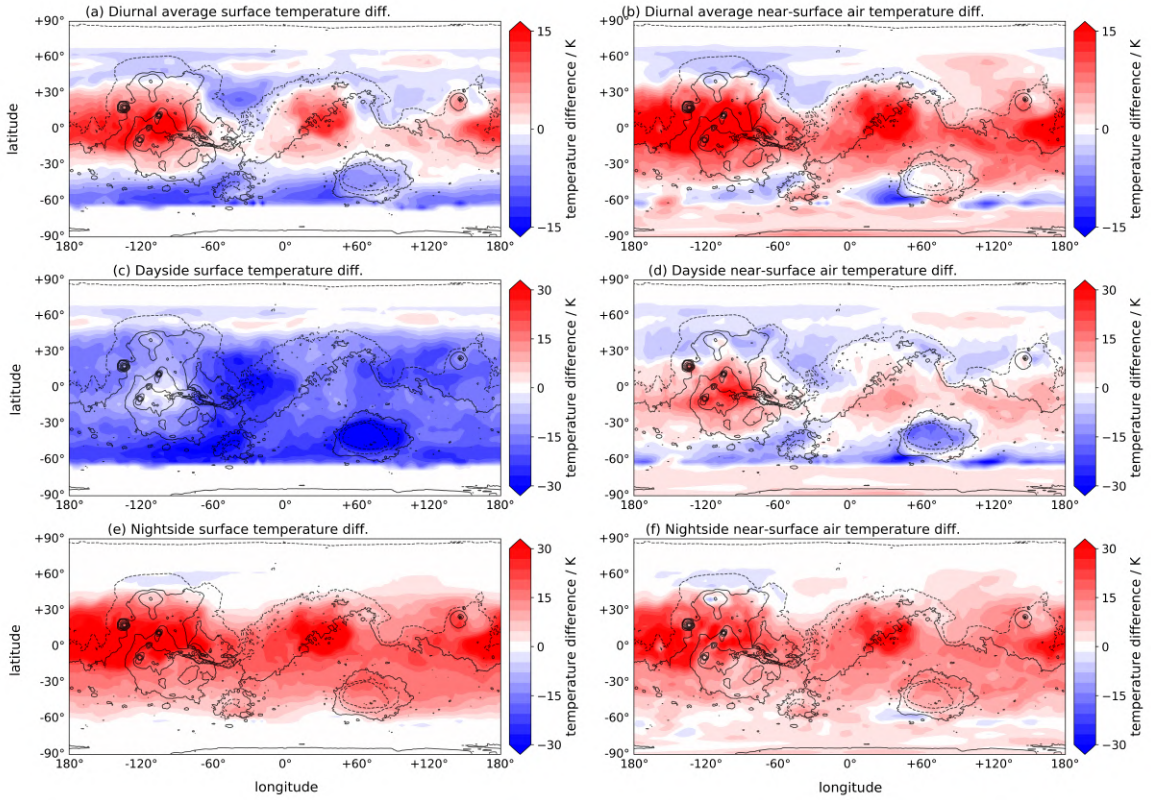

Fig. 4.1 (Left) surface temperature and (right) air temperature difference between MY 34 and MY 30 for the period L_S=200-220°; (top) diurnally averaged, (middle) at 15:00 (dayside), and (bottom) at 03:00 (nightside). Adapted from Streeter et al. (2020).

Mars' nightside surface underwent warming of comparable magnitude to the dayside cooling (Fig. 4.1.c), due to the effect of increased backscattering of longwave emission from the surface. This warming had a maximum magnitude of 42 K, with a globally averaged warming of 13 K. Nightside warming did not correlate as well with CDOD as dayside cooling, with a calculated $r = 0.37$ between CDOD and nightside surface temperature difference in the reanalysis. This is because the dominant radiative process during the clear-case martian night is surface cooling via emission of longwave radiation: highly efficient in Mars' thin, low thermal inertia atmosphere. This cooling rate is controlled by surface thermal inertia, rather than daytime solar (shortwave) insolation. Therefore, the locations of greatest relative night-time warming caused by enhanced longwave backscattering were determined by surface thermal inertia rather than by CDOD; there was a calculated high anti-correlation between surface thermal inertia and nightside surface temperature difference ($r = -0.68$). The warming was greatest at the high-topography regions of Tharsis and Elysium Mons, but also over the low-elevation Amazonis and Arabia regions. What these regions all had in common was low thermal inertia (Fig. 4.2.b), which indicates the presence of finer material on the surface.

In a globally-averaged sense, the 13 K nightside warming was almost enough to completely cancel out the 14 K dayside cooling; however, as the two were controlled by independent factors – thermal inertia and CDOD, respectively – the diurnally-averaged effect was not one of exact cancellation. Instead, there was strong spatial heterogeneity in surface temperature difference. Isidis and the southern highlands showed a rough cancellation, but most regions covered by the GDS did not (Fig. 4.1.a). While there was a net 5 K cooling over Chryse, a greater effect was a net warming up to 19 K over Amazonis, the low thermal inertia regions between approximately 160° E - 50° W and 15° S - 40° N (Amazonis/Tharsis/Elysium), between 0° E - 50° W and 10° S - 40° N (Arabia Terra), and Elysium Mons (Fig. 4.2.b). The globally-averaged effect of the MY 34 GDS was therefore a diurnally-

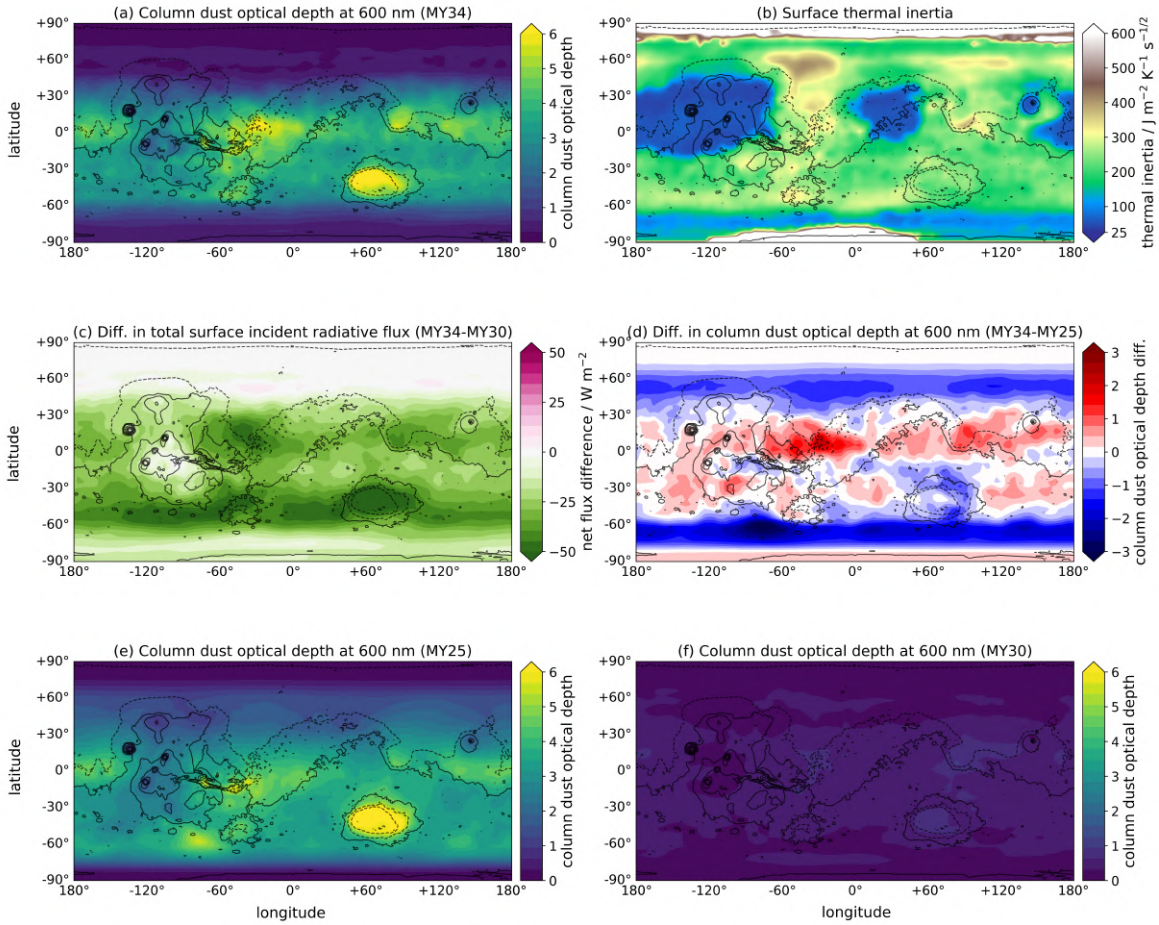

Fig. 4.2 As averaged over L_S=200-220°: (top left) CDOD in MY 34; (top right) surface thermal inertia map in the MGCM; (middle left) diurnally-averaged total surface radiative flux difference between MY 34 and MY 30; (middle right) difference in CDOD between MY 34 and MY 25; (bottom left) CDOD in MY 25; (bottom right) CDOD in MY 30. Adapted from Streeter et al. (2020).

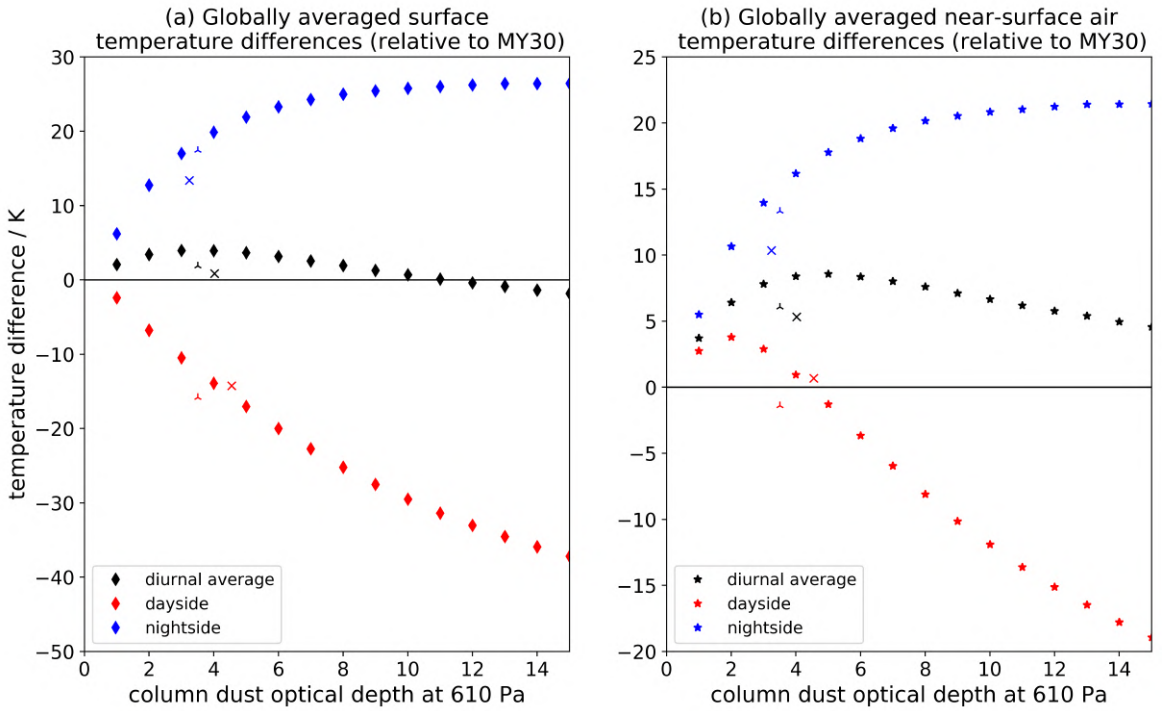

Fig. 4.3 (Left) surface temperature and (right) air temperature differences relative to MY 30, globally averaged (and area-weighted) over the period L_S=200-220° for a range of CDOD at 610 Pa. Presented are diurnal averages (black), dayside (15:00) values (red), and nightside (03:00) values (blue). The MY 34 GDS in the reanalysis is marked with a cross; the MY 25 GDS is marked with a three-pointed star. CDOD at 610 Pa are also at the relevant local times, and are averaged between latitudes 60° S to 40° N. Adapted from Streeter et al. (2020).

averaged increase in surface temperatures, due to this strong nightside warming. This was despite a decrease in the diurnal average surface radiative flux of 10-50 W m^{-2} over most of the planet's surface (Fig. 4.2.c), suggesting that the diurnal distribution of surface radiative flux was at least as important as the magnitude of the diurnally-averaged surface radiative flux in controlling diurnally-averaged surface temperatures.

Globally- and diurnally-averaged air temperatures displayed a 5.3 K increase during the MY 34 GDS. Nightside air temperature warming closely tracked surface temperature warming in being greatest over low thermal inertia regions (Fig. 4.1.e,f); the maximum nightside warming was 37 K. This is because Mars' air temperatures are mostly controlled by surface temperatures. As the nightside surface is warmer during the GDS, so too is the

nightside near-surface air. Less expected was the dayside near-surface warming over some regions, where the surface is cooler (Fig. 4.1.d). This dayside air warming reached up to 31 K over the highest parts of Tharsis. The pattern of dayside air warming mostly fell within a latitude band between 10° N and 30° S, corresponding to areas which saw the least dayside surface cooling. This was due to the coupling together of surface temperatures and air temperatures caused by dramatically increased absorption of both shortwave and longwave radiation in the atmosphere, a result of the increased dust presence. Another way of putting this is that the icreased absorption from dust effectively mimicked the effect of a denser atmosphere. Mars' thin atmosphere enables rapid heat transport away from the surface by convection in non-GDS conditions, creating a high surface-air temperature contrast; the GDS changed this and inhibited surface convection. The GDS-induced surface-air temperature coupling, together with the reduced shortwave flux on the surface, significantly reduced the surface-air temperature gradient (see Fig. 4.4.e,f). Therefore, despite the cooling in dayside surface temperatures, the decreased surface-air temperature gradient meant that dayside air temperatures could be up to 12 K (30 K over Tharsis) higher than in the clear-case. If GDS surface temperatures were higher than non-GDS air temperatures, therefore, then so were GDS air temperatures.

A range of CDOD (normalised to 610 Pa) were tested to explore the impact of greater dust loadings (over the same latitudinal extent and season as the MY 34 GDS) on surface temperatures and air temperatures (Fig. 4.3.a,b). Increasing CDOD resulted in increased nightside warming and dayside cooling (Fig. 4.3.a). However, for CDOD higher than 10 the nightside warming magnitude plateaued, remaining constant at $\sim$25 K due to longwave backscattering reaching its maximum efficiency. By contrast, the dayside cooling magnitude continued to increase with CDOD, albeit at a decreasing rate. This exponential-like decay follows from the definition of optical depth as the log of the ratio of incident to transmitted flux. The result was global surface warming for CDOD between 1 and 11, peaking at 3.9 K

for CDOD 3-4; this range includes the MY 34 GDS, which had an average CDOD in the latitude range 60° S to 40° N of ∼4. For CDOD >11 the continued increase in dayside cooling coupled with the stagnant nightside warming resulted in net global cooling , reaching 1.8 K for CDOD 15.

Globally averaged air temperatures showed a similar pattern to surface temperatures, albeit typically warmer by ∼ 6 K (Fig. 4.3.b). Nightside air temperatures exhibited the same plateau as nightside surface temperatures, due to the close coupling between the two described above. Dayside air temperature warming peaked at 4 K at CDOD 2, which was apparently sufficient to reduce the surface-air temperature gradient, coupling surface temperatures and air temperatures and thus causing warming, but sufficiently low that the warming was not outweighed by surface cooling. The diurnally-averaged effect was a globally-averaged increase in air temperatures for across the entire range of CDOD 1-15, peaking with a 8.5 K warming at CDOD 5.

Surface temperature and air temperature variation over the course of an average sol (Fig. 4.4) was examined at a low thermal inertia (10° N, 30° E) location and a high thermal inertia (5° N, 100° E) location. These locations were chosen as they had near-identical GDS-induced radiative flux differences, allowing for a fair comparison of the effects of thermal inertia specifically. The differences in the diurnal surface temperature cycle (Fig. 4.4.a,b) for the clear case can be seen in the substantially greater surface temperature variation at the low thermal inertia region, especially the much colder nightside temperatures from more efficient radiative cooling. The minimum surface temperature rose 18 K (from 195 K to 213 K) in the high thermal inertia region, and 40 K (from 156 K to 196 K) in the low thermal inertia region. Dayside cooling magnitudes were more similar, with maximum surface temperature falling 27 K (from 284 K to 257 K) in the high thermal inertia region and falling 26 K (from 301 K to 275 K) in the low thermal inertia region. This very similar reduction in dayside surface temperatures follows from the (deliberately chosen) close similarity in surface radiative

flux change between the two regions. This is therefore further support for the idea that the magnitude of dayside cooling depends on CDOD and reduced shortwave flux rather than surface properties. The overall effect of CDOD values above 2 was to reduce the diurnal amplitude of both surface temperatures and air temperatures, by nightside warming and dayside cooling, and to reduce the surface-air temperature gradient, by the coupling mechanism described above. For CDOD 15, the diurnal surface temperature variation decreased from 89 K to 5 K in the high thermal inertia location and from 145 K to 17 K in the low thermal inertia region, representing an almost complete absence of diurnal variability.

Finally, a major effect of high CDOD was to dramatically decrease the surface-air temperature difference on the dayside (Fig. 4.4.e,f). For MY 34, the peak surface-air temperature contrast was 11 K and 21 K for the high thermal inertia and low thermal inertia locations respectively, compared to 40 K and 55 K for MY 30. The nightside surface-air peak temperature contrast was also reduced from 10 K to 4 K (high thermal inertia) and from 21 K to 11 K (low thermal inertia), coupling nightside air temperatures even more tightly to nightside surface temperatures.

4.3 Comparison against observations

Given the novel nature of the results presented, which show a globally-averaged surface warming during the MY 34 GDS, it is important to compare the reanalysis to observational datasets. Fortunately, there are a number available both for the MY 34 GDS itself and previous GDS. The first and most pertinent comparison to make is against retrieved surface temperatures from MCS itself, for both MY 30 and MY 34, which provides a global dataset for the same years investigated with the reanalysis. Another orbital dataset is from TES, which provides observations of the MY 25 GDS; while a different storm, it had a remarkably similar seasonal start time and spatial extent to the MY 34 event (Kass et al., 2019). Older orbital observations during a GDS are available from Mariner 9, though not as extensive as

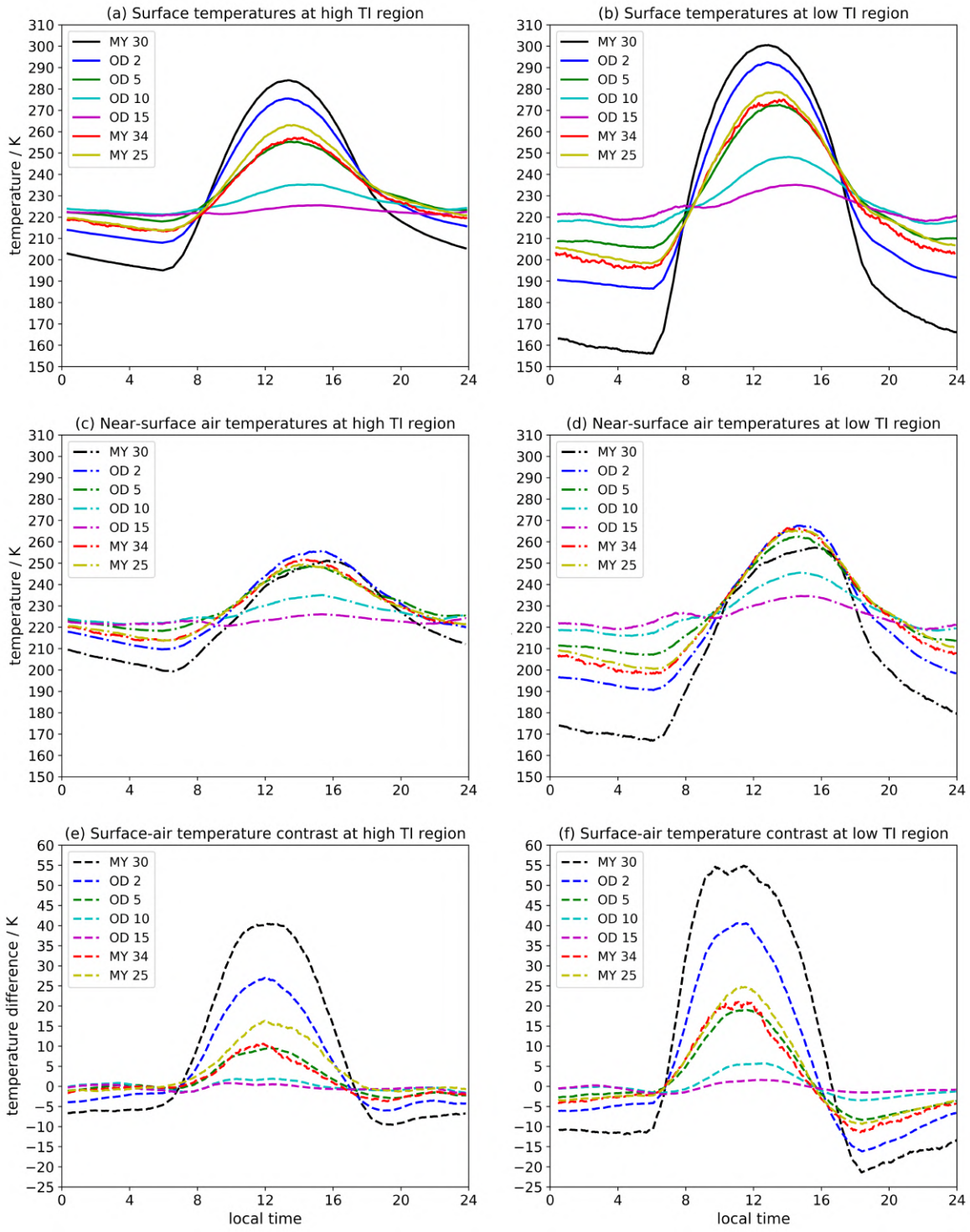

Fig. 4.4 The diurnal cycle in (top) surface temperature, (middle) air temperature, and (bottom) surface-air temperature contrast as averaged between L_S=200-220° for (left) a high thermal inertia region and (right) a low thermal inertia region. Diurnal cycles are presented for a range of CDOD and for MY 25, MY 30, and MY 34. Adapted from Streeter et al. (2020).

those from TES and MCS. Direct temperature measurements from rovers and landers are also available for the MY 34 GDS and Viking-era storms, though with the caveat that the comparison in this case is between point-source measurements and a much coarser model grid. Lastly, there are some ground-based telescopic temperature measurements from radio occultations for the MY 25 GDS.

MCS surface temperature retrievals from MY 30 and MY 34 provide the most relevant source for comparison, given that they were retrieved from the same instrument as that responsible for the data assimilated into the reanalysis. As averaged over L_S=200-220° (bearing in mind the local time constraints of MCS' orbit; see Chapter 3), the retrievals showed a globally averaged net surface temperature decrease of 2.1 K, compared to a decrease of 0.9 K from the MY 34 reanalysis using the same local times. Nightside warming agreed very well with the reanalysis on both spatial morphology, with the greatest warming occurring over low thermal inertia regions (Fig. 4.5), and in globally averaged value, with warming of 11.2 K and 9.1 K for the retrievals and reanalysis respectively. Note that data in Fig. 4.5 is presented with a seasonal CO_2 cap mask applied as any variation in MCS surface temperatures over CO_2 ice is most likely spurious, as this surface ice should have a constant surface temperature. Streeter et al. (2020) provide further justification for this mask in Supplemetary Text S5, which addresses some of the issues with retrieving surface temperatures over the seasonal ice caps.

Dayside cooling showed greater disagreement, with globally averaged cooling of 15.2 K and 11 K in the retrievals and reanalysis respectively, as well as some disagreement in spatial distribution (Fig. 4.5.c,d). Close agreement was found between the retrievals and the reanalysis, reflected in a high magnitude of cooling over Chryse and Hellas, but the retrievals also showed high (30+ K) cooling over the southern highlands and Amazonis/Elysium Planitia not seen in the reanalysis. There are a number of possible explanations. Error in CDOD is possible, especially given the high values involved (Montabone et al., 2015). However the

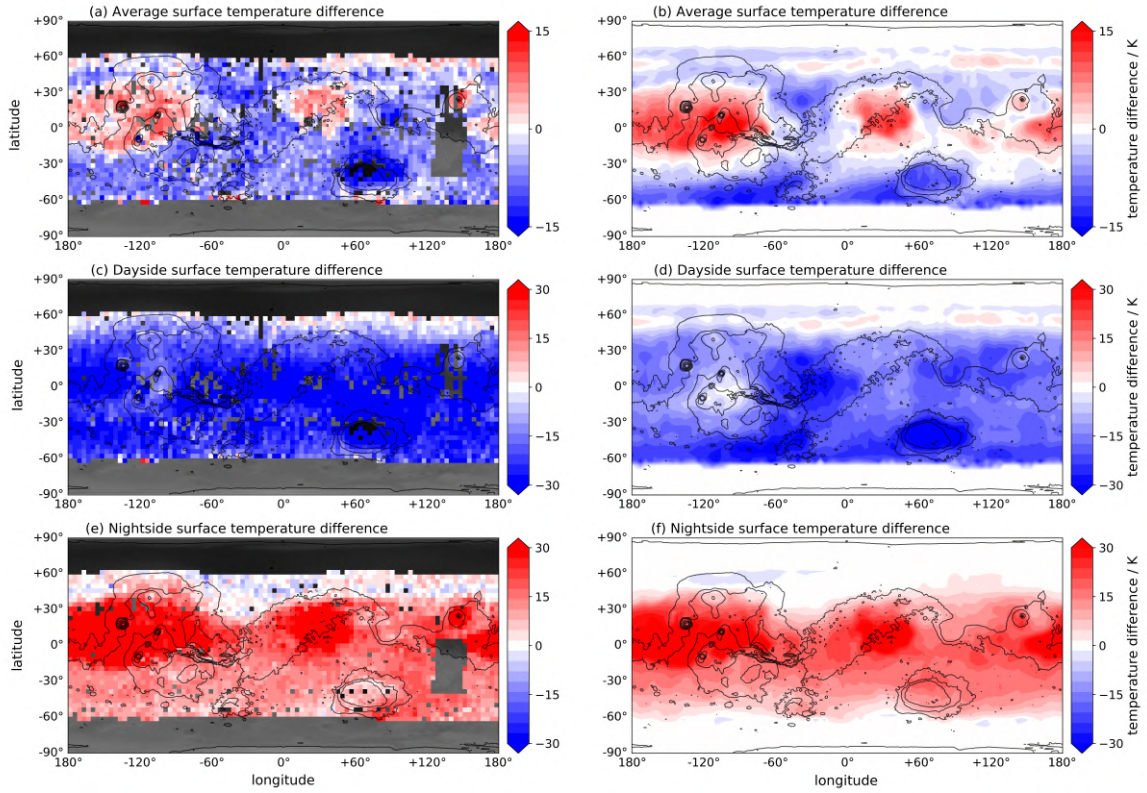

Fig. 4.5 Difference in surface temperatures averaged over L_S=200-220° between MY 34 and MY 30 in (left) MCS surface temperature retrievals and (right) the reanalysis for (top) the diurnal average as calculated from dayside (15:00) and nightside (03:00) only; (middle) the dayside (15:00); (bottom) the nightside (03:00). Adapted from Streeter et al. (2020).

results would imply greater CDOD (as inferred from the surface temperature retrievals) for the dayside, but also smaller CDOD on the nightside; this would require a greater diurnal dust variation than seen in the reanalysis. Another explanation is ω differences; the observed difference is greater than caused by the uncertainty in the MGCM ω values calculated by Wolff et al. (2009) (Fig. 4.6), but a 5% differerence in ω would be sufficient to cause dayside surface temperature differences of >10 K under GDS-scale dust loading (Fig. 4.7). To cause additional cooling specifically, ω would have to be in the "dark" part of the observed ω dichotomy on Mars, contradicting values derived from the 2007 GDS (Wolff et al., 2009). Additionally, the pattern of extra cooling from lower ω follows locations of greatest CDOD (Fig. 4.7), and thus does not replicate the cooling pattern in the retrievals; invoking ω would therefore require heterogeneity of ω in the global dust population. Another possibility is that the MGCM's particle size scheme (described in Chapter 3) under/overestimates particle sizes in particular areas, as with greater lifting occurring during a GDS the particle size structure could be far more heterogeneous than usual (Kahre et al., 2008); indeed, MSL measured unprecedented lofted dust particle sizes of up to 4 μm during the MY 34 GDS (Lemmon et al., 2019).

Surface albedo changes induced by the GDS could also play a role: large-scale albedo brightening from dust deposition would cause surface cooling by increasing shortwave reflectivity (e.g. Fonseca et al., 2018), and if surface deposition was thin enough this would not necessarily alter thermal inertia significantly, explaining the good reanalysis-retrieval agreement in nightside surface temperatures. Finally, there is the question of more systematic and not necessarily GDS-induced disagreement. While the reanalysis and retrieval nightside surface temperatures show very good agreement, there is a systematic dayside bias even in MY 30, a very clear year, of 12 K (Fig. 4.8.c,d), going up to 18 K for MY 34 (Fig. 4.9.c,d). This suggests that the dayside surface temperature disagreement is a broader issue not necessarily solely linked to the GDS. Further work is needed to investigate this bias;

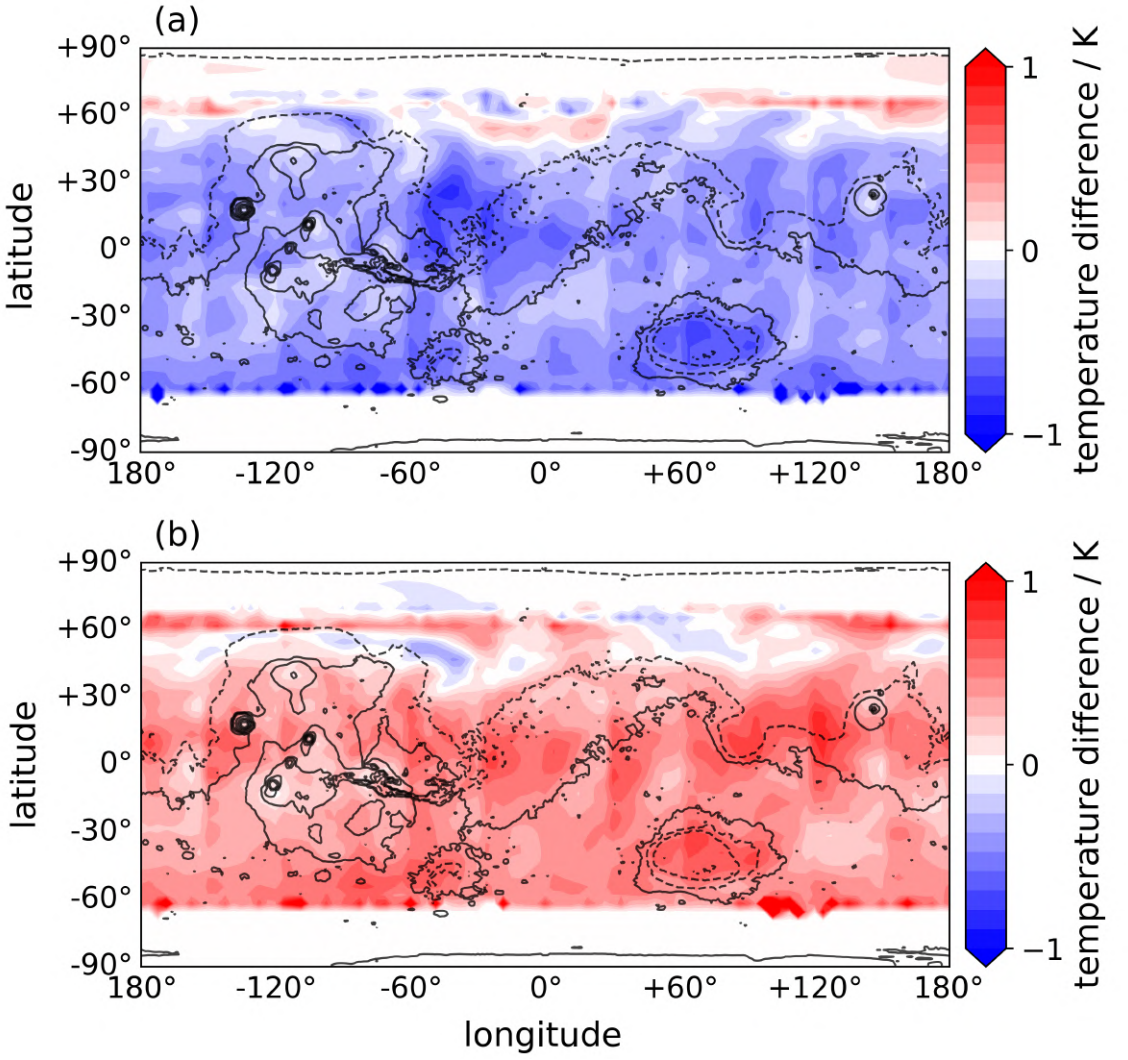

Fig. 4.6 Difference between dayside (15:00) surface temperatures averaged over L_S=200-220° in MY 34 of the reanalysis between (top) a run with $\omega = 0.937$ (ie. 0.94 - 0.3%) and a run with $\omega = 0.94$ and (bottom) a run with $\omega = 0.943$ (ie. 0.94 + 0.3%) and a run with $\omega = 0.94$. Adapted from Streeter et al. (2020).

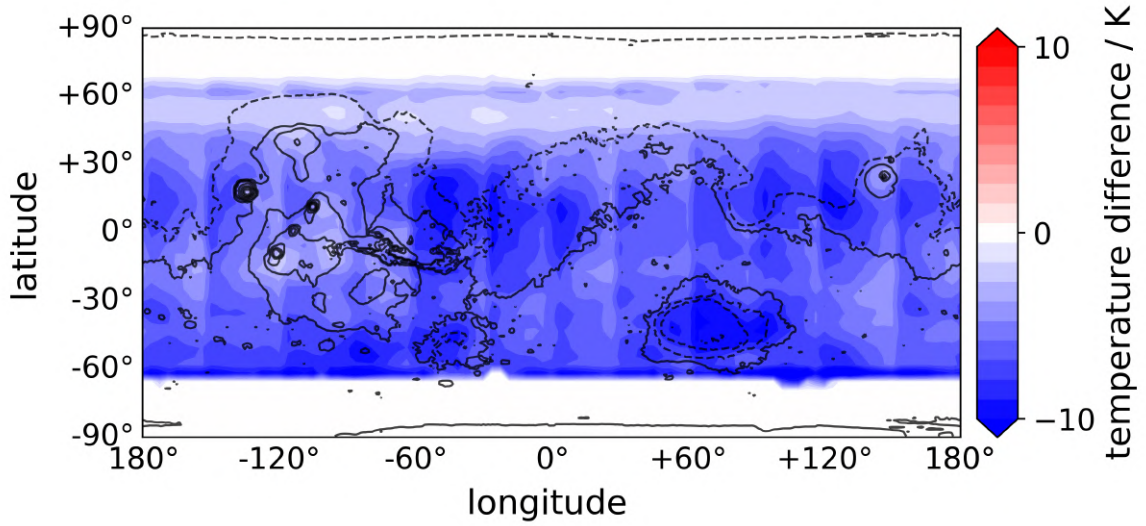

Fig. 4.7 Difference between dayside (15:00) surface temperatures averaged over L_S=200-220° in MY 34 of the reanalysis between a run with ω = 0.94 and a run with ω = 0.89 (ie. 0.94 - 5%). Adapted from Streeter et al. (2020).

this may result from MCS limb pointing being affected by topography and affecting surface retrievals.

Overall, the net surface temperature change showed good morphological agreement with the reanalysis: average warming was seen over low thermal inertia regions, average cooling elsewhere. One result of the greater cooling in the retrievals is that the net surface temperature change map shows fewer white regions representing little or no surface temperature change; boundaries between areas of net warming/cooling are sharper, showing the important effect of surface thermal inertia on the surface temperature response.

TES surface temperature retrievals from the MY 25 (2001) GDS are another source for comparison, particularly given the observed similarities between the MY 25 and MY 34 GDS (Kass et al., 2019). Globally-averaged surface temperature retrievals for the MY 25 GDS at L_S=210° showed a peak dayside cooling of 23 K and a peak nightside warming of 18 K, corresponding to a net decrease of 2.5 K (Smith, 2004). Analysis of the MY 25 reanalysis showed (this can be seen in Fig. 4.3), for the same time period, a dayside cooling of 21 K and a nightside warming of 16 K, also corresponding to a net decrease of 2.5 K (note

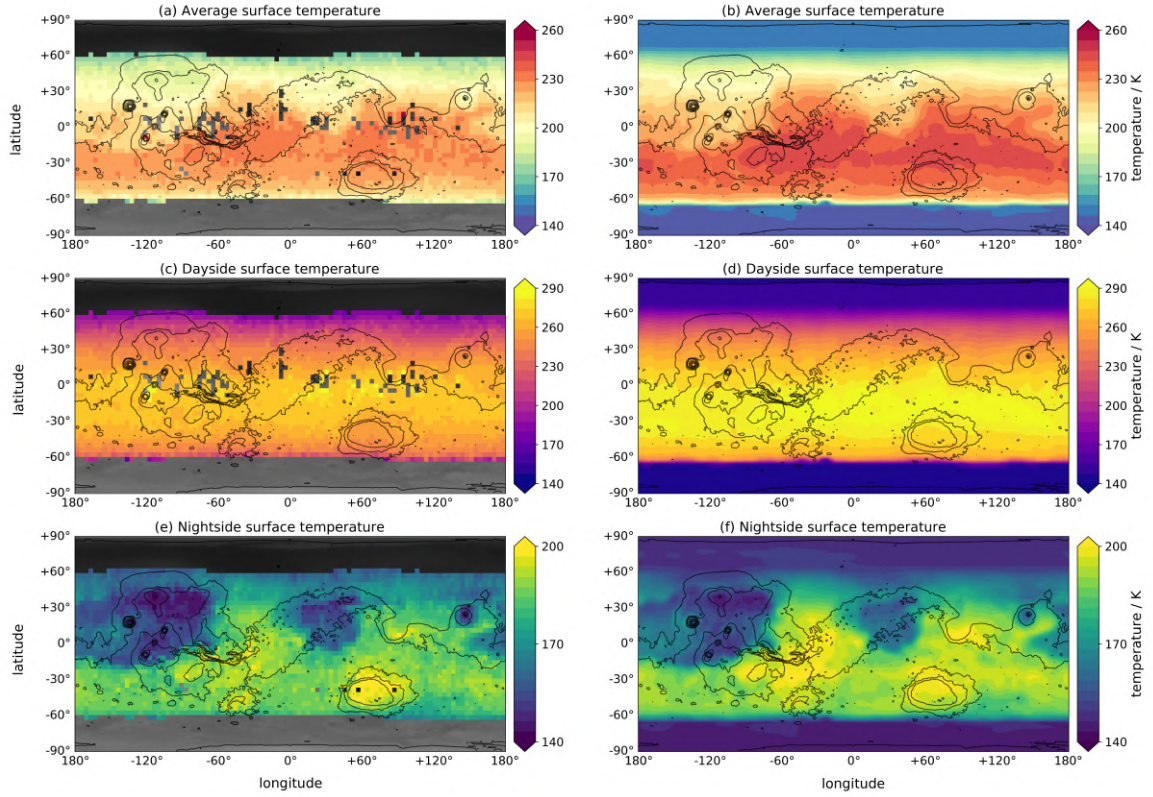

Fig. 4.8 Surface temperatures averaged over L_S=200-220° in MY 30 for (left) MCS surface temperature retrievals and (right) the reanalysis for (top) the diurnal average as calculated from dayside (15:00) and nightside (03:00) only; (middle) the dayside (15:00), and (bottom) the nightside (03:00). Adapted from Streeter et al. (2020).

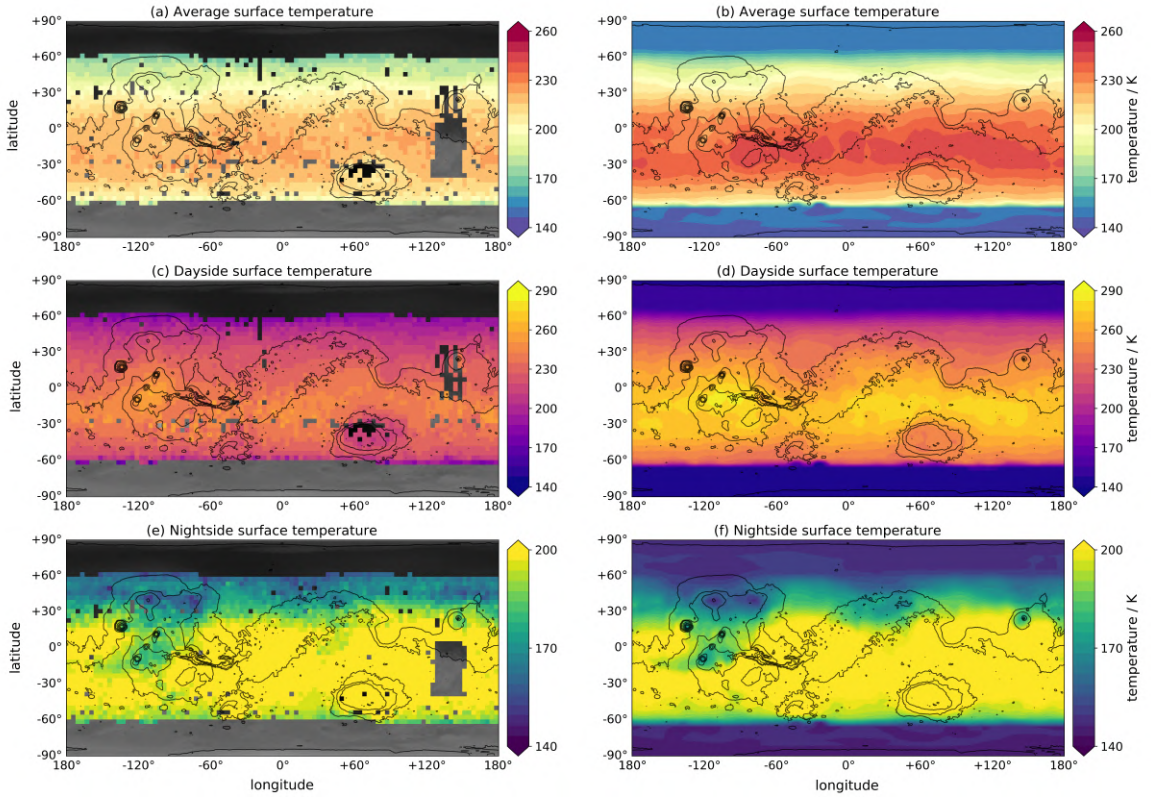

Fig. 4.9 Surface temperatures averaged over L_S=200-220° in MY 34 for (left) MCS surface temperature retrievals and (right) the reanalysis for (top) the diurnal average as calculated from dayside (15:00) and nightside (03:00) only; (middle) the dayside (15:00), and (bottom) the nightside (03:00). Adapted from Streeter et al. (2020).

that while nightside surface temperatures from the MY 25 reanalysis agree well with TES retrievals, there is a systematic ∼10 K disagreement with dayside surface temperatures; while the absolute temperature values disagree, the relative coolings due to the GDS agree well). Averaged over all local times, the reanalysis showed an average surface temperature change of 0 K.

Radio telescope observations of the 2001 GDS found a globally-averaged daytime surface brightness temperature decrease of ∼20 K (Gurwell et al., 2005); consistent with the surface temperature cooling in this study (Fig. 4.3.a) and TES observations (Smith, 2004). Hanel et al. (1972) used IR spectroscopy from the Mariner 9 orbiter to examine surface temperatures during and after the 1971-72 GDS; the results support broad dayside cooling and nightside warming, but it is difficult to draw any strong or quantitative conclusions given the limited coverage.

The MSL dataset offers a chance for comparison with in-situ surface temperature measurements of the MY 34 GDS. Guzewich et al. (2019) showed, over L_S=195-205°, a maximum/minimum surface temperature decrease/increase of 22.8 K/15.1 K, corresponding to a net 3.8 K decrease. The MGCM at the resolution used in this study cannot explicitly resolve Gale Crater, so an analogue location at the same latitude (-37.5° E, 5.625° S) was chosen, based on similarity in latitude (and hence solar insolation), topographic elevation (and hence surface pressure), and CDOD. The thermal inertia at this location was 294 J m^{-2} K^{-1} s$^{-1/2}$, compared to the highest published Gale value of 452 J m^{-2} K^{-1} s$^{-1/2}$, and the average CDOD was 5.3, compared to the MSL-measured 5.5. The maximum and minimum surface temperature decrease and increase in the reanalysis was 23.4 K and 20 K respectively, corresponding to a net 1.7 K decrease. Dayside cooling agreed well with the reanalysis, but the MGCM appeared to overestimate nightside warming. This is likely due to a lower model thermal inertia than that at MSL, which at the time was the high thermal inertia Vera Rubin Ridge (Edwards et al., 2018), and any local topographic effects not resolved by the MGCM. Dayside

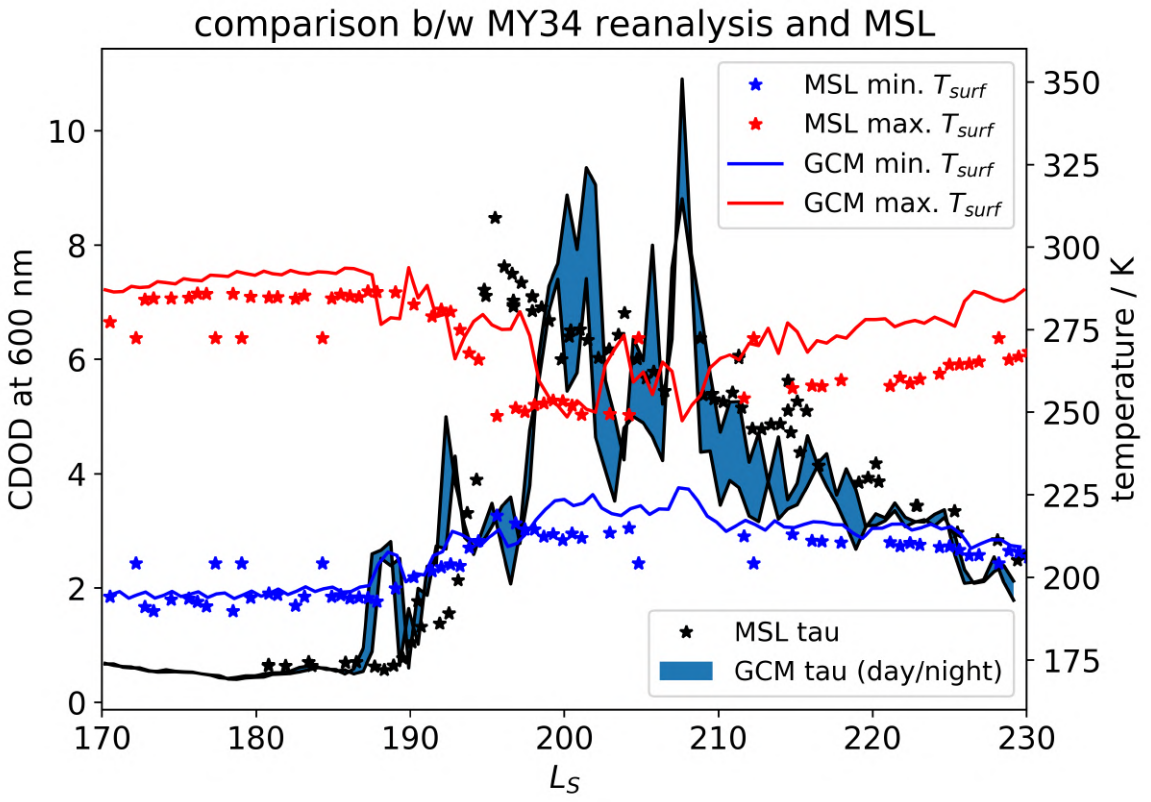

Fig. 4.10 Surface temperatures and CDOD in MY 34 for MSL surface temperature measurements and the reanalysis at -37.5° E, 5.625° S. From Streeter et al. (2020).

surface temperatures also started diverging after $L_S \sim 210°$ (Fig. 4.10), most likely due to albedo increases from dust deposition causing surface cooling (Fonseca et al., 2018); the MGCM uses a static albedo map (except for variations due to CO_2 ice coverage), and is therefore not able to incorporate albedo changes from dust redistribution. It should finally be noted that the MGCM's ∼250 km footprint makes meaningful comparison with a point source like MSL difficult; a mesoscale model could offer a better comparison.

Another *in situ* source is Viking Lander 1 (VL1), which recorded meteorological data from two major storms (Ryan and Henry, 1979); in both cases, max/min air temperatures at ∼1.3 m altitude rapidly decreased/increased by ∼16 K/∼12 K, decreasing on average. Qualitatively, given VL1's relatively high thermal inertia location, this matches expectations;

however, without better knowledge of the CDOD of the 1978-79 GDS a more rigorous comparison is not possible.

4.4 Discussion and Conclusions

The MY 34/2018 GDS decreased dayside and increased nightside surface temperatures, resulting in a reduced diurnal variability in surface temperatures. Surprisingly, the diurnally-averaged result was a robust and significant net warming over much of the planet. This warming correlated extremely closely with low thermal inertia regions, which in clear conditions experience rapid nightside cooling; these regions warmed even as diurnally-averaged total surface flux decreased, due to significant nightside warming from longwave backscattering, which caused nightside surface temperature increases sufficient to outweigh the dayside cooling. Over regions of higher thermal inertia, diurnally-averaged surface temperatures decreased or remained roughly constant.

The high dust loading of the MY 34 GDS reduced daytime solar radiative flux onto the surface and increased backscattering of infrared radiation back onto the surface, minimising the importance of surface thermal inertia in controlling surface temperatures and reducing the amplitude of the diurnal temperature cycle. Under normal, non-GDS conditions the strong effect of CDOD on blocking incident solar radiation makes CDOD the dominant factor in controlling dayside surface temperatures (aside from direct solar insolation due to latitude and season), when solar radiative flux is high. At non-GDS night by contrast, the dominant factor becomes the surface thermal inertia, which controls the cooling rate of the surface. Diurnally averaged surface temperature changes from the GDS therefore showed the greatest correlation with surface thermal inertia: regions of low thermal inertia underwent average warming and vice-versa, reducing the usual heterogeneity in nightside surface temperatures caused by the heterogeneity in thermal inertia. By contrast, CDOD over a region showed low correlation with the sign of the surface temperature change, showing the importance of

GDS spatial structure in CDOD (this CDOD structure being visible in Figs. 4.2.a,e). These correlation coefficients can be seen in Fig. 4.11.

Near-surface air temperatures also showed substantial alteration, driven by the surface temperature changes and the reduced surface-air temperature gradient. Even in the clear-case, heat transport in Mars' atmosphere is dominated by radiation (Barnes et al., 2017; Wolff et al., 2017). Increased dust loading strongly coupled air temperatures to surface temperatures by dramatically increasing radiative absorption (both shortwave and longwave, including of surface emission) in the bottom layers of the atmosphere while reducing shortwave radiative flux at the surface. This resulted in increased air temperatures at night and even on the dayside for regions where GDS-case surface temperatures surpassed clear near-surface air temperatures, ie. where the clear-case surface-air temperature contrast is greatest under non-GDS conditions.

Interestingly, the MY 34 reanalysis showed less surface warming than the free-running simulation with the same globally-averaged CDOD (Fig. 4.3.a); however, MY 34 surface cooling matched the free runs very well. This can be explained in terms of GDS geographical structure. The MY 34 GDS was not spatially homogenous; the highest CDOD was over high thermal inertia regions (Fig. 4.2.a,b), where the nightside warming effect is least. The MY 25 reanalysis, on the other hand, agreed well with the free runs on nightside warming but had stronger dayside cooling. Again, the explanation is geographical: the MY 25 GDS, as represented in the reanalysis (Fig. 4.2.d,e), had a greater latitudinal extent than the MY 34 GDS, with CDOD > 1 between 77° S to 66° N versus 69° S to 47° N. This extra area generally had a high thermal inertia, and therefore contributed a net cooling effect to the global average. Note that TES had latitudinal limitations in valid CDOD retrievals, due to low surface temperatures and surface-air temperature contrasts in the polar regions affecting the instrument signal-to-noise ratio and retrieval quality (see Montabone et al., 2015), and so the MY 25 reanalysis used is constructed from spatially-kriged observations (described in

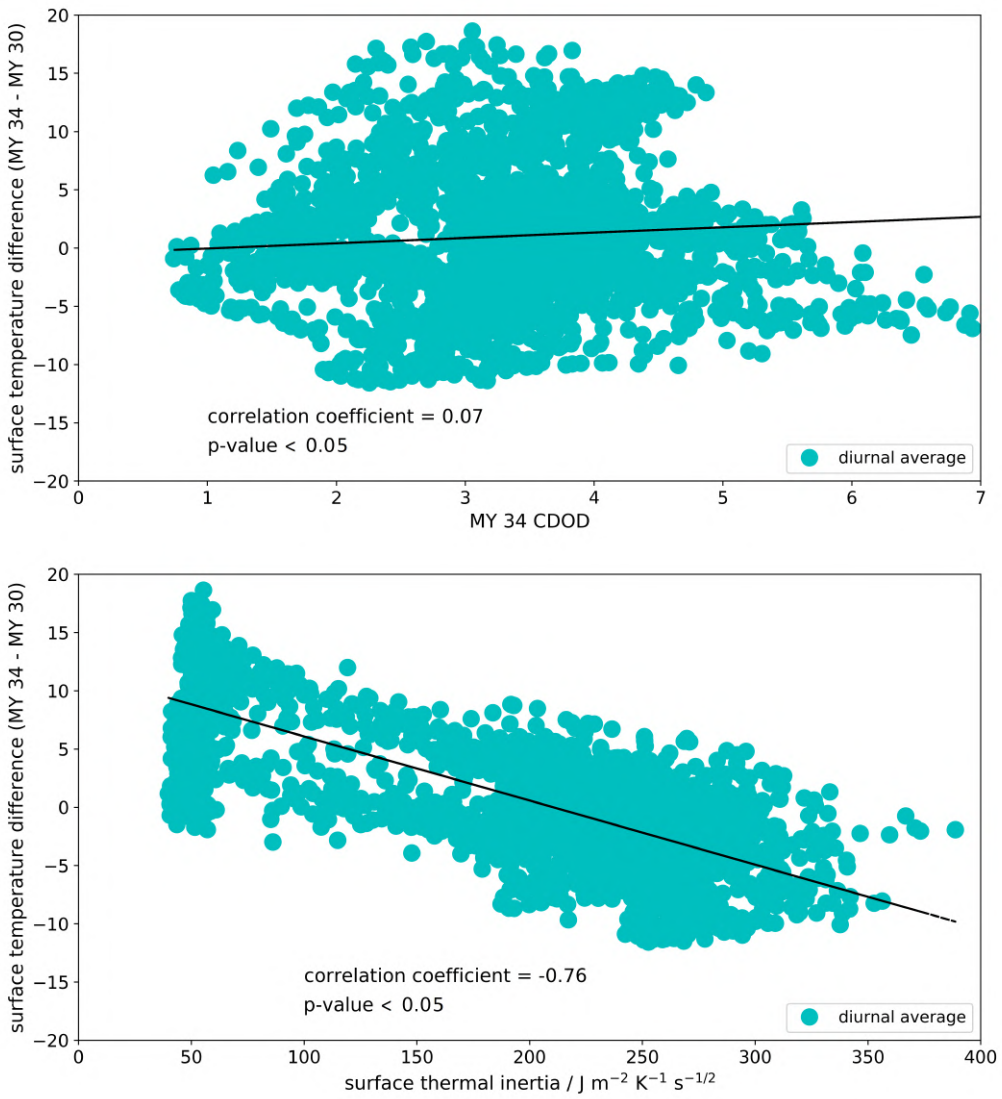

Fig. 4.11 (Top) CDOD values in MY 34 and surface temperature difference (MY 34 - MY 30) values, with Pearson correlation coefficient displayed. (Bottom) surface thermal inertia values and surface temperature difference (MY 34 - MY 30) values, with Pearson correlation coefficient displayed. For both plots, all values are from the reanalysis, from the latitude range 60° S to 40° N.

Montabone et al., 2015); different GDS decay rates could also potentially affect comparisons. The general conclusion holds, however, that GDS spatial structure is important for its overall radiative effects: specifically, the magnitude of dust loading over low vs high thermal inertia areas determines the net surface temperature and air temperature impacts. The MY 34 GDS also showed noticeable diurnal variation in CDOD (Fig. 4.3), which comes directly from the variation seen in MCS CDOD products (Kleinböhl et al., 2020); this resulted in slightly higher dayside cooling/lower dayside warming than in the diurnally uniform CDOD case. The extent to which this is intrinsic variability and not an artefact of MCS dust profile truncation is currently unclear (Montabone et al., 2020).

One general caveat is that the MGCM uses an almost static thermal inertia map, with seasonal variations coming solely from changes in surface coverage of CO_2 ice; surface thermal inertia has been shown to vary seasonally by up to $200\,\mathrm{J\,m^{-2}\,K^{-1}\,s^{-1/2}}$, and to show day-night variability (Putzig and Mellon, 2007). GDS have also been shown to cause lasting alteration of albedo and surface thermal inertia via dust redistribution over the planet (Fenton et al., 2007; Szwast et al., 2006). That said, seasonal thermal inertia variations are very small over low thermal inertia regions, suggesting that net warming over these areas is indeed a robust phenomenon. Nightside surface temperatures in the MY 34 reanalysis also agreed very well with MCS surface temperature retrievals, suggesting good representation of thermal inertia in the MGCM. As noted above though, surface albedo changes may affect representation of dayside surface temperatures. More generally, there appear to be systematic biases between retrieved surface temperatures from both MCS and TES, even in non-GDS conditions.

Finally, the nightside warming was more persistent in time than the dayside cooling, which mostly affected peak dayside temperatures. This makes sense from a physical perspective; dayside cooling was highly dependent on local time due to the dependence of incident surface solar radiative flux on local time, while nightside warming (relative to MY 30) was more

uniform due to its dependence on diurnally-constant surface thermal inertia. The result was that the warming had an outsized impact on diurnally-averaged temperature changes, with more warming in a true diurnal average than in net changes calculated from just two local times. Future retrievals from the instruments aboard the ExoMars Trace Gas Orbiter, which measures over varying local times, should provide a better understanding of this diurnal cycle. Simulations with varying CDOD suggest that a global surface cooling for a GDS with the same latitudinal extent as the MY 34 event would require a storm opacity of greater than 11; the actual threshold, however, would depend significantly on the storm's geographical structure. The vertical distribution of dust, via mediation of atmospheric radiation, may also have an impact.

Chapter 5

Dust lifting, deposition, and net transport

5.1 Introduction

As discussed in Chapter 2, understanding Mars' dust cycle has long been a major topic of research. Martian dust activity occurs at a multitude of scales, from the very local such as dust devils, to the global - the phenomenon of the Global Dust Storm. Given its prevalence and the planet's aridity and thin atmosphere, atmospheric dust is the most important substance influencing the meteorology and climate in the present era. This importance has been reflected in the scientific literature; from the early telescopic observations of transient "yellow clouds" - now known to be dust storms - to the multiple modelling, orbital, and ground-based studies of the most recent GDS in 2018.

This chapter aims to provide a characterisation and better understanding of the martian dust cycle with the aid of the MGCM, via the assimilation of six martian years' worth of temperature and dust retrievals from the Mars Climate Sounder. There have been numerous efforts to model the dust cycle, which have led to greater understanding of its seasonality and the roles played by different dust-lofting mechanisms. Likewise, there have been many

observational studies of martian dust events: their locations, seasonal distribution, and lifecycles.

The work presented in this chapter contributes a novel addition to the field in a number of ways. This is the first study that uses data assimilation, and its subsequently altered representation of atmospheric dynamics, to calculate lifted dust mass flux. Published lifting modelling studies to date have used free-running models (e.g. Basu et al., 2004, 2006; Chapman, 2018; Kahre et al., 2008, 2015, 2006, 2005, 2013; Mulholland, 2012; Mulholland et al., 2013, 2015; Newman et al., 2002a,b), which may not fully represent dynamical features important for dust lifting, such as sublimation flow, baroclinic wave activity, and low-level jets. Montabone et al. (2005) assimilated temperature and dust data from TES to calculate wind stress near the surface; this is a necessary initial part of the dust lifting calculation process but not sufficient to characterise lifting locations. The work in this chapter assimilates temperature and dust observations, both of which have significant impacts on modelled dynamics, to directly calculate lifting.

Secondly, thanks to the availability of multiple years of MCS observations, the work presented here shows calculations of dust lifting for six consecutive martian years (MYs 29-34), including one (MY 34) with a GDS. This affords an opportunity to examine how variable dust lifting is on a multi-annual basis, both for "normal" years and for the special case of a GDS.

Finally, the work described in this chapter also incorporates analysis of dust deposition onto the surface to investigate the sources and sinks of dust on Mars. This work provides a novel approach by incorporating deposition based on assimilated MCS-derived column dust optical depth (CDOD). This allows for comparison of lifting, as calculated from the model dynamics, with observationally-based deposition, thus combining modelling and retrievals to try to obtain the most comprehensive understanding of net surface dust transport.

There are some caveats which must be mentioned. While the MGCM has a dust devil lifting parameterisation, this is not used in the work presented here - the focus is on lifting by near-surface wind stress (NSWS). Dust devil lifting is an important contributor to the dust cycle, particularly during the aphelion season (see below) when it helps to maintain the constant background haze (Fenton et al., 2016); it is not though responsible for dust storms (e.g. Basu et al., 2004; Kahre et al., 2006, 2005; Newman et al., 2002a,b). For the sake of simplicity this work focusses on NSWS lifting and dust storms; the assimilated CDOD field implicitly includes dust devil lifting. Secondly, the lifting calculations performed are offline (see Methods below for more detail). This means that the modelled dust cycle is not inherently conservative of dust mass. For the purposes of comparing lifting and deposition, this is addressed in Section 5.3.3.

Finally, modelled dust lifting in MGCMs is a parameterised process which is dependent on the resolution at which the MGCM is run, both spatially and vertically (Chapman, 2018). Higher spatial resolution, in particular, results in greater calculated lifting due to better representation of topography and therefore slope winds (Chapman, 2018). Modelled atmospheric dynamics have also been shown to display some resolution dependence (Toigo et al., 2012). Ideally, all runs would be at the resolution of the dust lifting processes themselves, which are on the order of centimetres to metres, which is not possible with current Mars global climate models. The highest resolution the MGCM can be run at is a spectral resolution of T127; time and disk space considerations make this impractical, especially given the multi-annual nature of the work in this chapter. To reflect this, the phrase "large-scale" is often used throughout this chapter in relation to dust lifting and atmospheric dynamics. This is intended to reflect the fact that the MGCM grid boxes have sizes on the order of 100 km, and thus are unable to capture smaller-scale lifting, which may be significant for dust storms: events that can rapidly grow to MGCM scale from potentially subgrid origins. The work presented here does not purport to characterise every scale of the

martian dust cycle, but rather to provide a comprehensive overview of the most important lifting and deposition processes occurring at the global scale.

For the purposes of the work in this chapter, the aphelion season/clear season (from here on, the aphelion season) is defined as L_S=0-180°. This is the period in which Mars, due to its orbital eccentricity, is furthest from the Sun, receiving up to 44% less solar energy than during the perihelion season (Richardson and Wilson, 2002). Average atmospheric CDOD during this period is lower than during the perihelion season. Dust lifting by NSWS lifting is at a minimum during this period, and the dust budget has been modelled to be dominated by dust devil lifting (e.g. Newman et al., 2002a,b). This being the "clear" season does not necessarily preclude large dust events and storms; MY 35 experienced a large northern hemisphere dust event (see Fig. 5.15), and dust storms are frequent at the seasonal cap edges (e.g. Wang and Fisher, 2009), and have been detected as crossing the equator from north to south (e.g. Haberle et al., 2018; Wang and Richardson, 2015; Wang et al., 2003). In an average sense, however, the aphelion season is less "dusty" with fewer storms and lower CDOD.

This chapter is structured as follows. First, it discusses NSWS dust lifting as calculated offline from assimilated MGCM dynamics. Spatial lifting maps are presented for each 30° L_S period of each of the six martian years. Zonally-averaged lifting climatologies for each year are then shown, including an "average" year composed of the mean of the non-GDS years and a climatology of variation from the mean. The mechanisms behind the presented lifting are then discussed, in particular near-surface wind speeds which are also presented as both spatial maps and climatologies. For the purposes of this chapter, all fields described as "near-surface" are fields in the bottom layer of the MGCM, which has an altitude above the surface of $\sim$5 m. Wind speeds are further decomposed to investigate the roles of meridional and zonal winds; eddies; and tidal effects. The link between tropical dust loading and seasonal cap edge lifting is examined in closer detail. Dust deposition is then characterised using a model

variable, based on assimilated CDOD. Spatial and zonally averaged maps are presented and interannual similarity/variability is examined.

Next, lifting and deposition are combined using the assumption of annual dust cycle closure to investigate sources and sinks of dust. Once more, spatial and zonally averaged maps are presented and interannual similarity/variability is examined. Finally, the special case of the MY 34 GDS is investigated - lifting, deposition, and net sources and sinks. This is compared to the case of MY 30, a relatively quiet martian year in terms of dust activity. The results are summarised and discussed with comparisons to the existing literature.

5.2 Methods

For this chapter, the multi-annual reanalysis described at the end of Chapter 3 is used. Variables from this reanalysis were used to calculated lifted dust flux, as described below, while deposition was directly calculated in the MGCM.

5.2.1 Lifting

Lifting parameterisation

The results presented in this chapter arise from offline calculations of near-surface wind stress dust lifting fluxes, parameterised for each MGCM gridbox. In this context, "offline" signifies that the calculations are not performed as part of the MGCM's physical or dynamical calculations ("online"), but rather are done separately from the MGCM using its output fields after the simulation has finished. This means that the calculated dust lifting fluxes are purely diagnostic and do not affect model fields such as atmospheric dust opacity. Atmospheric CDOD is determined by the assimilation of MCS CDOD retrievals, coupled to the MGCM's dust transport parametrizations. Other studies (e.g. Basu et al., 2004, 2006; Chapman, 2018; Kahre et al., 2008, 2015, 2006, 2005, 2013; Mulholland, 2012; Mulholland et al., 2013,

2015; Newman et al., 2002a,b) have used online model dust lifting, using the same equations but where the lifted dust becomes suspended in the atmosphere and affects the atmospheric CDOD, with the aim of replicating a self-consistent martian dust cycle that is stable over periods of several martian years. The aim of the work in this chapter is not to attempt to reproduce a self-consistent dust cycle, but to use assimilation of MCS dust and temperature data to create the best estimate of the state of Mars' atmosphere. This should include the best estimate of large-scale wind speeds and atmospheric densities, both of which are directly invoked in the equation used to calculate dust lifting flux. In addition, this work uses an MGCM with an observationally-derived surface roughness map, rather than a fixed surface roughness value as used in previous dust lifting mass flux calculation studies (Basu et al., 2004, 2006; Chapman, 2018; Kahre et al., 2008, 2015, 2006, 2005, 2013; Mulholland, 2012; Mulholland et al., 2013, 2015; Newman et al., 2002a,b), which should better reflect actual lifting on Mars. Surface roughness is discussed later, in Section 5.2.1. The ensuing explanation of dust lifting theory follows Chapman (2018).

Lifting occurs when the friction velocity of the wind in the bottom ("near-surface") layer of the MGCM exceeds the threshold friction velocity, u_t^*. The friction velocity is defined as

$$u^* = \frac{\kappa U}{ln(1 + z/z_0)} \tag{5.1}$$

where U is the near-surface wind speed (the magnitude of the combined near-surface meridional and zonal wind components), κ is the von Kármán constant ($= 0.4$), z is the height (in metres) of the near-surface layer above the surface, and z_0 is the surface roughness length (in metres).

The threshold friction velocity is defined in terms of two variables: the fluid threshold, and the ratio of the impact threshold to the fluid threshold. The fluid threshold describes the minimum wind stress at which particles can be lifted from the surface directly by wind shear

alone. The fluid threshold velocity is defined, following Mulholland (2012)'s implementation of theory in Shao and Lu (2000), as

$$u_{ft} = \sqrt{\frac{0.0246(\gamma\rho_p g)^{0.5}}{\rho}} \tag{5.2}$$

where $\gamma = 3 \times 10^{-4} kg\,s^{-2}$, $\rho_p = 2500\,kg\,m^{-3}$ is the density of the dust particles, $g = 3.72\,m\,s^{-2}$ is the gravitational acceleration on Mars, and ρ is the near-surface atmospheric density. However, using the fluid threshold alone to calculate dust lifting would underestimate lifting by ignoring the importance of saltation: the process by which large particles carried above the surface, while they may not be suspended in the atmosphere, can on impact with the surface cause the lifting of smaller particles which then may be suspended. This mechanism lowers the effective wind stress at which dust lifting may occur. The threshold lifting velocity is subsequently defined as

$$u_t^* = Q_t u_{ft} \tag{5.3}$$

where $Q_t = 0.3$, Q_t being the ratio of the impact threshold to the fluid threshold; that is, the ratio between the threshold wind speed required to lift particles when saltation is and is not occuring, respectively. As saltation makes dust lifting more efficient, causing greater lifted mass for a given wind speed, the former will always be lower than the latter. The Q_t value for Mars is currently very poorly characterised, due to the inability to perform direct measurements on the surface. Estimates include $\sim$0.3 (Claudin and Andreotti, 2006), $\sim$0.48 (Almeida et al., 2008), and $\sim$0.1; all significantly lower than terrestrial values of $\sim$0.8 (Bagnold and Taylor, 1937) to $\sim$0.96 (Almeida et al., 2008), due to Mars' lower gravity and sparser atmosphere allowing saltating particles to achieve higher impact velocities. Attempting to characterise or validate a Q_t value is important but well beyond the scope of this thesis; as a compromise between the literature values, Q_t=0.3 was used for this work.

The amount of lifted dust - the dust flux into the atmosphere - is defined as

$$F_{dust} = \alpha_N F_H \tag{5.4}$$

where $\alpha_N = 1 \times 10^{-5}$ (as used in this chapter following Chapman (2018)) represents the efficiency of dust mass lifting, and F_H is the horizontal dust flux as derived by Mulholland (2012), defined as

$$F_H = 0.25\frac{\rho}{g}(u^*)^3((1-(\frac{u_t^*}{u^*})^2)(7+50(\frac{u_t^*}{u^*})^2)) \tag{5.5}$$

Equation 5.5 is an empirical equation, an approximate fit to numerical modelling results of the mass flux induced by saltation performed by Kok and Renno (2008), building on earlier experimental work showing that mass flux increases roughly cubically with u^* (e.g. Shao, 2008). F_H, the horizontal dust flux, describes the degree of dust mass flux in the entire horizontal plane induced by saltation; of that flux, only a certain proportion will actually be lifted into the atmosphere, hence the presence of the tuneable parameter α_N.

Impact of model resolution

The model simulations are, as described, run at a resolution of T42xL50. Previous work shows that both spatial and vertical resolution can have an effect on modelled dust lifting flux; for both, increasing resolution results in increased lifting amounts, while for the horizontal it also results in additional lifting areas being activated (Chapman, 2018). For a detailed analysis of the impact of model resolution on dust lifting in the MGCM, see Chapman (2018).

Impact of impact to fluid threshold ratio

As stated previously, a value for the ratio Q_t=0.3 was used for this work, based on estimated values in the literature for the martian environment. Some previous work using this MGCM for online dust lifting has employed notably higher Q_t values of 0.7, which was found to be

sufficiently low to provide a "reasonable" representation of dust storm activity while being high enough to prevent model crashes from dust overloading (Chapman, 2018; Mulholland, 2012). As this is an offline study, model stability and the need to maintain a self-consistent dust cycle are not necessary considerations. Therefore, literature values are used rather than previous modelling-specific values. In addition, recent experimental work suggests that Mars' low (relative to Earth) gravity means that saltation may begin occurring at $\sim$20% lower fluid thresholds than on Earth (Musiolik et al., 2018). These results provide further justification for the low Q_t value used here, which generally speaking causes "easier" lifting than previous modelling work.

Some brief sensitivity experiments were performed with different values of Q_t (not shown here). The experiments showed that while varying Q_t had a major impact on the absolute values of lifted dust mass flux, there was consistency in the locations and spatiotemporal pattern of calculated dust lifting. Given that this chapter focusses on the seasonal, spatial, and interannual patterns of dust lifting rather than the absolute values of lifted dust flux, a single value of Q_t was chosen for all the following results to maintain consistency.

Using a realistic surface roughness map

The roughness length of a surface describes the distance above the surface at which the wind speed theoretically goes to zero. A higher surface roughness value therefore means a more rapid drop-off in wind speed, making it more difficult to lift dust; and vice versa for a lower roughness value. Given the barrenness of the martian surface, the surface roughness on Mars is controlled by the size, distribution, and abundance of surface rocks (Hébrard et al., 2012), meaning that areas observed from orbit to have finer dust on the surface (such as the Tharsis Plateau) have corresponding lower roughness values and vice-versa. As mentioned above, previous studies of dust lifting on Mars have often used a uniform global value of 0.01 m for

the roughness length of the martian surface (Chapman, 2018; Kahre et al., 2005; Mulholland et al., 2013; Newman et al., 2002b).

The work in this chapter uses a roughness map employed in the MGCM based on rock abundance data measured from orbit by the TES instrument (Hébrard et al., 2012), shown in Fig. 5.1. This provides far more variability than expressed in the uniform map, with values ranging from 0 to 0.02 m. The area-weighted average surface roughness length in the observationally derived map is 0.003 m, significantly lower than the 0.01 m of the uniform map. This lower average surface roughness may help explain why the lower Q_t value used in this work gives comparable results to previous studies using higher Q_t but uniform surface roughness maps, as described previously.

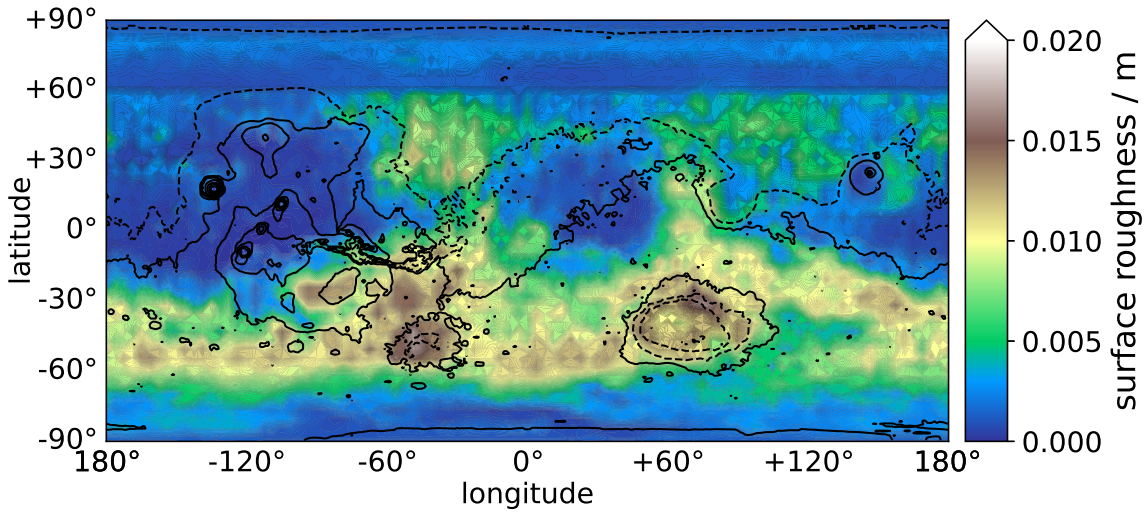

Fig. 5.1 Observationally-derived surface roughness maps as used in the MGCM.

5.3 Results

5.3.1 Lifting

Mean spatial lifting maps

This section shows dust lifting flux results for the mean of MY 29-33, dispayed in increments of 30° L_S in Fig. 5.2. A mean of these martian years was used to avoid overburdening the reader with separate dust lifting plots for each of the six martian years, for 12 periods of 30° L_S each. MY 34 was excluded from this mean due to the presence of the GDS, which had an outsize effect on lifting and deposition; the case of the MY 34 GDS is examined in detail in Section 5.4. Dust lifting is represented as average lifted mass flux per unit area per sol during the relevant period; for simplicity, this is henceforth referred to as "dust flux". Note that the scale bar is non-linear, and dust flux can vary by orders of magnitude between seasons.

The period L_S=0-30° is when Mars is beginning to transition from equinox to northern spring, with a northward shift in the subsolar latitude occuring and the planet moving further from the Sun. Lifting during this period is predominantly at northern mid-high latitudes, in particular around the seasonal cap. High lifting also occurs over northern Tharsis and parts of Amazonia. There is lifting by the southern seasonal cap, but of lower magnitude and area than in the north. L_S=30-60° represents northern spring moving into summer, as the subsolar latitude shifts further northward and the planet continues to approach aphelion. Lifting in general declines as incident solar energy is reduced, and northern seasonal cap edge lifting in particular decreases. This is due to the reduced thermal gradient at northern high latitudes, as the northern seasonal cap retreats. Correspondingly, as the southern seasonal cap grows, cap-edge lifting in the southern hemisphere intensifies: centred at Terra Sirenum, Aonia Terra, and Noachis Terra.

In the L_S=60-90° period, Mars approaches and passes aphelion (L_S=71°) and reaches northern summer solstice (L_S=90°). Incident solar energy is at its lowest in the orbital

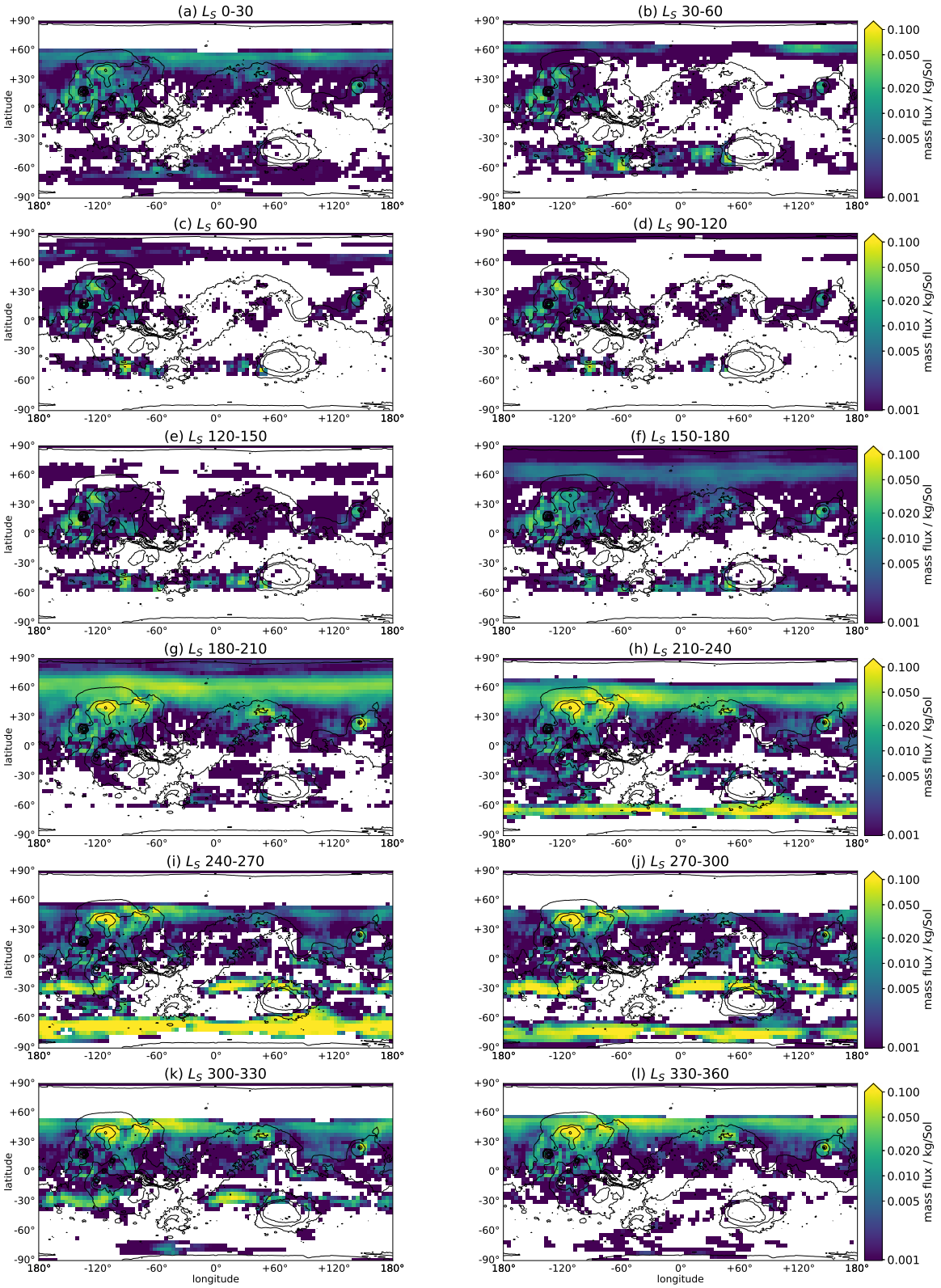

Fig. 5.2 Maps of dust mass lifting flux for the mean of MY 29-33 over 12 periods of 30° L_S. Note the non-linear scale.

cycle; correspondingly, there is a general decline in lifting everywhere from the previous period, including the tropics/mid-latitudes (Tharsis, Utopia, and Arabia/Sabaea), the southern seasonal cap, and the northern polar region. The lifting corresponding to the latter is also shifted northward as northern summer approaches its peak and the seasonal cap reaches its minimum extent. Despite the southern seasonal cap approaching its maximum extent, lifting is decreased compared to the previous period, showing the effect of the southern hemispheric solsticial pause in wave activity (Lewis et al., 2016; Mulholland et al., 2016), confirmed by observations of cap edge dust storms (Guzewich et al., 2015; Wang, 2018). At L_S=90-120°, Mars begins to move towards northern autumn. The planet's axial obliquity means that the subsolar latitude begins to drift northward again. In addition, with aphelion having passed, more solar radiation is incident on the planet, reflected in the increased lifting at tropics/mid-latitudes. The seasonal cap is at its minimum, however, and this is reflected in the sparse lifting which occurs at high northern latitudes. Southern cap edge lifting is also at a minimum due to the solsticial pause, despite the cap reaching its maximum extent in this period of ∼45-50° S.

L_S=120-150° sees a reintensification in lifting, particularly at the tropics/mid-latitudes (Tharsis/Amazonia, Arabia/Sabaea, Elysium) and at the southern seasonal cap edge. This can be explained by the greater incident solar energy as the subsolar latitude drifts equatorward and the planet moves towards equinox, in particular the enhanced lifting at the southern cap edge by the end of the solsticial pause period. This makes the L_S=120-150° period similar to L_S=30-60°. The key differences are in northern cap lifting, where L_S=30-60° shows significantly greater lifting due to the asymmetry in seasonal cap growth and decline. While both seasonal caps reach their maximum extent at the relevant winter solstice, growth starts late and occurs rapidly while decline occurs more slowly and ends later, meaning that L_S=30-60° (northern decline) has a larger seasonal cap than L_S=120-150°, despite their temporal symmetry relative to northern summer solstice. While the southern cap edge lifting

is more similar, there is slightly greater lifting in L_S=120-150° for the same reason. There is also the effect of greater insolation, as the L_S=180° equinox occurs as the planet is closer to the Sun than at the L_S=0° equinox. L_S=150-180° sees further intensification in lifting as Mars approaches equinox, greatly resembling L_S=0-30°. However, the asymmetry in seasonal cap growth and decline leads to asymmetry in intensity of cap edge lifting: northern lifting is greater during L_S=0-30°, and southern lifting is greater during L_S=150-180°. While following a similar geographic distribution, tropical/mid-latitude lifting is generally greater in the L_S=150-180° period: in particular, on the western border of the Tharsis plateau; in central Arabia; and on the Elysium/Utopia border.

In the L_S=180-210° period, Mars passes equinox and begins approaching southern summer solstice; this is northern autumn/southern spring. The subsolar latitude begins to drift poleward, and the planet is also moving closer to the Sun as it progresses towards perihelion. Compared to L_S=150-180°, northern seasonal cap edge lifting intensifies dramatically while shifting southward as the cap grows. Lifting is particularly high at the northern plains of Utopia, Acidalia, and Arcadia, as is topography-related lifting around Alba Patera, Tempe Terra, Elysium Mons, and the high topography feature at 40° N, 50° E; henceforth referred to as "Quenisset", due to the location of a crater of that name in said feature. Southern cap edge lifting, by contrast, is substantially reduced: from occurring at most longitudes in the 40-60° S latitude band during L_S=150-180°, to being limited to the region of Noachis east of Argyre Planitia, and the southern slopes of Hellas. This equinoctial pause may be due to a confluence of factors aligning: the retreating southern seasonal cap combined with the relative lack of insolation (as compared to later in the perihelion season). There is also additional lifting at the northeast edge of Hellas. The significant exception to these general statements is MY 34, the year of the 2018 GDS. This is discussed separately.

L_S=210-240° sees another southward shift and intensification of northern cap edge lifting, as northern winter solstice nears and the seasonal cap continues its growth. Meanwhile,

southern cap edge lifting drastically increases from the previous period, occuring at high intensity (>0.1 kg/sol per unit area) across most of the 60-70° S latitude band. Tropical/mid-latitude lifting also expands: Terra Sabaea, Terra Sirenum, Thaumasia, and Terra Cimmeria all see new lifting regions. Large regional dust storms are a common occurrence in this period (Kass et al., 2016), and "A"-type storms occur in all the studied MYs 29-33, though the MY 30 event was significantly weaker (Kass et al., 2016). Interestingly, the strength of these large regional storms does not appear to have a noteable effect on lifting, at least as averaged over a 30 L_S period.

At L_S=240-270°, Mars reaches perihelion (L_S=251°) and southern summer solstice (L_S=270°). Consequently, the subsolar point is at its southernmost latitude; the amount of solar energy reaching the planet is at its highest; and the northern and southern seasonal caps are approaching their greatest and least extents, respectively. Despite the high thermal contrast at northern high latitudes, however, northern cap edge lifting actually decreases from the previous period. This is due to the solsticial decline in high-latitude wave activity known as the solsticial pause, as well as the growth of the seasonal cap which obscures dust reservoirs from lifting. Topographic lifting on the northern slopes of Alba Patera and Tempe Terra remains high. There are striking increases in lifting at the 30° S latitude band, specifically at Terra Sabaea, Terra Cimmeria, southern Elysium Planitia, northern Terra Sirenum, and the Thaumasia Highlands. There are similarly large increases in lifting at the southern polar cap edge, with lifting extending further south as the cap retreats and intensifying in areas where it was already occuring such that the entire 60-80° S latitude band has a >0.1 kg/sol per unit area lifting flux. Given the weak wave activity in this region at this time of year, these high lifting rates may be associated with the sublimation flow of the southern seasonal cap (Chow et al., 2019). The location and seasonality of this lifting correlates well with high observed CDODs, and specifically "B"-type cap edge regional storms (Kass et al., 2016). Mars reaches and begins moving away from southern summer

solstice in the L_S=270-300° period. Southern cap edge lifting remains high, but declines and shifts poleward relative to the previous period, in accordance with the shrinking of the cap. Northern cap edge lifting remains at the same locations and intensity of the previous period. The lifting zones at the 30° S latitude band all see increased lifting and, in the case of Terra Sabaea, geographically expanded lifting. By contrast, northern hemisphere mid-latitude lifting shows a slight decrease.

L_S=300-330° shows a dramatic reduction in lifting extent and intensity by the southern seasonal cap, as the cap reaches its minimum extent. The lifting still occurring polewards of 60° S is primarily concentrated south of Argyre Planitia. Elsewhere, the mid-latitude lifting at 30° S remains, but at a significantly lower rate than the previous period. By contrast, lifting in the northern hemisphere grows in extent, covering nearly all regions between 0-50° N. Lifting in the low elevation plains of Acidalia, Arcadia, and Utopia intensifies. This time of year often sees the appearance of a "C"-type regional storm (Kass et al., 2016): such events occurred in all the martian years shown here. Finally, in the L_S=330-360° period Mars moves back towards equinox. The southern seasonal cap experiences a small amount of growth, but lifting by the cap edge remains sporadic and low intensity. The most immediately apparent change from the previous period is the disappearance of southern mid-latitude lifting, previously centred on the L_S=30° S latitude band. There is a slight intensification and poleward shift in northern seasonal cap edge lifting. Lifting in this period is fully dominated by the northern hemisphere, and in particular the northern plains of Arcadia, Acidalia, and Utopia; and topographic lifting at Elysium Mons, Quenisset, and the northern edges of Alba Patera and Tempe Terra.

Zonally averaged dust lifting and interannual similarity

This section shows zonally averaged dust lifting flux results for MY 29-34, and statistical analyses of MY 29-33: years without GDS. As in the previous sections, dust lifting is

represented as average lifted mass flux per unit area per sol during the relevant period, which are then zonally averaged. Note that some of the scale bars are non-linear, and dust flux can vary by orders of magnitude between seasons.

Fig. 5.3 complements the spatial lifting plots presented in the previous sections by allowing detailed temporal examination of interannual variation dust lifting in MYs 29-34, at the expense of some spatial detail. The interannual similarity in calculated dust lifting patterns between years is striking. There are a number of interesting major features present, some of which have been described previously in Section 5.3.1 but which are further characterised here.

From L_S=0-90° there is moderate ($\sim$0.01-0.025 kg/sol per unit area) lifting at the edge of the northern seasonal cap, which follows the cap edge's poleward movement as Mars moves into northern summer solstice. Northern cap edge lifting then effectively ceases until around L_S=150°.

There is low intensity (<0.01 kg/sol per unit area) lifting between 15° S and 45° N throughout the period L_S=0-150° this is largely well below 0.005 kg/sol per unit area except for at the 10°+/-5° N and 35°+/-5° N latitude bands, which correspond (respectively) to enhanced lifting at the western slopes of Tharsis, eastern Tharsis, Terra Sabaea, and northwestern Elysium Planitia; and at southwestern Alba Patera and western Elysium Mons.

There is a southern hemisphere lifting "gap" at mid-latitudes, between 15° S and 30° S, where little to no lifting occurs at any longitude from L_S=0-180°. This corresponds to the subsolar latitude being in the northern hemisphere, and solar insolation being at its lowest during the aphelion season.

Greater lifting occurs at the southern seasonal cap edge than at the northern cap, due to the thermal contrast being greater at the winter pole. Moderate lifting (0.01-0.02 kg/sol per unit area) occurs at the southern cap edge between L_S=0-180° moving equatorwards and then polewards again in that period as the cap grows and shrinks with the approach and

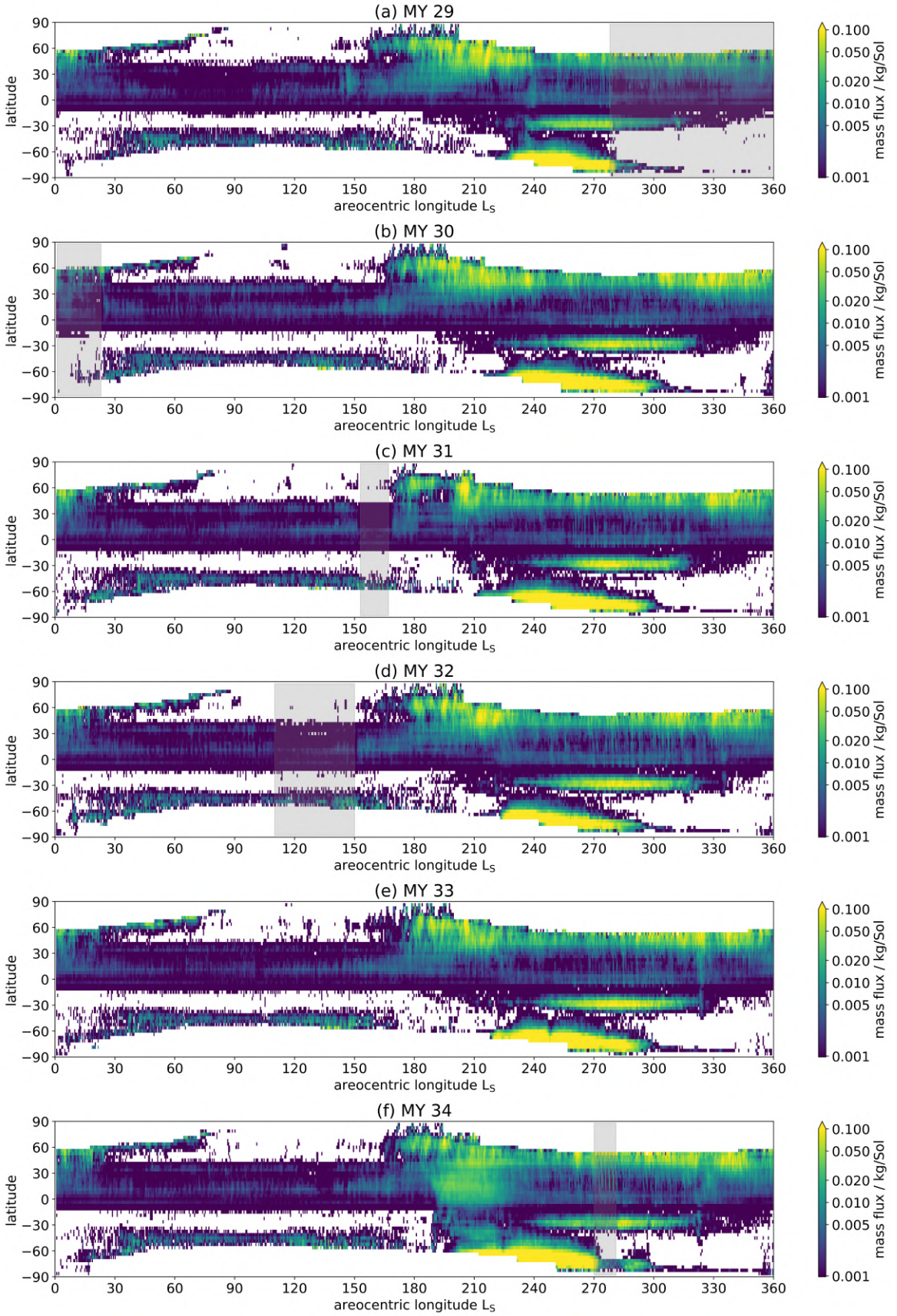

Fig. 5.3 Zonally averaged L_S-latitude maps of dust mass lifting flux for MY 29-34. Grey shaded areas correspond to times when the MGCM ran without assimilation. Note the non-linear scales.

passing of southern winter solstice. There is also a small but noticeable decline in cap edge lifting around southern winter solstice, attributable to the solsticial pause in wave activity (Lewis et al., 2016). This lifting is due to very high wind speeds in the reanalysis over the southern seasonal cap.

The "dusty season" on Mars begins somewhere in the period L_S=150-180°. L_S=150° sees an uptick in northern lifting between 0 and 30° N for MYs 29, 32, and 34; this occurs a little later for MYs 30 and 33. There is no MCS data for assimilation in this period for MY 31, and the resulting static dust distribution results in a sudden and drastic decline in lifting for the no-data period.

However, by L_S=170° of each year, the dusty season has unambiguously begun, as indicated by the rapid growth in northern cap-edge lifting, concentrated between the 40-75° N latitudes. This intense lifting, of $\geq$0.05-0.01 kg/sol per unit area, is at its greatest between L_S=180-240°, and tracks the growth of the northern seasonal cap. This period is when "A"-type regional storms occur, and while most of the lifting associated with those storms occurs at southern mid-latitudes, they likely originate from smaller storms at northern mid-latitudes which then cross the equator ("flushing" storms) before growing to regional scale (Kass et al., 2016). Nothern seasonal cap edge lifting continues after L_S=240°, but with a reduced magnitude in the L_S=240-300° period attributable to the solsticial pause (Lewis et al., 2016). This solsticial pause may be at least in part responsible for the usual lack of regional-scale tropical storms between the "A" and the "C"-type storms, ie. in the L_S=270-300° period. After L_S=300°, northern cap-edge lifting reintensifies through to the end of the year, rising from $\sim$0.02 to $\sim$0.05 kg/sol per unit area.

One notable lifting feature occurs between L_S=230-320°; high intensity lifting, of magnitude $\geq$0.01-0.1 kg/sol per unit area, centred at and just north of the 30° S latitude band and peaking in intensity around L_S=260-290°. Examination of the spatial lifting maps for this period reveals that this lifting did not occur at all longitudes, but only in certain locations:

northern Terra Sirenum, Daedalia Planum, northern Noachis Terra/southern Terra Sabaea, the northern rim of Hellas Planitia, and Terra Cimmeria; the highest intensity lifting occurred at the first three of these locations. Interestingly, this high lifting feature at southern mid-latitudes does not appear to correspond to enhanced CDOD or to tropical regional-scale storm activity; as mentioned in the previous paragraph, this is on average a quiet period in terms of large dust storms, and the existence of this lifting feature does not appear to compensate for the solsticial pause in northern cap-edge lifting.

The last major high-intensity lifting feature is visible at the southern seasonal cap edge, during the period L_S=220-300°. Lifting occurs at the rate of $\geq$0.1 kg/sol per unit area for almost the entire period, making it the highest magnitude lifting feature of the whole martian year. While low to moderate lifting extends almost 30° equatorward from the cap edge, the core of the high lifting (>0.1 kg/sol per unit area) extends approximately 20° equatorward. From looking at the relevant spatial lifting maps, this lifting takes place over the entire southern cap edge.

As well as areas of active lifting, it is also interesting to note locations and seasons were little to no lifting occurs. One such no-lifting zone is around the 30° S latitude band during the aphelion season; no dust lifting occurs for this entire season, despite the high lifting feature at this very latitude described above as occuring around L_S=230-320°. This implies that some aspect of the zonal wind structure at 30° S is substantially different between the aphelion and perihelion seasons.

Another no-lifting zone occurs at southern mid-to-high latitudes between L_S=300-360° (and indeed is temporally linked to the zone in the previous paragraph), extending at its maximum from 85° S to 45° S at around L_S=340°. Again, this is linked to particularly low wind speeds at these latitudes at this time of year. This no-lifting feature correlates with low CDOD around these regions between L_S=330-360°. Between L_S=300-330°, however, "C"-type storms often occur; like "A"-type storms, though, these are likely to originate in

the northern dust lifting zones (which are active once more after the solsticial pause) and travel southwards before growing to regional scale, rather than to originate in the southern hemisphere (Kass et al., 2016). These observations agree well with modelled lifting (and lack thereof) in the CT-MA reanalysis.

The last major no-lifting zone occurs at the northern pole around northern summer, between L_S=60-150°, and north of 45° N. This is another area/season where near-surface wind speed is at a minimum, likely due to the low thermal contrast in this area and lack of a strong zonal jet.

As well as no-lifting zones, there are also latitudes and seasons where lifting occurs but is at a local minimum. One such low-lifting band occurs in the aphelion season between approximately 20° N and 35 ° N.

In the perihelion season, there is a similar feature at similar latitudes: between L_S=230-320° and between latitudes 10° N and 30° N. There is then a band of stronger lifting between 5° S and 10° N, and a band of much weaker lifting northward of the strong latitude 30 ° S lifting feature described above. This same pattern is observed in the near-surface wind speeds, making it a feature of the zonal wind structure, or jet.

Interannual variability

Fig. 5.4 shows interannual variability in dust lifting by showing the differences in mass lifting flux between each year and the mean of MYs 29-33.

The aphelion season exhibits high interannual similarity, especially outside the seasonal cap edges. What variability there is occurs at the cap edges, where wind speeds and lifting are highest. This variability is generally of a stochastic nature, with both increases and decreases relative to the mean occurring at consecutive times and latitudes; see for example the variability in northern cap edge lifting between L_S=0-30° of MY 34 in Fig. 5.4.f. This variability is likely due to weather “noise”, introduced by assimilating temperature profiles

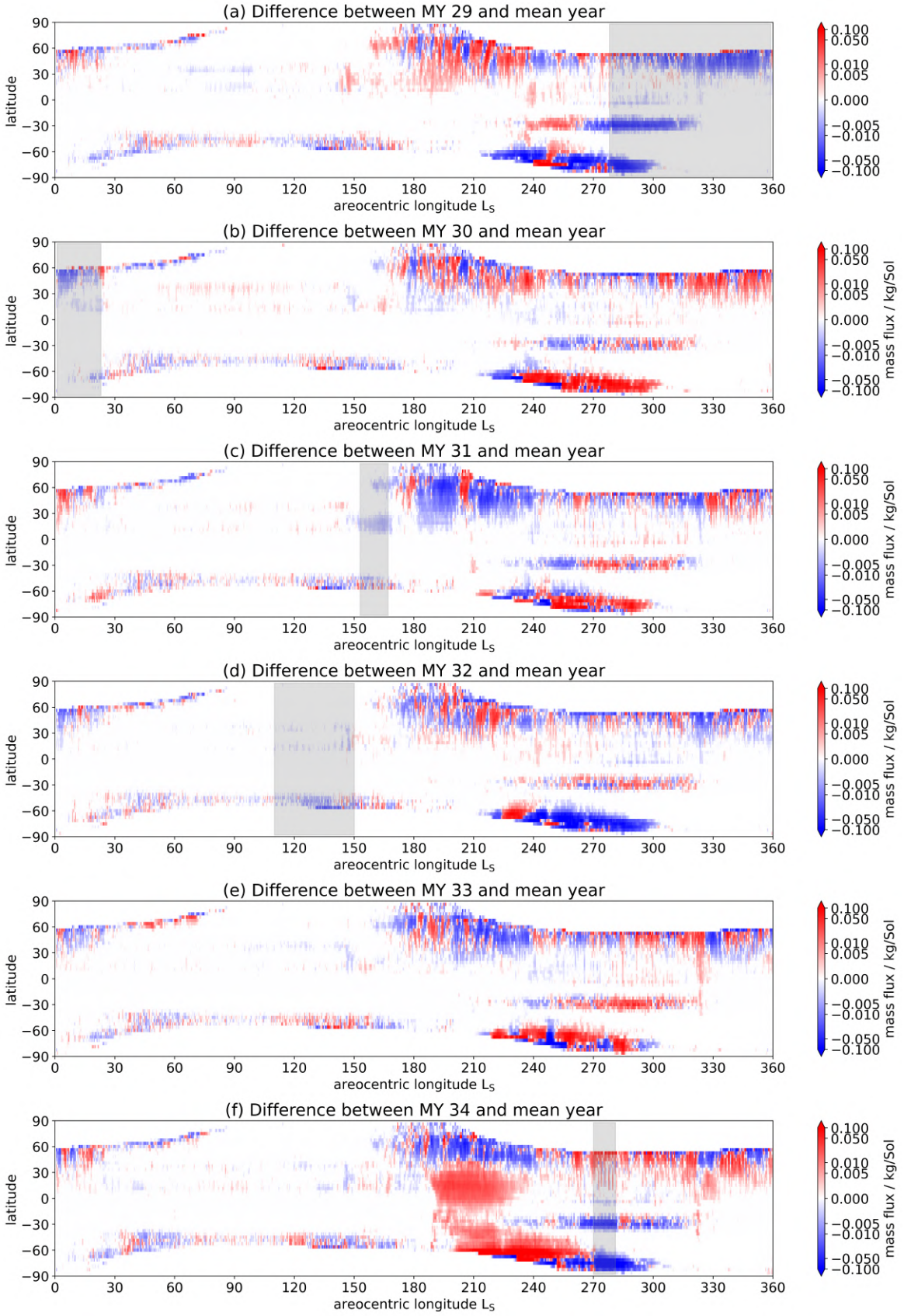

Fig. 5.4 Zonally averaged L_S-latitude maps of dust mass lifting difference from the mean of MYs 29-33 for MYs 29-34. Grey shaded areas correspond to times when the MGCM ran without assimilation. Note the non-linear scales.

and dust CDOD which vary according to specific meteorological conditions: different water ice cloud structures, different dust spatial and vertical distributions, and different seasonal cap morphologies to name a few.

There is more significant interannual variability during the perihelion season, which is after all the primary dust lifting season. Some of this variability can be ascribed to an absence of assimilated data during the relevant period, while some appears to be linked to dust storm activity.

The following periods contain gaps in assimilated data:

- MY 29-30, L_S=278-23°: The spatial dust opacity between MY 29 L_S=278° and MY 30 L_S=23°is set with the spatially krigged dust maps of Montabone et al. (2015). Temperatures are not assimilated throughout this period.
- MY 31, L_S=153-167°: the MGCM is allowed to run by itself for this period.
- MY 31, L_S=180-199°: the MGCM is allowed to run by itself for this period.
- MY 32, L_S=110-150°: the MGCM is allowed to run by itself for this period.
- MY34, L_S=270-281°: the MGCM is allowed to run by itself for this period.

The data gaps described all correspond with decreased dust lifting relative to the mean year, suggesting that the MGCM without temperature assimilation underestimates near-surface wind speeds. The question of how assimilation of MCS data affects wind speeds in the MGCM is addressed further in Chapter 7.

Link between tropical CDOD and southern seasonal cap edge lifting

Examination of Fig. 5.4 shows an interesting feature: there are distinct and consistent (within that year) differences in southern cap edge lifting for each year, relative to the mean. MYs 29 and 32 show noticeably less lifting than the mean year; MYs 30, 31, and 31 show noticeably

more lifting. Comparing this with the annual zonally-averaged CDOD maps in Fig. 5.17 appears to show a qualitative correlation between tropical/mid-latitude CDOD and southern cap edge lifting: dustier years correspond to reduced lifting, and vice versa.

To better establish whether this is in fact likely to be a real link, a Pearson correlation analysis was performed between reference CDOD at 610 Pa, as averaged between latitudes 15° S-15° N, and near-surface atmospheric temperatures, as averaged between latitudes 60-90° S, all averaged over the period L_S=240-300°. This was done for MYs 29-33, excluding the GDS year MY 34. The result, shown in Fig. 5.5, was a correlation coefficient of 0.92, indicating high positive correlation, with a p-value of 0.02 (<0.05), indicating statistical significance. This is with a small sample size, of 5, but the deterministic nature of the GCM and the temporal consistency of the pattern (visible in Fig. 5.4) indicate that there is a real link.

The most compelling explanation for this link is that increased atmospheric warming from higher tropical CDOD causes enhanced transport of warmer air from the tropics to southern high latitudes. This accelerates the sublimation at the southern seasonal cap and accelerates its recession. The recession of the seasonal cap reduces the area over which there is a sharp surface temperature contrast (between the seasonal cap and the surface which is not covered by CO_2 ice), reducing cap-edge lifting, and shifting the remaining lifting poleward (this is visible in the small patches of higher-than-average lifting at the southernmost latitudes in MYs 29 and 32 in Fig. 5.4). This latter effect also reduces the surface temperature contrast between the cap and the exposed land, as the additional exposed land is further from the subsolar point and thus cooler than exposed land at lower latitudes.

Fig. 5.6 shows surface temperature differences from the mean (of MYs 29-33) over the southern polar region, averaged over L_S=240-300°. MYs 29 and 32 clearly show surface temperatures up to 10 K higher than the mean, while MYs 30, 31, and 33 have surface temperatures up to 10 K lower than the mean. These significant temperature differences,

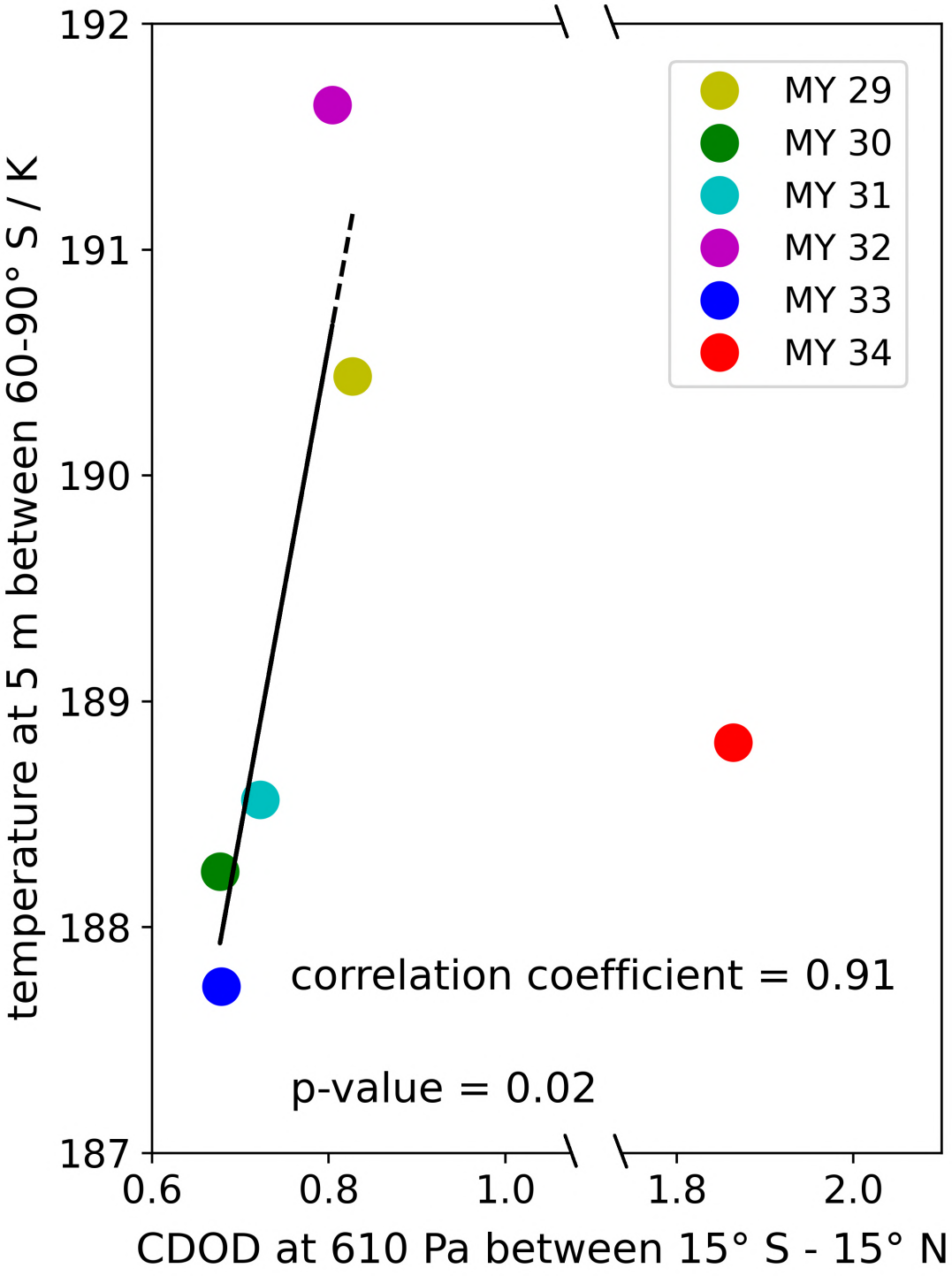

Fig. 5.5 Plot showing correlation between reference CDOD at 610 Pa, as averaged between 15° S-15° N, and atmospheric temperature at 5 m above the surface, as averaged between 60-90° S, for all six MYs. All values are also averaged over the period L_S=240-300°. The Pearson correlation values presented are for MYs 29-33 only.

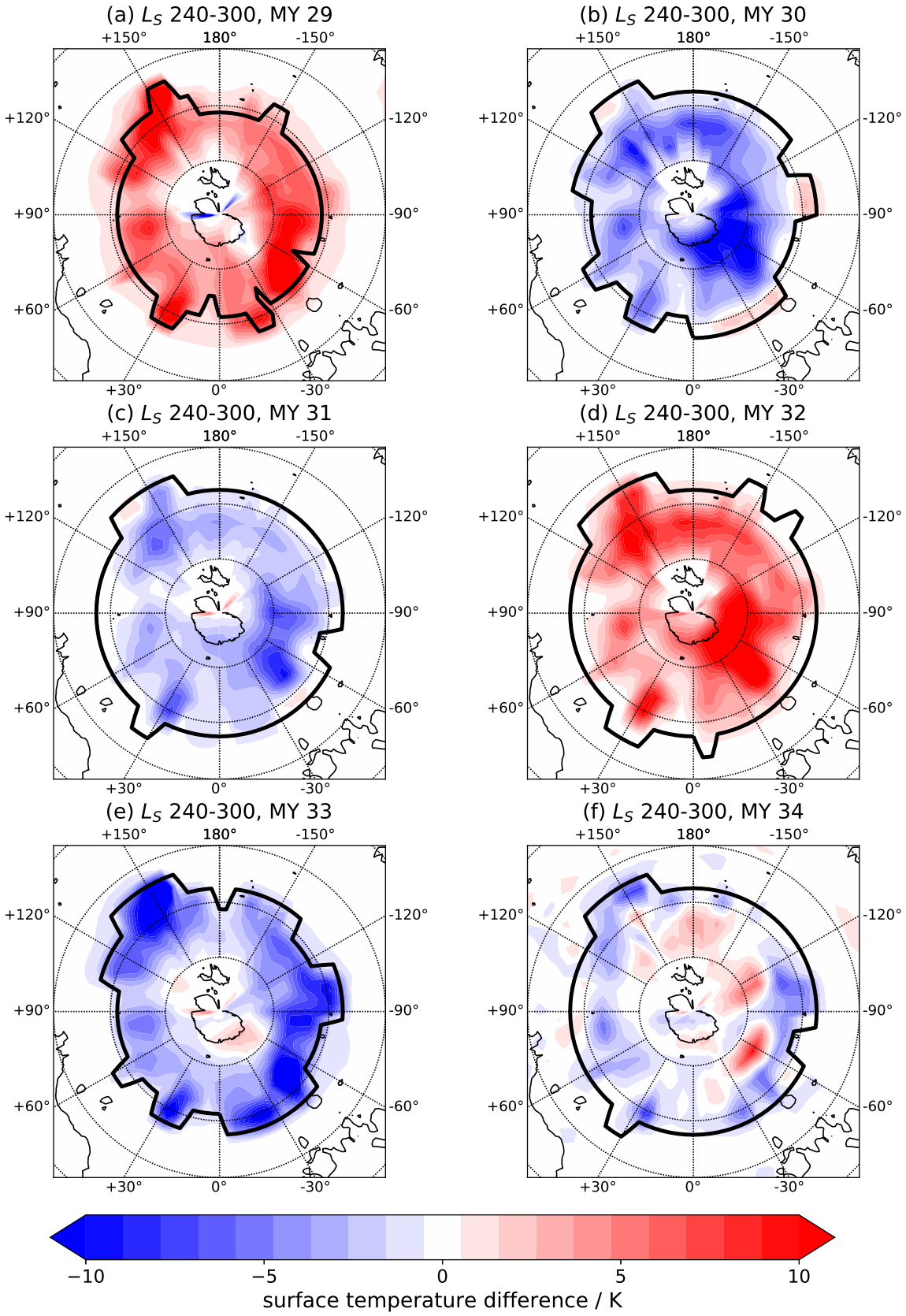

Fig. 5.6 South pole maps of surface temperature difference from the mean (of MYs 29-33) over the southern pole averaged over L_S=240-270°, for MY 29-34. Dotted circles represent 10° latitude increments, with the outermost full circle representing 60° S and the innermost representing 80° S. The thick black border represents the average location of the seasonal cap over the period.

however, are all confined to within the boundaries of the seasonal cap; outside the cap, there are no significant temperature differences between year. In other words, the surface temperature differences are entirely determined by whether a certain area has CO_2 ice cover or not, and for what proportion of the relevant period this is the case. This is evidence for the effect of dynamics-induced sublimation and recession of the seasonal cap: any direct radiative causes (such as dust cover) would likely have some influence over surface temperatures outside the seasonal cap boundary as well. The patchwork nature of the surface temperature differences also accords with changes in the seasonal cap extent, as the southern cap has been observed to show significant interannual variability in its decay (Piqueux et al., 2015).

Fig. 5.7 shows vertical velocity (ω) differences from the mean (of MYs 29-33) over the southern polar region, averaged over L_S=240-300°. While the spatial structure is complex, a clear trend is nevertheless discernible: MYs 29 and 32 show on average greater downward motion over the area of the seasonal cap, while MYs 30, 31, and 33 show less downward motion. The vertical velocity differences are particularly high around the 65° latitude band, which corresponds to the latitude of the downwelling branch of the anticlockwise Hadley cell. This is further evidence in support of the dynamical hypothesis.

As a final note, the changes seen in MY 34 do not accord to the hypothesis; the seasonal cap shows evidence of both inhibited and accelerated decay, and it does not fit within the tropical CDOD-southern high latitude surface temperature correlation described earlier, as seen in Fig. 5.5. Interestingly, an observational study found that while the southern polar atmosphere was warmer than climatology in the southern summer after the GDS, there was no discernible change in the rate of recession of the southern seasonal cap. Figs. 5.6 and 5.7 suggest that the effect of the GDS on the seasonal cap may have been strongly asymmetrical in longitude.

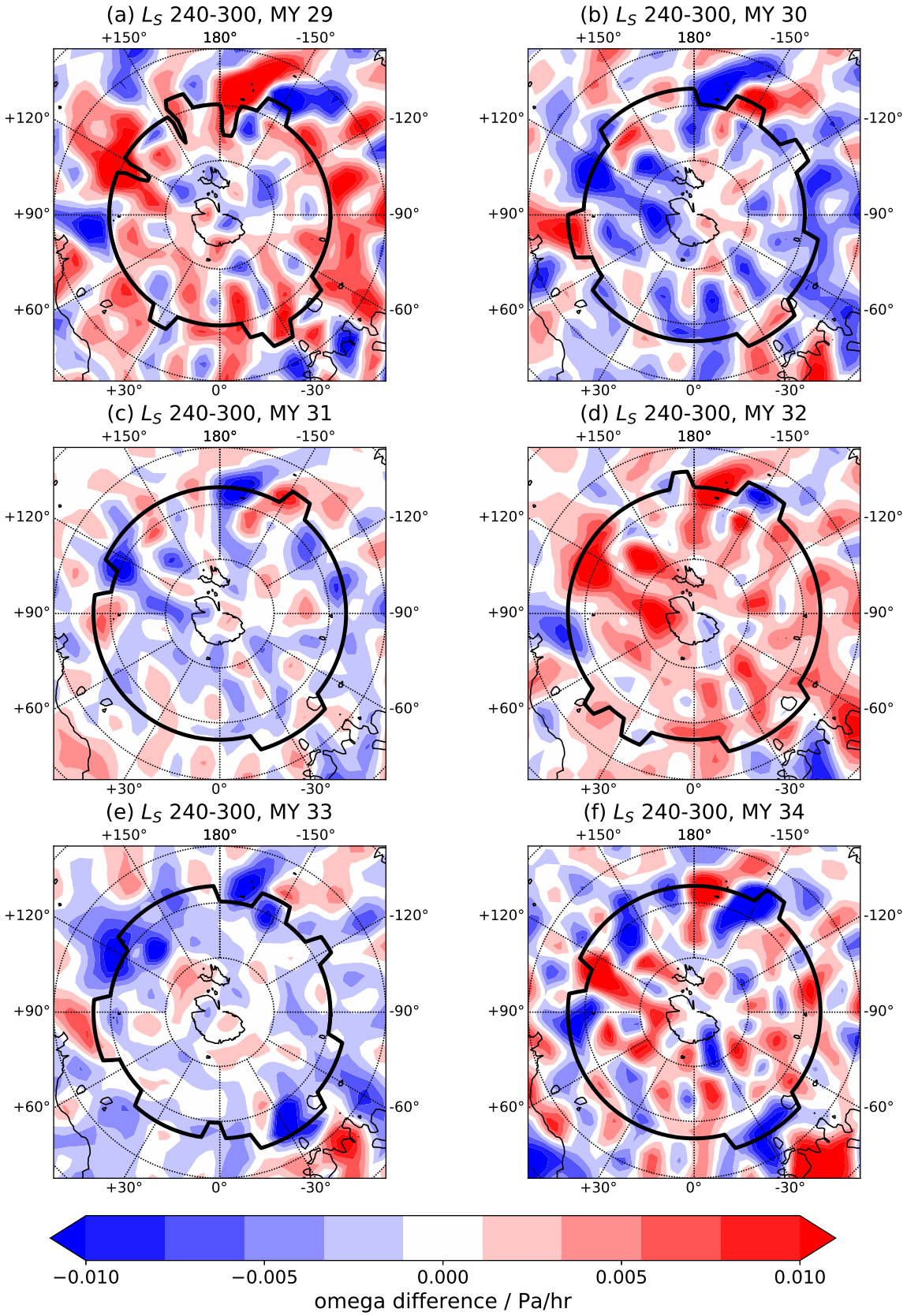

Fig. 5.7 South pole maps of near-surface vertical velocity (ω) difference from the mean (of MYs 29-33) averaged over L_S=240-270°, for MY 29-34. Positive (red) values represent difference in the downward direction and negative (blue values) difference in the upward direction. Dotted circles represent 10° latitude increments, with the outermost full circle representing 60° S and the innermost representing 80° S. The thick black border represents the average location of the seasonal cap over the period.

Wind speeds

Unsurprisingly, areas of intense lifting correlate very well with areas where near-surface wind speeds are highest. The plots in Fig. 5.8 show the same regions and time periods as Fig. 5.2, allowing analysis of where on the planet the highest winds speeds occur, and their subsequent contribution to dust lifting. The notable exception is high wind speeds over the seasonal caps, which are forbidden under the offline calculations to lift dust. The zonally-averaged time series of wind speeds is then shown and related to the broader circulatory structure.

Wind speeds in general are lower during the aphelion season, rarely exceeding 5 m/s over most of the surface. Sustained local maxima in each period are consistently found at certain locations. The elevated topography of the Tharsis plateau is one such region, with wind speeds there reaching or exceeding $\sim$15 m/s even during the quietest periods, e.g. L_S=30-90°. Wind speeds are particularly high around the individual volcanoes of Tharsis and Olympus Mons, and are consistently at their greatest in the region around the slopes of Alba Patera. The volcano Elysium Mons also shows consistently elevated wind speeds, again likely due to slope winds from the large topographic variation. Enhanced wind speeds are also visible at Quenisset, particularly at L_S=0-30° and L_S=60-180°. Aside from Quenisset, wind speeds at northern Arabia Terra generally are consistently elevated relative to the surrounding terrain. Finally, the eastern slope of Isidis Planitia/elevated region to the east of Isidis planitia also shows consistently high wind speeds.

In the southern hemisphere, it is the slopes of Hellas Planitia that consistently show elevated wind speeds. At L_S=0-30°, this is largely around the western, northwestern, and northern slopes; throughout L_S=30-120°, this is confined mostly to the southwestern slopes; and from L_S=120-180°, this expands once more to encompass the entire circumference, though with maxima at the southwestern and northeastern slopes. Another notable high-wind speed feature is at the Thaumasia Highlands, and particularly its southern slopes, which show high wind speeds from L_S=30-150°, coinciding with the peak of the southern polar jet.

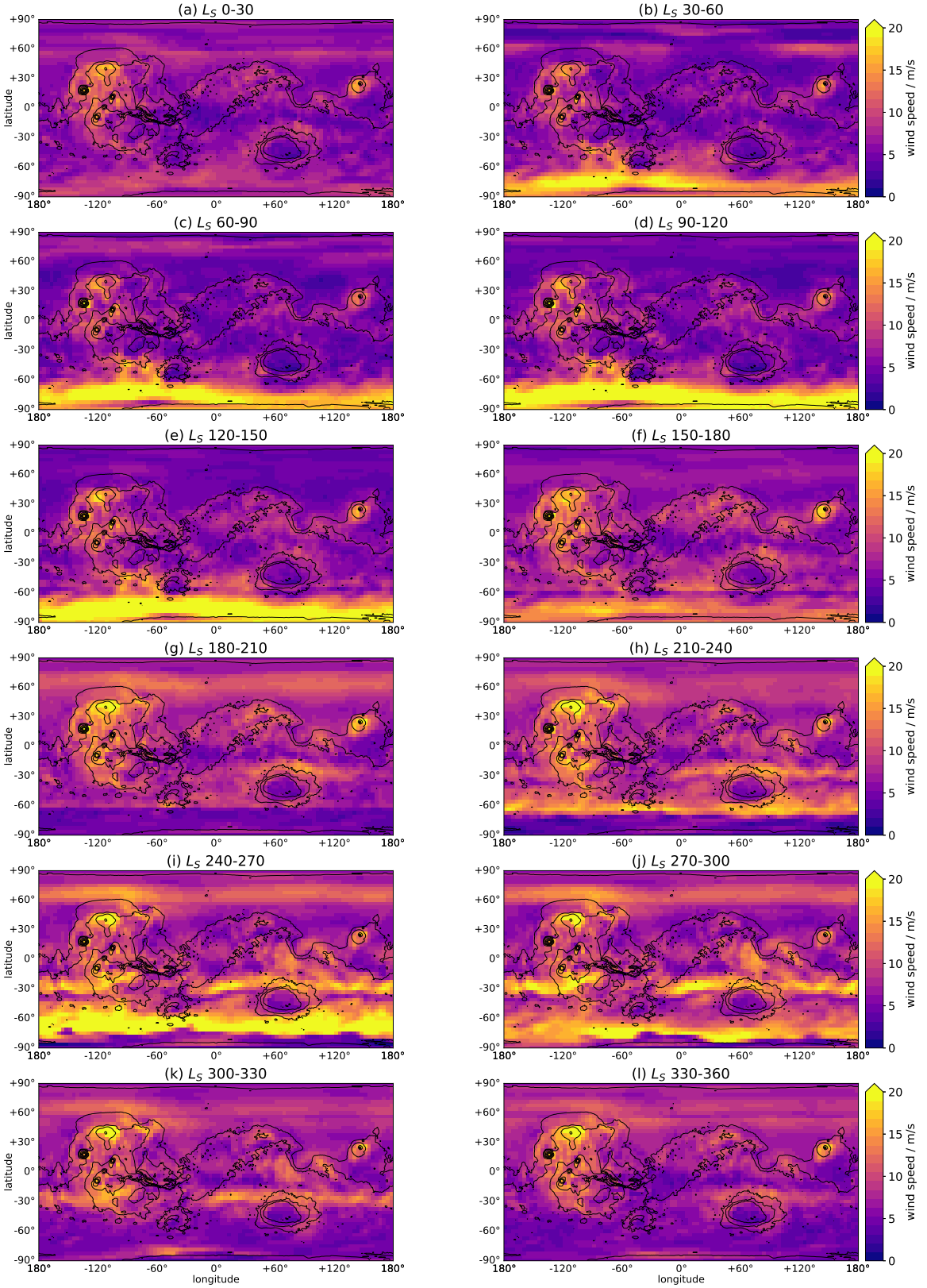

Fig. 5.8 Maps of near-surface wind speed for the mean of MY 29-33 over 12 periods of 30° L_S.

Evidence of cap edge winds can be seen from L_S=0-90° at northern high latitudes following the recession of the northern seasonal cap, with high wind speeds weakening in strength and retreating poleward as the year progresses. Northern high latitude wind speeds then remain low until L_S=0-90°, as Mars reaches equinox again and a northern polar jet is re-established.

Much more apparent is the effect of the southern polar jet, which is visible at southern high latitudes throughout the entire aphelion season but is particularly strong from L_S=30-150°, with an apparent maximum in strength and latitudinal extent between L_S=90-150°. This near-surface jet is largely confined to the southern seasonal cap, making it unable to directly lift dust despite its magnitude; it is still able to contribute to some cap-edge lifting however, as can be seen in Fig. 5.3. The structure of this surface jet is not zonally symmetric; as can be seen in Fig. 5.8.c, it is stronger and shifted equatorward in the western hemisphere, and weaker and shifted poleward in the eastern hemisphere. As discussed above, therefore, this means that its contribution to lifting is biased towards the western hemisphere: the Thaumasia Highlands, Aonia Terra, and southern Noachis Terra, where the jet's strength appears correlated to enhanced wind speeds at the southern cap edge.

The perihelion season shows higher winds speeds generally, as the planet receives greater insolation. The northern equatorial topographic high wind speed locations described above show consistently elevated wind speeds in this season as well, with even greater magnitude as wind speeds regularly reach and exceed 20 m/s on the slopes of Alba Patera. Throughout the whole perihelion period, the northern polar jet is visible, peaking in magnitude at L_S=270-300° at ∼16-18 m/s, but remaining relatively stable in its position at the latitude band 60-75° N. It shows some longitudinal asymmetry in magnitude, with higher wind speeds in the region north of Alba Patera/Tempe Terra (and in the western hemisphere generally), and lower wind speeds in the eastern hemisphere. This asymmetry may be related to the higher topography in the regions which show the higher wind speeds.

A mid-latitude jet can also be seen during this season. Its precursor is visible during L_S=180-210° as a band of elevated wind speeds of ∼15 m/s on the northern slopes of Hellas Planitia. This band grows eastward and westward in the L_S=210-240° period, extending from 0 to 180° E at the 30° S latitude band. A fully formed jet is then visible in the period L_S=240-330°, whereupon it reverts once more to the same slightly elevated pattern on the north slopes of Hellas as in L_S=180-210°. The peak of the jet's strength occurs at L_S=270-300° with wind speeds consistently reaching and exceeding 20 m/s. This jet is strong asymmetric in its longitudinal structure, with major implications for dust lifting. Fig. 5.8.j shows that the highest wind speeds occur over Noachis Terra, Terra Sirenum/the Thaumasia Highlands, and Terra Cimmeria, with much lower wind speeds of ∼10 m/s or less between 30° W and 90 ° W (northern slopes of Argyre Planitia and southeastern Tharsis).

Finally, there is a major contribution to lifting from a powerful high wind speed feature at the southern seasonal cap edge, linked to high zonal winds and henceforth referred to as a jet. This jet is visible from L_S=210-300° (with a small remnant at L_S=300-330°) at southern high latitudes, and retreats polewards concurrently with the seasonal cap retreat, peaking in magnitude at L_S=240-270° with speeds exceeding 20 m/s across the entire latitude band between 60-75° S. As can be seen in Figs. 5.8.i,j, this jet closely follows the edge of the seasonal cap and only occurs equatorward of the cap, not over the cap itself. This makes it a major contributor to lifting, as has been described previously, and it is linked both spatially and temporally to the occurrence of "B"-type cap edge regional storms.

Looking at the zonally-averaged wind speeds in Fig. 5.9 allows for examination of large-scale near-surface wind speeds in terms of seasonal trends. A brief characterisation of these will be provided, followed by a closer look at specific zonal and meridional wind speed trends contributing to these seasonal patterns.

The aphelion season is characterised by lower wind speeds than the perihelion season, with one notable exception at the southern seasonal cap. In general, zonally-averaged wind

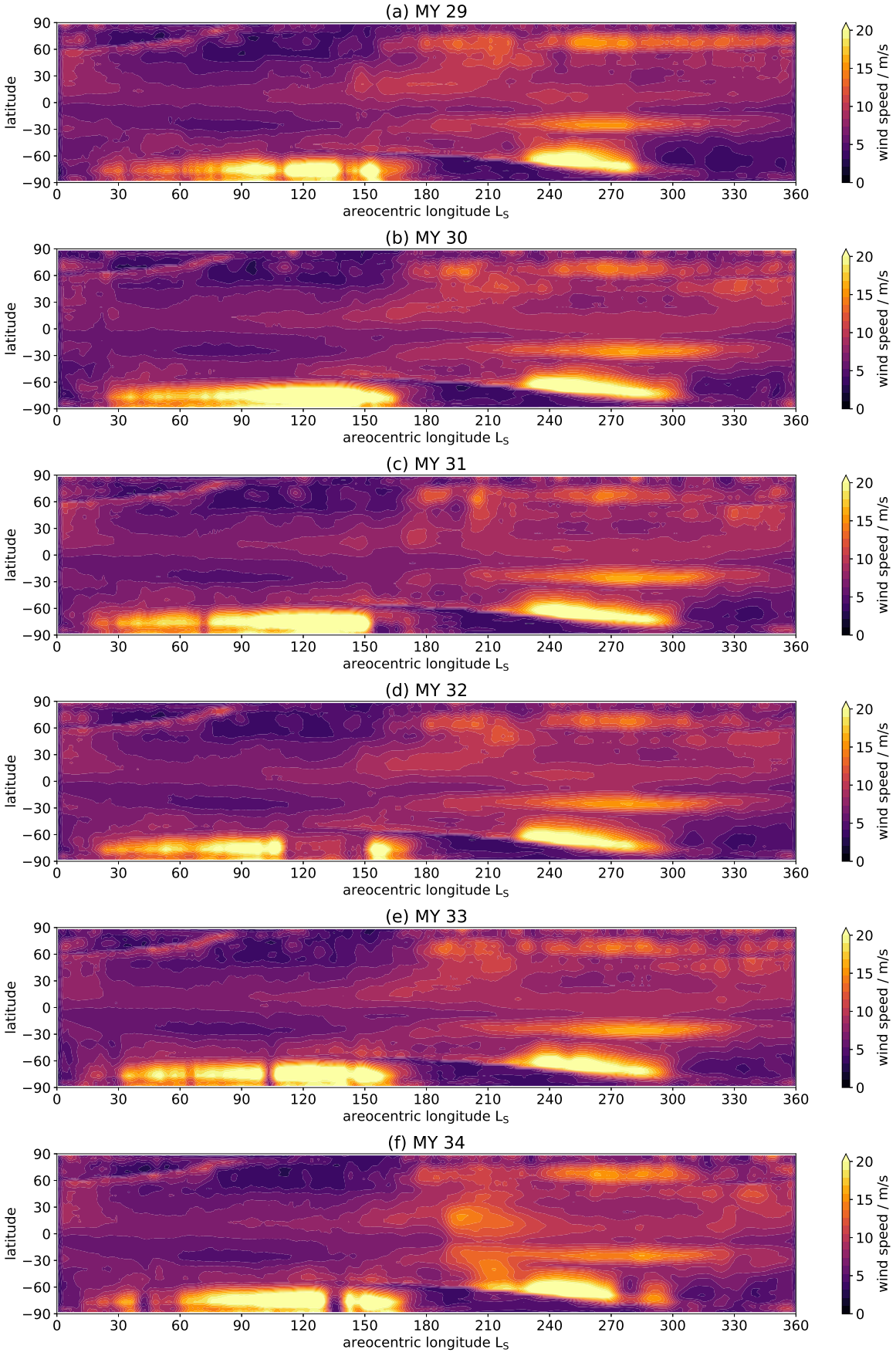

Fig. 5.9 Zonally averaged L_S-latitude maps of near-surface wind speeds for MYs 29-34.

speeds remain below 10 m/s at most. There is a band of enhanced wind speeds, of order ∼12 m/s, present at the northern seasonal cap edge from L_S=0-90° which progress polewards as the northern cap recedes. Equatorial wind speeds increase from ∼7 m/s to ≥10 m/s as the L_S=180° approaches, with distinct bands visible from L_S=150-180° at around 20° N and 30° S. Some low-magnitude (sub-10 m/s) pulsing behaviour is seen at northern high latitudes between L_S=90-150°, but for the most part wind speeds there remain sub-5 m/s during that period.

The most eye-catching feature during this period is the powerful wind speeds, of over 20 m/s, over the southern seasonal cap between L_S=20-170° that occur each year. The northern boundary of this feature corresponds exactly to the edge of the seasonal cap, meaning that despite the powerful winds, this feature has only a limited effect on actual dust lifting. Elevated but still far lower wind speeds equatorward of the cap edge, of magnitude ∼10 m/s, are responsible for the greatest lifting during this period and may be in part linked to this feature, as well as eddies (see below). This feature is also highly dependent on assimilated data; for example, the MCS data gap between L_S=110-150° of MY 32 causes a collapse in wind speeds there from over 20 m/s to ∼12 m/s. The potential mechanisms behind this particular jet are further discussed in Chapter 6.

The perihelion shows generally higher wind speeds, beginning almost exactly at equinox L_S=180°. There are consistently high wind speeds of 10-15 m/s at the northern seasonal cap edge, marked by a minimum between L_S=240-300°; this period also sees high wind speeds over the cap itself, of ∼15-17 m/s, though not as intense as the winds over the southern cap during the aphelion season. This cap edge lifting is also marked by an initial pulse at the beginning of the perihelion season, during L_S=180-220°, with wind speeds of up to 15 m/s. There is no corresponding pulse at the southern cap edge, suggesting an eddy origin for this pulse.

Equatorial winds, at 0°, also show elevation relative to the aphelion period, with speeds of ∼10 m/s. Another notable feature is the narrow latitudinal band of high wind speeds at 30° S, lasting from approximately L_S=180-350° and peaking around L_S=240-300° with maximum wind speeds of ∼18 m/s. This feature is a major contributor to dust lifting, occuring entirely within the southern hemisphere entirely outside the seasonal caps.

Finally, there is the intense jet at the southern seasonal cap edge, entirely on the equatorward side, occurring between L_S=230-300° of each year. This jet is characterised by very high wind speeds of over 20 m/s throughout its entire existence. It has a latitudinal width of ∼20° from the cap edge, and follows the cap edge as it recedes. Like the jet over the southern cap itself during the aphelion season, it appears to be highly dependent on assimilated data, as shown by its dramatic collapse between from L_S=278° onwards of MY 29 and between L_S=270-281° of MY 34, periods when the MGCM is not assimilating MCS data. This jet's position on the equatorward side of the cap edge makes it a major contributor to lifting.

Fig. 5.10 shows specifically the meridional (north-south) components of the wind speed throughout the martian year, enabling ascription of the major lifting features to specific circulatory patterns.

The aphelion season is characterised by two bands of enhanced meridional surface wind speeds. The first is a south to north flow between 0-15° N, for the entire aphelion season. Throughout most of the season this has wind speeds of ∼3 m/s, increasing to ∼5 m/s between L_S=90-150°. This is a shallow flow which appears to correspond to the returning flow of the cross-equatorial Hadley cell, going from north to south, which dominates the circulation at this time of year. The minor lifting that happens in this band, therefore, is attributable to this return flow, which as can be seen in the wind speed maps above, is concentrated over specific locations: this is the western boundary current described by Joshi et al. (1994) and Joshi et al. (1995), where returning Hadley cell flow is intensified at the western boundaries of high topography features.

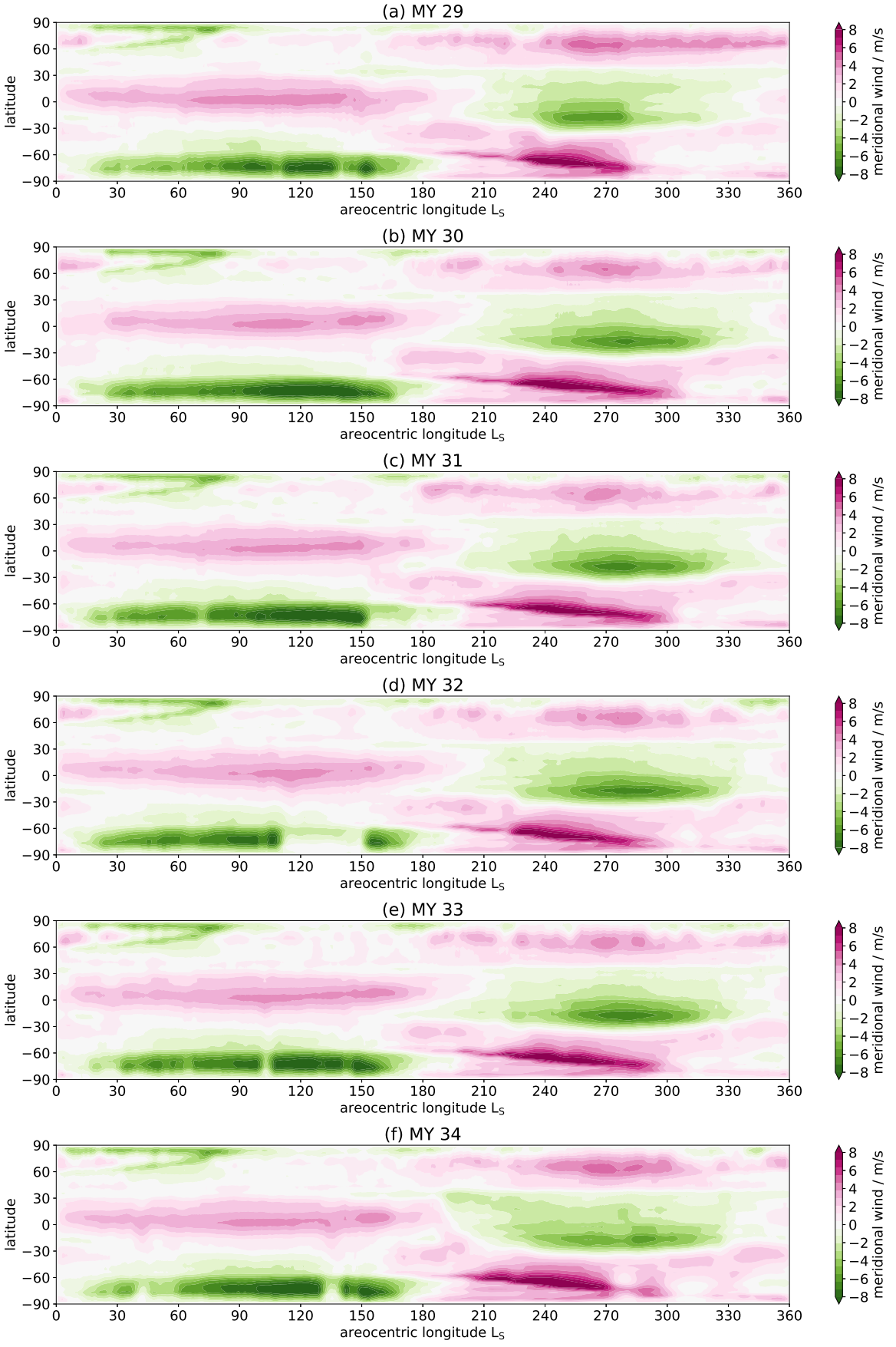

Fig. 5.10 Zonally averaged L_S-latitude maps of near-surface meridional wind speeds for MYs 29-34. Positive values represent southerly (south to north) flow, negative values represent northerly (north to south) flow.

The second notable aphelion feature is the intense north to south flow over the southern seasonal cap, up to and exceeding 8 m/s. This feature is extremely shallow, confined to the bottom ∼2 km of the atmosphere; above it, there is a much deeper south to north flow, suggesting an overall clockwise circulatory cell between 60-90° S. This may be related to condensation flow, as carbon dioxide condenses to form the seasonal cap; however, the magnitudes shown here are far greater than previously proposed for the condensation flow (Chow et al., 2019). However, this is beyond the scope of this chaper; the potential mechanisms behind this flow are further examined in Chapter 6.2 of this thesis.

Lastly, there is the evidence of a sublimation flow from the northern seasonal cap as it recesses between L_S=30-90°. This has a value of ∼3-4 m/s, making it significantly weaker than its southern equivalent during the perihelion season.

The perihelion season has three main features of interest. First is the south to north flow at the northern seasonal cap edge, persisting throughout the entire perihelion season with a speed of up to 4 m/s, peaking between L_S=240-300°. This peak occurs as the cap is at its maximum extent however, rendering it unable to contribute significantly to dust lifting. Examination of this feature shows it to be extremely shallow, with a deep north to south meridional flow above it, suggesting this feature is the returning flow for an anticlockwise circulatory cell. The large amount of eddy activity at these latitudes at this season (see below) implies that this is the zonally and temporally averaged effect of a wave-driven Ferrel cell.

The latitudes between 30° S and 30° N are characterised by a north to south meridional surface flow, again for the entire perihelion season but at its greatest between L_S=240-330°. There is also a maximum in latitude at around 15-30° S, where the flow reaches 7-8 m/s. The location of this flow and its seasonal behaviour indicate that this is the returning surface flow from the powerful cross-equatorial south to north Hadley cell that dominates the circulation throughout the perihelion season. Like its equivalent in the aphelion season, this flow organises into western boundary currents.

Lastly, there is a powerful south to north flow at the edge of the southern seasonal cap, proportional in strength to its distance from the cap edge itself. Meridional winds here exceed 8 m/s at the cap edge. This is a relatively shallow flow, confined to the bottom 1 km of the atmosphere above the pole itself and the bottom ∼5 km at 60° S. This flow is almost certainly due to the sublimation of the seasonal cap, given its beginning just after equinox (L_S=200°) and its end once the cap has disappeared almost entirely (L_S=300°). Southern seasonal cap sublimation has been shown in modelling to be able to cause a shallow and powerful flow at the seasonal cap edge (Chow et al., 2019). Here it is shown that it is a major contributor to dust lifting, and may be responsible for the regular pattern of "B"-type regional storms at this time and location.

Fig. 5.11 shows specifically the zonal (east-west) components of the near-surface wind speed throughout the martian year, enabling ascription of the major lifting features to specific circulatory patterns.

The aphelion season shows generally weak zonal near-surface wind speeds, except at southern mid-high latitudes. There are two related but distinct bands of high westerly zonal winds: a weaker one of magnitude ∼5 m/s equatorward of the seasonal cap edge, and a stronger one of ≥15 m/s poleward of the cap edge. There is undoubtedly some relation between the two, as seen by the fact the the minor gap in assimilated data at L_S=100-105° of MY 33 causes a sudden decrease in both; but this is also clearly not a straightforward linear relationship, as the gap in assimilated data between L_S=110-150° in MY 32 causes almost total destruction of the intense wind speeds over the cap itself while leaving the zonal wind pattern equatorward of the cap edge unperturbed. Both are linked to the southern winter polar jet, but the former is only being captured by the assimilated MGCM, while the equatorward cap edge wind speeds are captured by the non-assimilated MGCM.

The perihelion season shows three distinct zonal wind features of interest for dust lifting. The first is at the northern seasonal cap, where westerly flow dominates due to the presence

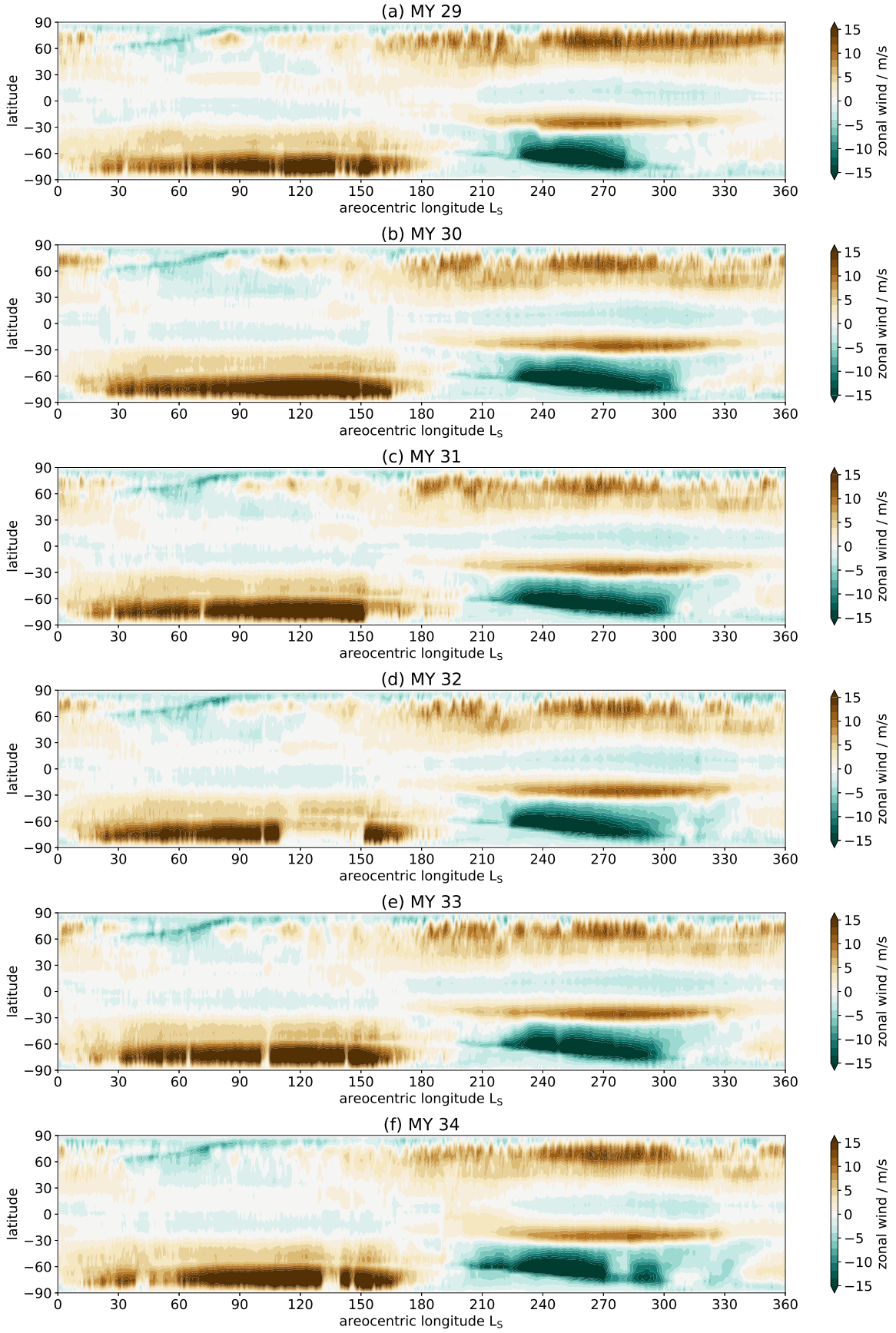

Fig. 5.11 Zonally averaged L_S-latitude maps of near-surface zonal wind speeds for MYs 29-34. Positive values represent westerly (west to east) flow, negative values represent easterly (east to west) flow.

of the northern polar jet. This flow shows a maximum of over 10 m/s between L_S=240-300°, but at high northern latitudes over the seasonal cap, and so unable to lift dust. A number of perturbations to this flow are visible between L_S=180-220°, likely due to baroclinic wave activity.

The second feature of interest is the narrow band of westerly flow, of magnitude up to ∼11 m/s, visible at the 30° S latitude between L_S=180-360° but at its maximum between L_S=230-330°. This narrow but intense jet likely relates to the ascending branch of the cross-equatorial south-to-north Hadley cell which dominates the mean meridional circulation throughout this period. Through simple conservation of angular momentum considerations, rising air at this latitude - the subsolar latitude - has to gain velocity in the westerly direction. Additionally, the near-surface meridional returning flow, corresponding to the bottom of the cross-equatorial Hadley cell, moves southward from the equator as visible in Fig. 5.10. The Coriolis effect means that this flow is deflected in the westerly direction. The result is an intense but narrow jet core at 30° S, and especially between L_S=210-330°.

Finally, there is a band of intense easterly flow at the southern seasonal cap edge between L_S=220-300°, of over 15 m/s throughout its entire lifetime. This easterly surface jet is linked to a broader, intense easterly wind structure extending well into the middle atmosphere. The maximum strength of this jet, during L_S=240-300°, matches the time when the cross-equatorial Hadley cell is at its strongest, with meridional velocities at their greatest. The easterly pattern of surface flow is evidence of sublimation flow being responsible for these high winds: Chow et al. (2019) note that their modelling of the southern cap sublimation flow at L_S=230° is characterised by strong but shallow (below 4 km) easterly flow, which they describe as “anticylonic”. This suggests that the sublimation of the southern cap creates a high pressure system, with associated anticlockwise flow on its borders; an anticylonic system.

Tides

It is possible to decompose near-surface wind speeds into components relating to Mars' thermal tides. This allows further investigation of the specific dynamical features which are responsible for the modelled lifting features shown earlier. Fourier analysis was performed on the data to extract the relevant modes in (temporal) frequency (f) and (spatial) wavenumber (ν). This was done by performing Fourier decomposition for each latitude band in time, and across each latitude circle in space. The tidal modes investigated in this chapter are the diurnal (ν=1, f=-1 sol^{-1}) and semidiurnal (ν=2, f=-2 sol^{-1}) thermal tides. The negative frequencies reflect the fact that these are westward migrating modes ie. sun-synchronous. The data in the following plots in this section has all had an additional 10-sol rolling average applied.

The diurnal tide, shown in Fig. 5.12 has the greatest wind speed amplitude of all the modes examined, with amplitudes of up to $\sim$11 m/s. During the aphelion season, the most prominent features are the high amplitude bands (4-5 m/s) at 10° N and 45° S. The former corresponds approximately to the subsolar point, and the latter follows the edge of the southern seasonal cap. Interestingly, there seems to be a solsticial pause in the latter, analogous to the observed solsticial pause in baroclinic wave activity. Both of these features correspond well with modelled bands of enhanced dust lifting, as described above.

The structure in the perihelion season is more complex. There is an increase in diurnal tidal amplitude, up to $\sim$6 m/s, between 30° N and the northern seasonal cap edge which occurs between L_S=180-240° before experiencing a solsticial pause until L_S=300°, and resuming until L_S=30° of the following year. This feature corresponds well with modelled enhanced dust lifting at the northern cap edge, with maxima near the equinoxes and strongest at the L_S=180° equinox.

The second main notable feature is a long-lasting but latitudinally narrow band of enhanced tidal amplitudes, of up to $\sim$10 m/s, occurring between L_S=190-350° at the 30° S

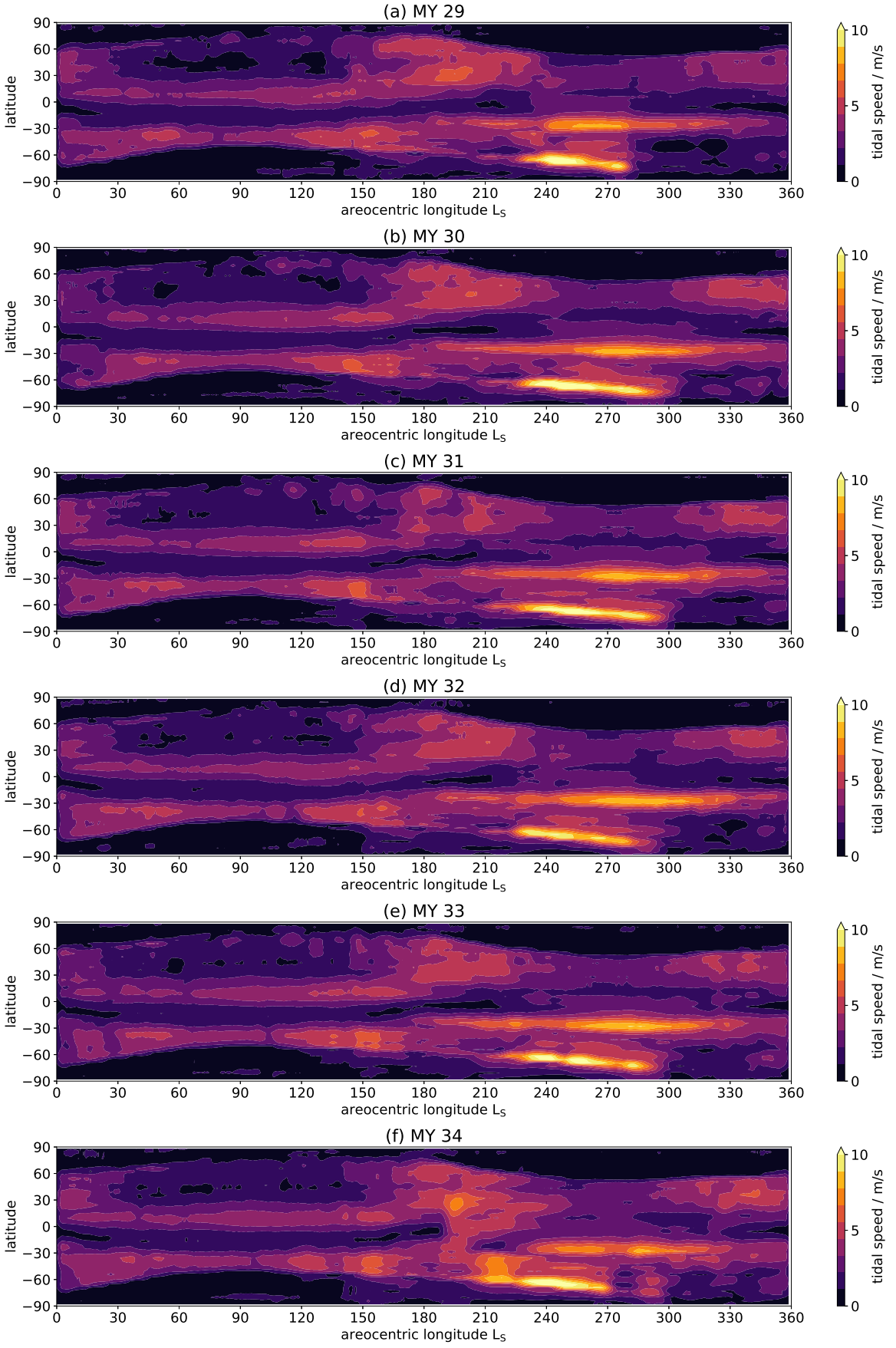

Fig. 5.12 Zonally averaged L_S-latitude maps of the diurnal tide components of near-surface wind speeds for MYs 29-34.

latitude band, and with a maximum around L_S=260-310°. This feature corresponds to a high-lifting feature at the same location, which appears as the tidal amplitude approaches its maximum at L_S=230° and disappears as the tidal amplitude diminishes at L_S=320°.

Lastly, there is a feature of very high amplitude (up to 11 m/s) diurnal tidal amplitudes which occurs at the southern seasonal cap edge around L_S=230-290°, with exceptions where there is a data gap at some point in this period (e.g. MY 29). This feature corresponds to the highest magnitude lifting feature, the southern high latitude jet, in the average martian year.

The semidiurnal tide, as expected, shows strong correlation with the diurnal tide, but with a decreased magnitude: the mean semidiurnal amplitude for MY 33, for example, is 40% that of the mean diurnal amplitude. As previous work has shown (e.g. Lewis and Barker, 2005), the semidiurnal tide has a particularly close relationship to dust loading in the atmosphere, showing stronger correlation in amplitude than the diurnal tide. For example, the semidurnal tide magnitude at L_S=240° is evidently stronger in MY 32, a dustier year, than in MY 30, a relatively clear year. However, this correlation is not as evident in Fig. 5.13 as it would be in a plot of tidal amplitude in, for example, surface pressure. This is because the large-scale surface wind speed features being examined here are largely tied to specific jet features in a way that surface pressures are not.

The semidiurnal structure follows the diurnal structure quite closely, with some exceptions. During the aphelion season, the only notable feature is the high amplitude band of $\sim$3 m/s around the edge of the southern seasonal cap at southern winter; there is no high amplitude band at 10° N as there is in the diurnal tide mode. Another difference is the apparent lack of solsticial minimum; the semidiurnal amplitude remains consistent through southern winter solstice.

Significantly, the very high wind speeds over the cap itself, as seen in Fig. 5.9, have no response either in the diurnal or semidiurnal tidal modes. These high wind speeds occur in

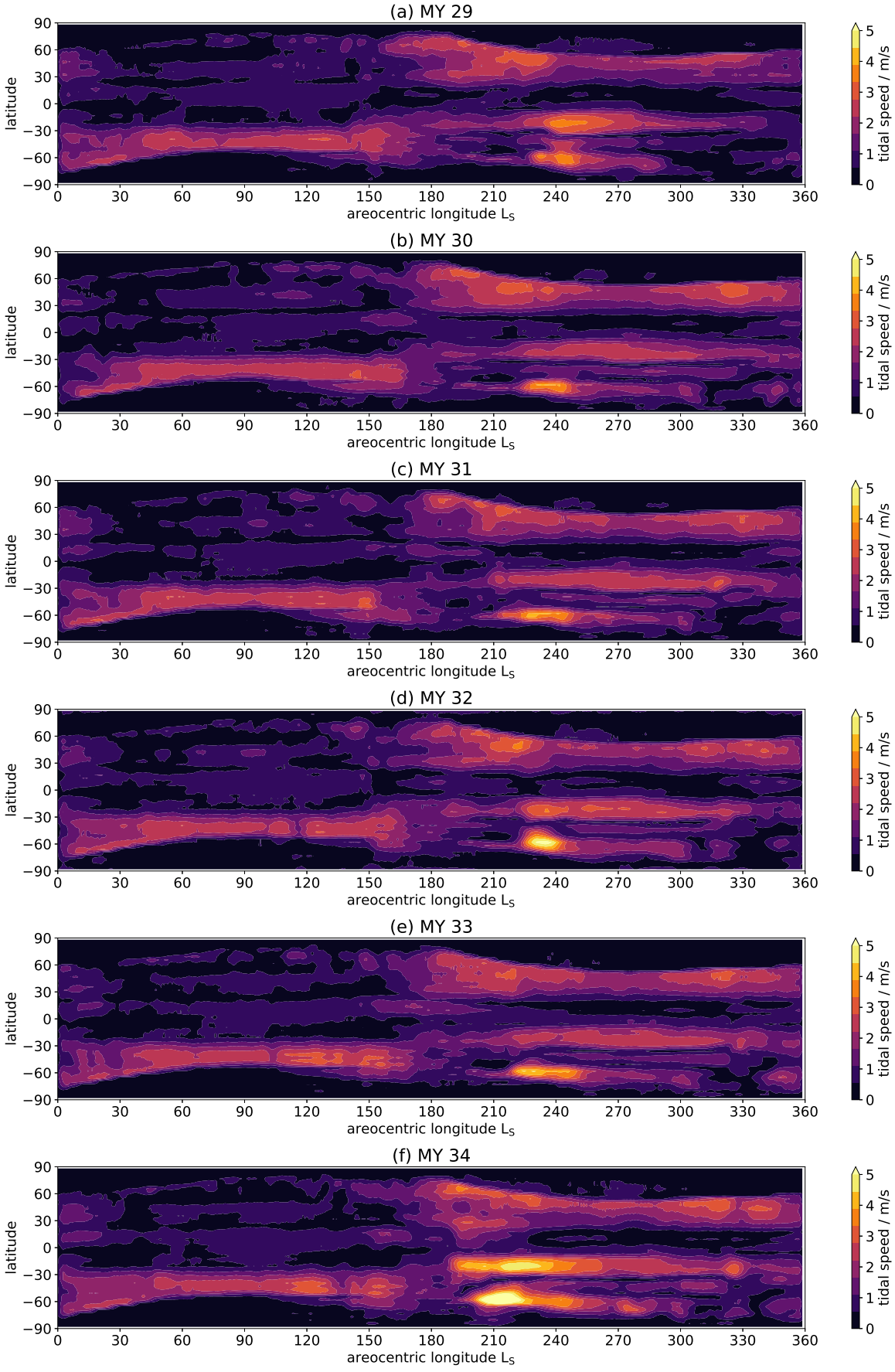

Fig. 5.13 Zonally averaged L_S-latitude maps of the semidiurnal tide components of near-surface wind speeds for MYs 29-34.

the polar night: solar heating is at a minimum anyway due to Mars' distance from the Sun, and southern winter means that little insolation reaches the southern polar cap.

The perihelion structure, again, follows that of the diurnal tide closely, with some subtle differences. The semidiurnal tide shows, in general, a narrower response than the diurnal tide; both spatially and temporally. For example, the semidiurnal tidal amplitudes, of $\sim$2-3.5 m/s, at the northern cap edge are more closely confined to within $\sim$20-30 degrees of the cap edge (but do also show a solsticial minimum); there is a sharper distinction between the high amplitude bands, of amplitude $\sim$3-3.5 m/s, at 30° S and by the southern seasonal cap edge, of amplitudes $\sim$2-5 m/s; and the southern cap edge semidiurnal amplitudes display a definite and short-lived maximum of $\geq$5 m/s at around L_S=220-250° while diurnal tide amplitudes remain consistently elevated throughout L_S=230-290°.

Both the diurnal and semidiurnal tidal amplitudes bear a striking resemblance to the lifting plots in Fig. 5.3: there is a strong correlation between the tidal amplitude maxima and the lifted mass maxima. This is particularly the case for the diurnal tide, as it shows the band of lifting at 10° N and captures the solsticial pause in lifting by the southern cap edge, both during the aphelion season. However, the semidiurnal tide better represents some of the gaps in lifting: for example, the temporal gaps before L_S=240° and after L_S=240° at the 30° S band, and the spatial gap between the 30° S band and the southern cap edge lifting during the perihelion season. Crucially though, both mask the high wind speeds over the seasonal caps, which cannot themselves contribute to significant dust lifting.

This correspondence raises the intriguing possibility of using near-surface wind speed tidal response as a rough proxy for dust lifting flux, something which is difficult to parametrize and incorporate into MGCMs. Developing such a scheme is well beyond the scope of this thesis, but some initial considerations are as follows. Using a simple linear relationship between tidal amplitude and lifting flux would overestimate southern cap edge lifting during the aphelion season and underestimate northern cap edge lifting during perihelion season, as

it would not account for the role of eddy lifting (which is greater at the latter) and does not account for near-surface atmospheric density, which is a factor in dust lifting. Some manner of convolution between the tidal amplitudes and the surface pressure and/or near-surface temperature (or density) tidal amplitudes could be able to incorporate this dependence.

The possible advantage of using this proxy method would be in the context of observational data or assimilation. Future orbital instruments able to measure wind speed would likely not be able to measure down to the surface itself. By performing tidal analysis of these wind fields, however, a crude diagnosis of dust lifting could still be made (given certain assumptions about the vertical wind structure). In a modelling context, if the tidal modes can be well constrained from temperature observations, they could be convolved with a non-assimilated near-surface wind field to obtain an idea of where lifting is occurring. The link between "actual" lifting and this proxy could be further investigated with NASA's Insight lander, which through its pressure sensors can obtain tidal modes in wind speed and compare to its own observations of dust lifting nearby.

Eddies

To analyse eddy contributions to the near-surface wind speeds, wind speeds were filtered to remove both climatological components, with a period of $\geq$15 sols, and tidal/diurnal variations, with a period of 1.3 sols or less. Elliptical bandpass filtering was applied to the initial time series of wind speeds, following Lewis et al. (2016) and Greybush et al. (2019). Here the same filtering process described by Greybush et al. (2019) was used, briefly summarised below.

The equation for the gain of an nth order lowpass elliptical filter is

$$G_n(\omega) = \frac{1}{\sqrt{1+\varepsilon^2 R_n^2(\xi, \omega/\omega_0)}} \tag{5.6}$$

where R_n represents the nth-order elliptic rational function, ω_0 is the desired cutoff frequency, ε is the ripple factor, and ξ is the selectivity factor. These latter two variables control the degree of "ripple", or perturbation, in the filtered frequencies.

A fourth order elliptical lowpass filter was first applied to identify the climatological (low frequency) components, and then removed from the initial time series. This new time series then had a sixth order elliptical lowpass filter applied to remove the tidal/diurnal (high frequency) components. The filters were performed using the openly available Python package SciPy and its signal processing library, `scipy.signal`. For more details on the exact values passed to the relevant filtering functions, see Greybush et al. (2019).

The mean eddy amplitude in near-surface wind speed for MY 33 was 1.1 m/s, only 45% that of the diurnal tidal amplitude for the same year. However, the amplitudes plotted are averaged over all eddies with period 1.3 to 15 sols, and so this relatively low value compared to the diurnal tide amplitudes does not preclude individual eddy wavenumbers having larger amplitudes.

The aphelion season shows a number of eddy features. Around the northern seasonal cap, there is the remnant of eddy activity from the more active perihelion season, which follows the cap edge and declines from a maximum of $\sim$3 m/s to background by L_S=45°, though with sporadic pockets of activity in around half the years (MYs 29, 32, and 33) lasting beyond L_S=60°. This ongoing eddy lifting activity may be responsible for a recent observed regional-scale dust event in early MY 35, as shown in Fig. 5.15; large dust events like this are rare at this time of year but clearly not impossible, and the event's location in the northern hemisphere suggests a northern cap edge origin.

There is also eddy activity in the southern hemisphere, at the southern seasonal cap; the activity actually occurring off the cap itself is of lower intensity than that in the north, with values of $\sim$2 m/s at most. This activity shows a strong solsticial pause, lasting from around L_S=45-135°, and being reduced entirely to the background level between L_S=75-

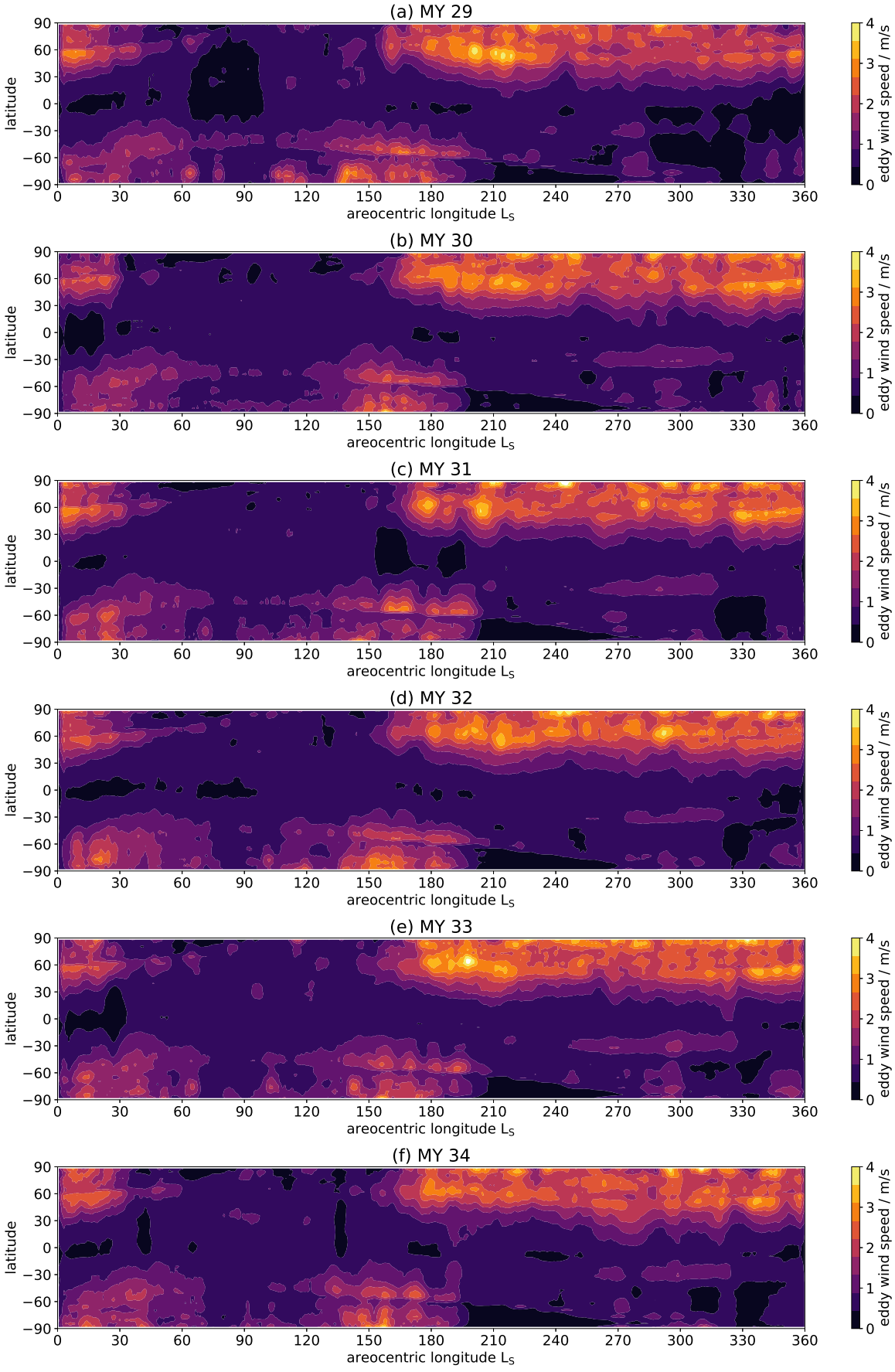

Fig. 5.14 Zonally averaged L_S-latitude maps of the eddy components of near-surface wind speeds for MYs 29-34.

120°, with only occasional pockets of activity in some years. From L_S=135°, eddy activity resumes stronger than before, attaining its southern hemisphere maximum with amplitudes consistently reaching 3 m/s between L_S=150-200°as the planet moves through equinox. Southern eddy activity effectively ceases after L_S=200°.

The perihelion season shows significantly more intense activity, almost all of it at northern mid-high latitudes by the seasonal cap edge. Intense eddy activity, reaching and surpassing amplitudes of 4 m/s, lasts from approximately L_S=165° to L_S=45° of the following martian year. Maxima in activity occur on either side of the solsticial pause, with the highest cap edge amplitudes consistently occurring at around L_S=180-225° and L_S=315-360°. The solsticial pause in the north is less well-defined than its southern equivalent, but still visible by eye. It has been noted previously that the solsticial pause in reanalyses using MCS data is less well-defined than in those using TES data, likely due to MCS' higher cutoff altitude for temperature profiles (Greybush et al., 2019). The pause extends from approximately L_S=240-300° each year, and results in a cap edge eddy amplitude drop from $\sim$3 m/s to $\sim$1.5-2 m/s.

5.3.2 Deposition

Calculation of deposition

The work presented in this chapter is concerned with broad lifting and deposition patterns, both spatial and temporal, rather than in trying to establish absolute values for lifting and deposition. This is because the large remaining uncertainties in the exact details of martian dust lifting and the coarseness of the MGCM grid make such attempts likely highly subject to MGCM resolution, exact values of free parameters used (such as the ratio of impact threshold to fluid threshold), and particle size distribution. This work aims to characterise areas and seasons of relatively higher or lower lifting and deposition, and net sinks and sources of dust.

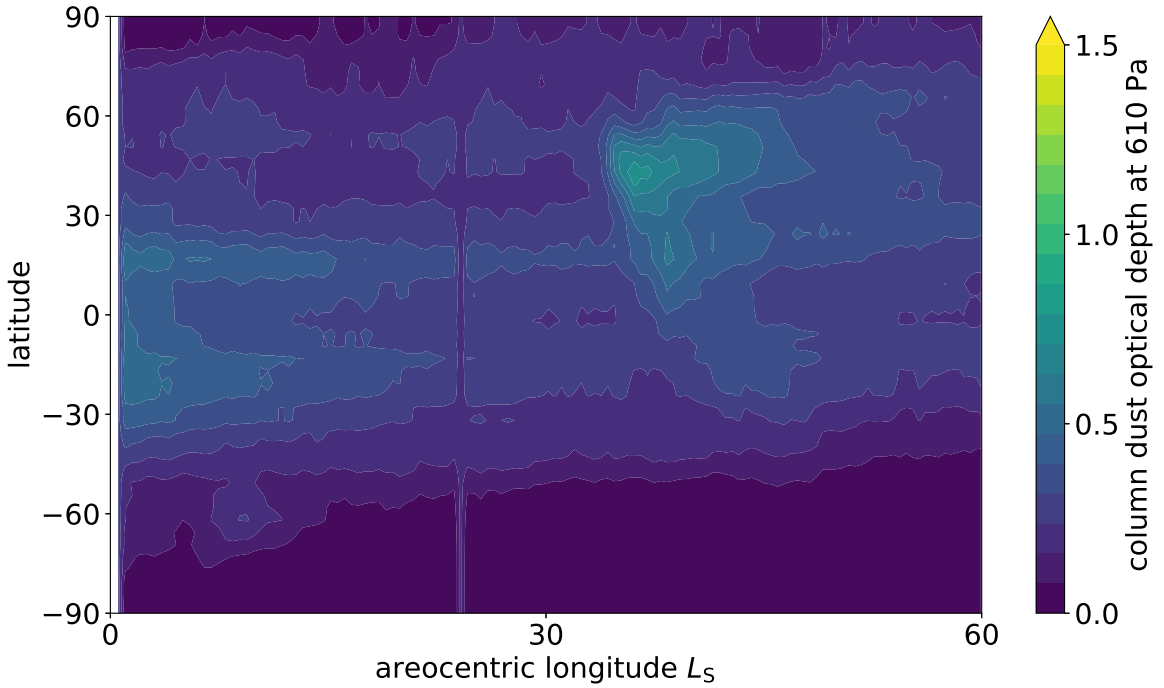

Fig. 5.15 Zonally averaged L_S-latitude map of column dust optical depth (CDOD) for MY 35.

In order to provide a reasonable basis of comparison for lifting and deposition mass fluxes, a key assumption is made: closure of the martian dust cycle on an annual basis. This proposes that the total mass of dust lifted during a martian orbital cycle is the same as the total mass of dust deposited. Note that this assumption is agnostic regarding where the dust goes on the planet; it only states that the entire lifted mass over the whole planet is equal to the entire deposited mass over the whole planet, and thus allows for net transport between different locations.

To calculate deposition and net changes, a scaling factor was therefore applied to deposition rates. This scaling factor was calculating for each year using the formula

$$SF = M_L/M_D \tag{5.7}$$

where SF is the scaling factor, M_L is the total lifted mass, and M_D is the total deposited mass, all either for a specific martian year or a mean of MY 29-33. The displayed deposition rates on the following plots are all pre-multiplied by SF.

The deposition variable used in the MGCM was `dqsdust`. This is a model-specific deposition rate, but scaled according to the `tauscaling` variable, which relates the calculated CDOD at each atmospheric column from the MGCM variables to the CDOD as provided from the assimilation scheme (see Chapter 3 for more details). In short, this scaling factor means that the `dqsdust` variable provides a sedimentation rate based on observed CDOD from MCS. This scaling based on observations (via the assimilation scheme) dominates over the effects of transport by the MGCM itself. The value of this variable is that it allows insight into how dust deposition might really be occurring on Mars' surface, based on derived MCS CDOD.

This section shows dust deposition (`dqsdust`) flux results for the mean of MY 29-33, dispayed in increments of 30° L_S in Fig. 5.16. Dust deposition is represented as average deposited mass flux per unit area per sol during the relevant period.

The deposition rate was in general lower during the aphelion season than during the perihelion season. The L_S=0-30° period shows a greater extent of deposition in the southern hemisphere, up to 85° but with a small band of more intense deposition at around 30° S; with minima poleward of 60 ° N and 80° S and between 15° S-30° N. Overall, the lowest non-polar deposition occurred over Tharsis, Elysium Mons, and the low thermal inertia region around Arabia Terra/Terra Sabaea (15° S-15° N, 0-50° E). There is relatively high deposition over Xanthe/Margaritifer Terra, anti-correlating with near-surface wind speeds (Fig. 5.8.a). The L_S=30-60° period shows a shift towards greater deposition in the northern hemisphere, particularly between 40-60° N (the northern lowlands); and a smaller-magnitude band of deposition at around 30° S; with minima poleward of 6 ° N and 45° S and between 0-30° S. There is little deposition in the southern hemisphere.

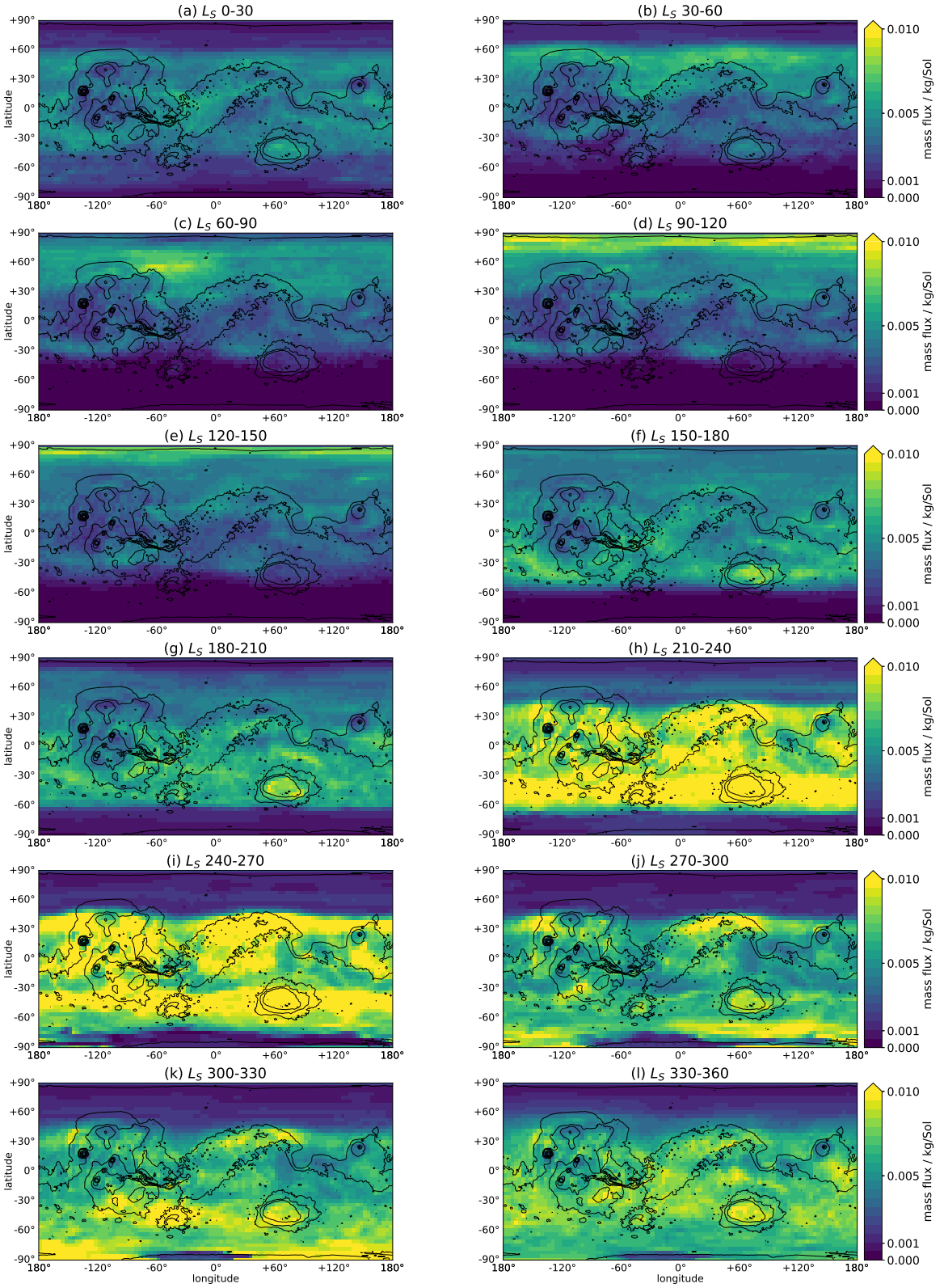

Fig. 5.16 Maps of dust deposition for the mean of MY 29-33 over 12 periods of 30° L_S.

The planet approaches northern summer solstice and moves through perihelion during L_S=60-90°, and the effect can be seen in the increased northern hemisphere dust deposition. Deposition is largely concentrated between 30-90° N, but with a weaker band at 30° S. There is then a deposition gap between 20° S-30° N, with minima over western Tharsis and Amazonia, and over the low thermal inertia region bordering Arabia Terra/Terra Sabaea. These regions tend to have higher near-surface wind speeds at this time of year, as can be seen in Fig. 5.8.c; largely driven by the returning Hadley cell flow. The maximum in deposition is located in Acidalia Planitia. There is no lifting predicted from the slopes of Tempe Terra (Fig. 5.2.c, but this does not preclude lifting at any scale smaller than the MGCM grid, which may be especially important for the smaller storms indicated by Fig. 5.16.c.

Northern summer is reached in the L_S=90-120° period. The pattern of deposition remains similar to the previous period, with significant interannual variability between 45-90° N reflecting the presence of local-scale dust storms. High deposition occurs all the way to the summer pole, likely due to the total destruction of the northern westerlies as northern summer reaches its apex (Fig. 5.8.d). This solsticial pattern is maintained in L_S=120-150°, but with the addition of greater interannual variability at northern mid-latitudes, such as in MY 29, indicating mid-latitude dust storm activity (compare with Fig. 5.17).

As the planet moves towards equinox at L_S=150-180°, northern high-latitude deposition decreases again. As a whole, the deposition maximum shifts towards the southern hemisphere, specifically between 30-60° S. This is a manifestation of enhanced southern cap edge storm activity across all years (Fig. 5.17); with particularly intense southern storms in MY 30 and MY 33. Deposition is greatest around Valles Marineris and Elysium Planitia; regions of notably low near-surface wind speeds (Fig. 5.8.f). The L_S=180-210° period is broadly similar to the preceding one. The majority of deposition occurs between 30-60° S, with deposition minima as usual over Tharsis and Arabia Terra/Terra Sabaea.

The spatial pattern of deposition changes at L_S=210-240°, intensifying dramatically. This is because this period captures the "A"-type regional storms for each year, as seen in Fig. 5.17; the high CDODs of these events have a large positive impact on deposition rates. For 4 of the 5 non-GDS cases (MYs 30-33), the bulk of dust deposition appears to occur at southern mid-latitudes, between 30-60° S: between the powerful cap edge winds and the subtropical jet (Fig. 5.8.h). Likewise, comparison with Fig. 5.8.h shows that deposition elsewhere, such as at the southern tropics between 20° W-60° E in MY 32, occurs at greater rates where wind speeds are relatively low. There is also an apparent preference for dust to deposit in latitidunal bands at mid-high latitudes, likely due to the influence of the mean meridional circulation (which carries dust) and mid-high latitude jets (which curtail its further transport).

The L_S=240-270° period also includes intense "A"-type regional storm activity. The stronger near-surface winds of this period, as Mars moves through perihelion and towards southern summer solstice, result in more stratified bands of deposition. Comparison with the wind speed maps in Fig. 5.8.i shows that deposition, particularly in the southern hemisphere, is strongly anti-correlated with wind speeds, suggesting that deposition is (like lifting) largely controlled by near-surface wind speeds. In the southern hemisphere, deposition preferentially occurs between the two bands of high wind speeds corresponding to the cap edge jet and the subtropical jet; this leads to preferential deposition along the latitude band $\sim$45° S, and particularly within Hellas and Argyre craters and at Terra Cimmeria. In the northern hemisphere there is no corresponding subtropical jet (as the cross-equtorial Hadley cell has its upwelling branch in the southern hemisphere), making deposition less stratified by latitude. However, high wind speeds over Hesperia Planum, Tyrrhena Terra, Isidis Planitia, Elysium Mons, Alba Patera, and to a lesser extent the Tharsis plateau, result in relatively low deposition over these regions. Instead, deposition preferentially occurs over northern Arabia Terra/Terra Sabaea, southern Arcadia Planitia, southern Utopia Planitia, Elysium Planitia, and parts of Tharsis. There is a well-defined deposition boundary at 45° N, poleward of

which almost no deposition occurs; however, this is south of the northern polar jet, which is therefore likely not responsible. Examining the surface meridional winds at this season in Fig. 5.10 shows that the 45° N band lies in between bands of northward winds to the north and southward winds to the south; this suggests that dust sedimenting in this region (from the downwelling branch of the Hadley cell) tends to be either transported south, to the "main" deposition regions of the northern mid-latitudes, or less frequently north, to form the faint deposition band visible at ∼70° N.

L_S=270-300° is the season of the "B"-type regional storm, which occurs by the southern seasonal cap edge. This and the recession of the southern seasonal cap lead to markedly increased deposition at southern high latitudes, between 70-90° S. The longitudinal structure of this deposition anti-correlates reasonably with locations of highest wind speeds (Fig. 5.8.j). Elsewhere on the planet, the structure of deposition is similar to that in the previous period, albeit with lower intensity due to the lack of "A"-type storm. By L_S=300-330°, Mars is moving away from southern summer solstice and there is a corresponding global decrease in near-surface wind speeds. As seen in Fig. 5.9.k large-scale near-surface wind structures are broadly interannually similar, with a band of high wind speeds corresponding to the subtropical jet at 30° S. Little deposition occurs in this band or over Tyrrhena Terra, Syrtis Major, Hesperia Planum, Elysium Mons, or Alba Patera, all high wind speed regions. Where deposition does occur, though, is more governed by the structure of the specific storms, resulting in a high degree of interannual variability in deposition in this period. Deposition is mainly concentrated in the southern hemisphere; Argyre Planitia is a consistent location of high deposition rates.

Finally, L_S=330-360° shows reasonably high deposition in the southern hemisphere, due to the frequent presence of "C"-type storms. The subtropical jet at 30° S has largely disappeared save for a remnant stretching from Terra Sabaea to Hesperia Planum along the northern boundary of Hellas, allowing deposition to occur more freely at all latitudes. Again,

the locations of highest deposition were therefore governed more by the structure of the dominant regional storm than by the large-scale winds.

Zonally averaged deposition and interannual similarity/variability

Fig. 5.18 complements the spatial deposition plots presented previously in Section 5.3.1 by allowing more detailed temporal examination of dust deposition in MYs 29-34, at the expense of some spatial detail. The clear seasonal dependence of dust deposition magnitude and extent is apparent, as well as the interannual variability due to storm structure.

The deposition rate, shown in Fig. 5.18, shows significant interannual variability, even in the aphelion season. This variability is primarily at the edge of the northern seasonal cap, indicating high cap-edge storm activity. Despite the variation in individual events, the "peak" of this activity appears to occur regularly at around L_S=90° of each year ("peak" meaning greatest temporal and spatial extent of >0.01 kg/sol per unit area deposition rates). The southern extent of this activity gradually moves from 30° N to 60° N throughout the aphelion season, following the retreat of the northern seasonal cap. South of this, deposition shows less interannual variability and a more defined structure, occurring at bands of 20-30° N and 15-30 ° S with a deposition minimum in between. As pointed out previously in Section 5.3.1, this can be explained in terms of near-surface wind speeds being higher at the equator and northern tropics, as can be seen in Fig. 5.9. Towards the end of the aphelion season, between L_S=150-180°, there is a large but interannually-variable intensification in deposition, usually limited to the southern hemisphere and in particular the seasonal cap edge (MY 29 being an exception). Again, this variability is likely due to storm activity during this season; mostly cap-edge storms (as seen in MY 29, 31, and 33) but also occasional larger events (e.g. MY 29).

The perihelion season shows even greater interannual variability, and dramatically high deposition rates. The deposition rates are almost entirely controlled by the intensity and

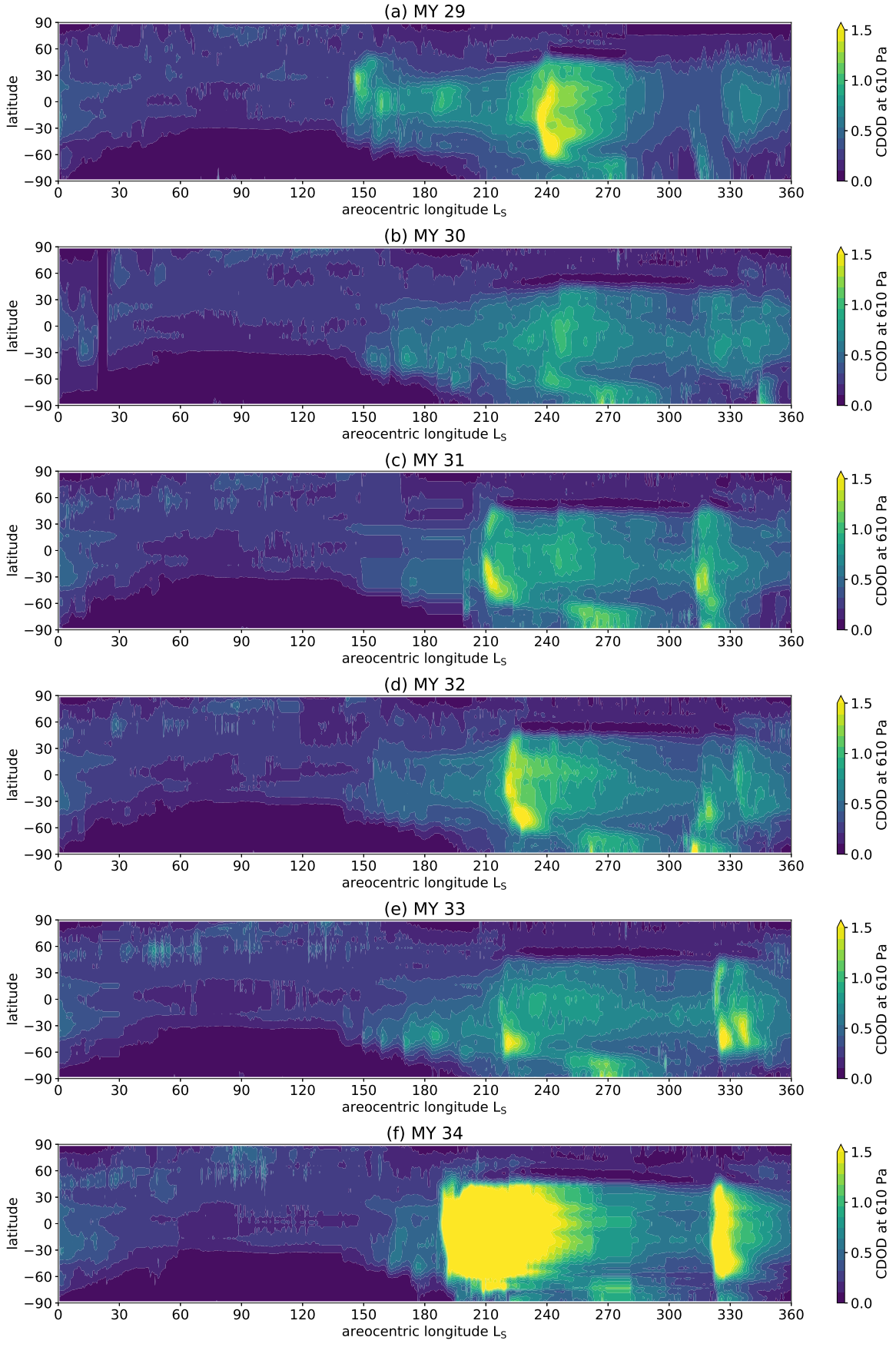

Fig. 5.17 Zonally averaged L_S-latitude maps of column dust optical depth (CDOD) at 610 Pa for MYs 29-34.

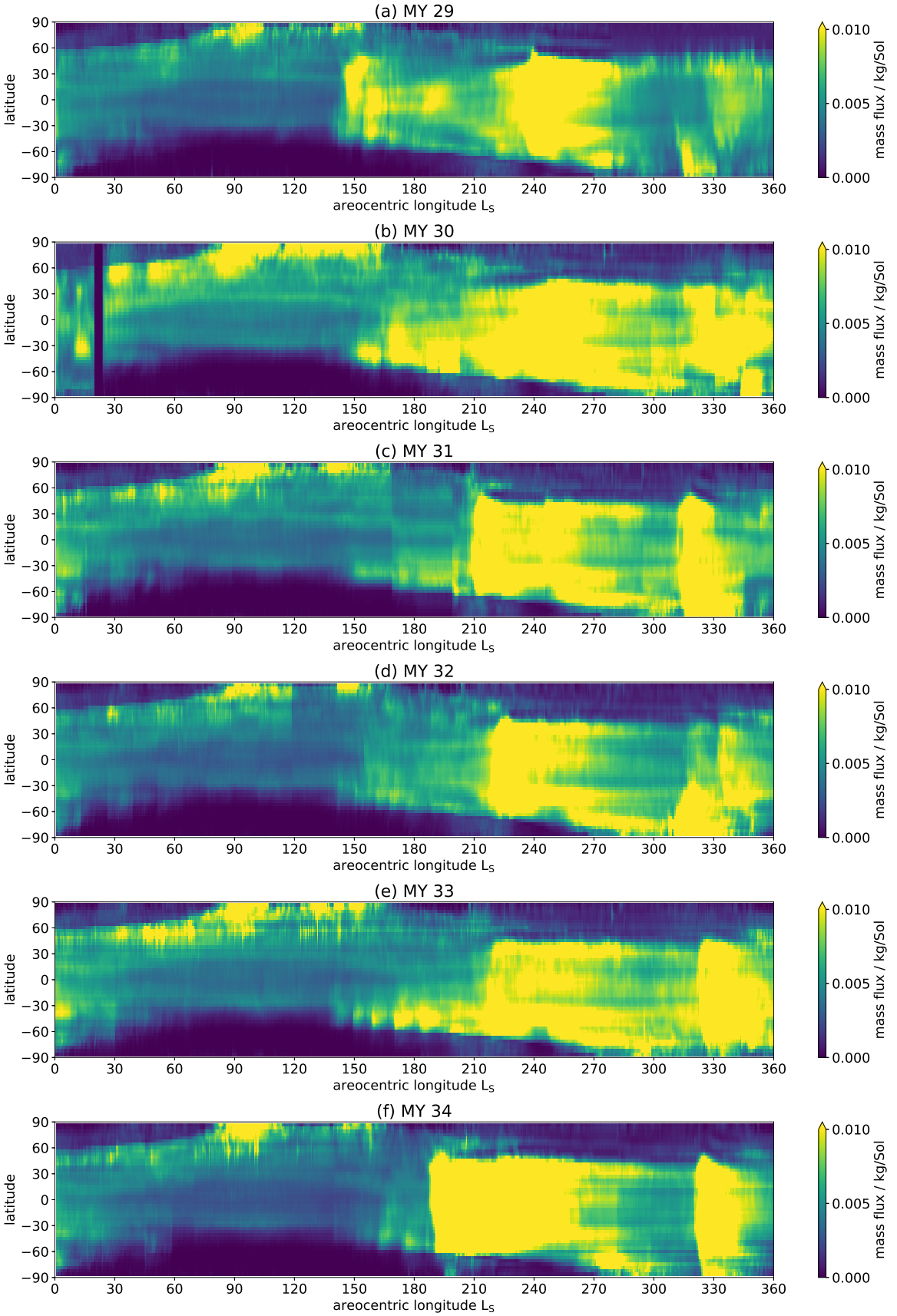

Fig. 5.18 Zonally averaged L_S-latitude maps of dust deposition for MYs 29-34.

spatiotemporal structure of the large storms which occur throughout this season, visible in CDOD space in Fig. 5.17. Therefore there is typically first high deposition at both northern and southern tropics to mid-latitudes from the "A"-type storm. This is followed by a period of relatively clear tropics to mid-latitudes but high deposition at high southern latitudes from the "B"-type storm. Finally, the "C"-type storm resembles the "A"-type storm in spatial structure but shows greater temporal variability. However, while the dust storm structure has the greatest effect on deposition rates, near-surface wind speeds do also have an impact. This is visible when examining the after-effects of the "A"-type storms; the 30° S latitude band remains clearer than other latitudes, due to the presence of the subtropical jet.

5.3.3 Sources and sinks

Calculation of sources and sinks

In order to ensure consistency between lifted and deposited masses, the globally and annually integrated values of each each were calculated and the deposited masses were scaled to match the lifted masses. This relies on the assumption that the martian dust cycle is closed over any given martian year; that is to say, as much dust mass is lifted as is deposited over the course of a year. This technique allows for characterisation of net sources and sinks throughout the year as it is agnostic as to where the dust is lifted or deposited; it simply assumes that the yearly net dust flux for the entire planet is 0.

Sources and sinks are calculated by treating lifting as a positive mass flux and deposition as a negative mass flux and adding the two mass flux fields. Therefore, areas of positive mass flux over a given period are sources over that period; areas of negative mass flux over a given period are sinks over that period.

Mean spatial sources and sinks

This section discusses net dust sources and sinks for the aphelion season for the mean of MY 29-33, dispayed in increments of 30° L_S. in Fig. 5.19. Net dust mass flux is represented as average mass flux per unit area per sol during the relevant period.

L_S=0-30° sees limited net lifting. Alba Patera is a consistent source, as are parts of western Tharsis, southern Noachis Terra (by the seasonal cap), and northern Utopia Planitia. This pattern changes radically in L_S=30-60°; western Tharsis remains a source but the sources in the northern plains (with the exception of MY 30) and at Alba Patera disappear. Instead, sources appear in the southern (winter) hemisphere: the southern slopes of the Thaumasia Highlands, the southwestern edges of Argyre Planitia and Hellas Planitia, and Noachis Terra just west of Hellas. This pattern roughly holds for L_S=60-90°. Sources remain in western Hellas and net lifting on the western slopes of Alba Patera increases, while southern cap-edge lifting at Thaumasia, Argyre, Noachis, and Hellas shows a decline likely attributable to the solsticial pause. L_S=90-120° is very similar to the previous period, but with reduced net lifting at Argyre, Hellas, and Noachis. L_S=120-150° sees renewed southern cap edge lifting, with sources at the southern slopes of Thaumasia, the southwestern edges of Argyre and Hellas, in Noachis just west of Hellas, and a new source in Noachis just east of Argyre. This renewed southern net lifting almost disappears again as the planet approaches equinox in L_S=150-180°, with the exception of some net lifting by Hellas and Argyre. Alba Patera disappears as a source, but some sources are evident in western Tharsis, in particular around Olympus Mons. Throughout this period, there is less net deposition at southern high latitudes, over Tharsis, over Terra Sabaea, and over Xanthe/Margaritifer Terra than there is elsewhere.

L_S=180-210° sees extensive net lifting in the northern hemisphere, in particular over the northern lowlands: Acidalia Planitia, Utopia Planitia, and Arcadia Planitia. This net lifting extends for most years across the entire latitude circle of ∼50-70° N, but with especially high intensity over Acidalia Planitia. There are also consistent lifting sources over Alba

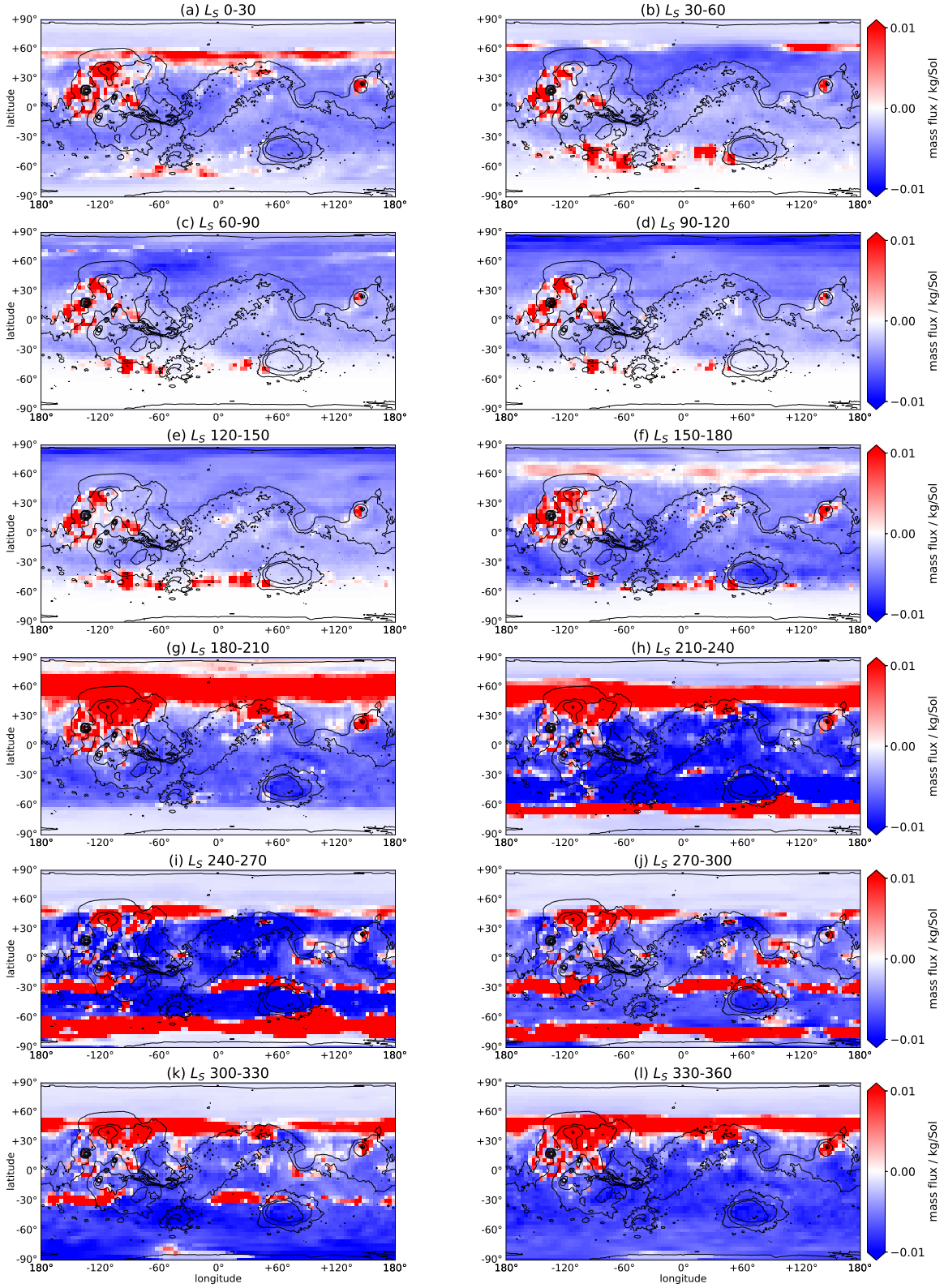

Fig. 5.19 Maps of net dust mass flux for the mean of MY 29-33 over 12 periods of 30° L_S.

Patera, Tempe Terra, Quenisset and Elysium Mons. The northern cap edge net lifting remains intense but narrows in latitude and shifts equatorward during L_S=210-240°, as the seasonal cap grows. Alba Patera remains a dust source, as does Elysium Mons, but not Quenisset. A narrow but intense band of net lifting emerges by the southern seasonal cap at ∼60-65° S, particularly intense on the southern edges of the Hellas and Argyre craters. This southern cap edge net lifting expands and intensifies in L_S=240-270°, dominating the latitude band 60-75° S. New dust sources arise along the 30° S latitude band, corresponding to the location of the subtropical jet: at northern Terra Sirenum/Daedalia Planum, northern Noachis Terra, the northern slopes of Hellas Planitia, and to a lesser extent over Terra Cimmeria. In the north, sources remain at Alba Patera, the northern slopes of Tempe Terra, western Acidalia Planitia, and Elysium Mons. In the L_S=270-300°, the southern subtropical net sources expand and intensify. Southern cap edge net lifting, by contrast, is reduced and no longer covers entire latitude circles. The most intense remaining cap edge lifting is located in the western hemisphere, around Aonia Terra. Northern net lifting retains a similar pattern to the previous period. MYs 30-33 also see a new dust source over Tyrrhena Terra, at the southwestern edge of Isidis Planitia. As Mars moves away from southern summer solstice and perihelion in L_S=300-330°, southern subtropical dust sources are diminished; some net lifting remains around northern Noachis Terra/southern Terra Sabaea. Southern cap edge net lifting disappears entirely. In the north, however, strong dust sources remain at Alba Patera, Acidalia Planitia, and Elysium Mons, and new net lifting emerges over Utopia Planitia/Arcadia Planitia, close to Elysium. Any remnant southern hemisphere sources disappear during L_S=330-360°. Net lifting is prevalent between 30-60° N, but apparent nowhere else. Dust sources are Alba Patera, Tempe Terra, Acidalia Planitia, Quenisset, Utopia Planitia, Arcadia Planitia, and Elysium Mons. Net deposition-wise, there is consistently (through the whole perihelion season) less net deposition over Chryse Planitia, Xanthe Terra, Margaritifer Terra, Tyrrhena

Terra, eastern Elysium Planitia/northern Hesperia Planum, and southern Utopia Planitia than there is over the rest of the (non-seasonal cap covered) planet.

Zonally averaged sources and sinks and interannual similarity/variability

Fig. 5.20 complements the spatial net mass flux plots presented previously by allowing more detailed temporal examination of net mass flux in MYs 29-34, at the expense of some spatial detail. The interannual similarities and variabilities are apparent.

The net mass flux plots (Fig. 5.20) show significant interannual variability. There is great net deposition at the northern pole for the deposition plot between L_S=90-160°, due to greater deposition at this time/region. There is also significant interannual variability in this deposition. The patchy nature of this deposition indicates the role of local dust storm activity. There is also an absence of any net deposition over the southern seasonal cap, *contra* the northern seasonal cap. This indicates a lack of transport of dust onto the southern seasonal cap at present day Mars.

The perihelion season shows notable interannual variability in net deposition due to the effects of the "A"-, "B"-, and "C"-type regional dust storms that occur during this season. Despite the reliable presence of these events, their actual durations, spatial structures, and CDOD display interannual variability. The footprints of the "A"- and "C"-type storms are visible, while that of the "B"-type southern cap edge events is obscured by the intense lifting that occurs at the same place and time. The "A"-type storm footprint is the most interannually similar, with a consistent enhanced net deposition between 30-60° S between approximately L_S=210-250°, and a lesser enhancement in net deposition between 30° S-30° N for a shorter duration; for approximately 20° L_S after the storm initiation. This pattern is particularly visible for MYs 30-33; MY 29 showed a different structure (with a later "A"-type event), as did MY 34 with the GDS. The "C"-type events show greater variation in intensity and spatial net deposition (MY 29 had a data gap during this period); MYs 30, 31, and 32 show

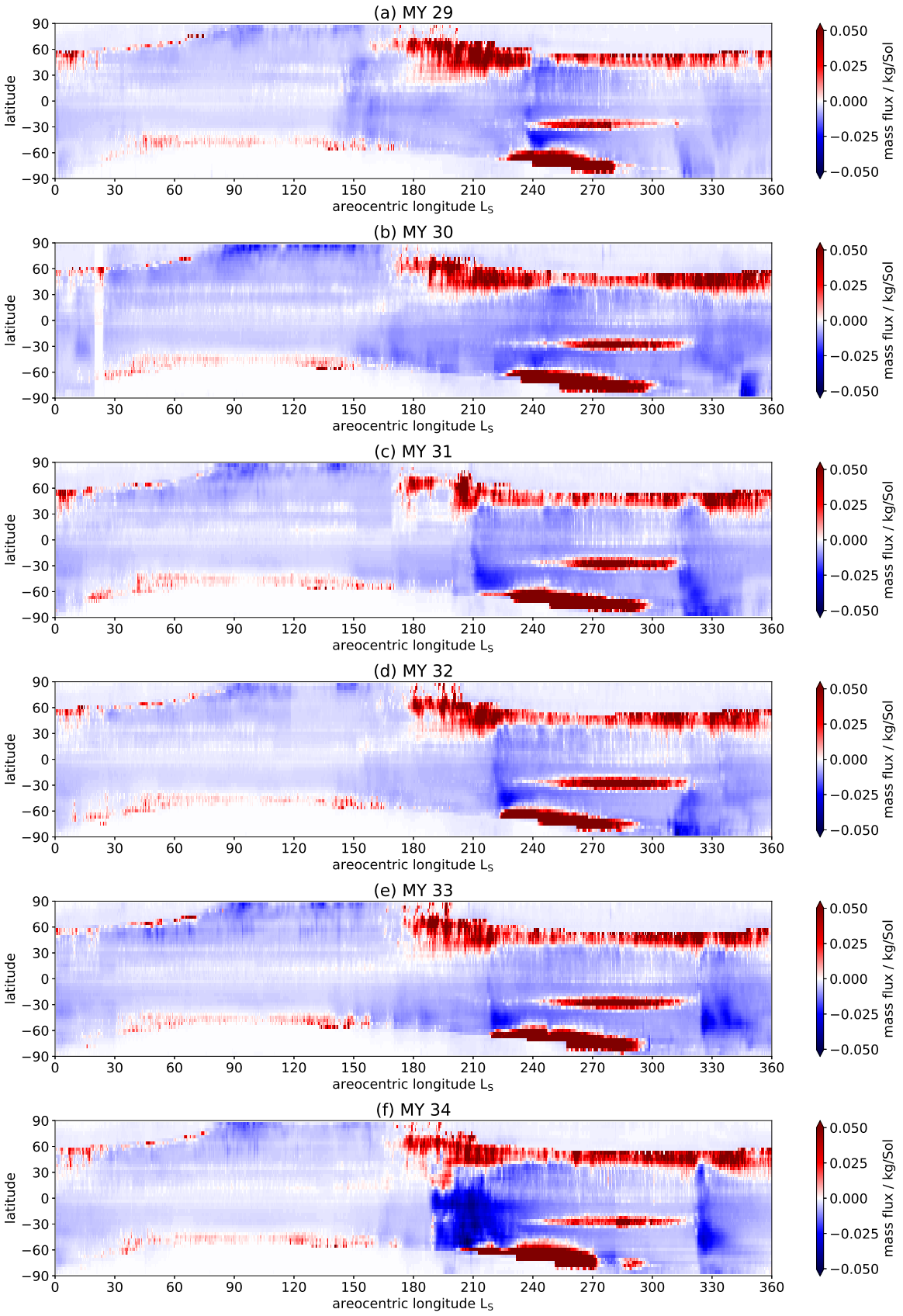

Fig. 5.20 Zonally averaged L_S-latitude maps of net mass flux for MYs 29-34. Positive (red) areas represent net dust sources; negative (blue) areas represent net dust sinks.

significant net deposition over the southern pole, while MYs 29, 33, and 34 do not. MYs 31-34 show significant net deposition over latitudes 30-60° S, while MYs 29 and 30 do not. MY 34 showed significant net deposition at northern mid-latitudes, while the other years do not. Temporally, the net deposition from "C"-type storms occurs some time between L_S=210-250°.

5.4 The MY 34 GDS

The 2018/MY 34 GDS, which started at around L_S=185° and had effectively decayed to a climatological CDOD by $L_S \sim$260°, had a significant impact on both lifting and deposition. Given the relative rarity of these events, the MY 34 GDS therefore provides an opportunity to examine how such events alter lifting and deposition relative to a "normal" martian year. For this purpose, MY 30 was chosen as a particularly clear/non-dusty year (see Fig. 5.17). Given the interannual similarity between non-GDS years, particularly in terms of large-scale atmospheric dynamics, MY 30 is taken to be reasonably representative of non-GDS years in terms of dust lifting patterns. Its relatively low CDOD compared to other years, meanwhile, makes it ideal for isolating the specific effects of the high dust loading of MY 34. All comparison terms used in the following section are therefore describing MY 34 relative to MY 30.

5.4.1 Lifting

Fig. 5.21 shows lifting for the initial stages of the GDS, and compares it to the same season for MY 30. There are two notable differences: a band of increased lifting at northern tropics/subtropics, and a band of decreased lifting at northern high latitudes: specifically over the northern lowlands. There is also some increased lifting in the southern hemisphere, around the northeast slopes of Hellas Planitia and eastern slopes of Argyre Planitia. The

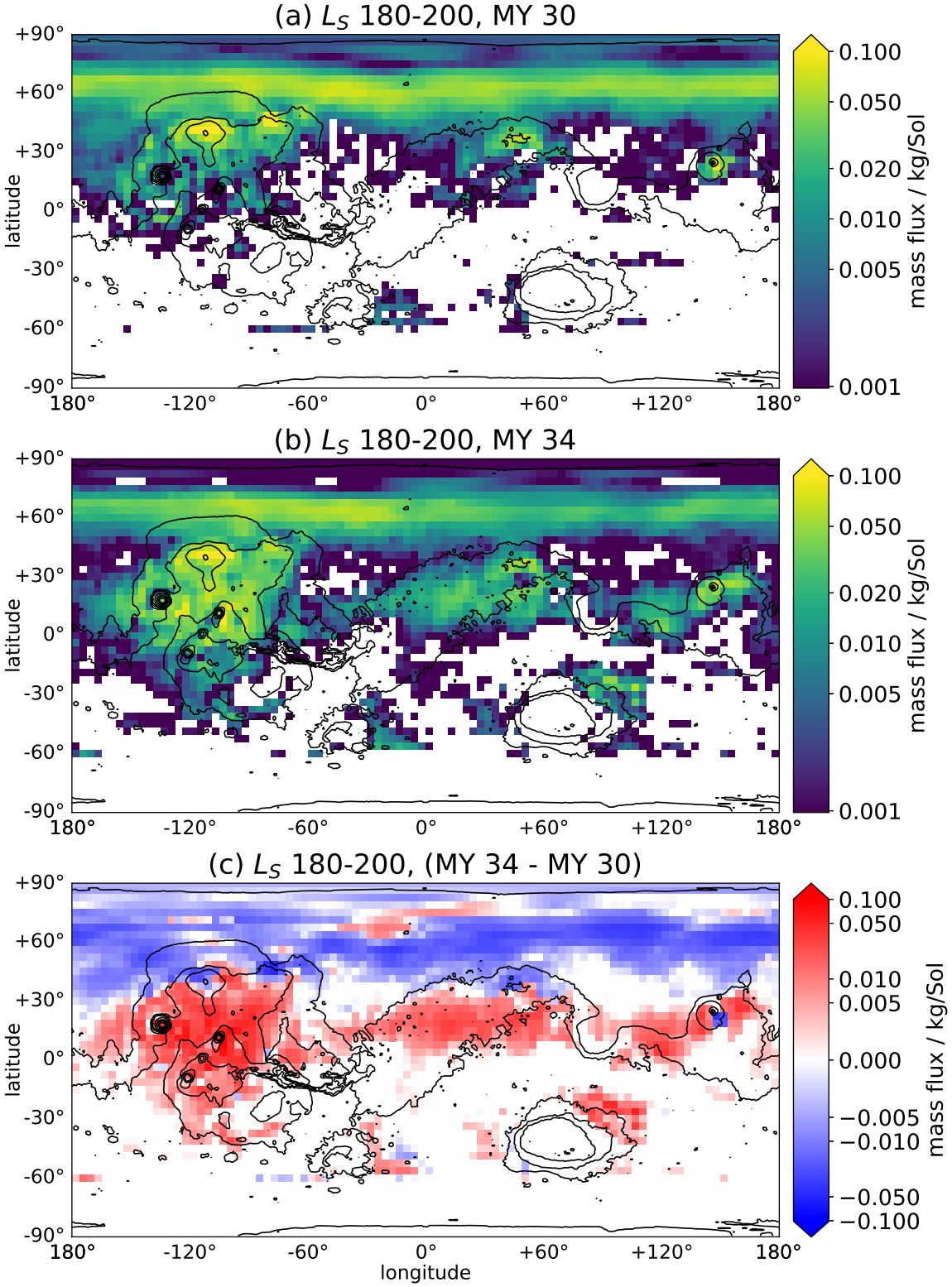

Fig. 5.21 Maps of dust mass lifting flux for the period L_S=180-210°, for MYs 30, 34, and the difference between the two. Note the non-linear scale.

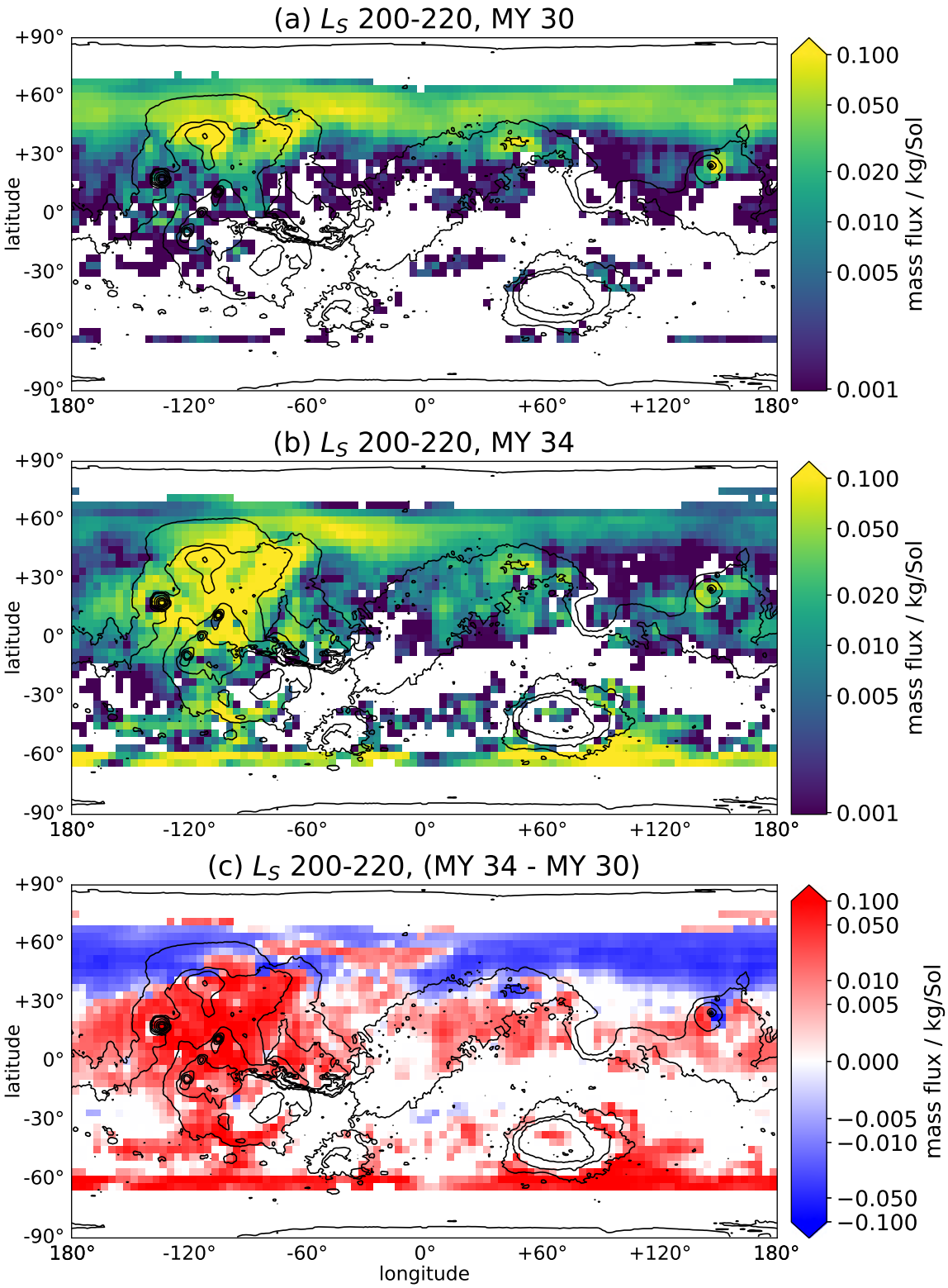

Fig. 5.22 Maps of dust mass lifting flux for the period L_S=200-220°, for MYs 30, 34, and the difference between the two. Note the non-linear scale.

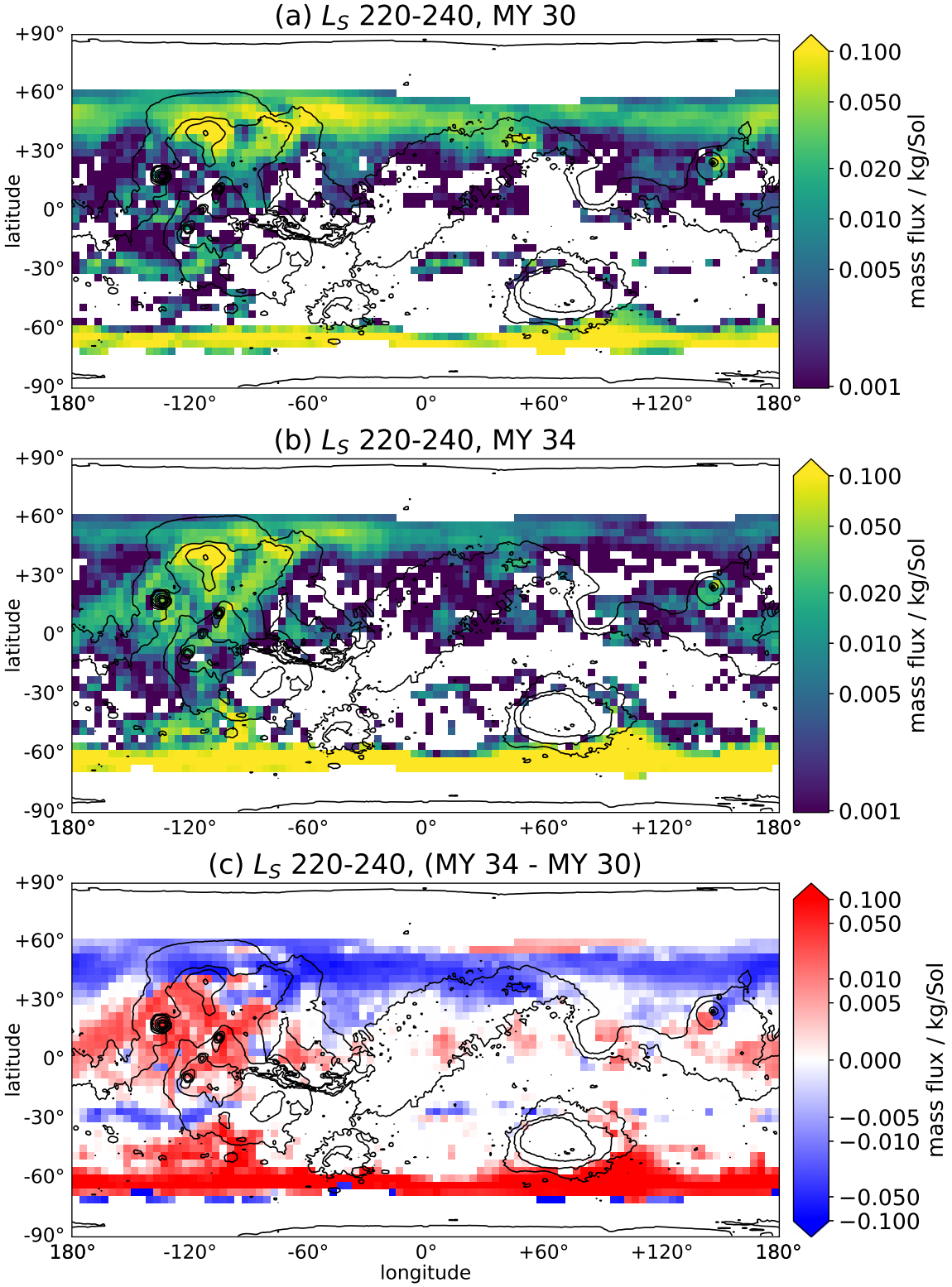

Fig. 5.23 Maps of dust mass lifting flux for the period L_S=220-240°, for MYs 30, 34, and the difference between the two. Note the non-linear scale.

increased lifting over the northern (sub)tropics is concentrated over the Tharsis Plateau, Arabia Terra/northern Terra Sabaea, Elysium Mons, and northern and eastern Elysium Planitia/southmost Utopia Planitia. These changes are linked to changes in the near-surface wind speed (not shown); increased wind speeds over the northern and southern subtropics, and reduced wind speeds over most of the northern lowlands.

Fig. 5.22 shows lifting for the most intense phase of the GDS; the GDS is at its maximum spatial extent, and average CDOD is at its greatest value. Northern lifting tendencies follow that of the initial stages of the GDS, but with greater lifting fluxes for MY 34. Lifting over the northern lowlands remains lower than in MY 30; however, the region of enhanced lifting over Acidalia Planitia has grown in both spatial extent (covering the entirety of Acidalia Planitia) and intensity. Increased lifting over Tharsis, Arabia Terra/Terra Sabaea, and Elysium Planitia attains even greater intensity. In the southern hemisphere, however, there is a notable difference in the structure of lifting from the previous period. MY 34 displays an intense band of lifting right by the seasonal cap edge, as well as lifting around Terra Sirenum, the Thaumasia Highlands, Noachis Terra, and the southern and eastern edges of Hellas Planitia. Again, this corresponds reasonably well with the differences in near-surface wind speeds, which can be seen in Fig. 5.24. However, there are a few differences between the two maps, specifically at southern mid-high latitudes. For example, despite the fact that Fig. 5.24 shows wind speed increases across the whole 30-60° S latitude band, there is not a corresponding increase in lifting everywhere, as the increased wind speeds are not necessarily high enough to reach the lifting threshold. Additionally, it is instructive also to compare the structure of the southern 30-60° S wind speeds with the surface roughness map in Fig. 5.1; the greatest wind speeds, wind speed increases, and lifting increases correlate with smaller roughness lengths; ie. “smoother” terrain. The surface roughness at the surface therefore has a large impact on lifting, and in particular on the longitudinal structure of where lifting occurs.

Throughout these two phases, there are also marked differences in the characteristics of the near-surface wind speeds. There is a boost in diurnal and semidiurnal tidal activity, clearly visible from L_S=190-250° in Figs. 5.12.f and 5.13.f. Specifically, the diurnal tidal component of wind speeds (Fig. 5.12.f) is immediately enhanced between 40° S-40° N, and especially at 30° N (by 2-3 m/s), as seen in the increase in amplitudes in those latitude ranges. There is then a secondary enhancement at southern mid-high latitudes, specifically 30-60° S, between L_S=210-220° (of $\geq$5 m/s). Interestingly, there is a diurnal tidal minimum at 20° S in that same period. The semidiurnal tidal component (Fig. 5.13.f) sees an immediate boost in amplitude at 30° N, 20° S, and 60° S, the latter two being greater than the first ($\geq$5 m/s vs 3 m/s). There is also a small boost in amplitude at the northern cap edge, around 60° N, of $\sim$1 m/s. The latter two enhancements also last through the duration of the GDS, while the former lasts between L_S=190-220°. This demonstrates the strong link between the semidiurnal tide and atmospheric dust loading.

There are also GDS-induced changes to eddy activity between L_S=190-250°, seen in Fig. 5.14.f. There is a small change to southern cap edge eddies, the higher amplitude features around 60° S; while they are already declining in magnitude in most years by the time of the GDS inception, the GDS seems to accelerate their disappearance: by L_S=190° eddy activity has dropped to effectively zero, while in most years some eddy activity is still visible until L_S=200-210°. Northern eddy activity, the higher amplitude features around 45-75° N, is also affected. The L_S=170-220° period represents a maximum in northern cap edge eddy activity for the other years. This is substantially reduced by the GDS, by 1-2 m/s. This has great implications for northern lowlands lifting, which is reduced as a result (as described above). A corollary is that the MY 34 northern solsticial pause is no longer a “pause”; eddy activity simply continues being low, with the outcome that the GDS year sees overall reduced lifting from the northern lowlands.

As seen in Fig. 5.9.f, the GDS induced higher near-surface wind speeds across almost the entire planet; however, its effect on near-surface zonal and meridional flow was more subtle. Fig. 5.10.f shows that between L_S=190-210° the GDS had the effect of changing the dominant tropical meridional flow, at 0-30° N, from the usual split north-to-south/south-to-north flow to a purely north-to south flow, approximately 30° L_S before this usually occurs. As this flow represents the returning flow of the dominant cross-equatorial Hadley cell, this shows that the GDS accelerated the transition between an equinoctal circulation (with two roughly symmetrical Hadley cells around the equator) to a solsticial circulation (with a dominant cross-equatorial Hadley cell). The effect on the near-surface zonal flow is visible at Fig. 5.11.f. The GDS effect was to, between L_S=190-220°, reverse the surface easterlies between 0-20° N into westerlies. This is the phenomenon of atmospheric superrotation, which has been previously modelled to occur on Mars in the case of GDS-level dust loading.

Fig. 5.23 shows lifting as the GDS remains intense, but decay is well underway. Again, lifting remains elevated relative to "normal" over Tharsis and southern Amazonia Planitia, but far less so over Arabia Terra/Terra Sabaea. There is a band of decreased lifting between 30-60° N which encompasses not just the northern lowlands but the higher topography regions by the planetary dichotomy boundary. The most striking feature in its intensity is the narrow band of ehnanced lifting at 60-70° S; this shares a very similar structure to that of MY 30, but greater in its intensity.

There are a few possible explanations for this. Given the possible role of sublimation flow from the southern seasonal cap in causing these high cap edge wind speeds, the GDS may have intensified southern cap sublimation during this period. Alternatively, the GDS may have increased near-surface atmospheric density at the cap edge; atmospheric density has a positive relationship with calculated lifting in the equations. There are a couple of arguments against the first hypothesis. A sign of increased sublimation due to dynamical heating would be an accelerated recession of the southern seasonal cap; as shown above when discussing

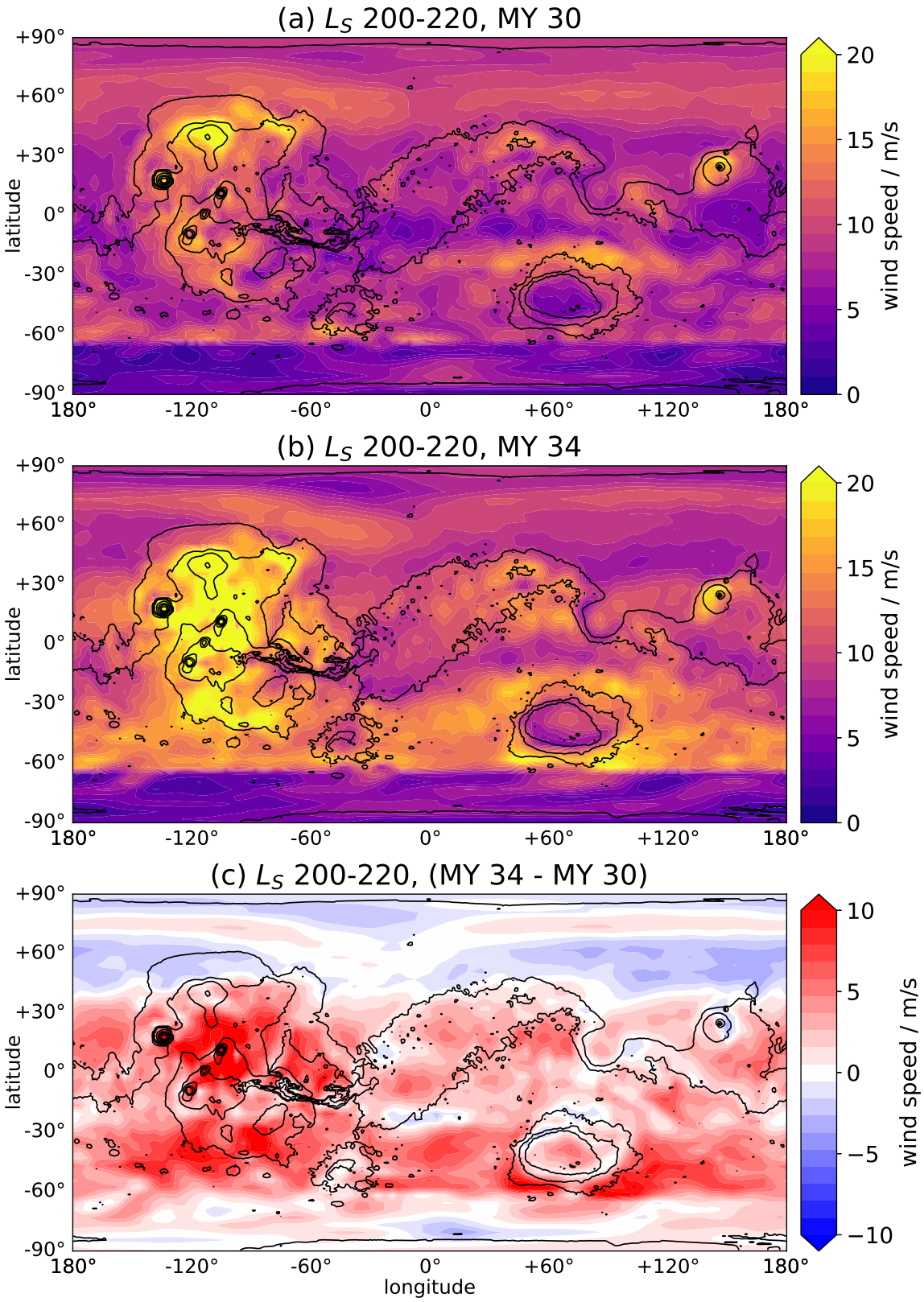

Fig. 5.24 Maps of near-surface wind speeds for the period L_S=200-220°, for MYs 30, 34, and the difference between the two.

the effects of tropical CDOD on southern cap edge lifting between L_S=240-300°, the MY 34 case does not appear to simply correspond to either a larger or smaller seasonal cap than the mean, indicating asymmetric effects. This contradicts the fact that the enhanced lifting occurred uniformly across the entire latitude circle by the seasonal cap edge.

The other explanation is that the MY 34 GDS substantially increased near-surface atmospheric density by the cap edge; given the positive relationship between density and lifting (as a thicker atmosphere results in a greater momentum for a given wind speed), this resulted in an increase in cap edge lifting. Fig. 5.25 shows how the atmospheric density near the surface was at least 5% higher by the southern cap edge than over the same period in MY 30. This density change had contributions from both atmospheric temperature (which has an inverse relationship with density), as seen in Fig. 5.27, and surface pressure (which has a positive relationship with density), as seen in Fig. 5.26. The near-surface temperatures are lower than in MY 30 in a series of patches at 60° S around the edge of the seasonal cap, implying a larger seasonal cap in MY 34. Meanwhile surface pressures are at least 10 Pa higher in MY 34 over the entirety of southern high latitudes, indicating enhanced dynamical transport of air from the tropics. Together, these effects result in an increased cap edge atmospheric density, resulting in enhanced lifting.

This effect persists in the period L_S=240-260°, as seen in Fig. 5.28. As the GDS decays, so the effects on lifting are reduced. There is though a notable enhancement in lifting at the 30° S latitude band. This is due to the enhanced Hadley circulation; as the upwelling branch of the Hadley cell is strengthened, so too is the resulting subtropical jet. There is also still an enhanced band of southern seasonal cap edge lifting due to increased atmospheric density (via the process described above). Interestingly, poleward of this there is a band of decreased lifting. These complex effects may be an artifact of the temporal averaging process, and could be explained in terms of highly asymmetric recession patterns. The specific polar dynamics which may lead to such patterns are discussed in Chapter 6.2.

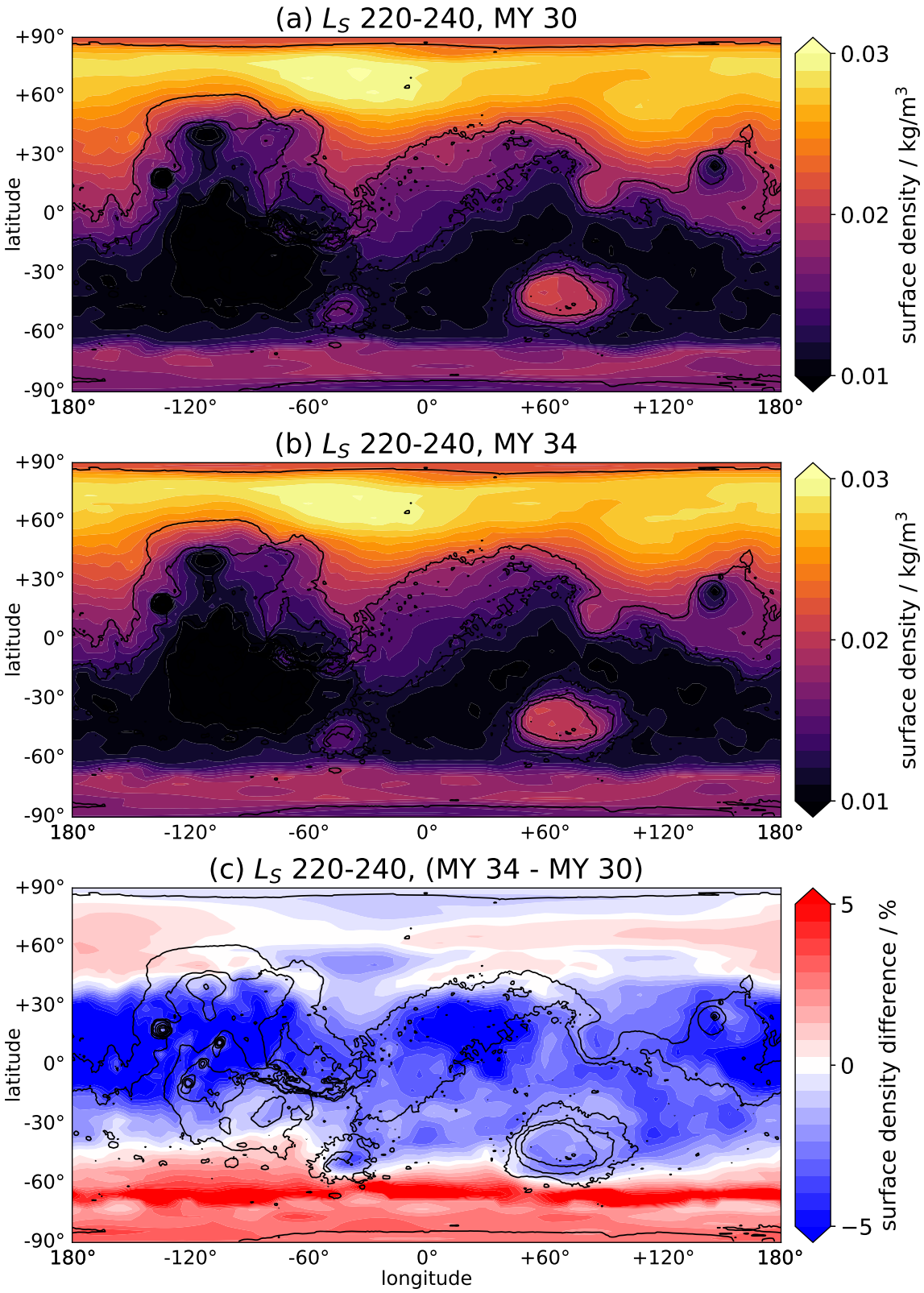

Fig. 5.25 Maps of near-surface atmospheric density for the period L_S=220-240°, for MYs 30, 34, and the proportional difference between the two.

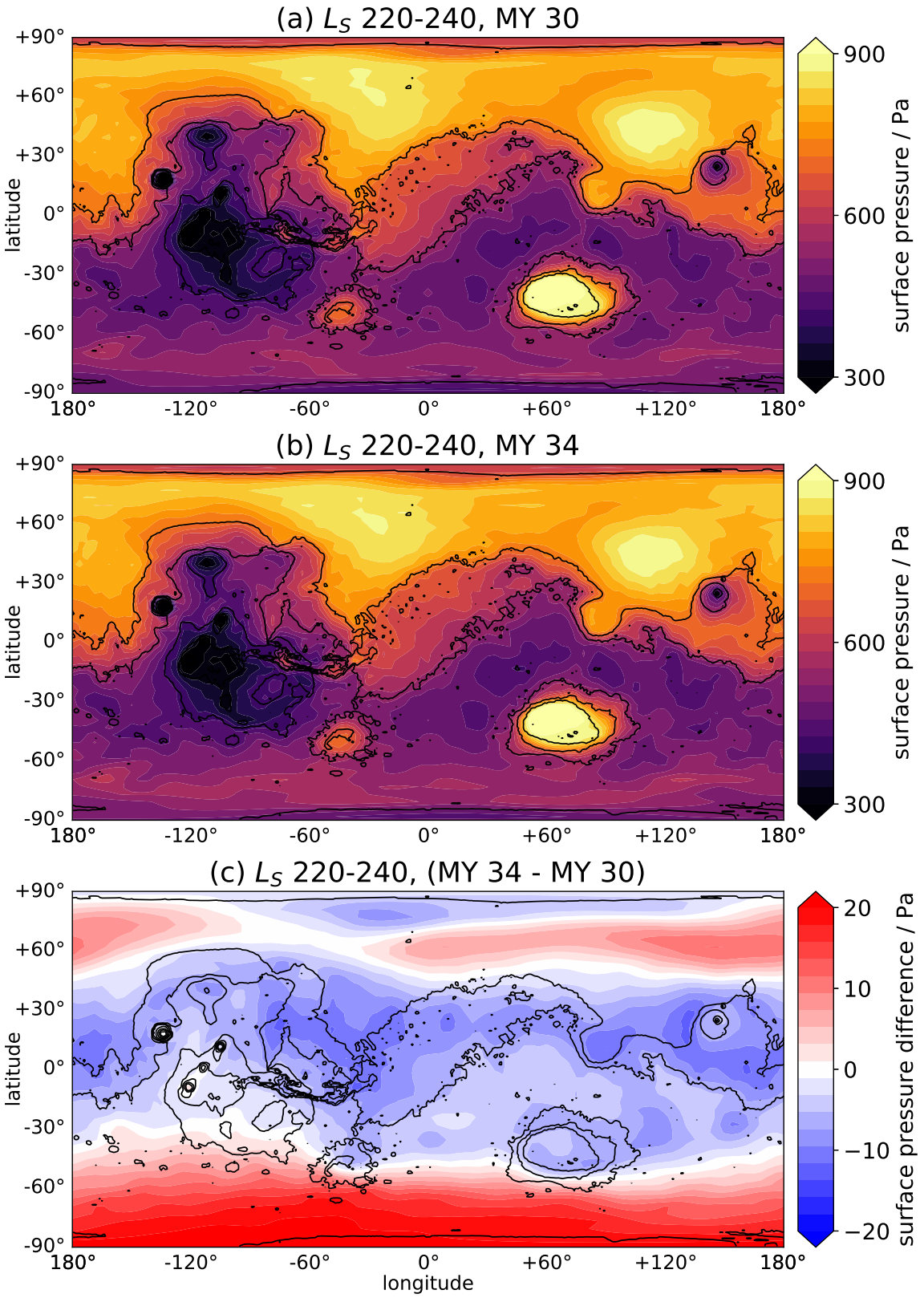

Fig. 5.26 Maps of surface pressure for the period L_S=220-240°, for MYs 30, 34, and the difference between the two.

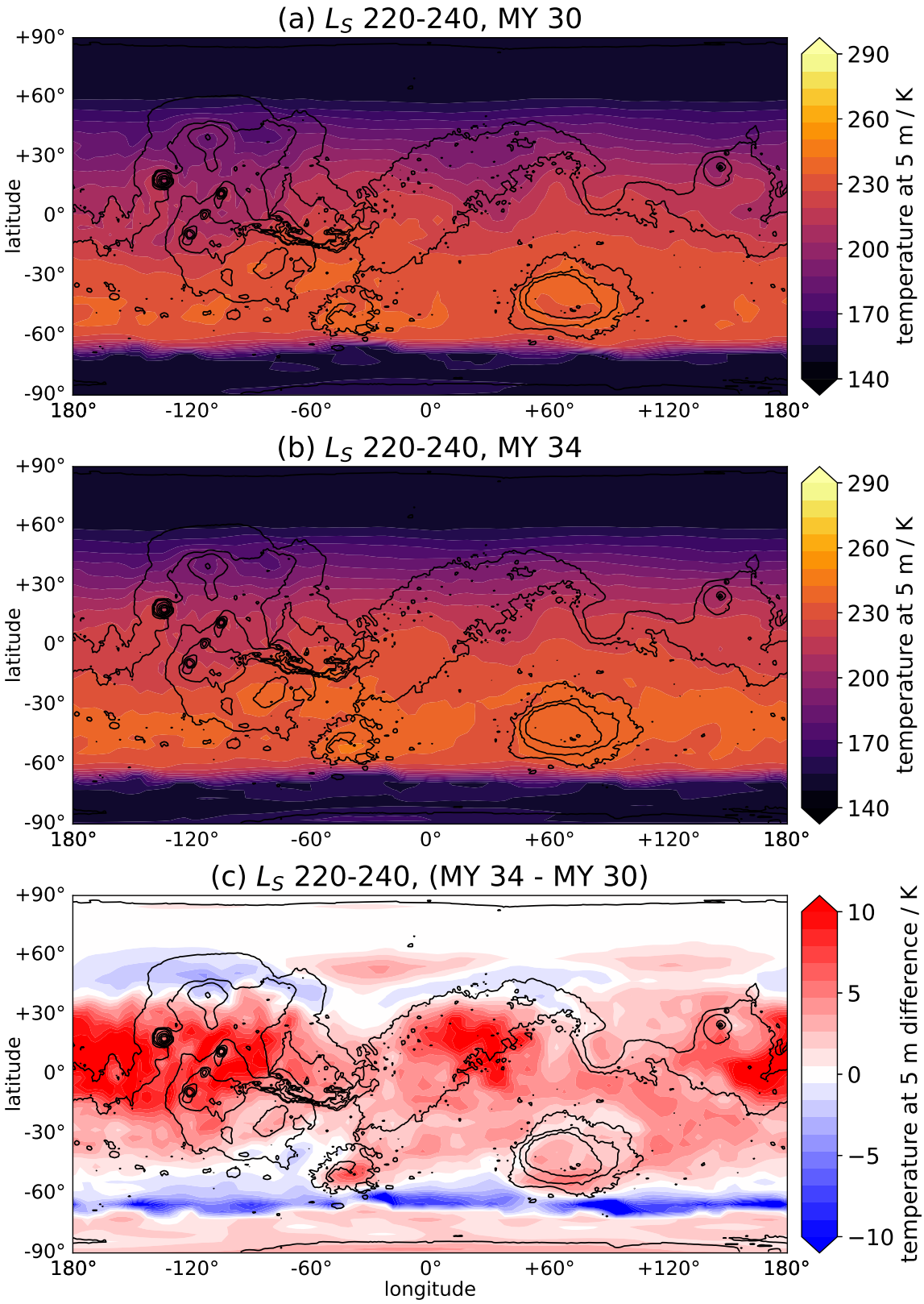

Fig. 5.27 Maps of near-surface atmospheric temperature for the period L_S=220-240°, for MYs 30, 34, and the difference between the two.

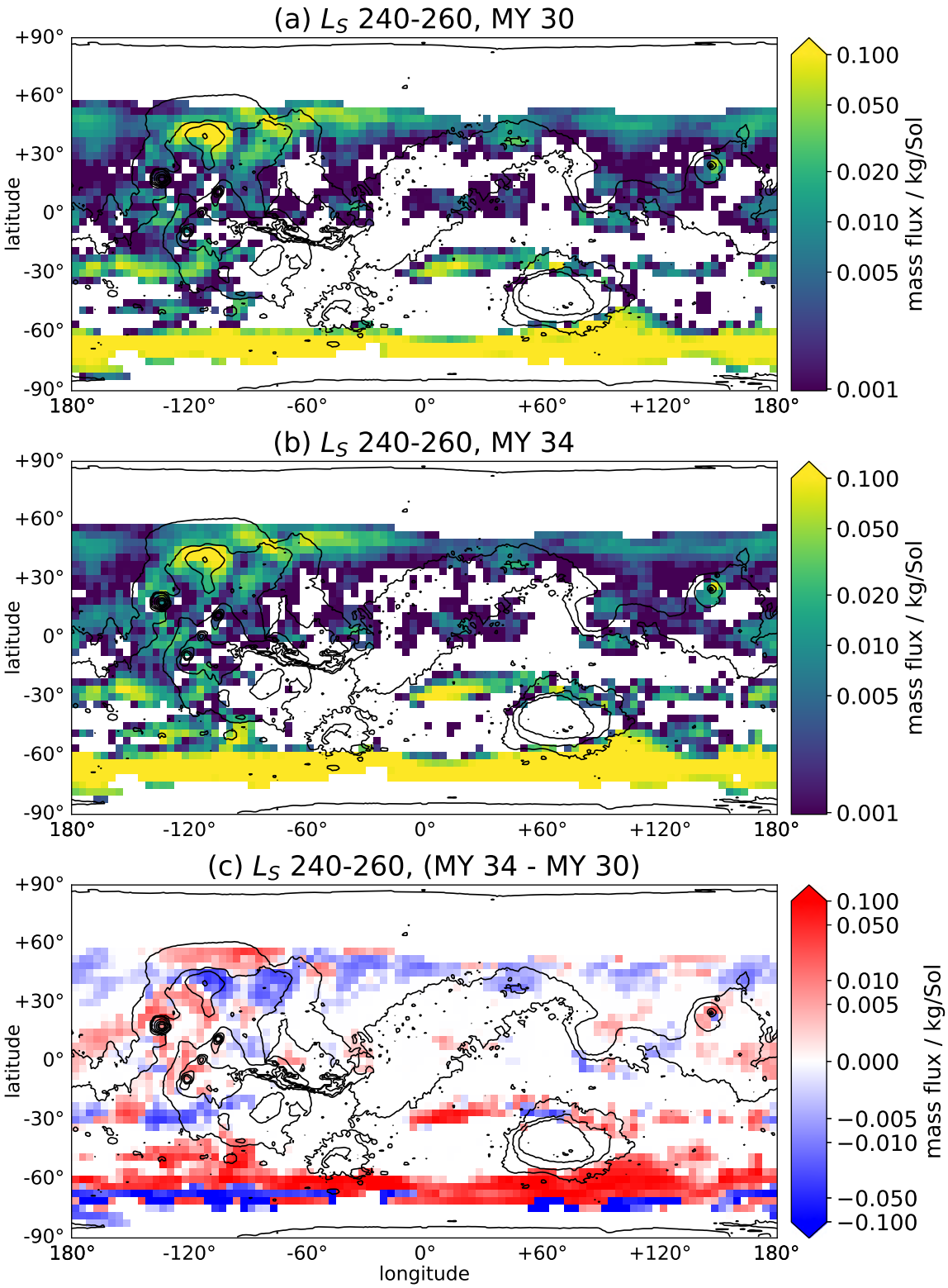

Fig. 5.28 Maps of dust mass lifting flux for the period L_S=240-260°, for MYs 30, 34, and the difference between the two. Note the non-linear scale.

5.4.2 Deposition

Fig. 5.29 shows dust deposition during the initial stages of the GDS, L_S=180-200°. Most of the enhanced deposition occurred at equatorial latitudes and the northern tropics. As the storm reached its peak in L_S=200-220°, seen in Fig. 5.30, this largely remained the case. The greatest deposition occurred over Arabia Terra and Terra Sabaea, with high deposition also over Isidis Planitia and southern Elysium Planitia. There was then a gap in deposition over the southern tropics, with a second band of highest deposition between 30-60° S. This was concentrated over Argyre Planitia, Hellas Planitia, and Terra Cimmeria (east of Hellas). As the storm subsequently decayed throughout L_S=220-240° (Fig. 5.31) and L_S=240-260° (Fig. 5.32), the bands of highest deposition shifted to higher latitudes. Particularly in the northern hemisphere, the highest deposition occurred around the 30-40° N latitudes. This implies that once the storm stopped spreading and activating new lifting centres, the remaining suspended dust became caught up in the Hadley circulation and therefore preferentially deposited around its downwelling branches.

5.5 Discussion

This section now moves back from the specific results of the MY 34 GDS to discuss the results of this chapter as a whole. In the broad sense, annual lifting was dominated by the perihelion season, which agrees with previous modelling work (e.g. Basu et al., 2004; Newman et al., 2002a,b) and matches with observations of higher global CDOD during this season (e.g. Montabone et al., 2015; Wang and Richardson, 2015). This is due to the higher insolation in this season, which enables higher near-surface wind speeds. However, these results do show greater southern hemisphere lifting during the perihelion season than previous studies using the same MGCM without assimilation (Chapman, 2018; Mulholland et al., 2015); specifically by the southern seasonal cap, which is associated with sublimation

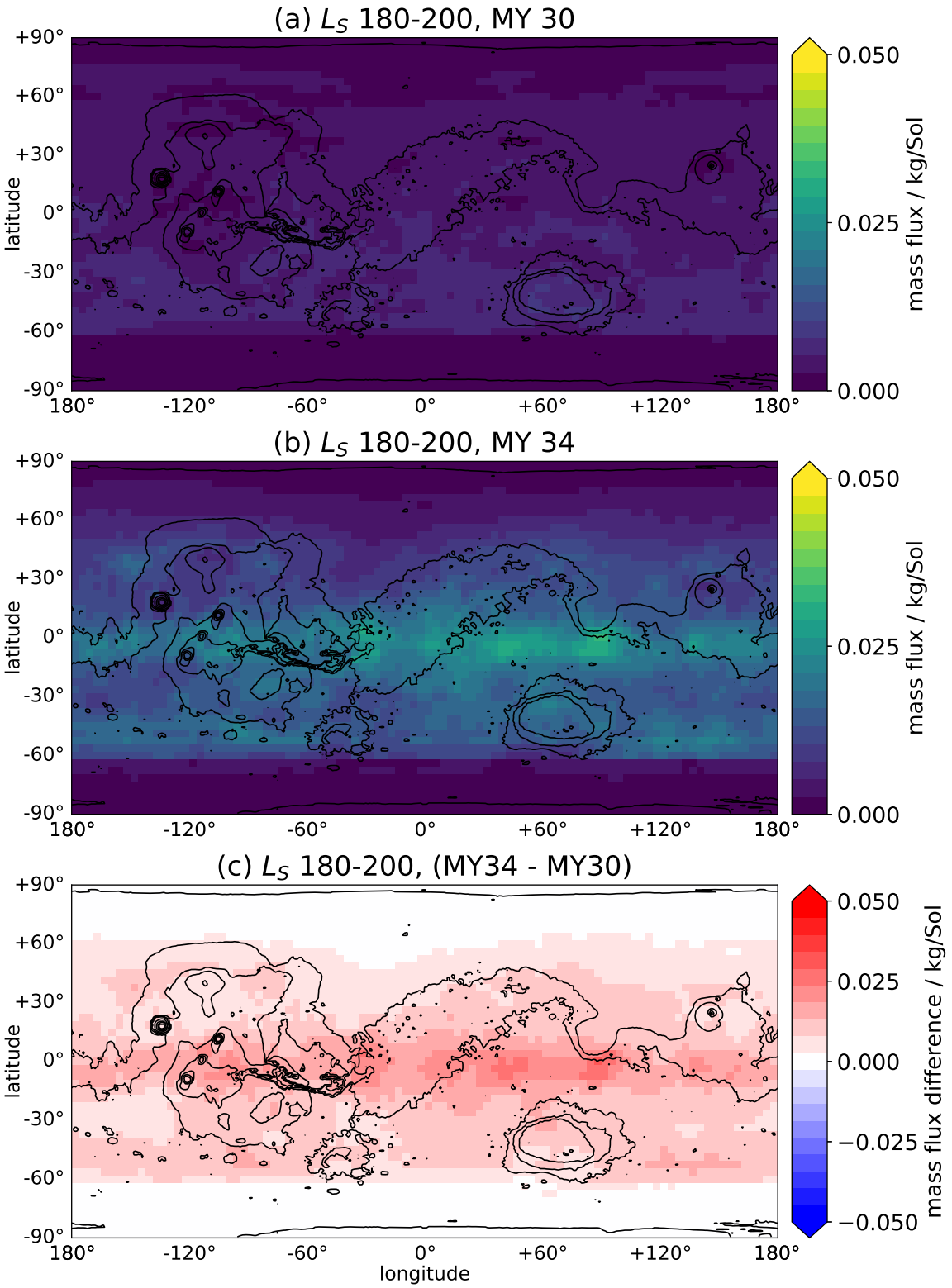

Fig. 5.29 Maps of dust mass deposition flux for the period L_S=180-210°, for MYs 30, 34, and the difference between the two.

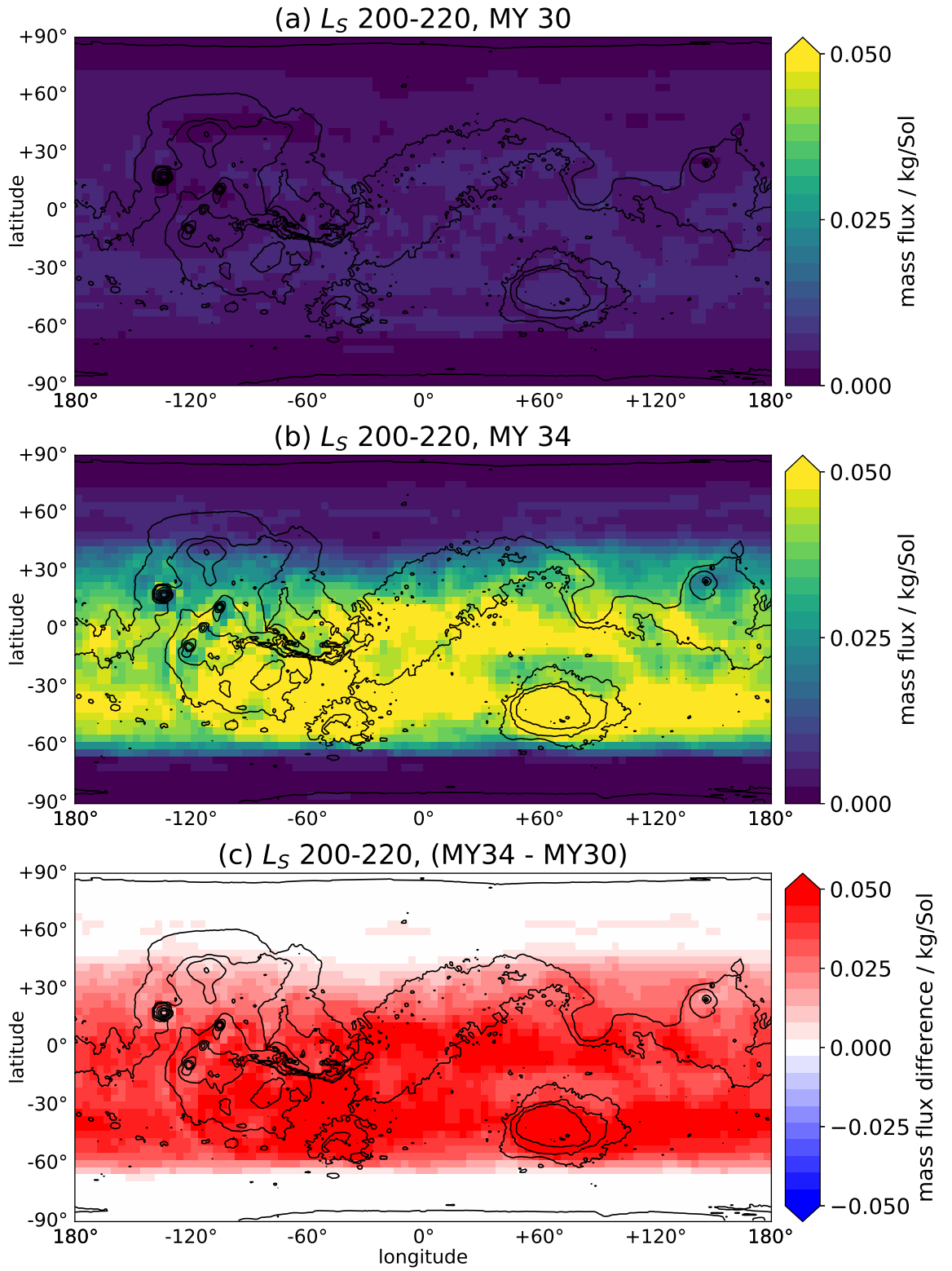

Fig. 5.30 Maps of dust mass deposition flux for the period L_S=200-220°, for MYs 30, 34, and the difference between the two.

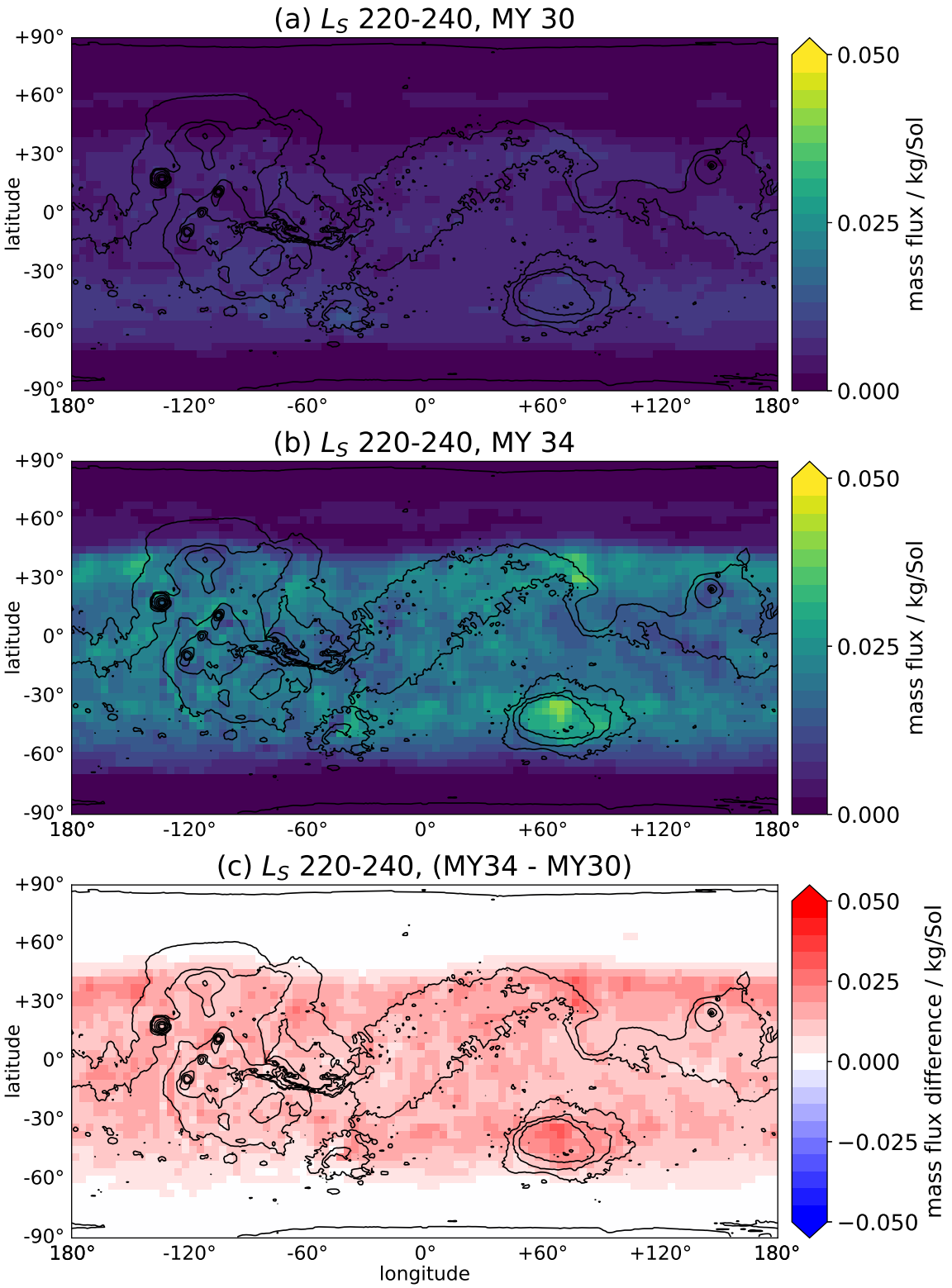

Fig. 5.31 Maps of dust mass deposition flux for the period L_S=220-240°, for MYs 30, 34, and the difference between the two.

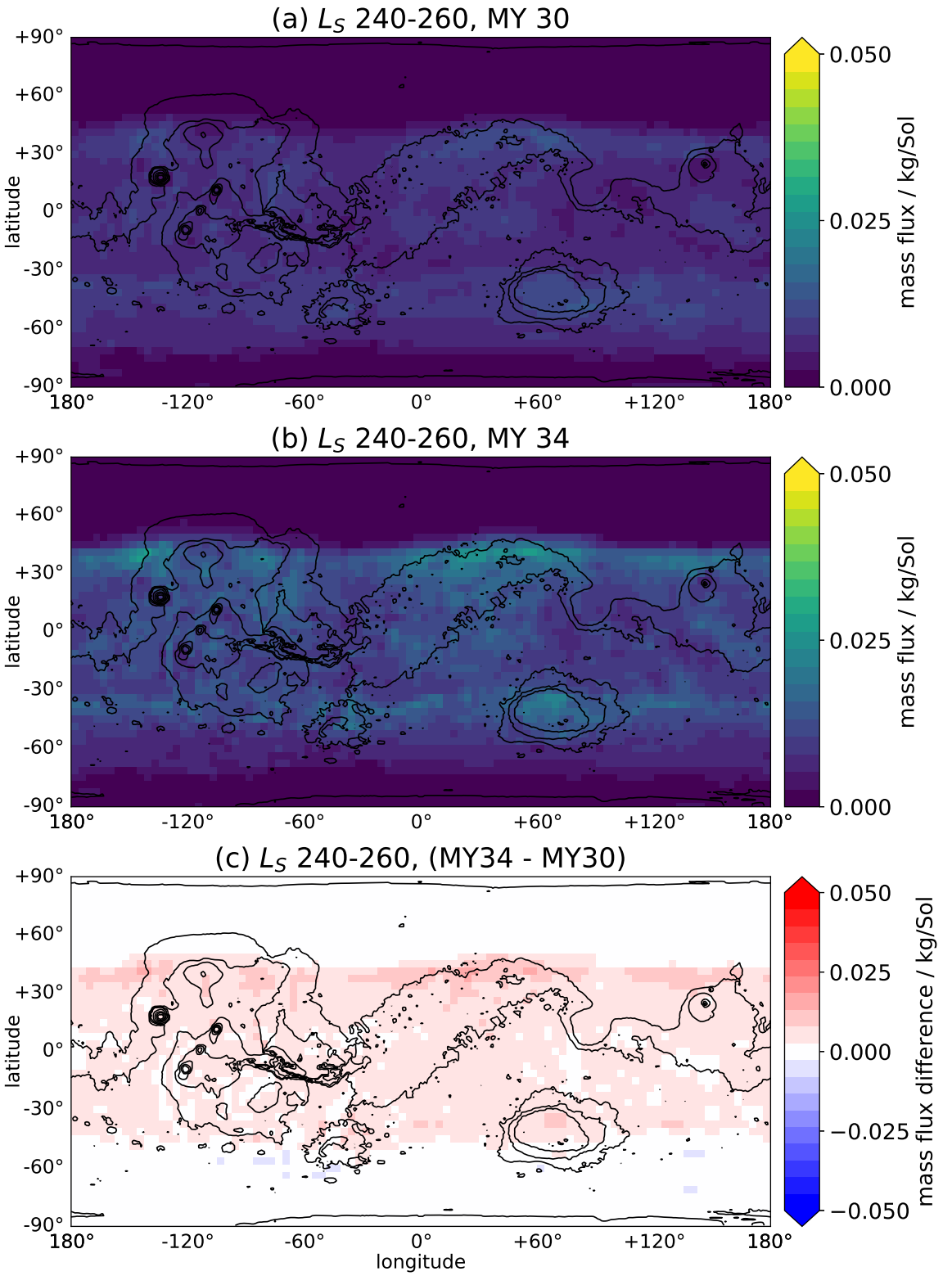

Fig. 5.32 Maps of dust mass deposition flux for the period L_S=240-260°, for MYs 30, 34, and the difference between the two.

flow and/or other mechanisms (see below). It is possible that the free-running MGCM is not accurately representing the large-scale atmospheric dynamics responsible for this jet. The role of assimilation in driving the southern cap edge feature is investigated in Chapter 6.2.

Throughout both seasons of the martian year, lifting was dominated by the contribution from the edges of both northern and southern polar caps. This was due to both baroclinic eddy activity and sublimation flow from the seasonal caps, both of which are discussed in greater detail below. This accords very well with observational datasets, which detail ubiquitous storm activity at both polar cap edges throughout the martian year (e.g. Cantor et al., 2002; Guzewich et al., 2015, 2017; Hinson and Wang, 2010; Hollingsworth et al., 1997; James et al., 1999; Wang, 2007; Wang and Fisher, 2009; Wang et al., 2005). Indeed, Fig. 5.33, which overlays storm observations from the Mars Color Imager (MARCI) in the Mars Dust Activity Database (MDAD) (Battalio and Wang, 2019) onto calculated lifting, shows a very good agreement between the near-constant cap edge lifting and near-constant cap edge dust storm activity. This cap edge lifting is highly repeatable between years, as has been observed from orbit (e.g. Cantor et al., 2002). This cap edge lifting is largely symmetrical around each solstice in terms of its spatial distribution; however, there is greater activity near the L_S=180° equinox than the L_S=0° equinox, due to the temporal asymmetry in seasonal cap growth/recession (Piqueux et al., 2015) and the greater insolation at the former due to the eccentricity of Mars' orbit.

The results show that baroclinic eddy activity plays a hugely important role in cap edge lifting, particularly at the winter pole, where the meridional temperature contrast is greatest. This agrees with previous modelling (e.g. Hinson et al., 2012; Wang et al., 2013; Xiao et al., 2019) and orbital (e.g. Hinson and Wang, 2010; Wang, 2007; Wang et al., 2005) studies linking cap edge storms to high-latitude baroclinic eddies. The eddy activity in the results is greatest between L_S=180-230°, or early northern winter/southern summer. Again, this agrees with previous modelling work showing that the most intense storm activity in the

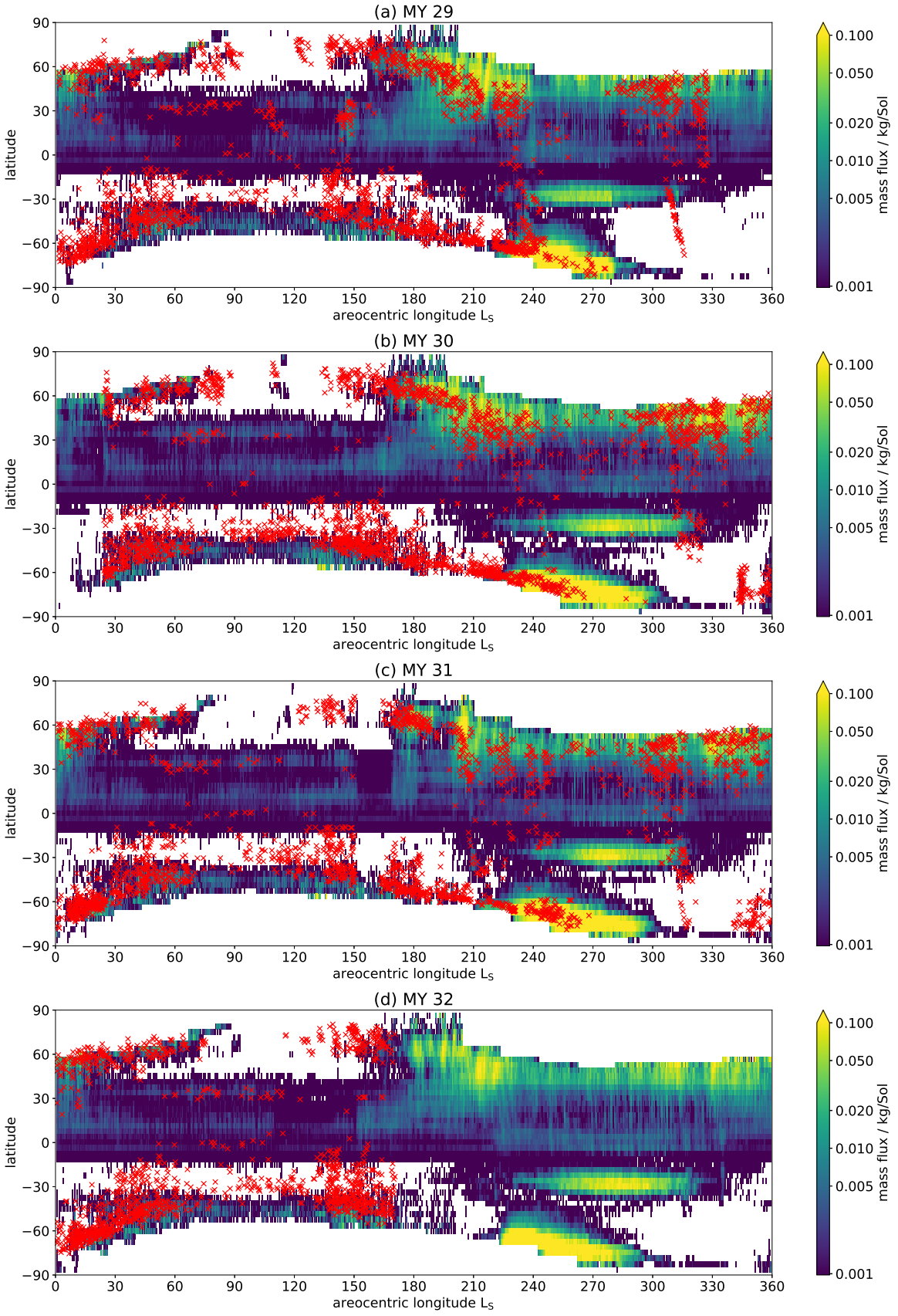

Fig. 5.33 Zonally averaged L_S-latitude maps of dust mass lifting flux for MY 29-34. Note the non-linear scales. Overlaid (red crosses) are the centroid latitudes of storms observed using the Mars Color Imager (MARCI) and recorded in the Mars Dust Activity Database (MDAD) (Battalio and Wang, 2019).

"storm zones" of the northern lowlands occurs in early northern spring, due to a maximum in transient eddy activity (Hollingsworth et al., 1997) during this period, even if there is some observed interannual variability within that period as to when exactly the most vigorous northern cap edge storms are seen to occur (Hinson and Wang, 2010).

A key feature of baroclinic eddy lifting at the winter cap edges is that it experiences a solsticial "pause", which is clearly evident in the results at both the northern and southern cap edges around each solstice. This pause, shown with the assimilation of TES data by Lewis et al. (2016) and reproduced with the assimilation of MCS data by Greybush et al. (2018), has complex causes linked to topography, the radiative effects of water ice clouds, and dust loading (Mulholland et al., 2016). The results show that the pause has a significant impact in decreasing cap edge lifting around the solstices, and shows striking interannual repeatability. The pause has been observationally verified through orbital studies (e.g. Guzewich et al., 2015, 2017), and indeed is visible in the overlaid MDAD data in Fig. 5.33. The northern hemisphere pause in particular may therefore be responsible for the observed paucity of large regional storms between L_S=240-305° in an orbital study of Mars Orbiter Camera (MOC) and MARCI images from MYs 24-30 (Wang and Richardson, 2015). Hinson and Wang (2010) also observed a decline in cross-equatorial "flushing" storm activity around the height of northern winter/southern summer of MY 26 and hypothesised that this may be due to one or several of depletion of dust sources, CO_2 condensation, and shift in the dominant eddy wavenumber; the results of this chapter indicate that the last of these is at the very least a significant component, if not the dominant one.

The results show that the other major contributor to cap edge lifting is sublimation flow from the recessing seasonal polar cap, which is especially a factor at the southern seasonal cap. While the recessing northern cap shows both evidence of a sublimation flow and eddy activity between L_S=0-90°, at the recessing southern seasonal cap between L_S=220-300° the near-surface wind speeds show little to no eddy contributions and are dominated by an easterly

zonal flow and south-to-north meridional flow indicative of near-surface sublimation flow. (Note that both of these features are referred to here as "sublimation flows" for simplicity; however, as stated the northern feature has contributions from both a likely sublimation flow and eddy activity, while the mechanisms responsible for the southern feature are not definitely solely sublimation - see the discussion below and Chapter 6.2.)

The northern cap edge lifting does agree with observed dust storm activity in the MDAD, as seen in Fig. 5.33; this is also the case for the southern cap edge lifting, but only for the first half of the period during which there is intense predicted lifting (see MYs 30 and 31, for which there is assimilated data for the whole L_S=220-300° period). It seems likely therefore that high wind speeds alone are insufficient for maintaining storm activity; the periodic nature of baroclinic eddies may be important for maintaining available surface dust for storm formation, while intense but consistent and coherent jets may be inhibitive to continued storm inception over long periods.

The results show a dichotomy between the northern and southern cap-edge flows, with the latter having a meridional flow 50-300% greater as well as a much greater equatorward latitudinal extent. This dichotomy in intensity is consistent with dedicated modelling of the sublimation flow, which shows much higher wind speeds (of up to 10 m/s) corresponding to the southern sublimation flow than to the northern, due to the increased solar insolation near perihelion (Chow et al., 2019). Chow et al. (2019) speculate that their modelled intense southern sublimation flow, occurring as it does during Mars' dusty season, may be responsible for dust lifting. There is also orbital observational evidence in favour of intense sublimation activity at the southern seasonal cap, in the form of CO_2 jets which erupt as the cap sublimes (e.g. Aye et al., 2019; Thomas et al., 2016).

However, there is also modelling evidence to suggest that even the southern sublimation flow may not be intense enough to support dust lifting, and that other mechanisms may be at play in driving high wind speeds around the southern seasonal cap. Burk (1976) used a

primitive-equation model to calculate polar cap winds and estimated they were insufficient to raise dust. Siili et al. (1997) modelled wind speeds at the southern cap edge and concluded that the combined sublimation flow and effects of the thermal contrast between the cap and the surrounding ice-free regolith were, even together, insufficient to cause wind stress values sufficient for dust lifting. Siili et al. (1999) incorporated the effects of slope winds as well and found that, in conjunction, the wind speeds resulting from the thermal contrast, sublimation flow, and (down)slope winds could drive wind speeds of up to 30 m/s. Likewise, Toigo et al. (2002) found that southern cap edge wind speeds could reproduce the observed dust distribution at this time of year, but that the primary drivers behind the sufficiently high wind stresses were the thermal contrast and slope winds, while the sublimation flow was relatively unimportant. The thermal contrast/slope wind explanation also fits with the results presented here, as the downslope winds would provide a south-to-north meridional flow while the thermal contrast and resulting high pressure system over the pole (due to differing thermal inertias of the ice and ice-free regolith) would result in a easterly flow, analogous to the terrestrial sea breeze (Fernández, 1997). The causes of the southern high latitude jets seen in this chapter are further investigated in Chapter 6.2.

Regardless of the causes of the southern high latitude jet presented in these results, it still provides a significant source of dust lifting. The discussion here is agnostic regarding the exact causal mechanisms behind the jet, which are discussed in Chapter 6.2 Significantly, the annually repeatable “B”-type storm occurs at the southern cap edge at around this season (Kass et al., 2016), suggesting that this annually repeatable intense jet is responsible for the regularity of the “B”-type storm.

Another result related to cap edge lifting is that tropical dust loading has a notable impact on lifting at the southern cap edge; specifically, tropical CDOD is anti-correlated with lifting there, as indicated in Fig. 5.5. It is hypothesised here that the higher tropical atmospheric temperatures due to the increased dust presence causes enhanced transport of warmer air

to the seasonal cap edge, accelerating the recession of the cap and thus reducing the area available for cap edge lifting. In addition, the cap-adjacent regolith is at a higher latitude, making it colder and thus reducing the thermal contrast with the cap. Piqueux et al. (2015) observed that the recession of the southern cap, in particular, shows distinct interannual variability in latitude of up to several degrees and speculated that regional-scale dust activity could be responsible for this variability. These results suggest that large regional dust storms, specifically "A"-type storms (Kass et al., 2016), at tropical latitudes can in fact influence the recession of the southern polar cap. This effect may occur with a lag of $\sim$40-100 sols, according to modelling of the age of air in the martian circulation (Waugh et al., 2018).

Speculating, there is a potential implication of this result and the hypothesis that the cap edge lifting is linked to "B"-type storms. A particularly intense "A"-type event would reduce cap edge lifting and shift it poleward. This could indirectly lead to a decreased chance of a "B"-type event; but it could also lead to more intense "B"-type events, as more dust would remain available to lift.

The MY 34 results do not fit with the other years, suggesting that other mechanisms are at play with a dust event of that magnitude, including potential indirect effects on cloud formation and potential direct effects of dust deposition onto the southern cap surface itself. de la Torre Juarez (in review) observed no apparent change to the southern seasonal cap from the MY 34 GDS (while the northern seasonal cap appeared to grow). This is despite the fact that the MY 25 GDS, which occurred at a very similar time of year to the MY 34 event, appeared to accelerate the southern cap retreat (Piqueux et al., 2015). The MY 34 GDS seemed to initially depress but later in its decay phase enhance southern cap edge lifting, the latter effect likely due to increased surface pressures over the southern cap leading to higher atmospheric density and therefore greater lifting.

Northern mid-latitude dust lifting was present to some extent throughout the aphelion season and corresponded to a small amount of dust storm activity, as visible in the MDAD

data in Fig. 5.33. This lifting was linked to areas of high topographic contrast: Alba Patera, Tharsis, Elysium Mons, and Quenisset, implying slope winds were responsible. This has been noted in modelling of northern hemisphere dust lifting (Xiao et al., 2019), including the important role of Alba Patera in particular and its slope leading down to the northern lowlands (Hollingsworth and Kahre, 2010). Lifting also occurs to the south of Olympus Mons and around the location of the Medusae Fossae Formation, which has been proposed as the major contributor to Mars' global dust reservoir (Ojha et al., 2018); these results suggest that this is an active lifting region on present day Mars. The topographic lifting over Tharsis' volcanoes has been proposed as the source of observed high-altitude detached dust layers, which are especially prevalent throughout the aphelion season (Heavens et al., 2015).

Dynamical features were also responsible for non cap edge lifting. One proposed lifting mechanism has been the western boundary current (WBC): narrow jets of meridional flow on the eastern slopes of high topography regions (specifically at ∼50°W, east of Tharsis, and ∼80° E, east of Syrtis), corresponding to the returning flow of the cross-equatorial Hadly cell and therefore at their most intense around each solstice (Joshi et al., 1994, 1995). These results suggest that the WBCs at around L_S=90° do not in fact contribute to dust lifting. This may be due to the high roughness length at both jet locations (see Fig. 5.1), as the L_S=270° WBCs do seem to lift dust. The generally enhanced wind speeds of the latter solstice may be enough to overcome the barrier of the high surface roughness lengths.

A major contributor to global lifting in the results was the southern subtropical jet at 30° S between L_S=220-320°. This feature is a result of the upwelling branch of the Hadley cells - rising air is shifted into westerlies due to the Coriolis effect, and it has previously been modelled in the martian atmosphere (Joshi et al., 1997). However, as seen in Fig. 5.33, there are almost no observed storms corresponding to it visible in the MDAD. There is the possibility that this feature does not in fact exist or is weaker than shown in the reanalysis; this is explored in Chapter 6.2. An alternate explanation is that the consistently high wind

speeds at this latitude band, which has been inferred from orbital thermal inertia and albedo measurements to be climatologically relatively free of surface dust cover (Putzig et al., 2005; Ruff and Christensen, 2002; Szwast et al., 2006), inhibit dust deposition. This is supported by the dust deposition results presented in this chapter. Without a surface source of dust to feed storms, these intense near-surface wind speeds cannot become a storm zone.

Non cap edge lifting has a distinct tidal amplitude, both in the diurnal and semidiurnal modes. This includes both the topographic and dynamical lifting described above. Previous modelling work has also shown that northern hemisphere topographic lifting has a period of 1 sol, corresponding to the diurnal tidal mode (Xiao et al., 2019). The tidal variation of winds can have significant effects; Wang et al. (2003) proposed that there is a tidal "window" when the tides amplify the returning Hadley cell flow, boosting it and allowing the cross-equatorial transport of "flushing" dust storms from the northern cap edge into the southern hemisphere. Indeed, the results presented here support the idea that both wind speeds and their tidal variation are highest on either side of the northern solsticial pause, which is when flushing storms are observed (Wang, 2007).

The results appear to show that large enough storms (consistently high CDOD over a long period) can also induce their own changes to the lifting. MY 29 was unusually dusty compared to the other years studied between L_S=150-180°, and analysis of the results shows apparently enhanced lifting in the northern hemisphere; both over high topography and the northern lowlands. The dust loading was of sufficient scale (>10^6 km) and temporal extent (> 10 sols) to impact atmospheric dynamics in such a way as to maintain itself, as proposed by Toigo et al. (2018). Observations of cap edge lifting have also shown that lifting can occur across the storm fronts themselves, allowing a positive lifting feedback (Wang and Fisher, 2009; Wang et al., 2003).

As a final note, the results indicate an interesting correspondence between perihelion lifting features and the repeatable "A"-, "B"-, and "C"-type large regional storm systems

described by Kass et al. (2016). "A"- and "C"-type storms, generally at tropics/mid-latitudes, occur when northern cap edge lifting is at a maximum ie. not during the solsticial pause $L_S \sim$240-305° (Wang and Richardson, 2015). "B"-type storms, as mentioned above, occur towards the beginning of southern summer by the polar cap edge, during the first half of the temporal extent of the southern high latitude jet. This implies that the interannually repeatable nature of these large storms flows from the interannually repeatable nature of the relevant large-scale atmospheric dynamics.

The GDS had a significant effect on calculated dust lifting. Enhanced near-surface wind speeds from the increased dust loading resulted in greater lifting over northern hemisphere high topography. In the southern hemisphere, there was a slight intensification of lifting from the subtropical jet. At the southern cap edge, increased atmospheric density from heightened surface pressures (due to a boosted Hadley circulation) increased calculated lifting. However, lifting actually decreased over the northern lowlands. This is due to the suppression of eddy activity by the enhanced static stability, and the poleward shift of the Hadley cell's descending branch (Barnes, 1984; Ryan and Henry, 1979). This lends credence to the idea espoused by Haberle (1986) that GDS cycles may be linked to shifts between dominant southern hemisphere lifting (in GDS years) and dominant northern lowlands dust lifting (in non-GDS years). However, there was one exception to the decline in northern lowlands lifting: over Acidalia Planitia, downslope from Tempe Terra/Alba Patera, lifting actually increased, likely due to enhanced slope winds.

The GDS also altered the near-surface meridional and zonal flow, as described in Section 5.4.1. Zonal easterlies were reversed to westerlies, signifying atmospheric superrotation; this occurred due to the angular momentum contribution from the thermal tides enhanced by the GDS (Lewis and Read, 2003). The meridional flow transitioned rapidly from an equinoctial state, characterised by symmetrical equatorward flows around the 0 latitude, to a

north-to-south flow across the equator indicative of a solsticial circulation dominated by a clockwise cross-equatorial Hadley cell.

Like lifting, dust deposition showed a surprising dependence on near-surface wind speeds. Bands of higher wind speeds, such as at the subtropical jet during perihelion at 30° S, showed decreased deposition as dust was prevented from settling. This shows that both lifting and deposition are to an extent controlled by near-surface wind speeds, making their proper characterisation and understanding all the more important. This "cleaning" of certain regions has been invoked before to analyse surface albedo maps by Szwast et al. (2006), who described how southern seasonal cap sublimation flow might "clean" dust deposited early in the perihelion season in that region. And indeed, surface albedo (Szwast et al., 2006), surface thermal inertia (Putzig et al., 2005), and dust cover index (DCI) (Ruff and Christensen, 2002) maps indicate that the latitude band corresponding to the southern subtropical jet location is climatologically a low-dust zone. Likewise, while there is dust storm activity corresponding to the perihelion season southern cap edge lifting, this ceases only half way into the lifetime of this jet. This suggests that dust is being depleted by the storm activity, and it is unable to be replenished due to the consistently high and coherent near-surface wind speeds.

Deposition occurred preferentially at high latitudes of both hemispheres, corresponding to the descending branches of the Hadley cells. This provides an explanation for why the seasonal cap edges are such consistent storm zones throughout almost the entirety of each martian year. While there is steady lifting, there is also steady deposition, resupplying high latitudes with dust to be lifted by storm systems.

Deposition, especially in the perihelion season, was also controlled by the spatial and temporal structure of large dust events, such as the large regional storms catalogued by Kass et al. (2016) and Wang and Richardson (2015) and the MY 34 GDS. Given the duration, spatial extent, and high CDOD of these events, characterising their deposition patterns is

important for understanding deposition on annual timeframes and may give insights into interannual variability in, for example, the timing and location of "C"-type storms.

The MY 34 GDS deposited dust preferentially over the northern (sub)tropics, especially over Arabia Terra/Terra Sabaea; which is climatologically a major lifting centre. There was less intense deposition in the southern hemisphere, implying a net transport of dust from the southern to the northern hemisphere, which has been proposed previously (e.g. Haberle, 1986). Once the storm began its decay phase and was no longer spreading and activating new lifting centres, the Hadley circulation became the dominant driver of deposition, leading to preferential deposition at high latitudes of both hemispheres.

5.6 Conclusions

Data assimilation has proven to be a valuable tool for estimating large-scale dust lifting and deposition throughout the martian year. Assimilation of atmospheric temperature has revealed new and important lifting features, whose proper characterisation and understanding relies on having the best possible estimate of atmospheric dynamics. The most novel of these features is an intense southern cap edge jet as the cap recesses. Assimilation of CDOD has provided better understand of where deposition occurs and its control by the Hadley circulation, the spatiotemporal structure of large regional and global storms, and near-surface wind speeds.

Comparison with existing dust storm observations provokes some novel hypotheses about how storm zones operate on large-scale, seasonal basis. The seasonal caps of both hemispheres are almost constant sources of lifting, according with the ubiquitous observations of cap edge storms at almost all times of year. An explanation of this behaviour can be formulated as follows. There is near constant cap edge dust lifting, by both baroclinic eddies and (to a lesser extent) sublimation/thermal contrast/slope flow, leading to storms which may

travel and deposit their dust elsewhere. However, the Hadley circulation ensures that high latitudes of both hemispheres are constantly replenished with dust.

By contrast, despite high calculated lifting at southern mid-latitudes due to the intense subtropical jet, almost no storms are observed around this feature. Observations show that this is already a dust-poor region. Any dust finding itself at these latitudes is transported away by the Hadley circulation, and deposition is inhibited by precisely those high wind speeds. Without a supply of surface dust, this erstwhile high lifting zone cannot become a storm zone. At the southern cap edge, the large dust supply means that the powerful sublimation/thermal contrast/slope wind can loft dust for a while and create storms; once this supply is exhausted, though, storm activity ceases despite wind speeds remaining high. Over the next year, the Hadley cell replenishes southern high latitude dust, enabling the process to be repeated. Understanding martian storm zones therefore requires knowledge of both lifting and deposition, both intimately linked with near-surface wind speeds.

The large lifting features of the perihelion season can be deployed to understand the interannually similar behaviour of the large regional "A"-, "B"-, and "C"-type storms. The first and last of these are linked to northern cap edge eddy lifting, explaining their absence during the northern solsticial pause. The second is a cap edge phenomenon, and is linked to the southern seasonal cap edge lifting. The repeatable nature of these events can therefore be understood as flowing from the repeatable nature of the large-scale atmospheric dynamics, reliant as they are on the seasonal cycle of solar forcing. The interannual variability in these events - their exact timing, intensity, and spatial structure - is likely more reliant on the history of previous deposition, by the Hadley circulation and large dust events.

Speculatively, the substantial alterations to the normal deposition process caused by a GDS event have knock-on effects on the more repeatable cycle of large dust events. MY 29 is an unusual year in the sense of its high CDOD, with large dust events beginning unusually towards the end of the aphelion season. This is a year after a GDS (the MY 28 event).

Likewise, the MY 34 “C”-type event immediately succeeding the GDS was unusually intense compared to the previous five years. Early in MY 35, a large regional storm occurred in the northern hemisphere; another unusual event.

In other words, the martian dust system is composed of a regular forcing element - large-scale atmospheric dynamics, driven by the seasonal cycle of solar insolation - and a more stochastic “memory” - the pattern of deposition on the surface. The idea that the martian system consists of regular forcing combined with some variable threshold-like element is not a new one (e.g. Basu et al., 2006; Fenton et al., 2007; Haberle, 1986; Mulholland et al., 2013; Newman and Richardson, 2015; Pankine and Ingersoll, 2002, 2004). In this chapter it is simply put forward that the key stochastic memory element which results in interannual variability is the deposition of dust.

Finally, future work may wish to focus further on the question of dust deposition, which has not been as widely studied as dust lifting. Assimilation of dust observations provides a valuable tool to aid this, but other ways of incorporating empirical dust data could also be rewarding. As orbital exploration of Mars continues, the analysis of many years of martian observations also provides a promising way forward to understand the complex relationships between lifting, deposition, and dust storm activity.

Chapter 6

Dust and the Polar Atmosphere

This chapter investigates polar dynamical phenomena related to martian atmospheric dust. In Section 6.1, the impact of the MY 34 GDS on polar vortex dynamics is studied, with a focus on how the morphology of the polar vortices was affected by the high atmospheric dust loading. Both the diurnally-averaged effects and the local time variations are examined, and the morphology of the modelled polar vortices is linked to wave-mean flow interactions. In Section 6.2, two interannually-repeatable, high wind speed phenonema – henceforth, "jets" – at southern high latitudes are investigated in detail. These jets were noted in the previous chapter, where they appeared to be responsible for some dust lifting, but do not appear in other reanalyses of the martian atmosphere. The potential causes and feasibility of these jets are discussed, and their dependence on the particular observational data assimilated into the MGCM.

6.1 Impact of the 2018/Mars Year 34 Global Dust Storm on polar dynamics

6.1.1 Introduction

Mars' winter atmosphere is characterized by a polar vortex of low temperatures around the winter pole, circumscribed by a strong westerly jet (Mitchell et al., 2015; Waugh et al., 2016). These vortices are a key part of the atmospheric circulation and are heavily involved with dust and volatile transport (e.g. Holmes et al., 2017). Planetary polar vortices are a common feature of atmospheres in the Solar System, but Mars' differ from Earth's in several important respects. Among the most notable and visible is their peculiar annular structure. On Earth, the potential vorticity (a way of diagnosing the presence and strength of the polar vortex; see discussion below) of the polar vortices increases monotonically towards the pole; on Mars, there is a distinctive ring of higher potential vorticity around the pole, then a minimum over the pole itself (Mitchell et al., 2015; Waugh et al., 2016). This annular potential vorticity structure should be barotropically unstable but appears to persist over seasonal timescales; modelling indicates that Mars' low radiative relaxation timescales can help maintain this equilibrium (Seviour et al., 2017). The current best explanation for the annular structure itself appears to be diabatic heating from CO_2 condensation over the winter pole; as the CO_2 condenses, it releases latent heat energy, warming the lower atmosphere and destroying potential vorticity (Rostami et al., 2018; Toigo et al., 2017). Mars' polar vortices also appear to show a hemispheric asymmetry, with the northern hemisphere vortex being stronger in reanalyses than the southern hemisphere vortex (Mitchell et al., 2015).

Another feature of the martian polar vortices is their elliptical shape, particularly in the northern hemisphere (Waugh et al., 2016). It has been speculated by Rostami et al. (2018) that this ellipticity could be linked to topography, something not incorporated into their simplified model of the martian circulation. This elliptical shape is only visible when

averaged over time periods of 10s of sols; over smaller timescales, the polar vortex structure is less coherent and composed of smaller regions of high potential vorticity (Waugh et al., 2016). Rostami et al. (2018) attributed this to inhomogeneous deposition of condensing CO_2 ice. Meanwhile, Mitchell et al. (2015) found that the martian polar vortices are consistently centred over the pole itself at the solstices, suggesting a relatively minimal (compared to Earth) role for wave-mean flow interactions in controlling the shape of the polar vortices.

The martian polar vortices appear to have a complex relationship with atmospheric dust loading. Mitchell et al. (2015) found that in the MACDA reanalysis, there was little seasonal variability in the polar vortex structure linked to planetary Rossby wave activity and resulting sudden stratospheric warming, as there is on Earth; rather, any variability was linked to dust-induced changes to the Hadley circulation and resulting intensified polar warming. Specifically, they investigated the effect of a regional dust storm at L_S=320° in MY 26 (a "C"-type storm; see Kass et al. (2016)), and found that it acted to shift the northern vortex towards the equator by $\sim$10° in latitude and weaken the vortex circulation overall. Guzewich et al. (2016) used an MGCM with an analytically prescribed CDOD scenario to investigate the effects of high southern hemisphere dust loading on the northern polar vortex, and vice-versa. They found that regional and GDS events could produce sudden transient vortex warming, disrupting the northern polar vortex for periods of up to 10s of sols, by shifting the downwelling branch of the cross-equatorial Hadley cell poleward. By contrast, the southern polar vortex was significantly more robust to high northern hemisphere dust loading. The exact relationship between the polar vortices and atmospheric dust content is an important one to understand, as it has implications for the transport of both volatiles and dust itself through the vortices (e.g. McCleese et al., 2017; Smith et al., 2017).

The study conducted in this chapter has several novel features compared to previous studies cited above. The use of data assimilation to create a meteorological reanalysis is a key one. Previous studies have used reanalyses to investigate Mars' polar vortices, but to date

have only used those which assimilate TES data, namely the MACDA reanalysis (Mitchell et al., 2015; Waugh et al., 2016) and a preliminary version of the EMARS reanalysis (Waugh et al., 2016). This study assimilates MCS retrievals; MCS CDOD products (see Chapter 3) are not limited like TES CDOD nadir measurements were to areas with relatively warm surface temperatures (>220 K) (Smith, 2004), allowing greater coverage over the seasonal CO_2 caps and therefore more CDOD data for assimilation over these regions. It also uses the newer 2D retrievals which should give improved retrievals over the polar regions specifically (Kleinböhl et al., 2017) (these are discussed in more detail in the second half of this chapter). As noted in Chapter 3, however, MCS CDOD products are not nadir retrievals but extrapolations of profile retrievals, and therefore unable to directly retrieve dust in the bottom few kilometres of the atmosphere. This caveat should be borne in mind when discussing work using MCS CDOD products, as they may underestimate CDOD in the clear polar winter atmosphere.

Crucially for the understanding of how large-scale dust loading affects Mars' polar dynamics, this study assimilates CDOD and temperature data from the real GDS that occurred in MY 34. Guzewich et al. (2016) used a prescribed idealised dust scenario to investigate the effects of a generic GDS-like event at solstice. The use of a reanalysis allows the study of a realistic GDS-level dust loading closer to equinox, affording a chance to study GDS effects at a different season. This also allows comparison of a study on the MY 34 GDS using MCS data directly, and its findings of significant diurnal variation in southern polar vortex structure (Kleinböhl et al., 2020). Finally, this study devotes time to investigate wave-mean flow interactions, and specifically study how the horizontal structure of the polar vortices at this season might be affected by such interactions; for the first time using a full Mars GCM.

A diagnostic used frequently throughout Section 6.1 is potential vorticity (PV). PV is a measure of air circulation derived from the vorticity and thermal stratification of the atmosphere, and is valuable as a quantity that is conserved under adiabatic processes, making it especially useful for the study of polar dynamics. PV can be defined as

$$PV = -g(\xi + f)\frac{\partial \theta}{\partial p} \tag{6.1}$$

where g is the gravitational acceleration (3.72 m/s^2 on Mars), ξ is the relative isentropic vorticity (the relative vorticity of the air mass on that particular isentropic surface, where an isentropic surface is a surface of constant potential temperature), f is the Coriolis parameter (which accounts for the vorticity associated with the planetary rotation at a particular latitude), θ is the potential temperature, and p is the pressure. Equation 6.1 shows that PV has both dynamical elements, in the form of the vorticity of both the air mass itself and the planetary rotation, and thermodynamic elements, in the form of the potential temperature structure and static stability of the atmosphere. As stated, the PV of an air mass is conserved under adiabatic motions; therefore a full-scale destruction of PV implies significant changes to the potential temperature structure via atmospheric heating.

PV is given as a value on a particular isentropic surface; this study uses the 300 K isentropic surface. This is used for consistency with previous studies of the martian polar atmosphere (e.g. Mitchell et al., 2015; Waugh et al., 2016). This corresponds to an approximate altitude range of 20-30 km across the planet, and when zonal and meridional wind quantities are presented in this section they are integrated between 20-30 km.

Finally, PV is typically positive in the northern hemisphere and negative in the southern hemisphere, and increases in magnitude near the poles, due to the value of f. The term "magnitude" is used throughout this chapter for PV values, to make it clear that a larger negative PV value means a greater absolute value of PV. For simplicity, 1 "PVU" (potential vorticity unit) is defined throughout this chapter as 1×10^2 K m^2 kg^{-1} s^{-1}.

For the purposes of this section, MY 33 was chosen as a non-GDS year to compare against MY 34. The reason for this is that MY 33, as seen from the multi-year CDOD plots in Fig. 5.17 in the previous chapter, was a very typical MCS year in terms of dust loading, including in the timing and magnitude of its regional "A"-, "B-", and "C"-storms. Another

comparison year used throughout this thesis was MY 30, an unusually dust-free year. This is helpful in some contexts, such as when trying to disentangle the effects of dust loading from other effects. In this case, however, the very average dust loading of MY 33 affords a better comparison between a situation of "normal" dust loading and a situation of GDS-scale dust loading. The L_S=200-220° period was focussed on as it represents the height of global, homogeneous dust loading during the GDS period in MY 34 (see Fig. 5.17 in the previous chapter).

6.1.2 Results

Diurnally averaged changes

The 2018 Global Dust Storm (GDS) had a significant impact on polar atmospheric dynamics. This section explores its effects over both the north and south poles (occasionally referenced as "NP" and "SP" respectively throughout) as averaged over all local times.

Fig. 6.1 shows the changes to the average structure of the NP and SP polar vortices in the L_S=200-220° period caused by the MY 34 GDS. NP PV saw an overall reduction (Fig. 6.1.e) of up to 15 PVU, with the greatest reduction in PV around latitudes 60-70° N. This reduction was highly longitudinally asymmetric, with maxima in PV reduction at longitudes 180-90° E and -30-30° E. Broadly speaking, most of the PV reduction occurred in the eastern hemisphere, with little change in the western hemisphere. Despite the general tendency of a reduction in PV, PV actually increased slightly right over the pole itself. Despite these changes, the gross morphology of the NP polar vortex (Fig. 6.1.a,c) showed minor changes compared to the SP. The MY 33 morphology is more elliptical than the MY 34 morphology, which shows greater longitudinal symmetry; there is also a local PV minimum right over the pole in the MY 33 case which is no longer present in the MY 34 case.

NP zonal winds also saw an alteration, tending to increase in the GDS case by up to 20 m/s (Fig. 6.1.e). The wind speed increases align perfectly with the PV decreases described in the

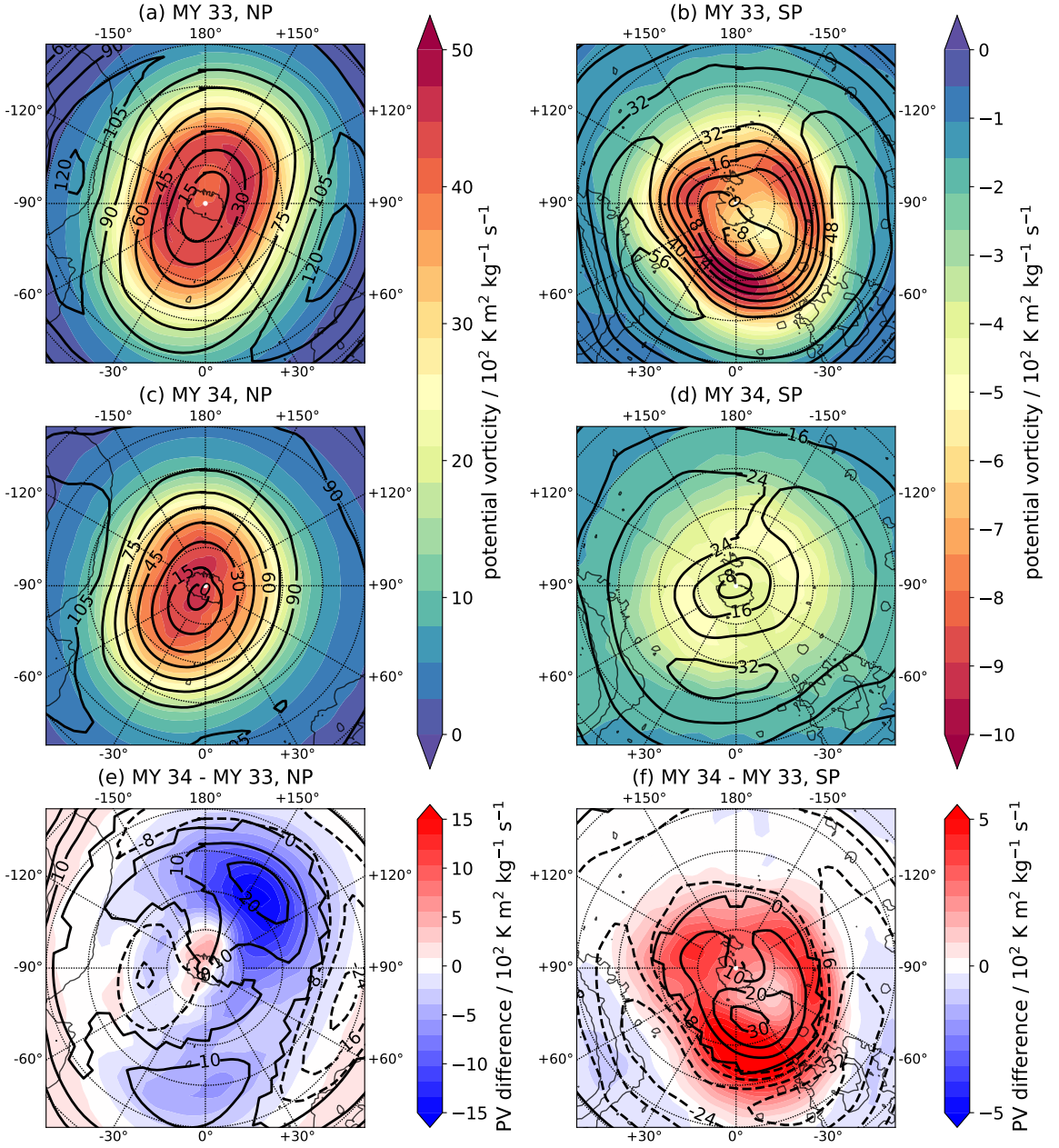

Fig. 6.1 Potential vorticity (colours) as averaged over the L_S=200-220° period on the 300 K isentropic level and zonal wind speeds (contours) as averaged between 20-30 km for (top) MY 33, (middle) MY 34, and (bottom) the difference between MY 34 - MY 33, over the (left) north pole and (right) south pole. Plots are stereographic projections where each latitude circle is 10° separate from its neighbours and the innermost circle represents the 80° latitude band. Lower absolute values indicate lower magnitude of potential vorticity, and vice-versa. Note the difference in scales and colours.

previous paragraph, with the eastern hemisphere once again showing the greatest change. In the western hemisphere there was little change to zonal wind speeds except between latitudes 70-80° N, where zonal winds decreased by an average of 8 m/s between longitudes -120° to 30° E. As with PV, the GDS-induced changes were highly longitudinally asymmetric. At the lower latitudes of 50-60° N, in (primarily) the eastern hemisphere, zonal wind speeds decreased by up to 16 m/s. This shows that the polar jet was shifted poleward by the GDS. Again, though, this shift was longitudinally asymmetric. As seen by comparing Figs. 6.1.a and 6.1.c, the GDS-induced changes to zonal winds were asymmetric and such as to make the MY 34 wind structure more symmetric and less elliptical than the MY 33 wind structure. In particular, a strong local wind maximum of up to 120 m/s in the eastern hemisphere (centred around 55° N, 60° E) in the MY 33 case was completely destroyed in the MY 34 case, creating a more longitudinally symmetric westerly jet. By contrast, a strong local wind maximum of up to 105 m/s in the western hemisphere (centred around 55° N, -90° E) in MY 33 was still present in MY 34. Despite the generally more symmetric and less elliptical wind structure in the MY 34 case, the jet appears shifted slightly off-pole towards -30° E. Finally, the closer clustering of contours in the MY 34 case shows a latitudinal narrowing of the westerly jet. There was a visible anticorrelation between PV and zonal wind speeds.

SP PV also saw an overall reduction (in magnitude terms), of up to 5 PVU. The pattern of reduction (Fig. 6.1.f) correlates exactly with the structure of the polar vortex in the non-GDS case (ie. the PV minima) (Fig. 6.1.b). The distinctive annular PV structure visible in MY 33 is both longitudinally asymmetric, being weaker generally in the western hemisphere and stronger in the eastern hemisphere, and centred well off-pole, with the central PV minimum located around 80° S and -30° E. For the GDS case in MY 34, the PV structure is far more uniform; there is still a (much weaker) annular pattern, which is now centred around the pole itself, and there is reduced longitudinal asymmetry. Lastly, the proportional decrease of PV at the SP (up to 50%) was much greater than at the NP, resulting in a totally altered polar

vortex morphology and a much diminished polar vortex, with PV destroyed across the entire polar vortex, suggesting great dynamical and/or radiative flux changes.

SP zonal winds generally increased around the locations where PV decreased, by up to 30 m/s, and decreased elsewhere (ie. outside the polar vortex) by up to 32 m/s (Fig. 6.1.f). The greatest wind speed increases were at the former location of the local PV minimum which described the centre of the polar vortex in MY 33 (Fig. 6.1.b); this calm "eye" had very low wind speeds in MY 33. Again, this signifies a shift of the (remnant) polar vortex from being centred off-pole to being centred over the pole itself. In contrast to the situation at the NP, zonal wind contours are more spaced apart in the MY 34 case, showing a less latitudinally focussed westerly jet. There is a decrease in zonal wind speeds equatorward of 60° S everywhere, as the increased dust loading from the GDS reduces the equatorward temperature gradient. As with the NP, the MY 34 wind structure was more longitudinally asymmetric than in MY 33, the latter showing (as with PV) an off-pole centre of the westerly jet; this explains the longitudinal asymmetry of changes to the wind structure. Also as with the NP, there was a visible anticorrelation between PV and zonal wind speeds.

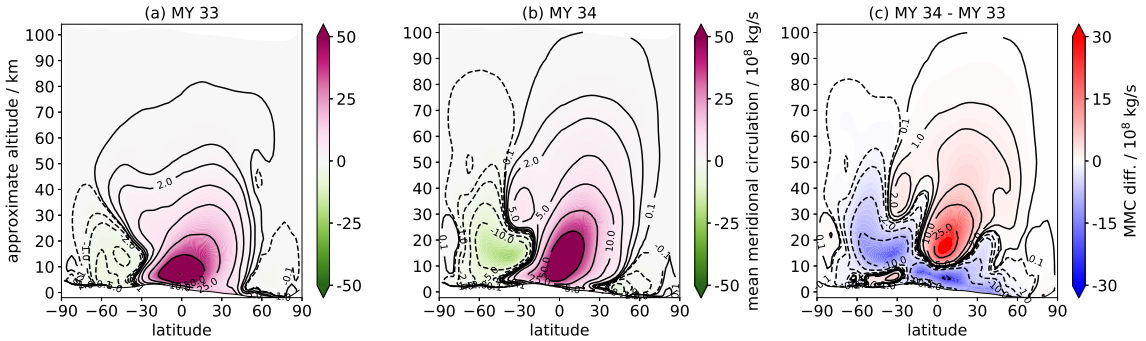

Fig. 6.2 Mean meridional circulation as averaged between L_S=200-220° for (left) MY 33, (middle) MY 34, and (right) the difference between them (MY 34 - MY 33). Positive values indicate a clockwise flow; negative values indicate an anticlockwise flow.

Fig. 6.2 shows the diurnally-averaged mean meridional circulation (MMC) as calculated for MY 33 and 34, and the difference between them, for the time of the MY 34 GDS. It is immediately apparent that the GDS significantly boosted the circulation. Both the dominant

cross-equatorial clockwise Hadley cell and the smaller southern anticlockwise Hadley cell were stronger during the time of the GDS (with an interesting exception sub-10 km). A stronger Hadley cell signifies greater transport of (warmer) air from equatorial and mid-latitudes towards higher latitudes, causing adiabatic heating. As well as being stronger, the cross-equatorial Hadley cell also extended further poleward in the northern hemisphere in the MY 34 case, signifying air transport towards higher latitudes than under non-GDS conditions; from up to $\sim$60° N in MY 33 to up to $\sim$75° N in MY 34. This further latitudinal extension does not appear to be the case for the southern anticlockwise Hadley cell, however.

It is also worth examining how the meridional circulation was altered at different longitudes, to see if the increased longitudinal symmetry in the MY 34 polar vortex structure was reflected in the circulatory structure. Fig. 6.3 shows the mean meridional circulation as calculated for six different longitude ranges, at increments of 60°. Here it should be noted that the mean meridional circulation is defined as a zonal average field, and so these longitudinally-specific fields are not necessarily real circulations that exist at any particular time on the planet, given the existence of zonal transport and therefore the interconnectedness of the meridional circulation at different longitudes. But the MMC itself as calculated is also a mathematical construct; not necessarily a perfect representation of what the planetary global circulation actually looks like (for example, a modelled overturning cell is multiply realisable and could be due to roughly symmetric air uplift and subsidence, but could also be due to more localised rapid uplift and more spatially broad slow subsidence (Rafkin, 2012)), but an instructive guide as to how it appears to behave at large scales based on our model representation of the meridional wind field. Analysis of Fig. 6.3 could therefore still provide some insight into the longitudinal asymmetry of the large-scale circulation and its interaction with large-scale polar dynamics.

With that caveat, Fig. 6.3 does indeed show that there is huge variation in the modelled meridional circulation at different longitudes. The zonally-averaged MMC, as seen in Fig.

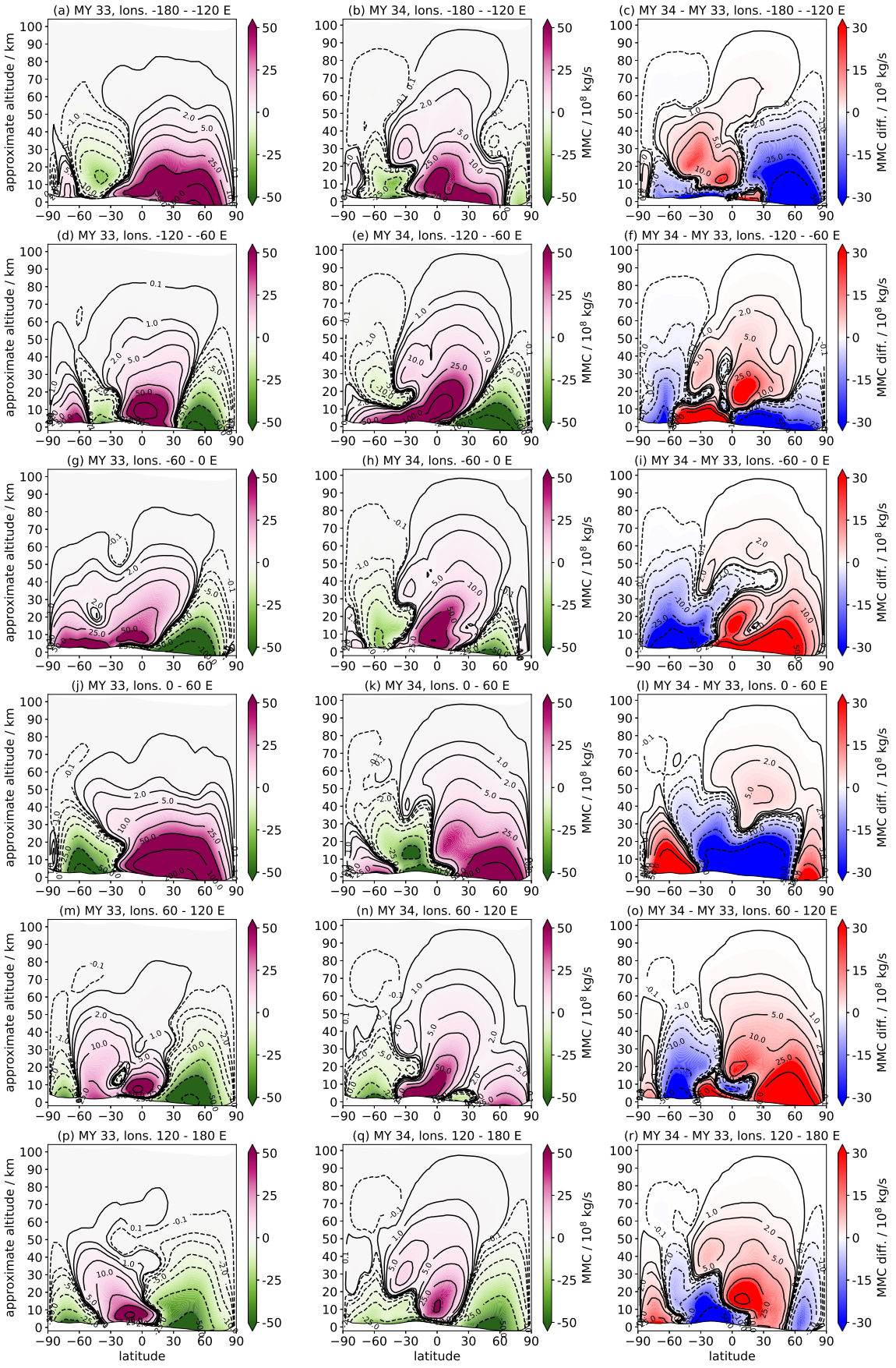

Fig. 6.3 MMC calculated for different longitude ranges, averaged between L_S=200-220°. Positive values indicate a clockwise flow; negative values indicate an anticlockwise flow.

6.2, is composed of a dominant cross-equatorial clockwise Hadley cell and a smaller southern anticlockwise Hadley cell. In addition to these thermally direct circulatory cells, there is frequently another cell at mid-high northern latitudes. This cell is thermally indirect, as it is not directly driven by solar heating as are the thermally direct cells, which upwell at the subsolar latitudes. In the terrestrial literature, such thermally indirect features at mid-latitudes are called "Ferrel cells", but are not strictly speaking real circulatory cells; rather, they indicate the presence of mechanical forcing from planetary wave activity due to thermal contrasts at mid-latitudes (Salby, 2011, Chapter 15), and their very presence in the Eulerian mean meridional circulation is an artefact of the averaging process (see Andrews et al., 1987, Chapter 3). In other representations of transport such as the transformed Eulerian mean circulation, which accounts for wave-driven transport, these thermally indirect "cells" disappear (Holton, 2004a). For the purposes of this chapter, these features are referred to as thermally indirect cells. Given the thermal contrast at northern mid-latitudes at this time of year (L_S=200-220°, early northern winter) the presence of these cells implies baroclinic planetary wave activity.

Looking at MY 33, this pattern is replicated at some longitude ranges: -180-120° E (Fig. 6.3.a) and 0-60° E (Fig. 6.3.j) show this rough structure the most clearly. But at some longitudes the circulatory structure is very different. For example, northern wave activity is significantly greater at the longitude ranges -120- -60° E (Fig. 6.3.d), -60-0° E (Fig. 6.3.g), 60-120° E (Fig. 6.3.m), and 120-180° E (Fig. 6.3.p). The latter three of these four ranges correspond to the longitudes of the northern topographic depressions, as seen in Fig. 6.4, where baroclinic wave activity is strongest (e.g. Barnes et al., 1993). At some longitude ranges, such as -180- -120° E (Fig. 6.3.a) and 0-60° E (Fig. 6.3.j), the dominant clockwise Hadley cell extends all the way to the north pole. At some, such as 0-60° (Fig. 6.3.j), 60-120° E (Fig. 6.3.m), and 120-180° E (Fig. 6.3.p), the southern anticlockwise Hadley

cell extends all the way to the south pole (broadly speaking, this encompasses the eastern hemisphere), though there is also a strong southern Hadley cell at -180- -120° E (Fig. 6.3.a).

Comparing these circulatory patterns to the MY 33 polar vortex longitudinal structure in Fig. 6.1.b, there appears to be a correlation. In the south, the presence of an anticlockwise Hadley cell (Hadley meaning thermally direct, ie. rising from around the subsolar latitude) extending to the SP correlates to where the polar vortex (defined as the annular band of high PV and its corresponding lower zonal wind speeds) is shifted poleward: between -180- -120° E (Fig. 6.3.a), 0-60° E (Fig. 6.3.j), and 120-180° E (Fig. 6.3.p). Likewise, where the polar vortex bulges further equatorward, there is instead a strong clockwise circulation extending from the SP equatorward: between -120- -60° E (Fig. 6.3.d) and -60-0° E (Fig. 6.3.g). In the north, the presence of a strong clockwise Hadley cell extending to the NP appears to correlate with where the polar vortex is shifted poleward, as can be seen in the PV contour lines (Fig. 6.1.a): between -180- -120° E (Fig. 6.3.a) and 0-60° E (Fig. 6.3.j). Where there is instead a strong anticlockwise thermally indirect cell dominant at northern high latitudes, the polar vortex extends further equatorward: such as between longitudes -60-0° E (Fig. 6.3.g) and 120-180° E (Fig. 6.3.p).

The equivalent longitude ranges in the MY 34 case show significant and complex differences as compared to the MY 33 case, but some broad patterns can be identified. In general, the circulations at different longitude ranges show greater zonal symmetry than in MY 33, and resemble the zonally averaged MMC (as seen in Fig. 6.2) more closely. Specifically, the circulations at -180- -120° E (Fig. 6.3.b), -120- -60° E (Fig. 6.3.e), -60-0° E (Fig. 6.3.h), and 120-180° E (Fig. 6.3.q) all bear greater morphological resemblance to the zonally averaged case in MY 34 than they do in MY 33. The exception is between 0-120° E (Fig. 6.3.k,n), where the northern hemisphere is dominated by a clockwise cell extending all the way to the pole.

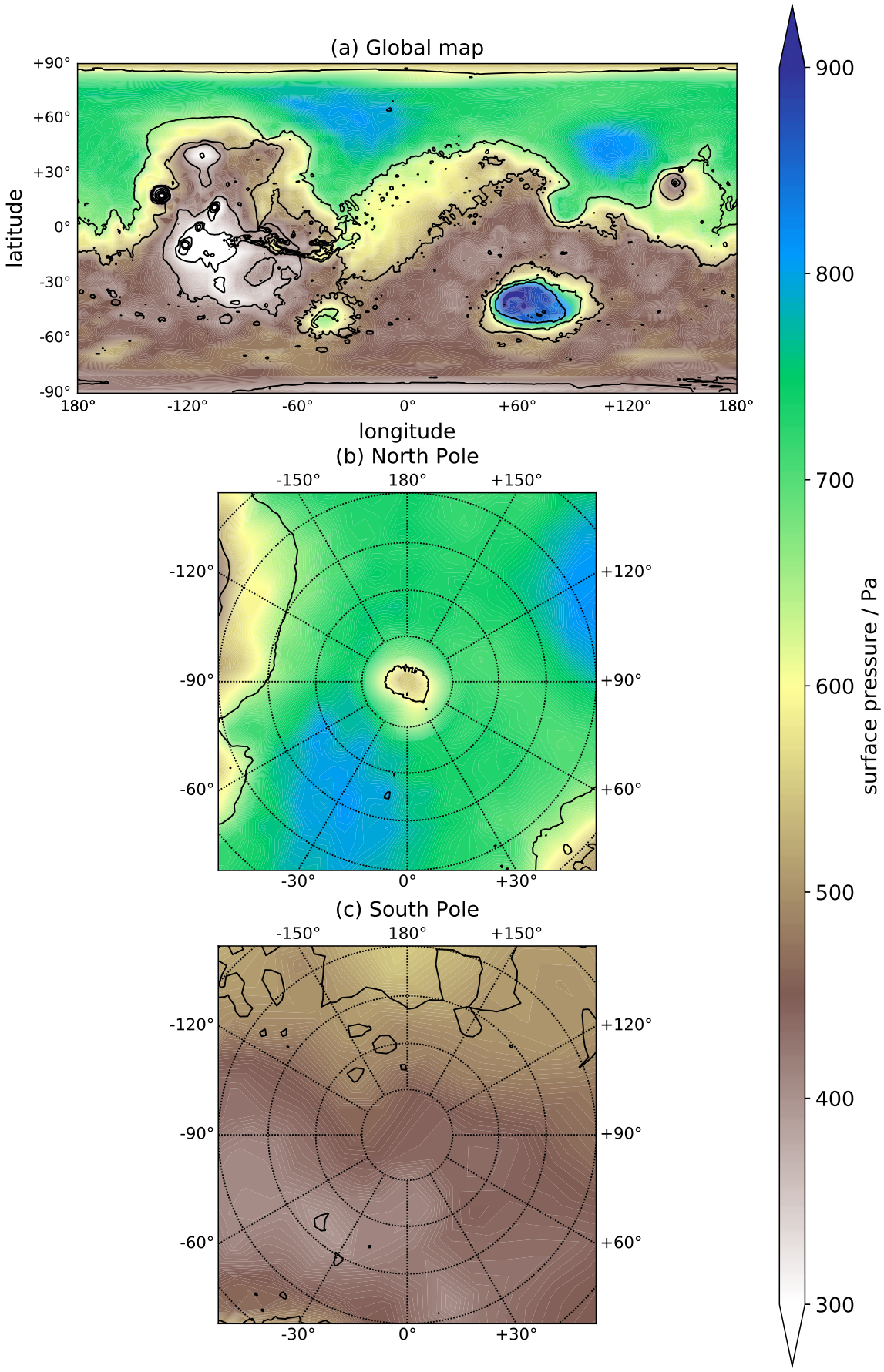

Fig. 6.4 Surface pressures as averaged between L_S=200-220° in MY 33, in (top) a global cylindrical projection and (middle, bottom) a polar stereographic projection for the north pole and south pole perspective. Contours indicate lines of topography.

This more longitudinally symmetrical circulation correlates well with the more longitudinally symmetrical polar vortices in MY 34 at both the NP and SP (Fig. 6.1.c,d). At the longitudes identified above where there exists a strong anticlockwise Hadley cell extending to the SP in MY 33, in MY 34 this cell is significantly weakened; for example, at longitudes 0-60° E (Fig. 6.3.l) and 120-180° E (Fig. 6.3.r). Likewise, at southern longitudes where there is instead a strong clockwise flow from the SP in MY 33, in MY 34 this is diminished and/or reversed; for example, at longitudes -120- -60° E (Fig. 6.3.f) and -60-0° E (Fig. 6.3.i). At the northern longitudes identified above where there exists a strong clockwise Hadley cell extending to the NP in MY 33, in MY 34 this is significantly altered. At longitudes -180- -120° E (Fig. 6.3.c), the clockwise Hadley cell no longer extends to the NP. At longitudes 0-60° E (Fig. 6.3.l), the strength of the clockwise Hadley cell is strongly diminished below 30 km up to latitude 60° N, but increases between 60-90° N. Meanwhile, at northern longitudes where thermally indirect cell activity dominates near the NP in MY 33, in MY 34 this is generally diminished, though the effects are complex. At longitudes -60-0° N (Fig. 6.3.i), northern high-latitude wave activity is completely diminished and the cross-equatorial clockwise Hadley cell increases in both latitude and latitudinal extent in the northern hemisphere. At longitudes -120- -60° E (Fig. 6.3.f) and 120-180° E (Fig. 6.3.r), high latitude (60-90° N) thermally indirect cell activity actually increases, but in conjunction a strengthened clockwise Hadley cell extending into higher northern latitudes (approximately extending from 30° N in MY 33 to 60° N in MY 34). And at longitudes 60-120° E (Fig. 6.3.o), high latitude thermally indirect cell activity is completely replaced by the clockwise Hadley cell, which extends all the way to the NP.

It has been shown so far that the modelled longitudinal asymmetries in the polar vortices are related to longitudinally asymmetric meridional circulatory patterns; but what is the cause of this longitudinal asymmetry in meridional circulation? Fig. 6.5 shows the meridional wind deviation as integrated between altitudes 20-30 km. The meridional wind deviation

is defined as the difference between the time mean (in this case, between L_S=200-220°) of meridional wind field and the time and zonal mean of the meridional wind ($\overline{v} - [\overline{v}]$, where the overbar and brackets represent time and zonal means respectively), and hence indicates the presence of stationary planetary waves. Fig. 6.5.a shows the stationary wave pattern in MY 33, a non-GDS year. A clear spatial wavenumber 2 signal is visible at northern mid-high latitudes; this pattern is due to the zonal topographic differences present at northern mid-high latitudes, with two notable depressions at the plains of Acidalia and Utopia and higher topography around Alba Patera and northern Arabia Terra (see Fig. 6.4), which induce differential heating and thus drive adjacent clockwise and anticlockwise circulations (Haberle et al., 2019; Hollingsworth and Barnes, 1996; Nayvelt et al., 1997). The presence of this wavenumber 2 feature, including the associated wind directions, has been seen in observations of north polar hood clouds (Haberle et al., 2019). There is a south-to-north flow between approximately -10-70° E and 160- -120° E, and a north-to-south flow between approximately -110- -10° E and 70-160° E. There is also stationary wave activity at southern high latitudes - this is more ambiguous, indicating a wavenumber 2 feature at mid latitudes which transitions into a wavenumber 1 feature poleward of 75-80° S; other modelling work suggests that this becomes a more unambiguous wavenumber at southern winter (Hollingsworth and Barnes, 1996), and this is borne out in this reanalysis (not shown). There is a south-to-north flow between approximately -70-10° E, and a north-to-south flow between approximately 90-180° E, both extending all the way to the pole. There are also lower latitude flows: a north-to-south flow between approximately -20-60° E, and a less well-defined south-to-north flow between approximately 60-120° E.

The MY 34 GDS drastically changed the stationary wave structure in both hemispheres, as seen in Fig. 6.5.b,c. In the north, the amplitude of all the waves and troughs was decreased by up to 20 m/s. Morphologically, there were still two significant remnants: the north-to-south flow at around -110- -10° E, and the adjacent south-to-north flow at around -10-70° E. This

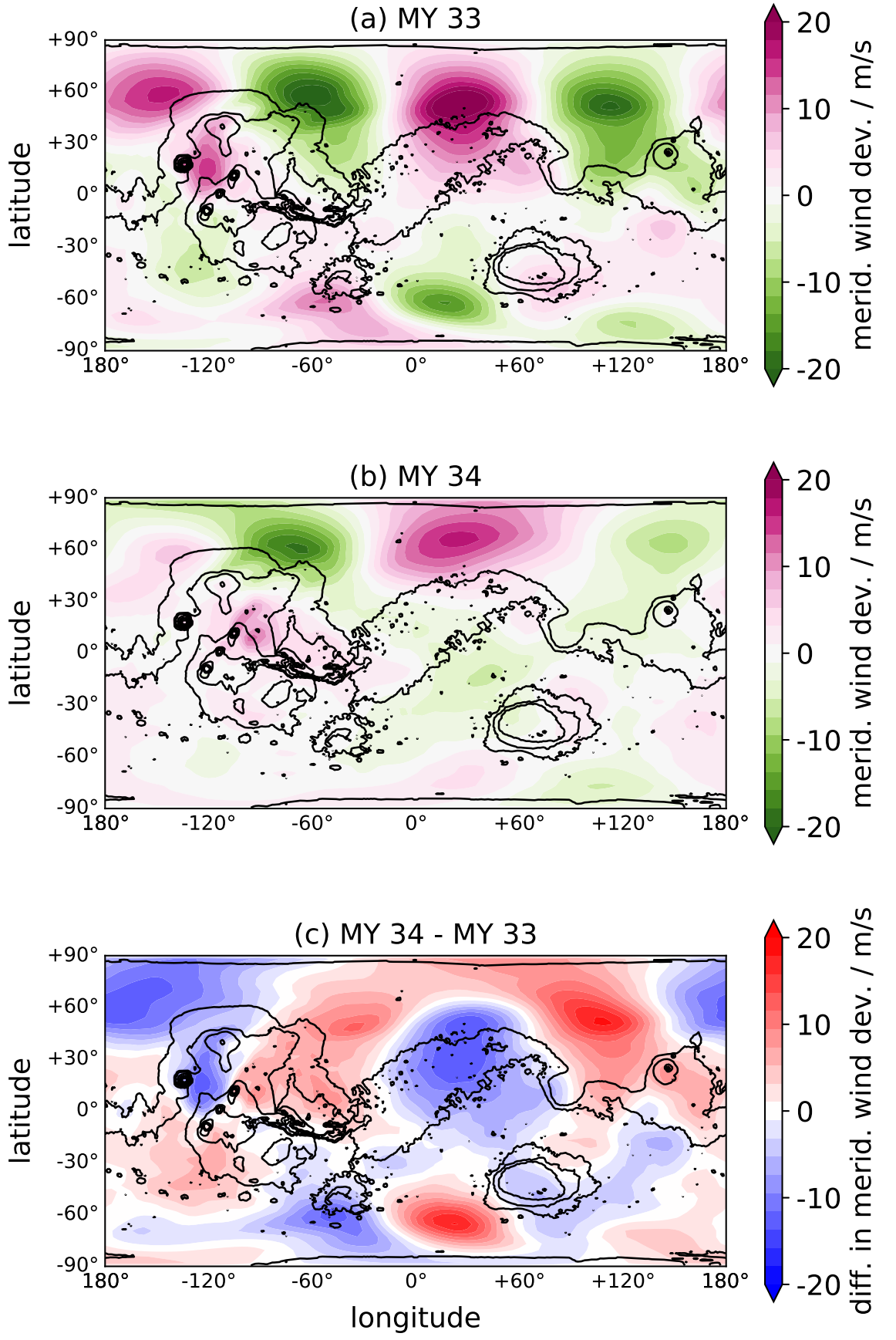

Fig. 6.5 Meridional wind deviation ($\overline{v} - [\overline{v}]$) at 20-30 km for L_S=200-220° for (top) MY 33, (middle) MY 34, and (bottom) the difference between MY 34 - MY 33.

remnant flow was also shifted poleward, from extending to mid-latitudes in MY 33 to being limited to ∼45° N in MY 34. Meanwhile the other two flows described above were reduced to almost zero. In the south, the mid-high latitude wavenumber 2 structure was completely destroyed, leaving only a very weak wavenumber 1 feature near the pole. This consisted of, roughly, a weak south-to-north flow between -180-60° E and a weak north-to-south flow between 60-180° E.

This stationary wave structure, and the changes induced to it by the GDS, correspond well to the modelled circulation and polar vortex structure, and their associated GDS-induced changes. In the northern hemisphere, the MY 33 stationary wave structure - a wavenumber 2 pattern - matches well with the modelled longitudinal asymmetry of the elliptical polar vortex (Fig. 6.1.a). Where the vortex extends further equatorward - the elongated parts of the ellipse - is where the meridional wind deviation consists of a north-to-south flow, namely between -110- -10° E and between 70-160° E. Where the vortex is more constrained towards the pole - the narrow parts of the ellipse - is where the meridional wind deviation consists of a south-to-north flow, namely between -10-70° E and between 170- -110° E. As stated, the MY 34 GDS significantly diminished the northern stationary wave amplitudes, in particular between -180- -120° E and 70-180° E. This correlates very well with the longitude range of greatest PV reduction (Fig. 6.1.e). Where the pre-existing stationary wave structure remained relatively intact, on the other hand, such as between -120- -60° E, there was minimal change in PV.

In the southern hemisphere, there is also a correspondence between the stationary wave pattern and the polar vortex structure (Fig. 6.1.b). Where the vortex extends further equatorward is where the meridional wind deviation consists of a south-to-north flow, namely between -70-10° E. Where the vortex is more constrained towards the pole is where the meridional wind deviation consists of a north-to-south flow, namely between 10-180° E. The MY 34 GDS almost completely destroyed any southern stationary wave activity (Fig.

6.1.f), resulting in the modelled highly symmetrical MY 34 polar vortex (Fig. 6.1.d). The greatest change was to where the MY 33 stationary wave amplitudes were greatest, between -60-60° E; this is where the MY 33 polar vortex was most latitudinally extended and hence longitudinally asymmetrical.

While the NP PV structure was largely unaltered in a significant sense during the GDS except so as to make it more longitudinally symmetric and less annular, the SP polar vortex saw a proportionally much greater and more longitudinally extensive reduction in PV, even at longitudes where the stationary planetary wave pattern was not significantly altered; this suggests that in addition to dynamics, other factors were at play in the southern polar vortex. Fig. 6.6 shows zonally averaged temperatures and dust opacities for MY 33 and MY 34. It is apparent that GDS-induced atmospheric heating at southern high latitudes was much greater (up to 33 K in the 20-30 km range) than at northern high latitudes (up to 15 K in the 20-30 km range, and significantly less within the polar vortex itself). The southern hemisphere saw an almost complete destruction of the polar vortex, while in the north the polar vortex narrowed in latitudinal extent but remained coherent and clearly defined. Crucially for the thermal winds around the SP, the meridional temperature gradient in the southern hemisphere was substantially reduced except nearest the pole, as visible from the increased spacing between vertical contour lines. This matches with the GDS-induced increase in dust opacity, which occurred primarily between latitudes 75° S to 50° N (Fig. 6.6.f), though there was also a large increase (up to 0.02) betwen 60-90° S up to 20 km altitude. There was little increase in dust opacity north of 60° N (<0.01), and any increase occurred below $\sim$10 km. This implies that direct diabatic heating from the increased dust presence may have had a role in affecting the southern polar vortex, but not the northern.

To better ascertain the roles of diabatic and adiabatic/dynamical heating, Fig. 6.7 shows shortwave (SW), longwave (LW), and net (SW+LW) radiative heating rates in the atmosphere and how they differ between MY 33 and MY 34. SW heating relies solely on the dust

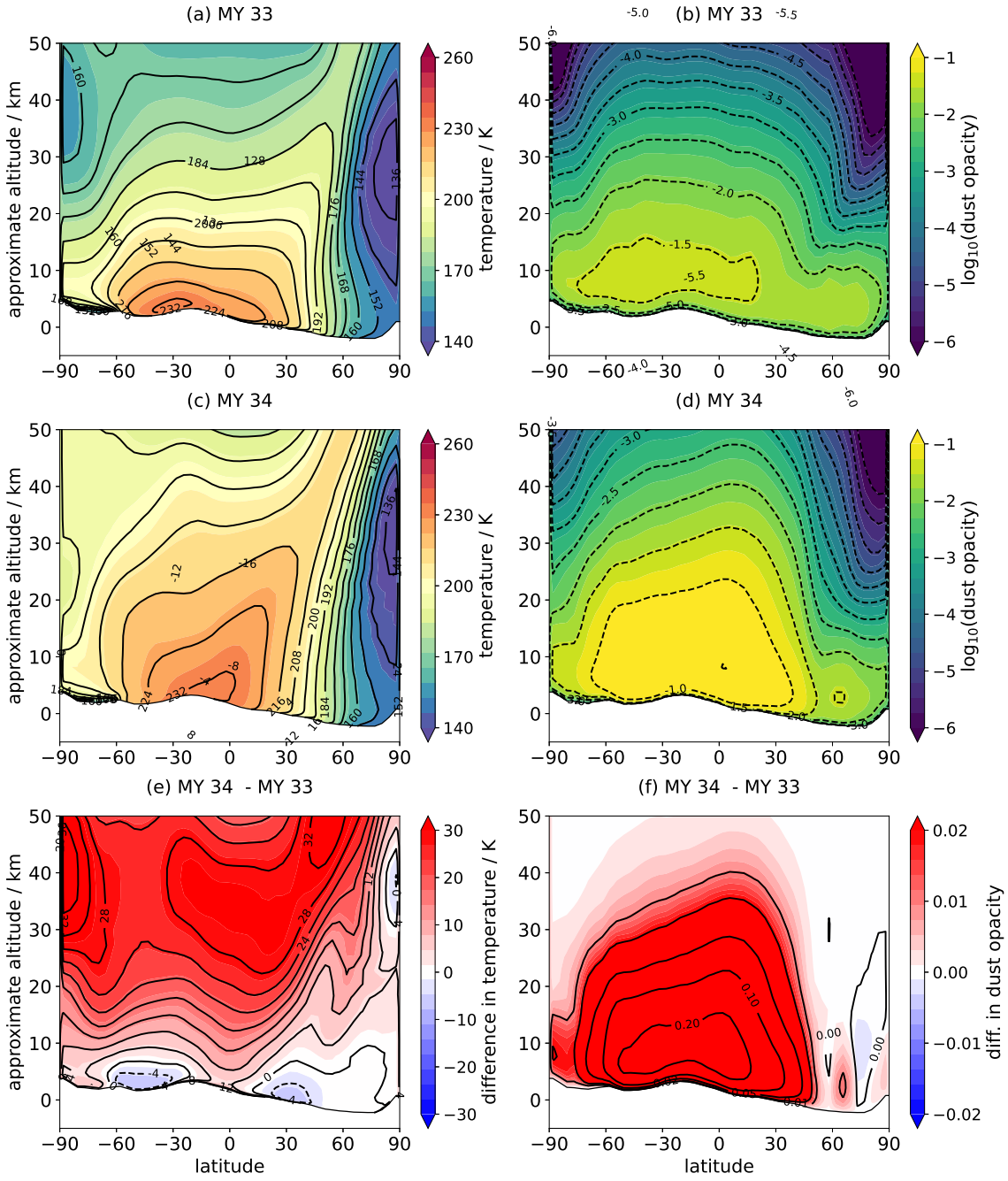

Fig. 6.6 Zonally-averaged (left) temperatures and (right) dust opacities averaged between L_S=200-220° for (top) MY 33, (middle) MY 34, and (bottom) the difference between MY 34 - MY 33. The plotted dust opacities in subplots b. and d. are $\log_{10}$ values; the coloured values in subplot f. are actual dust opacities while the contour lines are $\log_{10}$ values. All dust opacities are at 600 nm, as used in the MGCM. Altitude was cropped to 50 km for the plots.

presence in the atmosphere, while LW heating is dependent on both dust and atmospheric emission. Given the short radiative timescale of the martian atmosphere, the SW and LW heating rates should be in approximate balance in a radiative-convective model (except for in the planetary boundary layer); in a model containing dynamical processes, the deviations from radiative balance indicate the presence of dynamical heating/cooling (Wolff et al., 2017). For example, in MY 33 (Fig. 6.7.c) dynamical cooling is visible between latitudes 0-60° S and altitudes 10-30 km, showing the presence of the upwelling branch of the two Hadley cells, while dynamical heating is visible at high altitudes between 30-60° N and 60-90° S, showing the presence of the downwelling Hadley circulation and Mars' famous polar warming.

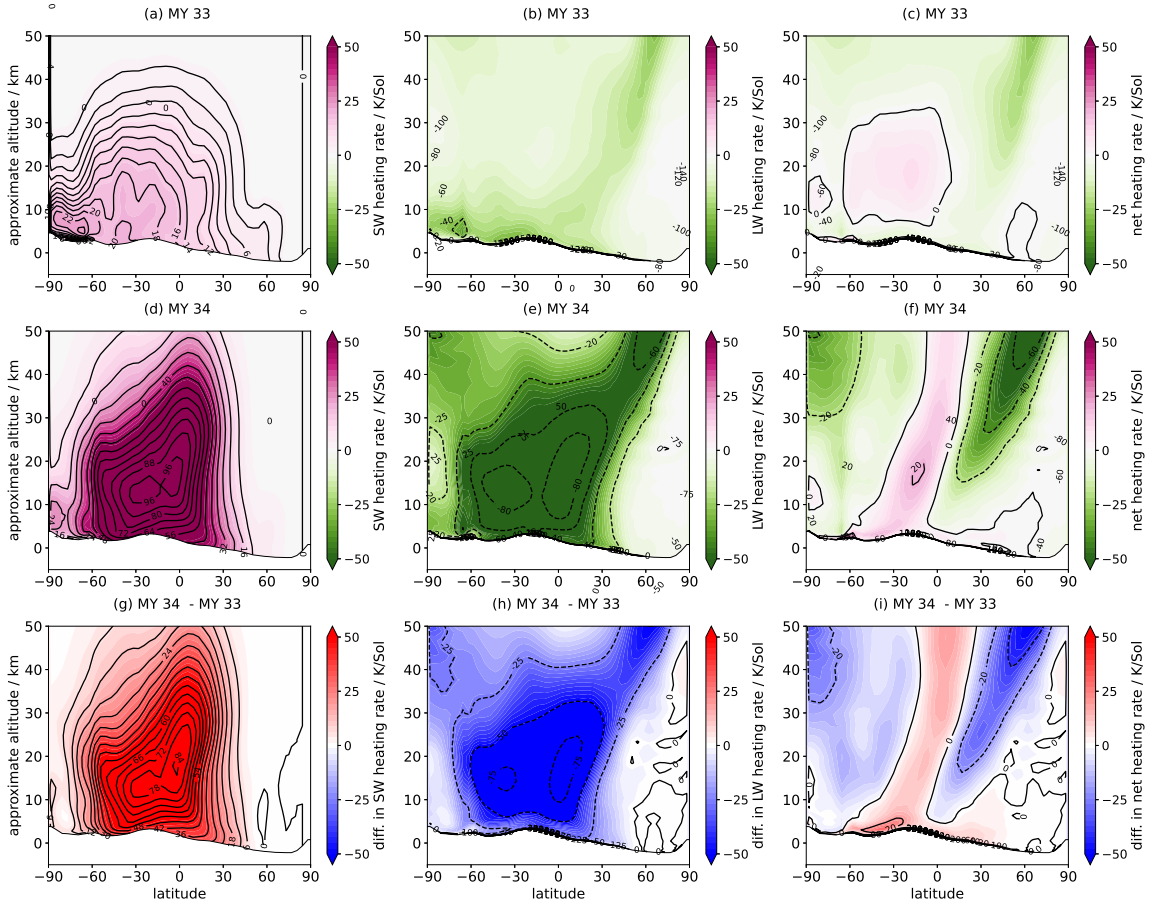

Fig. 6.7 Zonally averaged (left) shortwave (SW), (middle) longwave (LW), and (right) net (SW+LW) radiative heating rates averaged between L_S=200-220° for (top) MY 33, (middle) MY 34, and (bottom) the difference between MY 34 - MY 33. Altitude was cropped to 50 km for the plots.

The increased dust loading in MY 34 caused increases in both SW heating of up to 6 K/sol (Fig. 6.7.g) and LW cooling (Fig. 6.7.h) rates, particularly between latitudes 75° S to 45° N. Fig. 6.7.g,h shows how southern SW heating and LW cooling rates increased over the southern pole and especially at and above 20 km altitude, indicating the important role of direct dust-related atmospheric heating at southern high latitudes. These net diabatic cooling effects altered the thermal structure of the atmosphere and helped cause a local reduction in potential vorticity from equation 6.1. In the north, by contrast, there was minimal alteration to diabatic heating rates poleward of 45° N, due to the absence of dust. Fig. 6.7.i shows how dynamical heating was altered by the GDS. Dynamical heating can be identified by summing SW heating and LW cooling, with residual negative values showing the transport of warmer air from elsewhere (diabatic and adiabatic heating therefore have opposite signs), thereby indicating adiabatic heating by dynamical processes. There was an increase in polar warming at both the NP and SP due to the enhanced Hadley circulation, and a corresponding increase in dynamical cooling (ie. residual SW heating) over the tropics. The increased dynamical heating over the SP occurred primarily above 30 km, though there was also a $\sim$10 K/sol increase between 20-30 km at 65° S. In the north, the increased dynamical heating narrowed the size of the polar vortex, but a coherent polar vortex remained with no net radiative flux changes.

The results from analysis of atmospheric temperatures, dust opacities, and radiative heating rates suggest that the GDS induced significant dynamical changes at both poles, but also impacted the SP alone through increased diabatic heating. The effect in the north was to narrow the latitudinal extent of the polar vortex and make the polar vortex structure less elliptical and more longitudinally symmetric, but not otherwise destroy PV across the whole pole or change polar vortex temperatures. The effect in the south, by contrast, was both to create a more symmetrical polar vortex and also to significantly reduce PV across the entire

pole by reducing the thermal gradient of the southern polar atmosphere (as seen in Fig. 6.6.c, leading to a much diminished southern polar vortex.

Diurnal behaviour

This section investigates how each polar vortex was affected by the GDS at different local times. As well as the NP/SP notation described above, this section also employs the concept of Mars Universal Time (MUT). MUT is the local time at longitude 0° (east longitude), e.g. MUT 00:00 is when it is midnight at longitude 0°, midday at longitude 180°, etc. Note that the MGCM uses Mars hours and minutes, of which there are the same number in a martian sol as there are SI hours and minutes in a terrestrial day; seconds are SI seconds.

The southern polar vortex exhibited a high degree of variation throughout the diurnal cycle, as seen in the plots of PV and CDOD at different local times in Fig. 6.8. This behaviour during the GDS was first noted in MCS temperature and CDOD observations from MCS by Kleinböhl et al. (2020): there appears to be a mass of colder, more isolated air (indicated by higher PV) and absence of dust (indicated by lower CDOD) that follows the nightside of the planet, centred around MUT 06:00. This is reproduced in the reanalysis, as shown in Fig. 6.8: the patch of higher (absolute) PV is centred at MUT 06:00, and is followed around the nightside by a corresponding minimum in CDOD (< 0.6). Interestingly, there does appear to also be a diurnal variation in the magnitude of the high PV zone, with (for example) the PV being much greater (again, in absolute terms) at MUT 14:00 than at other local times. This asymmetry suggests that there may still be some longitudinally asymmetric processes at work, even despite the almost total elimination of the southern high-latitude wavenumber 1 feature mentioned previously in Section 6.1.2.

Kleinböhl et al. (2020) attribute the diurnal behaviour of the southern polar vortex during the GDS to the variation of the MMC throughout the day, with the GDS-enhanced circulation amplifying a pre-existing pattern. To argue for this point, they present the MY 34 MMC as

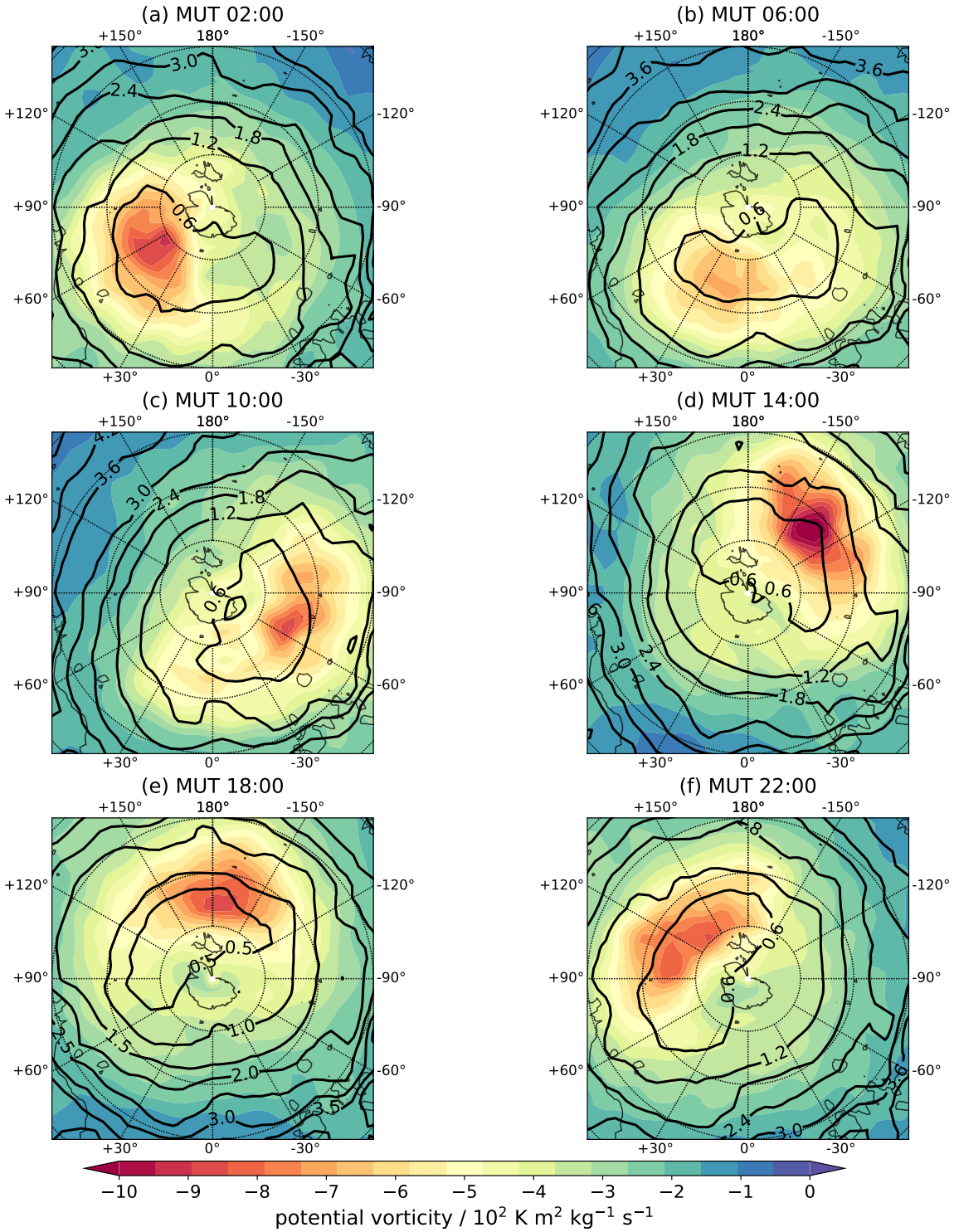

Fig. 6.8 Potential vorticity (colours) as averaged over the L_S=200-220° period on the 300 K isentropic level and CDOD at 610 Pa (contours) over the SP for MY 34 at six different MUTs. Each MUT is averaged over the 2 hours before and after, or 4 hours in total. Plots are stereographic projections where each latitude circle is 10° separate from its neighbours and the innermost circle represents the 80° latitude band. Lower absolute values indicate lower potential vorticity, and vice-versa.

calculated for different local time ranges in an MGCM, with the spatial dust distribution set using an MY 34 CDOD map (Montabone et al., 2020). They show a daytime circulation that transports air to the south pole, and a nighttime circulation that transports air away from it, explaining the presence of dust and warmer air (expressed as lower absolute PV) on the south polar dayside.

To corroborate and further explore these results, the MMC at different local times was calculated at various local times for both MY 34 and also MY 33, to see if the described pattern holds in a non-GDS year. Fig. 6.9 presents these results, and the difference between the MY 34 and MY 33 circulation at each local time. The MY 34 results (Fig. 6.9) show very good agreement with Kleinböhl et al. (2020); there is a strong circulation away from the SP at the nighttime MUTs of 02:00 and 22:00, a strong circulation towards the SP at the daytime MUTs of 10:00 and 14:00, and a weaker transitional circulation towards the SP at the dawn/dusk MUTs of 06:00 and 18:00. The presence of an albeit weak circulation towards the SP at the dusk and dawn cases explains why the PV minimum covers a small longitudinal extent, rather than an entire hemisphere.

The MY 33 MMC results in Fig. 6.9 provide a means to confirm whether the MY 34 local time circulatory pattern holds in a non-GDS year, and thus whether it is in fact the GDS-boosted circulation that is responsible for the SP polar vortex behaviour. These results show that the MY 33 circulation does indeed closely morphologically resemble the MY 34 circulation at nearly all local times, simply in a comparatively weakened form in both hemispheres. This is evident at MUTs 02:00, 10:00, 14:00, 18:00, and 22:00. The sole possible exception is the circulation at MUT 06:00. At this time the MY 33 circulation is dominated by a clockwise flow with some slight anticlockwise circulation near the SP; there is a much stronger and more latitudinally extensive anticlockwise circulation in MY 34. Even this difference is minor in the context of the diurnally averaged flow, however, given the weaker dawn circulation compared to other MUTs even in MY 34.

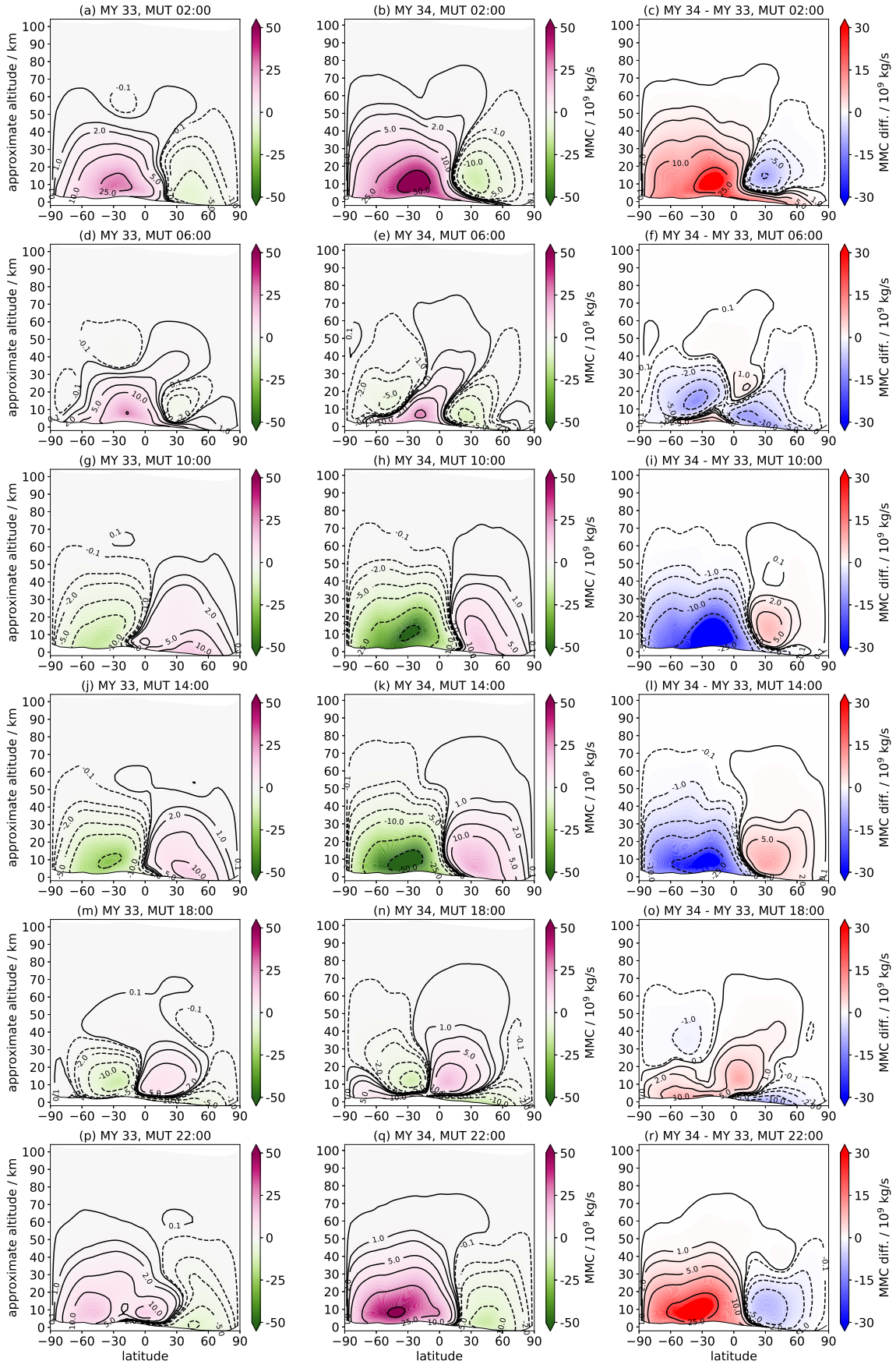

Fig. 6.9 MMC calculated for different MUTs, averaged between L_S=200-220°. Positive values indicate a clockwise flow; negative values indicate an anticlockwise flow.

The final corroborative step in following the Kleinböhl et al. (2020) hypothesis is to see if the modelled flow structure in MY 33, being morphologically almost identical but weaker in magnitude than that in MY 34, also has a morphologically almost identical but weaker effect on the diurnal behaviour of the MY 33 southern polar vortex. In other words, one would expect to see a similar effect in MY 33 where a higher absolute PV air mass, coupled with a local CDOD minimum, follows the nightside of the planet. Fig. 6.10 displays the diurnal variation of the southern polar vortex and CDOD. The first thing to note is that the distinctive annular shape of the vortex is maintained at all local times, including the location of its central eye at around 80° S and -60° E and the corresponding latitudinal extension of the vortex at some longitudes and narrowing at others. This accords with the results in Section 6.1.2; as the southern stationary wave structure appears to be responsible for this longitudinal asymmetry, and stationary waves are by definition constant in their spatial phase, one would expect the longitudinal structure to hold. That said, there is also a definite variation in local time of both PV and CDOD. While there is a clear ring of higher absolute PV present at all MUTs, a localised increase in absolute PV appears to follow the nightside of the planet. The magnitude of this localised increase is highly asymmetric with longitude, however; for example, the PV minimum is over 3 PVU greater at midnight at longitude 0° (Fig. 6.10.a) than at longitude 180° (Fig. 6.10.d). This seems likely to be due to the influence of stationary wave activity, as described previously in Section 6.1.2. While less obvious than in MY 34, there also appears to be a CDOD minimum which follows MUT ∼06:00, which is most visible in subplots Fig. 6.10.b,d,e,f. To summarise, then, these results corroborate the Kleinböhl et al. (2020) finding that the observed MY 34 southern polar vortex behaviour is due to an enhanced MMC at all local times boosting an already present mechanism by which warmer, dustier air is transported to the dayside of the pole and colder, clearer air remains on the nightside. As well as the local time effect, there is also a complex interplay with southern stationary waves.

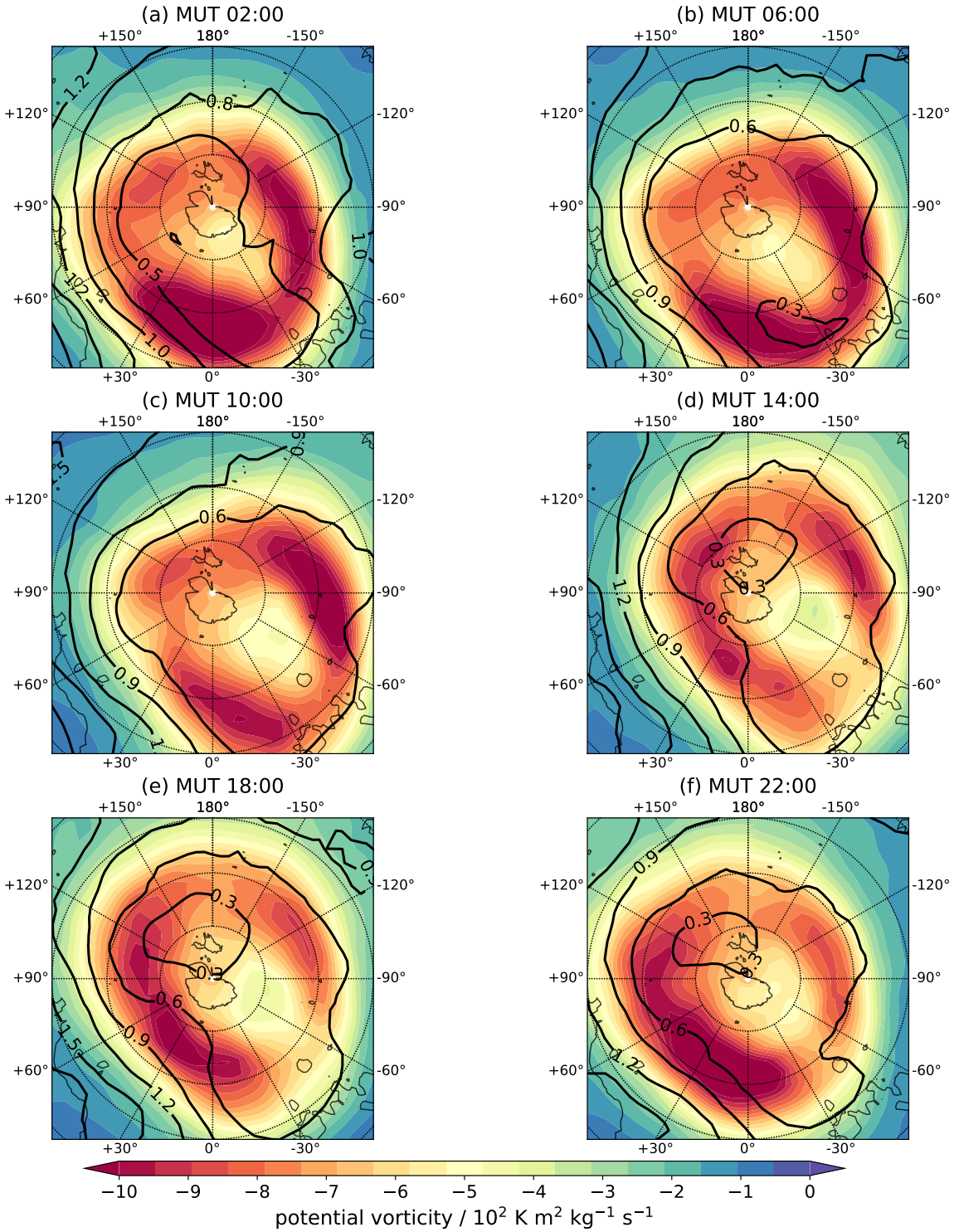

Fig. 6.10 Potential vorticity (colours) as averaged over the L_S=200-220° period on the 300 K isentropic level and CDOD at 610 Pa (contours) over the SP for MY 33 at six different MUTs. Each MUT is averaged over the 2 hours before and after, or 4 hours in total. Plots are stereographic projections where each latitude circle is 10° separate from its neighbours and the innermost circle represents the 80° latitude band. Lower absolute values indicate lower magnitude of potential vorticity, and vice-versa.

Finally, it is worth investigating whether a similar vortex-shifting behaviour occurs at the northern polar vortex, as would be implied by the plots in Fig. 6.9. Interestingly but perhaps not surprisingly given the location of the subsolar latitude in the southern hemisphere, these plots show that the northern hemispheric circulation is at every local time and in both MY 33 and MY 34 weaker than the southern one. One would therefore *a priori* expect a similar but weaker diurnal cycle at the NP. Fig. 6.11 shows the diurnal behaviour of the northern polar vortex in MY 34. While there does appear to be some diurnal variation, it is less clear than in the south, and more dominated by apparent intrinsic longitudinal asymmetries. PV is consistently high at around longitudes -60-0° E for about half the diurnal cycle, and at around longitudes 150- -150° E for the other half; elsewhere, it is notably weaker than at the noted longitudes even when it receives a boost from the presence of local nighttime (MUT 02:00-06:00). This pattern is consistent with the observed residually elliptical PV structure visible in the diurnally averaged plot (Fig. 6.1.c), which, as mentioned, is linked to the stationary wavenumber 2 feature at northern high latitudes. Meanwhile there is no discernible pattern to CDOD diurnal variation. These results suggest that even in the case of an enhanced MMC as in MY 34, the local time variations in the northern PV structure are largely obscured by planetary wave effects. The MY 33 northern polar vortex (not shown) shows the same persistent PV maxima at the mentioned longitude ranges, a similar slight minimum in PV following the nightside, and again no discernible consistent pattern in CDOD variation.

6.1.3 Discussion

The MY 34 GDS had a significant effect on the morphology of both the southern and northern polar vortices, through both altered dynamics (in the north) and a combination of altered dynamics and altered radiative heating (in the south). For both hemispheres, the change in the dynamics came in the form of changes to the meridional circulation, linked to changes to the high latitude stationary wave structure. This stationary wave structure appears to

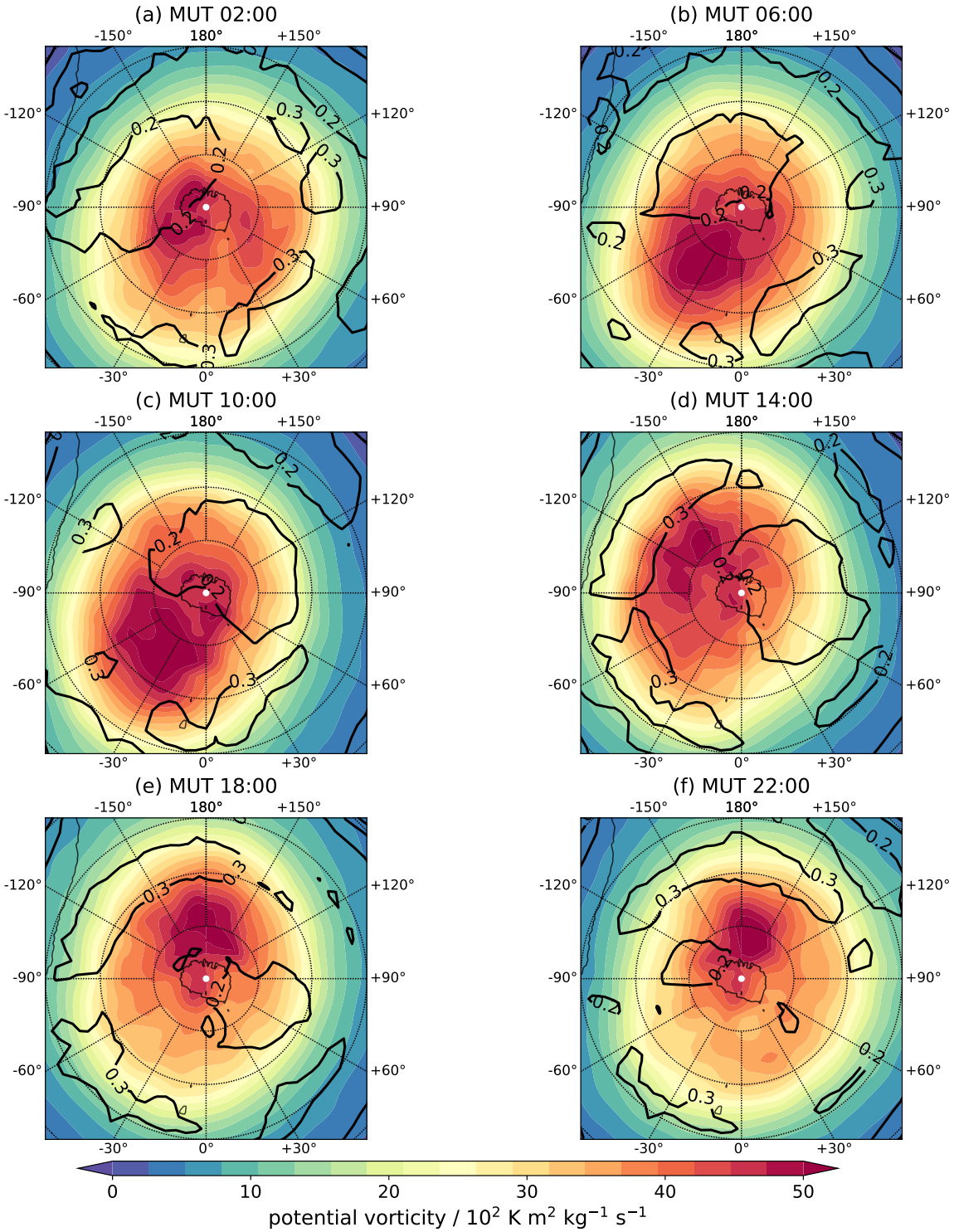

Fig. 6.11 Potential vorticity (colours) as averaged over the L_S=200-220° period on the 300 K isentropic level and CDOD at 610 Pa (contours) over the NP for MY 34 at six different MUTs. Each MUT is averaged over the 2 hours before and after, or 4 hours in total. Plots are stereographic projections where each latitude circle is 10° separate from its neighbours and the innermost circle represents the 80° latitude band. Lower absolute values indicate lower magnitude of potential vorticity, and vice-versa.

be an extremely important part of the modelled morphology of both polar vortices at this time of year, with the northern wavenumber 2 feature following the northern polar vortex's characteristic elliptical shape. Here, a point must be made regarding causality. It cannot strictly be said that the stationary wave structure causes the polar vortex structure as part of any physical causal chain. Rather, the stationary wave structure is the polar vortex structure. From a wave perspective, there is a stationary wave structure; from a PV perspective, there is an elliptical polar vortex morphology. Essentially, these are two perspectives on what is the same phenomenon.

The GDS-induced changes to the stationary waves were reflected in changes in the shape of polar vortices, specifically reducing their longitudinal and, in the southern case, latitudinal asymmetry. Indeed, the northern changes to stationary wavenumber 1 feature's amplitude exactly correlate to modelled changes in PV. In the south, the GDS-induced changes to the heating rates in the atmosphere also had a crucial effect on the polar vortex structure. Increased atmospheric heating from the high southern dust loading in conjunction with dynamical heating destroyed potential vorticity, substantially reducing the strength of the polar vortex, and shifted the remnant westerly jet to a tighter area circumscribing the pole. This dramatically accelerated the already ongoing decay of the southern polar vortex. In the north, by contrast, there were minimal changes in radiative heating rates at high latitudes, preserving the strength of the polar vortex even as its area and eccentricity decreased by the (longitudinally asymmetric) expansion of the Hadley cell to higher latitudes.

One way of putting this is that the GDS acted as a great leveller, reducing intrinsic wave-driven asymmetries in polar vortex structure by overpowering the specific topographic features which give rise to the stationary waves, namely topographically driven differential heating at different longitudes. This resulted in a more longitudinally symmetrical meridional circulation. In this way, the GDS afforded a valuable diagnostic tool - it acted as a natural laboratory, causing massive changes to Mars' normal atmospheric conditions and thus

allowing isolation of specific interrelated phenomena, such as stationary waves and polar vortex morphology.

The stationary wave interpretation explains not only the elliptical polar vortex shape, but why the elliptical shape is more prevalent in the northern hemisphere, as noted by Waugh et al. (2016). The non-GDS northern hemisphere has, at the L_S=200-220° period, a strong and latitudinally extended wavenumber 2 feature. The southern hemisphere, by contrast, has a more ambiguous stationary wave structure at this time, with a mid-high latitude wavenumber 2 feature transitioning to a wavenumber 1 feature near the pole. Given the most probable topographically-induced origin of these wave features (e.g. Haberle et al., 2019; Hollingsworth and Barnes, 1996; Nayvelt et al., 1997), this seems to confirm the speculation by Rostami et al. (2018) that the elliptical polar vortex shape is linked to large-scale topography.

Interestingly, there was apparent disagreement with previous literature on the effects of high dust loading on polar vortex structure, though this may be due to the time of year under consideration, among other factors. Mitchell et al. (2015), using the MACDA reanalysis, found that a regional-scale dust storm at L_S=320° caused a $\sim$10° latitude shift in the northern polar vortex, as well as an overall weakening in PV. This study shows little change in the broad morphology of the northern polar vortex even from the very high dust loading of a GDS, and only a localised weakening in PV. A couple of factors could be responsible for this disagreement. First, and likely most importantly, the times of year are different. At L_S=320° the northern polar vortex is already weakening as the planet approaches equinox, while in the L_S=200-220°period the northern polar vortex is strengthening as the planet approaches northern winter solstice. While a proper intercomparison between this reanalysis and MACDA is called for, at first glance this suggests that orbital factors and what one might call their associated “momentum” - ie. the trajectory of orbital change, whether it is towards or away from the relevant winter solstice - might be crucial in determining polar

vortex response to sudden high dust loadings. The second factor is the nature of the regional storm in question itself, and specifically its spatial location. This could have an impact on its resultant dynamical and radiative effects.

There was also some apparent disagreement with Guzewich et al. (2016), who found that in a MGCM with a prescribed high-dust map the northern polar vortex was subject to disruption, while the southern polar vortex remained relatively unaffected. In the study presented here, by contrast, the southern polar vortex was disproportionally affected by the high southern hemispheric dust loading. Again, however, seasonal variations likely explain the discrepancy. Guzewich et al. (2016) investigated the effects of high dust loading in the summer hemisphere at the winter pole for each solstice; this study focusses on a period when the northern and southern polar vortices are strengthening and weakening, respectively. Given that GDS events generally occur either around the L_S=180° equinox or the L_S=270° solstice, it is worth investigating both in turn and acknowledging the likely significant effect of the orbital cycle.

At this point it should be noted that despite the evidence of wave-related effects on the southern polar vortex structure, wave structure alone is not the whole story in explaining its broad morphology. Notably, planetary wave structure does not explain the off-pole presence of the eye of lower absolute PV. Following the hypothesis that the central absolute PV minimum is the result of localised diabatic heating from latent heat release as CO_2 condensation occurs over the pole (Rostami et al., 2018; Toigo et al., 2017), one would expect that this location in the reanalysis - approximately 80° S, -60° E - undergoes greater CO_2 condensation than the surrounding seasonal cap. The reanalysis and the MCS surface CO_2 ice observations from Piqueux et al. (2015) (discussed more in the second half of this chapter) offer an opportunity to try to further validate this hypothesis. Fig. 6.12.a shows the extent of southern seasonal CO_2 ice coverage from MCS observations as averaged between L_S=240-270, closer to southern summer solstice than this study. There is a clear ice remnant

present between 70-90° S and -120-60° E, even as the ice in the opposite hemisphere has almost completely disappeared. While the reanalysis shows a greater latitudinal extent of CO_2 ice coverage than the retrievals (Fig. 6.12.b), it does agree with the observations regarding where the most CO_2 ice mass is located, at the same latitude range noted earlier. The location of this remnant surface ice feature agrees very well with the location of the low absolute PV eye seen in for example Fig. 6.1.b.

The observations suggest that this location is indeed an area of greater CO_2 condensation, resulting in a thicker and therefore longer lasting ice cap; alternatively, it could be that this region is colder than the surrounding areas, thereby promoting greater CO_2 condensation and less rapid sublimation. These "cold spots" could also be linked to the presence of CO_2 ice clouds (Hayne et al., 2012), and are an ongoing area of study. In any case, this would seem to be further supporting evidence for the Toigo et al. (2017) hypothesis for the cause of the annular PV structure. There is a complication though: the local time variation in Fig. 6.10 appears to show that the eye has greater absolute PV around local daytime, and lower absolute PV around local nighttime. One would expect the opposite, with CO_2 sublimation and therefore latent heating and PV destruction occurring preferentially during the day. Given that the PV values are calculated at the 300 K isentropic surface, or around 20-30 km altitude, there could be a lag between the surface condensation and latent heating higher up. This remains to be investigated in future work. Finally, it is interesting to note that the GDS appears to remove this preferential condensation, at least for the L_S=200-220° period, resulting in a polar vortex centred over the SP itself.

Lastly, analysis of local time variations in the southern polar vortex during the GDS reproduce the Kleinböhl et al. (2020) results of an isolated (high absolute PV), dust-clear air mass trapped on the nightside. This study provides further evidence that the proposed mechanism, a boosting of the meridional circulation in MY 34 intensifying an existing local time pattern of nightside transport away from the SP and dayside transport towards, is indeed

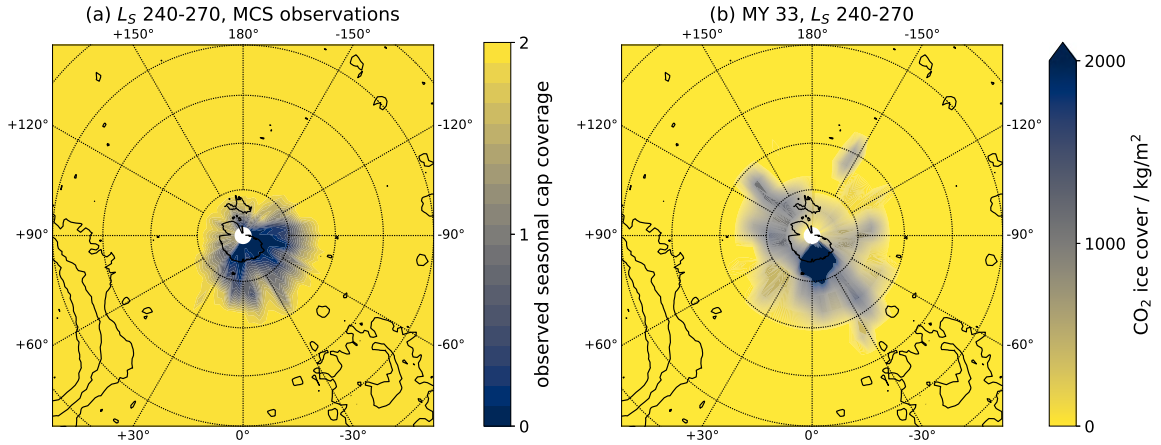

Fig. 6.12 (Left) climatologically averaged seasonal CO_2 cap extent at the SP averaged over L_S=240-270° from Piqueux et al. (2015), as derived from MCS surface temperature data. In this notation, "2" signifies no CO_2 ice coverage during the relevant period, "1" indicates a boundary state, while "0" signifies the presence of surface CO_2 ice. See the Supplementary Information from Piqueux et al. (2015) for more information. (Right) CO_2 ice mass at the SP from the MY 33 reanalysis averaged over L_S=240-270°. Plots are stereographic projections where each latitude circle is 10° separate from its neighbours and the innermost circle represents the 80° latitude band.

correct. This pattern is shown to exist at the same time period in MY 33, with a weaker but still visible impact on the diurnal variation of PV and CDOD. The weaker meridional circulation and stronger stationary wave activity means that the diurnally-averaged structure, consisting of an off-pole eye of lower absolute PV with a surrounding annulus of higher PV, remains visible at all local times. There is some diurnal variation in PV at the NP in MY 34, but this is much weaker than in the south.

6.1.4 Conclusions and future work

To provide a brief summary of the results discussed above: the GDS had a significant impact on both the northern and southern polar vortices. In the north, the polar vortex structure (reflected via PV and zonal wind speeds) became less elliptical and more longitudinally symmetric. PV increased slightly at the pole itself and decreased at lower latitudes, indicating a narrowing of the area of the polar vortex as the Hadley cell descending branch extended

further poleward. In the south, there was significant destruction of PV across the entire polar vortex, and a corresponding increase in near-pole wind speeds and decrease in wind speeds at lower latitudes. The remaining polar vortex was significantly more symmetric than in the non-GDS case, and centred at the pole itself rather than off-pole. The non-GDS asymmetries in polar vortex shape at both poles were found to be linked to a longitudinally asymmetric meridional circulation, reflected in the stationary planetary wave structure in each hemisphere. The GDS significantly reduced the amplitude of the wavenumber 1 feature in the north and almost entirely destroyed the stationary wave feature in the south, which translated into more symmetrical polar vortices.

The MY 34 GDS also caused a peculiar feature at the SP: a mass of colder, isolated air coupled with a minimum in dust which followed the nightside of the planet, first seen in direct MCS observations (Kleinböhl et al., 2020). This feature was successfully replicated in the reanalysis and its suggested causal mechanism, a boosted mean meridional circulation enhancing a pre-existing (non-GDS) pattern of nighttime air transport away from the SP and daytime air transport towards the SP, further corroborated. This pattern was shown to be present at the SP, albeit in a weakened form, in the non-GDS year MY 33.

These results have implications for the transport of dust and volatiles into the polar vortices. The shape of the polar vortices and their corresponding westerly zonal jets control what can be transported above and onto the poles themselves. The non-GDS shape and GDS-induced alteration of the vortices therefore has potentially important consequences for both seasonal and long-term deposition of dust onto the seasonal CO_2 caps. For example, if the poleward shift of the westerly jets is a consistent effect of equinoctial GDS, this implies that tracers can be transported to higher latitudes during these intense dust events. If this kind of pattern holds over the course of the thousands of years that Mars maintains its particular axial obliquity, this has further implications for the record of deposited dust at the southern

and northern polar layered deposits, for example as measured by the SHARAD subsurface radar on MRO (Seu et al., 2018).

Validation is an important consideration when contemplating results from a meterological analysis, particularly when based on fields (PV, zonal wind speeds) that are not directly measured by orbiting spacecraft. The most valuable possible future measurements would be of atmospheric winds from an orbiter. These would allow better constraints on the shape and locations of the polar vortices, and (combined with temperature measurements) for direct calculation of PV. Cloud measurements at the polar hoods could also be helpful in tracing the edges of the polar vortices. In the near future, ongoing temperature and dust retrievals from the ExoMars Trace Gas Orbiter and its NOMAD (Patel et al., 2017; Vandaele et al., 2015) and ACS (Korablev et al., 2017, 2015) spectrometer suites will allow for further investigation of tracer transport and an opportunity to both cross-validate and jointly assimilate NOMAD/ACS and MCS data. NOMAD/ACS will also provide the crucial feature of observing over a range of martian local times, which will enable investigation of the diurnal cycles of tracer transport and atmospheric dynamics at the poles.

There is also still a wealth of possible research which could be conducted with existing datasets. The following is non-exhaustive lists of relevant open questions. This work focusses specifically on the period L_S=200-220°, in order to compare with the MY 34 GDS; but how does the variation of the meridional circulation over different longitudes and different local times affect the polar vortex throughout all other times of the martian year? Does the relationship with the stationary wave structure still hold, or do other factors become more important in determining polar vortex morphology? What are the precise mechanisms by which the MY 34 GDS impacted the planetary stationary waves? What are the impacts in the reanalysis of non-GDS dust events, such as the MY 34 “B” storm late in the year or the northern hemispheric dust event in early MY 35, on the polar vortices? What explains the longitudinal asymmetry present in the southern seasonal CO_2 ice cap as it recesses, and

what is its relation to the large-scale dynamics and the modelled shape of the polar vortex? And how exactly did the MY 34 GDS affect the seasonal CO_2 caps, including condensation, growth or recession, and direct dust deposition and resulting possible changes in energy balance? Meteorological reanalyses will continue to play a prominent role in addressing these questions as our observations increase and our models improve.

6.2 Novel high-speed polar jets

6.2.1 Introduction

This section discusses two jets at southern high latitudes, present in the reanalyses used in the previous two chapters but not in previous free-running MGCM simulations (e.g. Chapman, 2018) or reanalyses such as MACDA, which assimilated TES temperatures and CDOD (Montabone et al., 2014), and the OpenMARS assimilated dataset, which assimilated MCS v4.3 data (Holmes et al., 2020) (as stated in Chapter 3, the work in this thesis uses the v5.2 dataset). The two jets are characterised in detail, the causes of the features are investigated, and their plausibility as real martian phenomena is examined through consideration of the MGCM's physical processes and comparison with orbital observations, in situ measurements, and other modelling work.

This section uses reanalysis data of MY 30. MY 30 was chosen as a particularly clear year, having no global dust events and relatively low regional-scale dust activity compared to other MCS reanalysis years. This allows for better decoupling of the underlying processes from the effects of stochastic dust activity, given that the jets are present in every martian year of the reanalysis (see Chapter 5) and are therefore not primarily dust-driven.

The jets described below are present in reanalyses using the newer, re-processed v5.2 MCS retrievals described by Kleinböhl et al. (2017) and discussed in Chapter 3. These retrievals use more realistic assumptions in the retrieval process regarding planetary geometry

than the previous version, by taking into account strong horizontal gradients in atmospheric parameters - such as temperature - that pose issues for the previous assumption of spherical symmetry. These new retrievals will henceforth be called the "2D" retrievals, due to the incorporation of horizontal heterogeneity, while the older v4.3 (spherical assumption) retrievals will be called the "1D" retrievals. These labels also apply to the relevant reanalyses. This update therefore leads to different results particularly around the winter poles, where there are strong horizontal gradients in temperature. Kleinböhl et al. (2017) note that at the southern winter pole in particular, atmospheric temperatures in the 2D retrievals can be over 10 K colder than the 1D retrievals, while the southern polar vortex is less dusty. In fact, both southern and northern winter poles are on the whole clearer of dust in the 2D reanalyses.

Figs. 6.13 and 6.14 present zonal cross-sections of the aphelion and perihelion jets, showing the zonal and meridional components respectively for the 1D reanalysis, the 2D reanalysis, and the difference between them. Both figures show the stark difference between the reanalyses at southern high latitudes, including in south polar surface pressures as reflected in the zonal-mean topography. The westerly jet at aphelion in the 1D reanalysis is significantly intensified by >30 m/s in the 2D reanalysis (Fig. 6.13, with the difference especially notable near the surface between 70-80° S. At perihelion, the weak easterly structure in the 1D reanalysis is a more fully developed jet in the 2D reanalysis, with zonal winds again being >30 m/s higher and extending down to the surface. At both aphelion and perihelion, the 2D reanalysis shows a consistent enhancement of the existing zonal flow at all altitudes up to the top of the MGCM (here truncated to 80 km), with a lack of vertical shear in the zonal flow.

The meridional flow at both aphelion and perihelion also shows a substantial enhancement in the 2D reanalysis of the existing trends in the 1D reanalysis (Fig. 6.14). At aphelion, the 1D reanalysis shows a weak (<3 m/s), shallow flow towards the south pole at southern high latitudes. The 2D reanalysis shows a stronger (>10 m/s) shallow flow in the same direction,

with a countervailing equatorward flow (∼3 m/s) at 2 km and higher . At perihelion, the flow directions are reversed but the structure is otherwise similar. The 1D reanalysis shows a weak (<7 m/s), shallow towards the equator, while the 2D reanalysis shows a stronger (>10 m/s) shallow equatorward flow and a countervailing poleward flow (∼2 m/s) from 2 km to 25 km above the surface, at which altitude the flow reverses again ensuring conservation of angular momentum. At both aphelion and perihelion the strongest flow and the greatest changes are constrained within ∼2 km of the surface, but the effects of using the 2D retrievals are apparent throughout the entire altitude range displayed. Together with the zonal wind differences, it is clear that these southern high latitude jets are not simply surface-level phenomena but extend into the middle and upper atmosphere.

Most relevant for potential dust lifting, while the jets extend >20 km into the atmosphere they are remarkable for their high near-surface wind speeds, "near-surface" here defined as in the bottom layer of the MGCM (∼ 5 m above the surface). Both jets are centred around the solstices, but extend temporally beyond them. For clarity, from here on they will be referred to as the aphelion jet and the perihelion jet. Most of this characterisation will centre on the near-surface expression of these jets as this is the most relevant aspect for dust lifting, though as stated above these jets extend well into the atmosphere. Fig. 6.15 shows the large temporal extent of both jets, but particularly the aphelion jet which is apparent throughout most of the aphelion season. This jet is visible between L_S=20-170°, and average wind speeds up to 12 m/s greater in the 2D case. The perihelion jet is shorter-lived, and is visible between approximately L_S=240-310°. It also has a lower magnitude, with averaged wind speeds of up to 7 m/s greater. Note however that these wind speeds are averaged over a large latitude range, and do not therefore necessarily reflect the actual difference in the intensity of the winds at any particular location; a narrow latitude band of high intensity wind speeds would display the same signal as a wider band of lower intensity wind speeds. Fig. 6.15 is, though, useful for characterising the seasonal extent of the two jets.

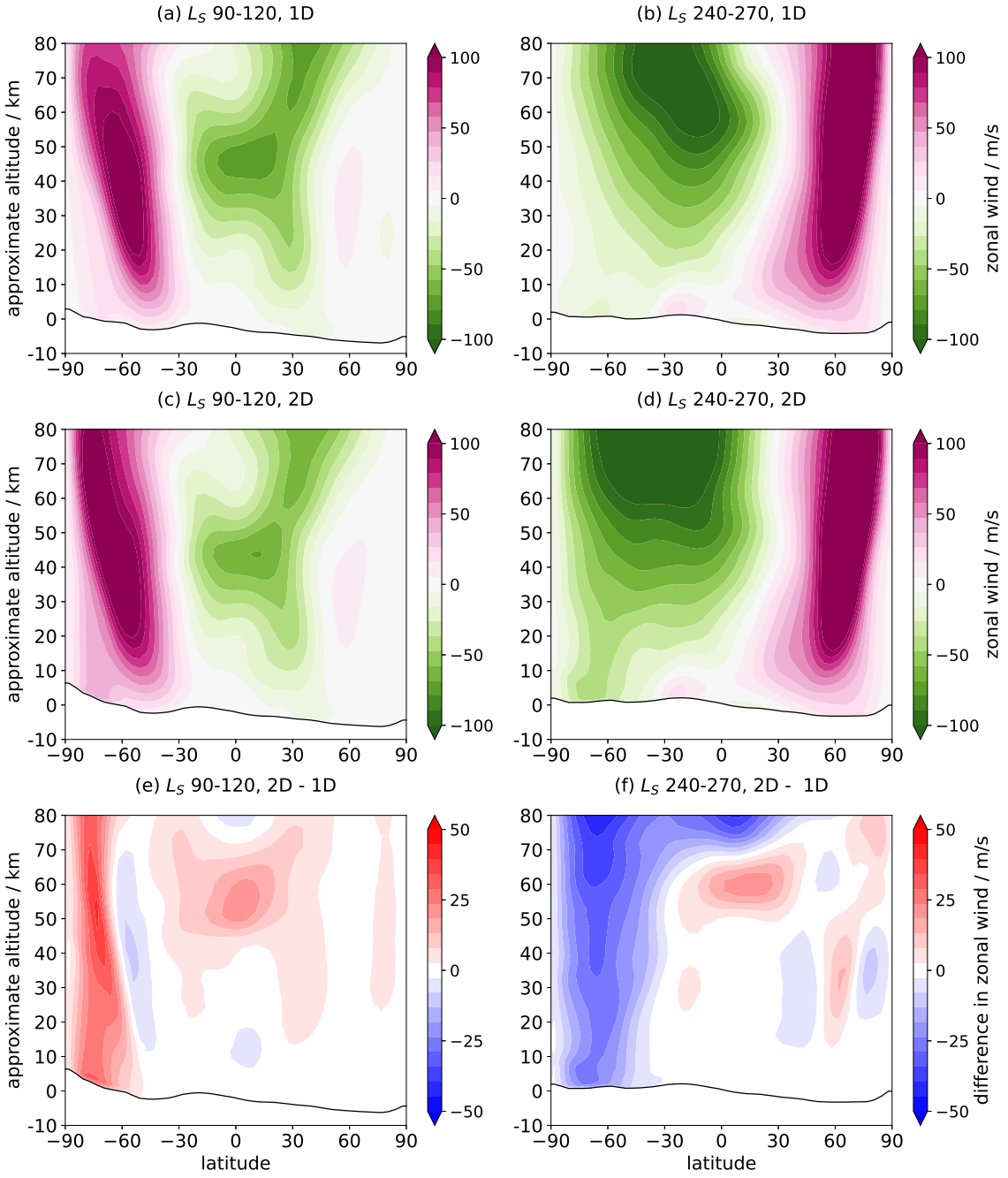

Fig. 6.13 Zonally-averaged zonal winds in MY 30 at (left) L_S=90-120° and (right) at L_S=240-270°, and for (top) the 1D reanalysis, (middle) the 2D reanalysis, and (bottom) the difference between the reanalyses (2D-1D). Positive/negative values represent westerly/easterly flow. The black border at the bottom of each plot represents zonally-averaged topography, as calculated from surface pressures. Altitude was cropped to 80 km for the plots.

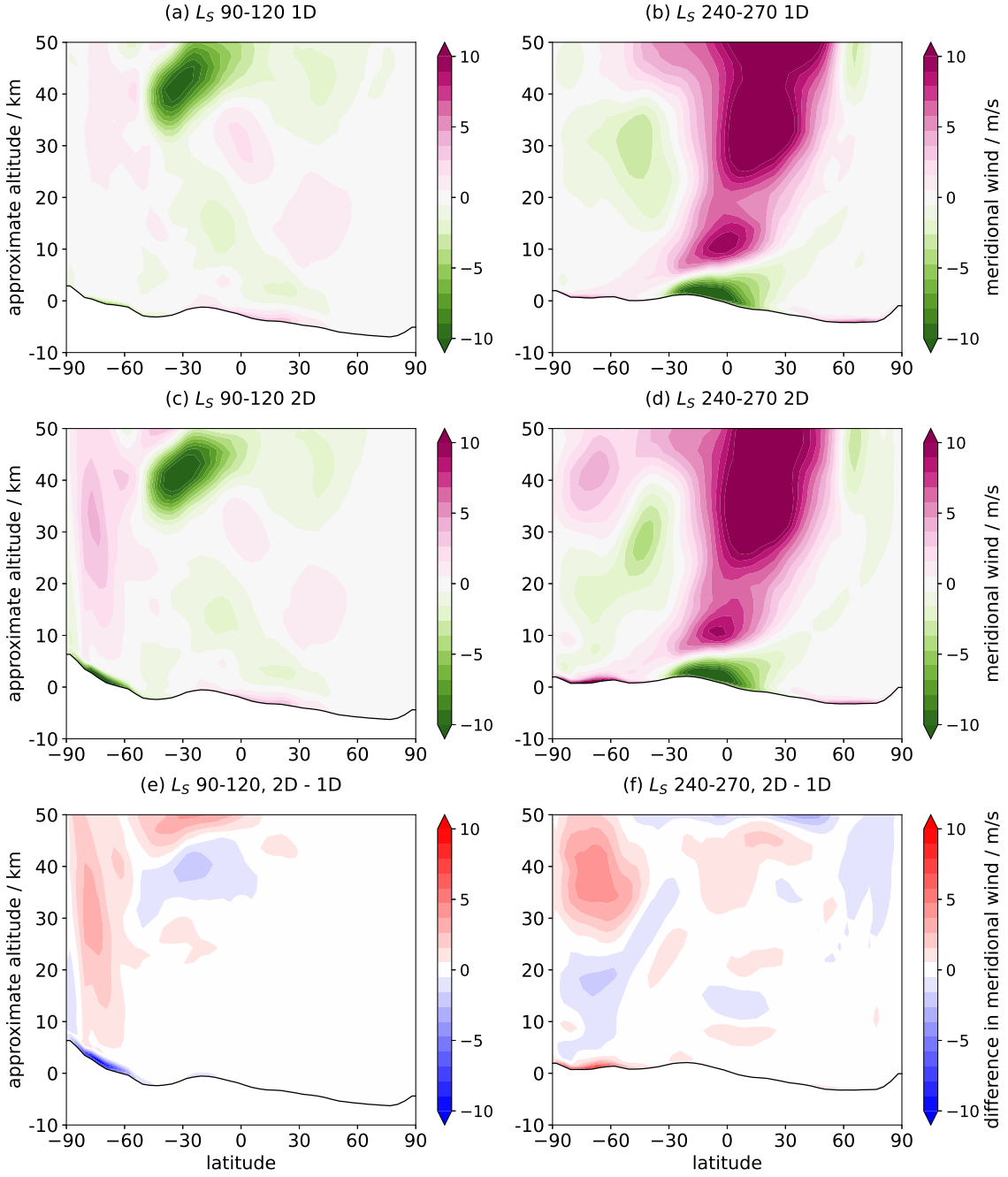

Fig. 6.14 Zonally-averaged meridional winds in MY 30 at (left) L_S=90-120° and (right) at L_S=240-270°, and for (top) the 1D reanalysis, (middle) the 2D reanalysis, and (bottom) the difference between the reanalyses (2D-1D). Positive/negative values represent southerly/northerly flow. The black border at the bottom of each plot represents zonally-averaged topography, as calculated from surface pressures. Altitude was cropped to 50 km for the plots.

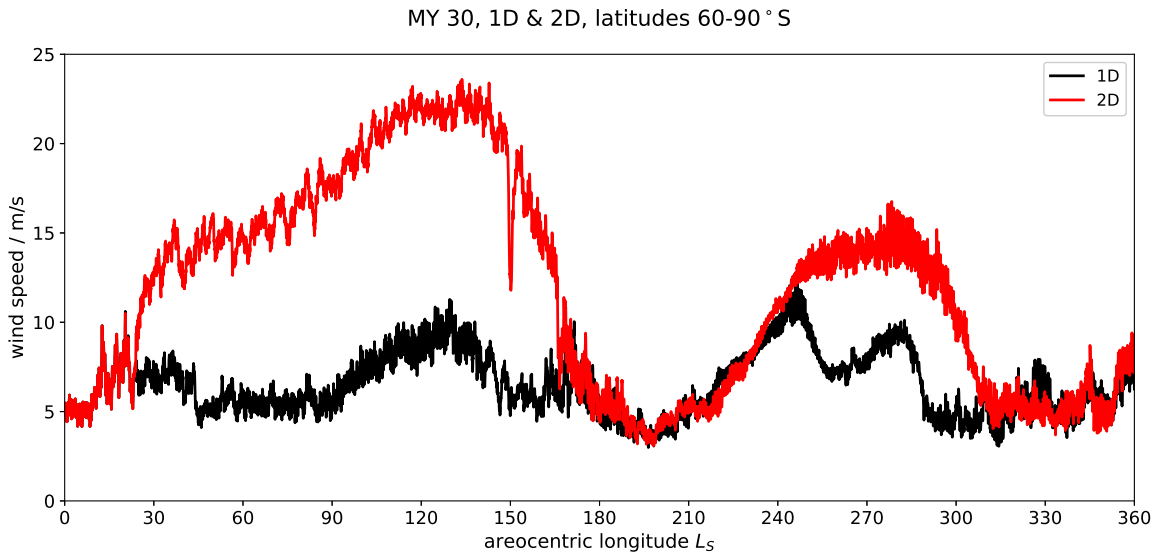

Fig. 6.15 MY 30 zonally-averaged wind speeds at ∼5 m as averaged between latitudes 60-90° S, for the 1D and 2D reanalyses.

The rest of this section will characterise each jet in turn focussing on their near-surface expression, offer explanations as to their causes, and compare to existing observations and modelling work.

6.2.2 Aphelion jet (L_S=90-120°)

As described above, the aphelion jet is present throughout the period L_S=20-170°. This analysis focusses on the subperiod L_S=90-120°.

Characteristics

Fig. 6.16 shows meridional winds, zonal winds, and total wind speeds near the surface for the L_S=90-120° period. Total wind speeds in the 2D reanalysis reach up to 31 m/s; zonal winds reach up to 31 m/s and meridional winds up to 22 m/s. The highest total (Fig. 6.16.d) and zonal (Fig. 6.16.e) wind speeds are seen in the western hemisphere, corresponding to regions of greater equatorward topographic slope. Despite this asymmetry, they show a distinct annular pattern centred off-pole, around ∼ 85° S, -60° E. This "eye" consists of a minimum

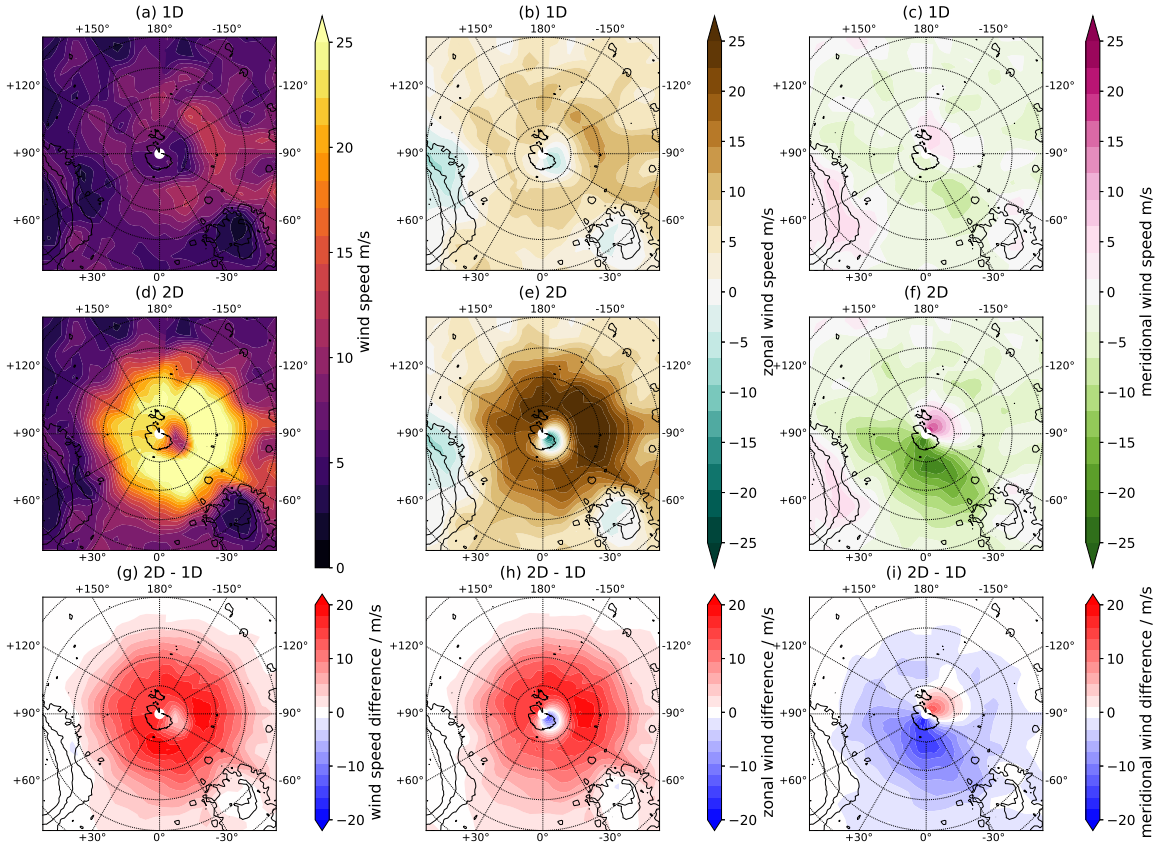

Fig. 6.16 MY 30 near-surface (left) wind speeds, (middle) zonal winds, and (right) meridional winds over the SP as averaged between L_S=90-120°, and for (top) the 1D reanalysis, (middle) the 2D reanalysis, and (bottom) the difference between reanalyses (2D-1D). For zonal winds, positive/brown (negative/teal) represents westerly (easterly) flow. For meridional winds, positive/pink (negative/green) represents south-to-north (north-to-south) flow. Plots are stereographic projections where each latitude circle is 10° separate from its neighbours and the innermost circle represents the 80° latitude band.

of total wind speeds, including a small patch of easterly zonal flow. The meridional flow (Fig. 6.16.f) shows a different and distinct pattern. There is a strong north-to-south flow directly to the pole between roughly -60-120° E, and a weaker south-to-north flow between 150- -90° E. The latter is spatially limited between 75-90° S. This is the signal of a stationary planetary wave of spatial wavenumber 1; it is also visible (albeit weaker) in the 1D case (Fig. 6.16.c) and in other modelling work (e.g. Chow et al., 2019), and is likely due to the longitudinal variation in topography around the southern pole. It is also important to note that these winds all occur over the southern seasonal CO_2 cap itself, and not at the boundary between the cap and the surrounding regolith.

The general flow pattern described above in both the 1D and 2D reanalyses shows a predominantly north-to-south flow towards the south pole, with the flow being substantially magnified in the 2D case while the pattern remains basically identical. The zonal flow is also intensified while retaining the same pattern, which is cyclonic. The north-to-south flow in the southern hemisphere is associated with this westerly (cyclonic) flow. These elevated wind speeds occur entirely over the seasonal cap itself (which has an almost uniform surface temperature across its area) and not at the boundary, ruling out thermal contrast as the cause.

Fig. 6.17 shows how the near-surface wind speeds vary with local time. Given the location of the jet within southern polar night, there is unsurprisingly very little diurnal variation. The highest wind speeds are consistently located in the western hemisphere, in particular around -30° E and -90° E.

Possible causes

A number of possible causes for the 1D-2D discrepancy were investigated, including the effect of the lower southern polar vortex dust opacity and the possible impact of dynamical heating from the mean meridional circulation. Neither was found to be convincing. The former explanation is undermined by the fact that the polar winter means that shortwave

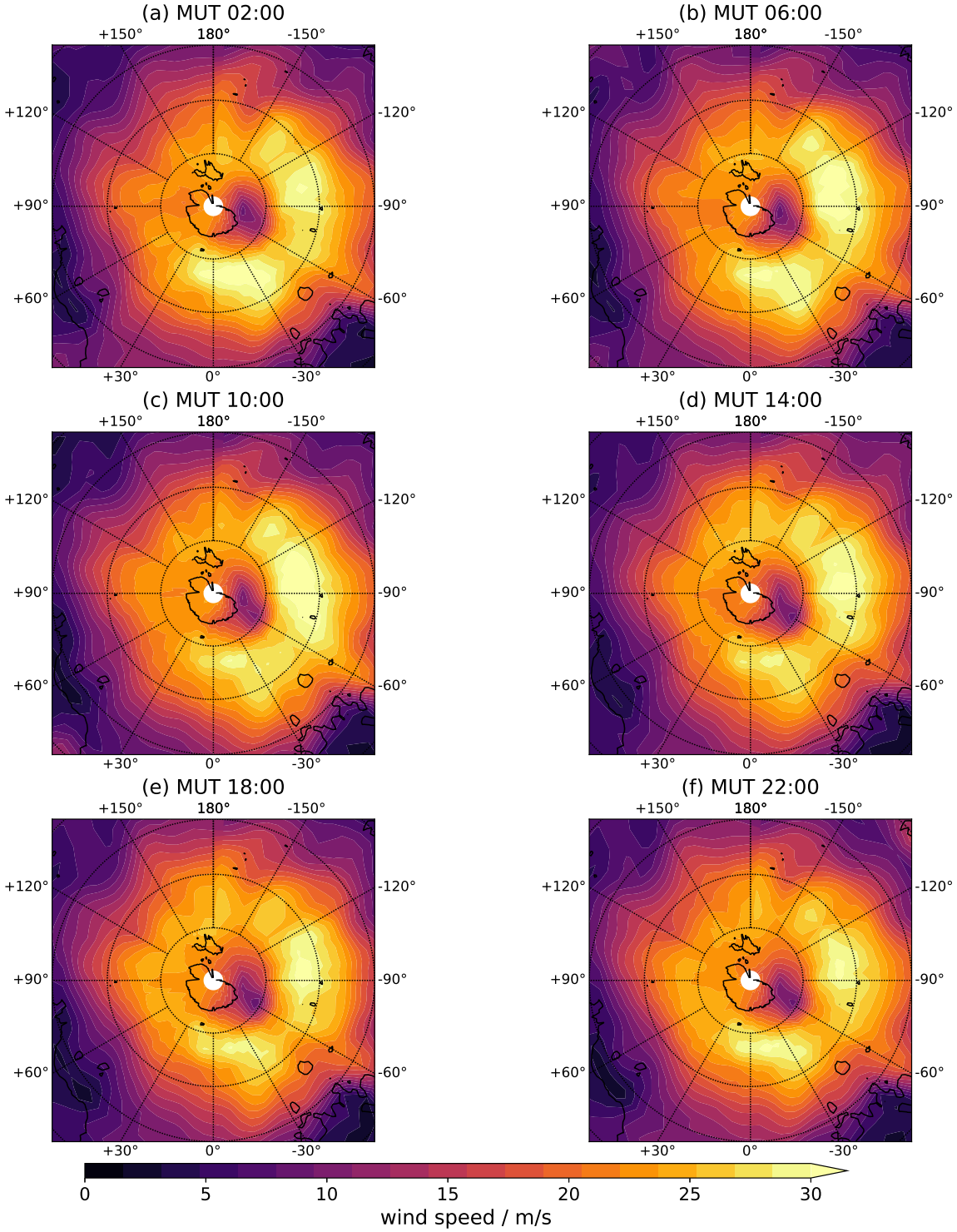

Fig. 6.17 MY 30 near-surface wind speeds over the SP for the 2D reanalysis at different local times. Plots are stereographic projections where each latitude circle is 10° separate from its neighbours and the innermost circle represents the 80° latitude band.

radiative flux at the southern pole is close to zero anyway, and therefore the difference in CDOD (large in percentage terms but small in absolute terms) makes little difference to net radiative surface flux. This was borne out by specific analysis of the net radiative surface flux. This is also supported by previous modelling finding that elevated polar dust opacity actually correlates with enhanced atmospheric condensation, as higher dust content increases the thermal emissivity of the polar atmosphere, thus enhancing cooling rates and lower atmospheric temperatures (Pollack et al., 1990). The mean meridional circulation was also investigated, but no conclusive difference was observed between the vertical velocities of the 1D and 2D cases over the south pole.

The most compelling explanation for the sheer scale of the disparity between 1D and 2D reanalysis wind speeds at L_S=90-120° was linked to the difference in surface pressure over the southern pole. This is shown in Fig. 6.18.a,c,e (Fig. 6.18.b,d,f are discussed in Section 6.2.3). The surface pressure at the south pole during this period can be over 100 Pa lower in the 2D case than the 1D case, or 20-30% lower in proportional terms. This extreme difference is clearly visible in the lower zonal-mean topography at the south pole as calculated from surface pressure in the 1D (Figs. 6.13-6.14.a, Fig. 6.19.a) than in the 2D (Figs. 6.13-6.14.c, Fig. 6.19.c) reanalysis during aphelion; this shows a lower atmospheric mass at the south pole in the 2D reanalysis. This surface pressure difference matches the correspondingly extreme difference in near-surface wind speeds. The surface pressure difference between the reanalyses is centred off-pole, and matches well with the zonal/total wind speed difference between them described above. The surface pressure difference declines with lower latitudes. The result is that the 2D reanalysis has a much greater pole-to-equator surface pressure gradient than the 1D reanalysis, with surface pressure increasing as latitude decreases. This meridional surface pressure gradient and the fact the that the zonal jet extends into the upper atmosphere (Fig. 6.13.c,e) imply that this is a barotropic phenomenon, or barotropic jet. The

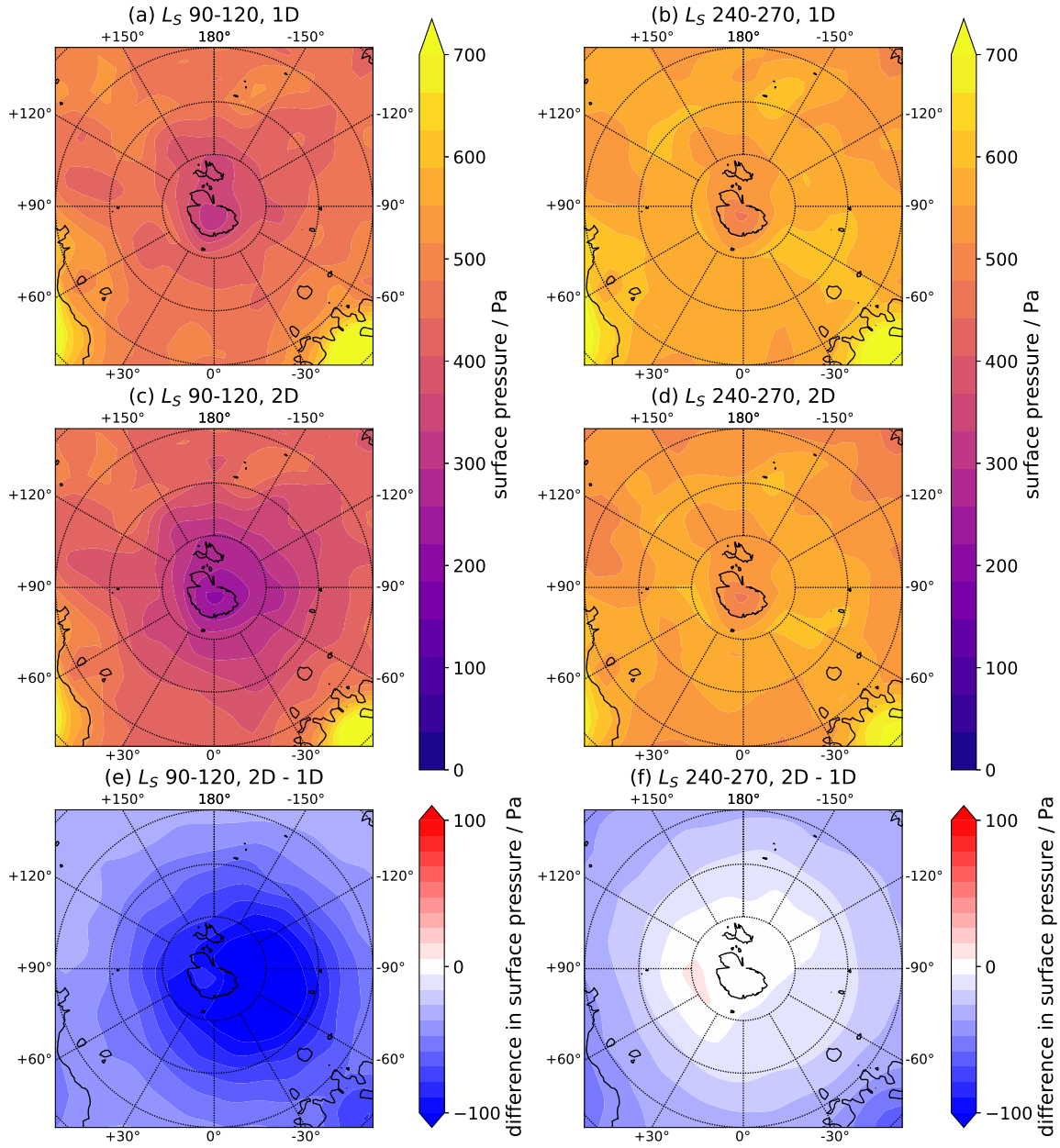

Fig. 6.18 Surface pressure in MY 30 for the southern pole (left) at L_S=90-120° and (right) at L_S=240-270°, and for (top) the 1D reanalysis, (middle) the 2D reanalysis, and (bottom) the difference between the reanalyses (2D-1D). Plots are stereographic projections where each latitude circle is 10° separate from its neighbours and the innermost circle represents the 80° latitude band.

barotropic nature of the jet is demonstrated by the consistent magnitude of the zonal jet in the vertical dimension (Fig. 6.13.c), which displays no vertical shear.

In general, at high latitudes pressure gradients are linked by geostrophic balance (the balance between Coriolis force and pressure-gradient force) to zonal winds, rather than meridional winds, as evidenced by the existence of high velocity zonal jets on both Earth and Mars; within the boundary layer, though, this balance is modified due to the presence of an extra frictional drag force from the surface itself (Holton, 2004d). The new balance between these three forces results in "Ekman flow", flow orientated away from high pressures/towards low pressures, expressed as meridional winds. This flow has been previously modelled to occur at high latitudes on Mars in the presence of CO_2 condensation, which causes lower pressures over the seasonal cap (Ogohara and Satomura, 2010). This Ekman flow explains the high meridional near-surface winds associated with the modelled surface pressure gradients. This drastically increased meridional pressure gradient drives much greater zonal winds and shallow north-to-south meridional winds. As seen previously in Fig. 6.13, the increase in zonal winds extends into the upper atmosphere, while the strong meridional flow remains confined to the bottom $\sim$2 km of the atmosphere (Fig. 6.14). This is consistent with the horizontal pressure gradient and associated barotropic jet interpretation.

The cause of this surface pressure difference lies in the atmospheric temperatures of the two reanalyses. The only differences between the reanalyses, which uses the same MGCM and are run at the same time of year for the same martian year, are the assimilated observations. As discussed above, while there is a difference in the assimilated CDOD, this was not found to have a significant effect on the southern pole's energy budget. This leaves only the assimilated temperature retrievals. As mentioned above, the 2D retrievals themselves show a southern polar vortex that can be over 10 K colder than the 1D retrievals in the lower atmosphere ($\sim$20-40 km). Indeed, assimilated temperature retrievals in the 2D case can frequently drop below the relevant CO_2 condensation temperature at their altitude (this is

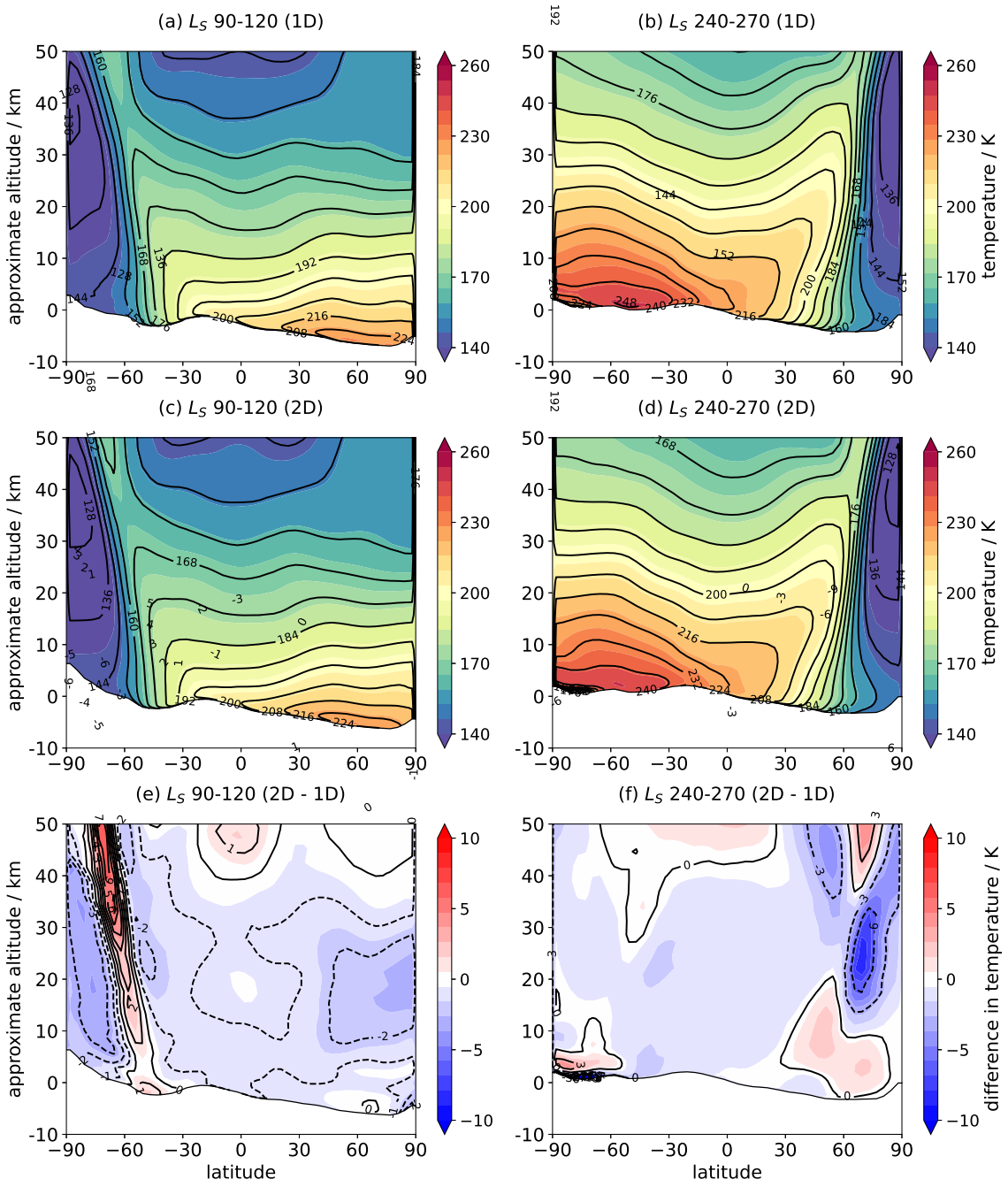

Fig. 6.19 Zonally-averaged atmospheric temperature in MY 30 (left) at L_S=90-120° and (right) at L_S=240-270°, and for (top) the 1D reanalysis, (middle) the 2D reanalysis, and (bottom) the difference between the reanalyses (2D-1D). The black border at the bottom of each plot represents zonally-averaged topography, as calculated from surface pressures. Altitude was cropped to 50 km for the plots.

discussed in greater detail in Section 6.2.4). Likewise, in the reanalyses zonally-averaged lower atmospheric temperatures in the southern polar vortex are up to ∼4 K colder than in the 1D case, along with a warmer polar warming feature (Fig. 6.19.e).

Within the MGCM's CO_2 cycle parameterizations, these lower atmospheric temperatures induce greater condensation of the atmosphere onto the seasonal cap. This greater condensation lowers the atmospheric pressure over the cap by reducing the mass of the atmosphere, leading to the modelled surface pressure bias. Given Mars' low atmospheric pressures and highly global, inter-connected climate, these surface pressure deficits have global reverberations. This is discussed further in Sections 6.2.4 and 6.2.5.

6.2.3 Perihelion jet (L_S=240-270°)

As described above, this jet is present throughout the period L_S=240-310°. This analysis focusses on the subperiod L_S=240-270°.

Characteristics

Fig. 6.20 shows meridional winds, zonal winds, and total wind speeds near the surface for the L_S=240-270° period. The outline of the seasonal cap is clearly visible in all the plots, showing that the high winds are limited to the terrain around the cap edge, and not over the cap itself, creating a sharp dichotomy in all places. Total wind speeds in the 2D reanalysis reach up to 30 m/s; zonal winds reach up to 27 m/s and meridional winds up to 18 m/s. The longitudinal structure of the total and zonal winds is fairly symmetric; the greater asymmetry is in the latitudinal structure, as winds follow the boundary of the latitudinally asymmetric seasonal cap (Fig. 6.20.d,e). The meridional winds show greater longitudinal asymmetry, with the highest and most latitudinally extensive winds located in the western hemisphere (Fig. 6.20.f).

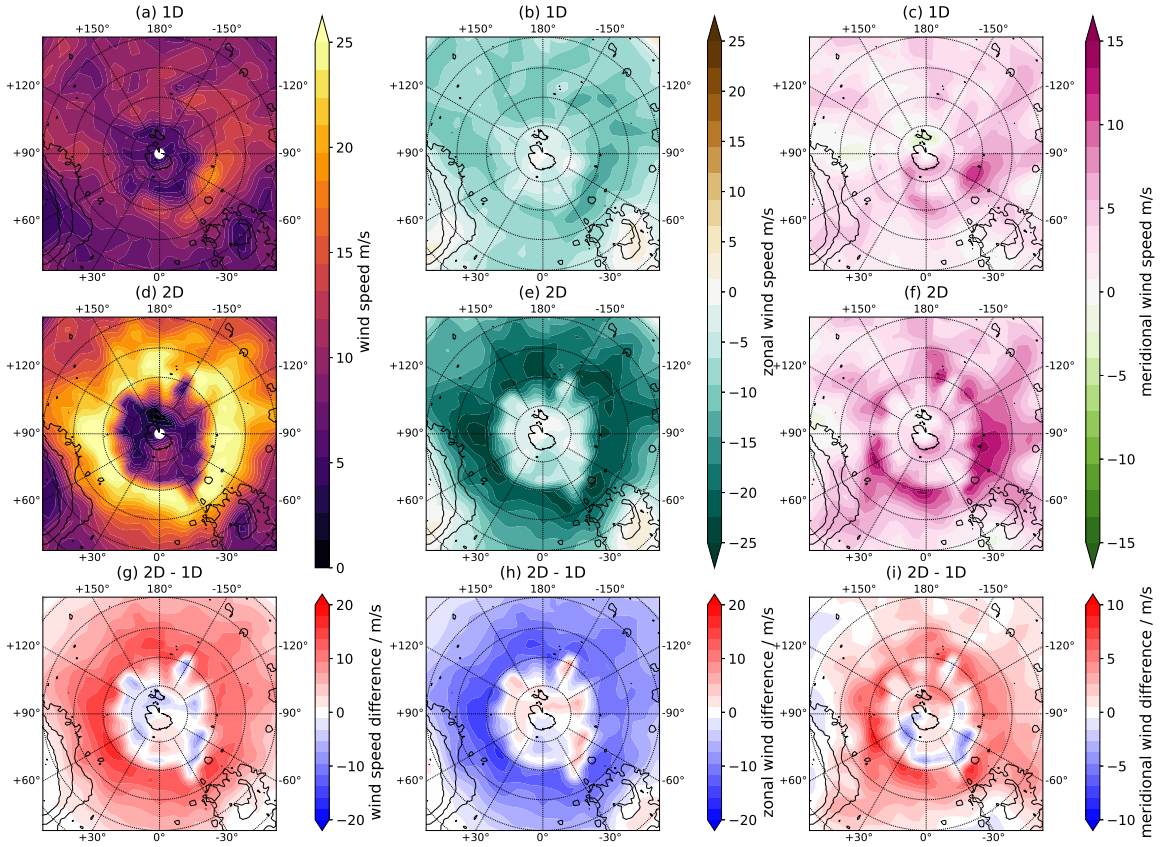

Fig. 6.20 MY 30 near-surface (left) wind speeds, (middle) zonal winds, and (right) meridional winds over the SP as averaged between L_S=240-270°, and for (top) the 1D reanalysis, (middle) the 2D reanalysis, and (bottom) the difference between reanalyses (2D-1D). For zonal winds, positive/brown (negative/teal) represents westerly (easterly) flow. For meridional winds, positive/pink (negative/green) represents south-to-north (north-to-south) flow. Plots are stereographic projections where each latitude circle is 10° separate from its neighbours and the innermost circle represents the 80° latitude band.

Both zonal and meridional flows are directionally uniform. The zonal flow is uniformly an easterly (anticyclonic) one, circulating around the cap edge. The meridional flow is uniformly south-to-north, away from the seasonal cap. The phenomenon of Ekman flow, previously invoked to explain the aphelion jet, therefore also appears to apply here as there is once more a strong vertically extended zonal jet and an associated strong but shallow meridional flow.

Fig. 6.21 shows how the winds vary with local time. There is significant diurnal variation, with the arc of the highest wind speeds following local daytime, centred around MUT $\sim$14:00. On the nightside, the wind speeds are significantly decreased. This pattern provides further evidence for the role of sublimation in driving these wind speeds, as cap sublimation occurs on the dayside due to the presence of high shortwave/solar radiative flux.

Possible causes

As for the aphelion jet, dust opacity and the large-scale meridional circulation were also investigated as possible causes of the wind speed disparity; but again, the significant feature responsible was found to be in surface pressure. Fig. 6.18.f shows how the surface pressure is close to identical over the seasonal cap itself in the 1D and 2D cases, but decreases towards the equator in the 2D case relative to the 1D case. In fact, surface pressures everywhere but at the southern pole are lower by up to $\sim$100 Pa in the 2D case (not shown). This is a reversal of the aphelion situation. In a mirror image of the aphelion situation, this surface pressure gradient (decreasing towards the equator) is linked to a strong easterly barotropic zonal jet, which is deflected by the Coriolis force and balance with the surface into a shallow equatorward meridional flow (Ekman flow). This extends all the way to the north pole (not shown), with surface pressures over the northern polar region being up to 100 Pa lower in the 2D reanalysis.

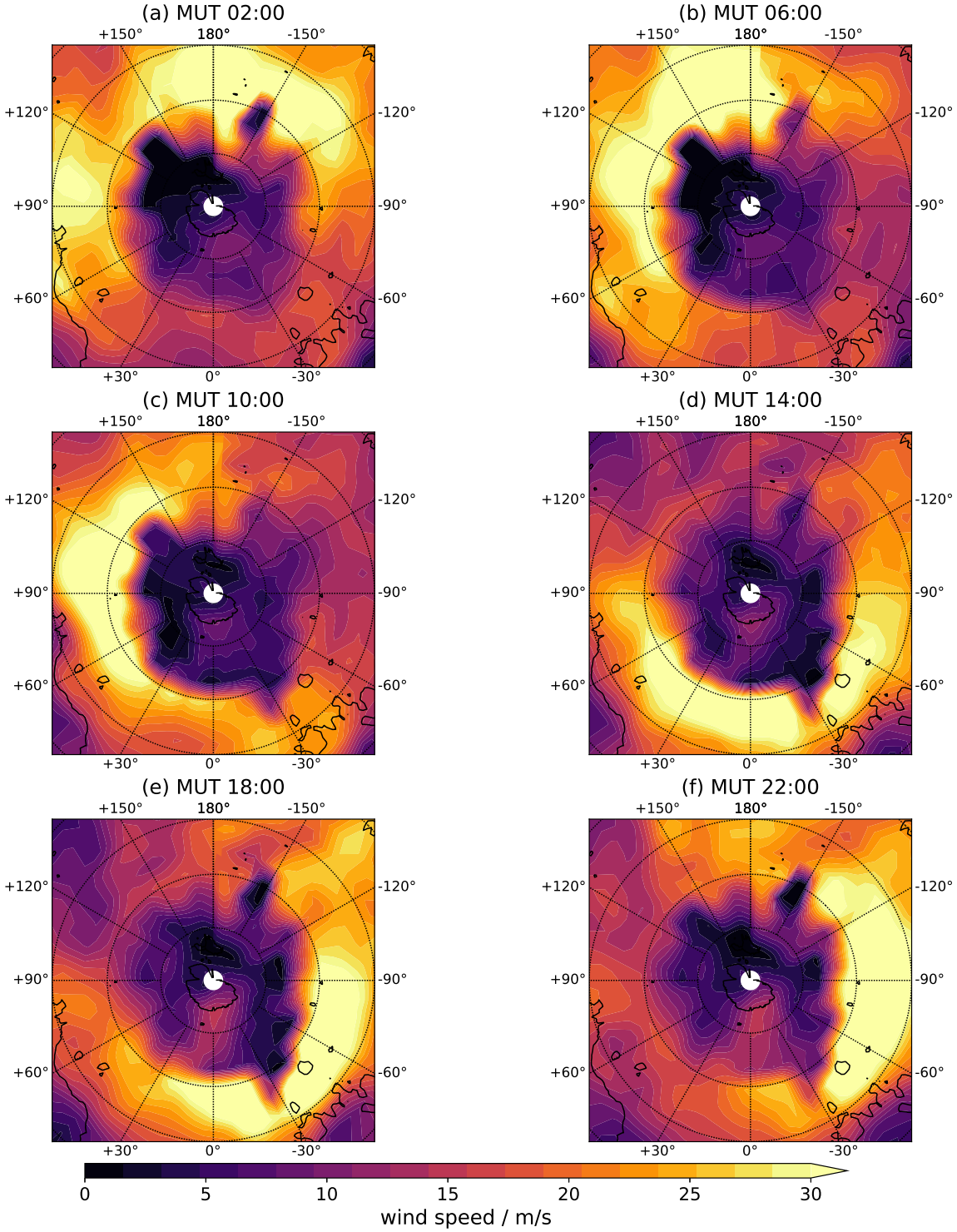

Fig. 6.21 MY 30 near-surface wind speeds over the SP for the 2D reanalysis at different local times. Plots are stereographic projections where each latitude circle is 10° separate from its neighbours and the innermost circle represents the 80° latitude band.

This surface pressure difference is less directly attributable to the atmospheric temperature structure of the period than in the aphelion case; Fig. 6.19.f shows that there is little difference in the atmospheric temperature above 10 km over the south pole (10 km is the approximate lower limit for MCS temperature retrievals). Despite this lack of a strong meridional temperature gradient, there is still a strong zonal jet which extends into the upper atmosphere (Fig.6.13.d), giving further support to the hypothesis that both aphelion and perihelion jets are barotropic phenomena. Therefore, the broader pressure cycle must be taken into consideration to explain the results. This is discussed further in Section 6.2.4; but broadly speaking, global surface pressures are consistently lower in the 2D reanalysis and the southern seasonal CO_2 cap is consistently larger, implying that in the 2D reanalysis a greater percentage of the atmosphere is condensed into the seasonal caps, leaving less in gas form. Again, this is discussed and compared to observed surface pressures and seasonal cap extent in Section 6.2.4.

6.2.4 Comparison with observations and modelling

Unfortunately there are no direct measurements of wind speeds at high southern latitudes to compare against. Global orbital measurements of atmospheric wind speeds, such as would be taken by the proposed COMPASS mission (Byrne et al., 2020), would not be able to directly measure to the surface but would certainly be able to constrain lower atmospheric winds and thus provide insight into the surface behaviour, including through assimilation into MGCMs. In situ surface measurements at southern high latitudes are less likely to happen in the forseeable future, given the difficulty of landing vehicles in the topographically elevated southern hemisphere. Therefore, for the time being comparison against observed wind speeds is not possible.

In lieu of direct wind speed observations, and given the highly global and interconnected nature of Mars' weather system - where, for example, high latitude wave activity is detectable

at the equatorially located Gale Crater (Haberle et al., 2018) - it is possible to use indirect methods to try to compare these results to observations. One method is to compare surface pressures in the reanalyses to those measured by the Viking Landers. While Mars Science Laboratory/Curiosity also has a surface pressure dataset, it is located in a crater approximately 4 km below the surrounding mean terrain; the crater is too small to be resolved in these reanalyses. This would skew the surface pressure results. Viking Landers 1 and 2 (henceforth VL1 and VL2 respectively), on the other hand, are located on fairly flat terrain, making them better suited for MGCM comparison. However, this only provides an indirect comparison, as agreement or disagreement with the MGCM is dependent on various factors such as the surface roughness length, the albedo and thermal emissivity of the seasonal CO_2 cap (Hourdin et al., 1995), and the parameterisation used for sublimation and condensation of the cap. As discussed further in Section 6.2.5, there are strong caveats regarding the use of Viking pressures for validation of this phenomenon, as the MGCM itself is tuned to agree with the Viking pressures. Specifically, MGCM CO_2 mass budgets and the albedo of the CO_2 ice formed by physical processes (which incorporate CO_2 cloud effects) in the MGCM are not directly measured, but were tuned to provide a good fit to said pressures (Hourdin et al., 1995). The agreement or disagreement with Viking shown by the reanalyses in the following plots is therefore by no means conclusive as to which provides a better representation of the martian atmosphere, as polar albedo/CO_2 mass values could theoretically be re-tuned to allow disagreeing reanalyses to match observed surface pressure data. Viking comparisons should therefore be viewed within the context of how the MGCM is tuned, rather than as an comparison to independent observations.

Fig. 6.22 compares surface pressures from the reanalyses to those from VL1 and VL2. Note that the period L_S=0-20° lacks MCS observations, and so the two reanalyses are identical. There is very good agreement between both reanalyses and the Viking pressures in the periods L_S=0-60° and L_S=290-360° (the “bump” in the Viking pressures shortly after

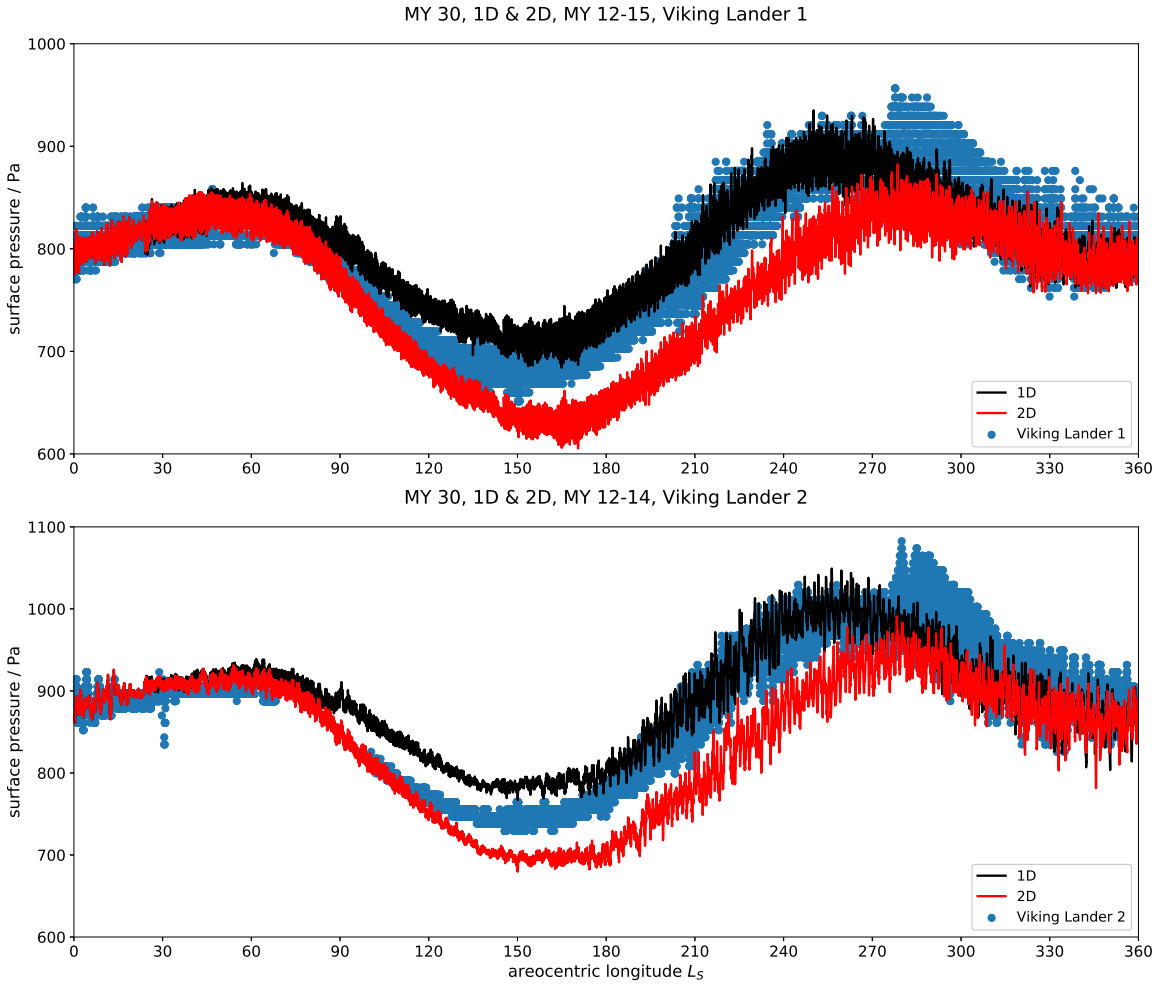

Fig. 6.22 Surface pressure at the Viking Lander (top) 1 and (bottom) 2 locations for the martian years specified, from the 1D and 2D reanalyses and the Viking Landers themselves. No running mean has been implemented in order to show the range of diurnal variability.

L_S=270° is due to the presence of a Global Dust Storm); in between, there is divergence in the results.

At both locations, the 1D reanalysis pressures are consistently higher than or on the upper end of the Viking pressures, while the opposite is the case for the 2D pressures. The greatest difference between the 1D and 2D cases occurs around L_S=150-180°, and is close to 100 Pa; the Viking pressures lie in between. At the VL1 location, the 1D pressures show a better general agreement with Viking, while the 2D pressures are consistently below by up to 70 Pa. The situation is more complex at the VL2 location, as the 2D case shows better agreement between L_S=90-120, while the 1D case shows better agreement between L_S=180-270.

Another way of comparing the reanalysis results to observations is to compare the sizes of the seasonal CO_2 caps to orbital observations of the caps. Fig. 6.23 shows south polar CO_2 surface ice mass from the reanalyses and MCS-derived maximal CO_2 ice coverage for the same period. In the L_S=90-120° period (Fig. 6.23.a,c,e) during which the southern seasonal cap is at its greatest extent, both reanalyses show reasonable agreement with the observations. The greatest difference between the reanalyses appears not to be the extent of the ice coverage, but the thickness, as expressed in the ice mass: the 2D case has >1000 kg m^2 CO_2 ice mass in some near-pole, indicating thicker/longer-lasting CO_2 surface ice presence. This implies a larger mass of the seasonal cap in the 2D case, despite the similar latitidunal extents, with implications for the atmospheric mass budget and global surface pressures.

The L_S=240-270° period (Fig. 6.23.b,d,f) shows greater differences in latitudinal extent. The 2D reanalysis shows a larger seasonal cap than the 1D reanalysis, extending equatorward of 70° S at several longitudes, and a much greater (>1000 kg m^2) CO_2 ice mass. The 1D reanalysis agrees very well with the MCS observations in terms of the longitudinal and latitudinal extent of CO_2 ice coverage, reproducing the observed high latitudinal asymmetry where the seasonal cap is almost exclusively located between -120-60° E.

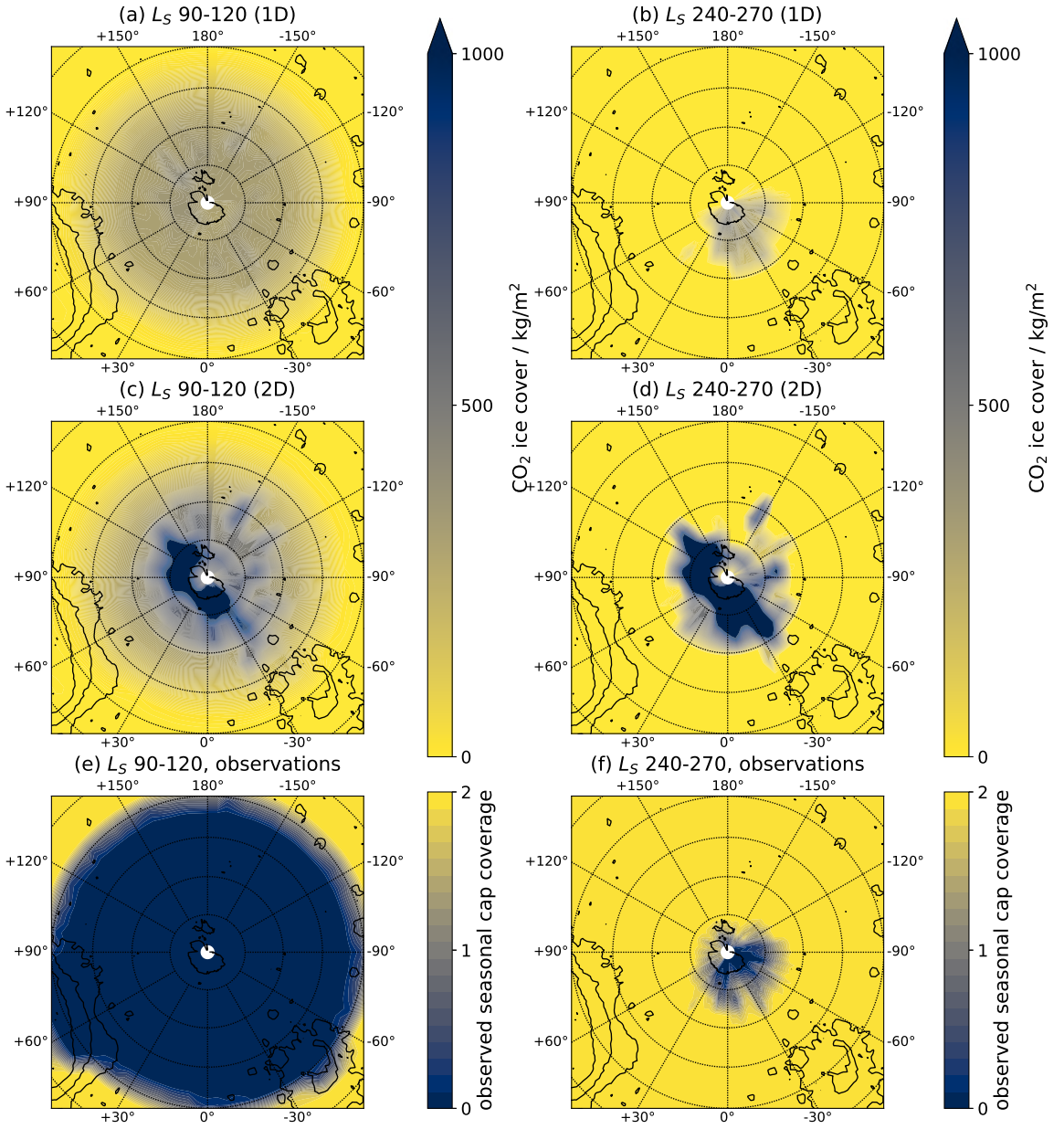

Fig. 6.23 MY 30 CO_2 surface ice mass at the SP (a,b,c,d) for the periods (left) L_S=90-120° and (right) L_S=240-270°, for the (top) 1D reanalysis and (middle) 2D reanalysis; climatologically averaged seasonal CO_2 cap extent at the SP (e,f) for the same periods from Piqueux et al. (2015), as derived from MCS surface temperature data. In this notation, "2" signifies no CO_2 ice coverage during the relevant period, "1" indicates a boundary state, while "0" signifies the presence of surface CO_2 ice. See the Supplementary Information from Piqueux et al. (2015) for more information. Plots are stereographic projections where each latitude circle is 10° separate from its neighbours and the innermost circle represents the 80° latitude band.

Finally, in lieu of observational comparison it is possible to compare to other modelling work looking at condensation and sublimation flow around the seasonal caps. Chow et al. (2019) used the MarsWRF MGCM to specifically model these flows for the northern and southern polar caps. They found that the sublimation flow was significantly greater than the condensation flow, and that the southern cap-related flow was much greater than that in the north. Their results disagree with the condensation flow feature present in the 2D reanalysis, seeing zonally-averaged meridional wind speeds of $\sim$0.5 m/s. This is far more in line with the results of the 1D reanalysis. The sublimation flow is, by contrast, fairly strong, with typical wind speeds of $\sim$10 m/s (Chow et al., 2019). This falls somewhere between the 1D and 2D cases, though closer to the 1D case, suggesting that while wind speeds should be higher than in the 1D case, they are being drastically overestimated in the 2D case.

6.2.5 Discussion

The broad implication of the results presented here is that the 1D and 2D reanalysis show different high southern latitude wind speeds because of large differences in the pressure cycle and atmospheric mass budget. Specifically, the larger seasonal CO_2 ice cap in the 2D reanalysis results in lower surface pressures everywhere else on the planet, driving greater sublimation flow during the perihelion season. Correspondingly, during aphelion a greater condensation flow drives the growth of a larger seasonal cap.

Given the complex nature of these processes and the various feedbacks, it is important to try to establish a clear causal chain. The proposed causal chain is as follows: a colder southern polar vortex (during the aphelion season) in the 2D reanalysis causes greater condensation onto the southern seasonal cap, resulting in a strong condensation flow, a thicker cap, and correspondingly lower global surface pressures; as this larger seasonal cap retreats during southern summer (the perihelion season), this greater surface pressure differential necessitates a stronger sublimation flow. This interpretation is supported by the modelled lower southern

polar vortex atmospheric temperatures (well below the CO_2 condensation temperature in places); the modelled surface pressure gradients at L_S=90-120° and L_S=240-270°; the lower surface pressures at VL1 and VL2 locations for the 2D reanalysis throughout the whole period during which the southern seasonal CO_2 cap exists; and the larger/more massive modelled seasonal cap in the 2D reanalysis.

Given the caveats described in Section 6.2.4, establishing the reality of these wind phenomena is not a straightforward task. Hourdin et al. (1993) found that using point-source surface pressures, such as from the Viking Landers, was not by itself sufficient to validate the global atmospheric mass budget; this is partly due to the intense dynamics at high latitudes. That said, certain MGCM parameters - specifically, the emissivity and albedo of the CO_2 surface ice - have been subsequently tuned in order for the MGCM to match the reported Viking pressures. The systematically below-Viking pressures seen in the 2D reanalysis do therefore raise the question of whether the reanalysis is providing a realistic estimate of the state of the atmosphere, and most directly the amount of condensation occuring during southern winter and the mass of the atmosphere locked in the southern seasonal cap. However, this is not possible to determine by comparison to Viking alone, due to the caveats already mentioned: the Viking pressure data is not an independent source of observations to compare the MGCM (as it is currently tuned) against.

A possibility is that the many sub-CO_2 condensation temperature retrievals being assimilated into the MGCM in the 2D case is driving too much condensation. Previous data assimilation efforts using TES temperature retrievals have filtered out temperatures below the surface CO_2 condensation temperature to avoid problems with condensation in the MGCM parameterisations (e.g. Greybush et al., 2019; Lewis et al., 2007). Sub-condensation temperatures also suggest the possibility of supersaturation, something which likely occurs in the middle-upper polar atmosphere (Listowski et al., 2014) but is not currently parameterised in the MGCM. However, to the extent of the author's knowledge this filtering has not been

applied to MCS temperature retrievals. The key difference is that TES temperature retrievals go down to the surface from 40 km, whereas the MCS limb sounding technique means that the lowest measurements occur around 8-10 km above the surface. These results show that sufficiently low temperatures in the lower atmosphere, even if not directly above the surface, can still induce enhanced condensation rates.

In an effort to gauge the impact of filtering sub-CO_2 condensation temperatures, therefore, an additional limited reanalysis was performed. This reanalysis ("2D filtered") used the same CDOD observations as the 2D case, but filtered temperature retrievals at each atmospheric pressure level according to the equation

$$T_{CO_2} = 149.2 + 6.48ln(0.135p) \tag{6.2}$$

where T_{CO_2} is the CO_2 condensation temperature and p is the pressure in millibars, following Pollack et al. (1981). Temperatures that fell below T_{CO_2} were set equal to T_{CO_2} before being assimilated. This represented 1.1% of individual temperature observations (not profiles) over the course of the whole of MY 34, with an average shift of 5.3 K.

The results are presented in Figs. 6.24, 6.26, and 6.27. Interestingly, the 2D filtered reanalysis shows very good agreement with the 1D reanalysis (Fig. 6.24), also overestimating surface pressures as compared to the Viking Lander data by up to 30 Pa during the period L_S=90-180°. Meanwhile, Fig. 6.26 shows that the 2D filtered wind speeds during the aphelion season are actually lower than in the 1D reanalysis. This can be explained as due to the fact that the 1D reanalysis doesn't filter sub-CO_2 condensation temperatures, of which there are still a few (despite there being far fewer than in the 2D case). There is therefore even less condensation and resulting flow. What is surprising is that the surface pressure at the Viking locations is almost identical to the 1D case in the aphelion season, suggesting that there is equal mass locked up in the seasonal ice caps. This implies that the explanation for the aphelion high wind speeds presented above (more condensation means

higher condensation flow and larger ice cap mass, hence lower global surface pressures) is incomplete.

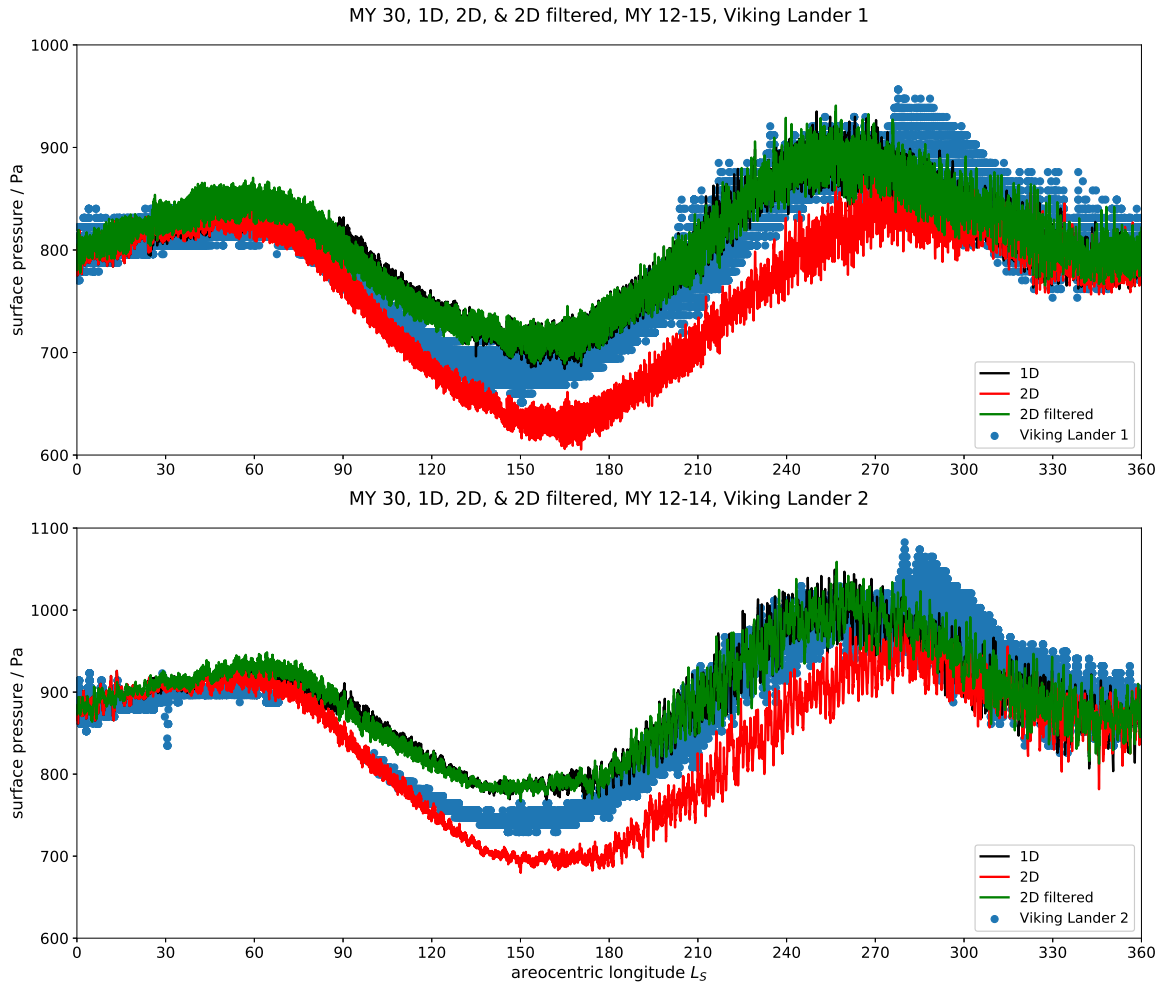

Fig. 6.24 Surface pressure at the Viking Lander (top) 1 and (bottom) 2 locations for the martian years specified, from the 1D, 2D, and 2D filtered reanalyses and the Viking Landers themselves. No running mean has been implemented in order to show the range of diurnal variability.

Another source for surface pressure data is the Insight lander, which has been measuring surface pressure at its equatorial location since December 2018. While a full martian year of surface pressure data is not yet available, the currently available data is plotted against surface pressures from the 1D, 2D, and 2D filtered reanalyses in Fig. 6.25. The advantage of the Insight measurements is that they are independent from the original tuning of the MGCM,

which was done using Viking pressure data, making them better sources for comparison. As with the Viking location, the 2D filtered and 1D cases agree almost exactly. Both appear slightly overestimate surface pressures as compared to Insight (by up to 30 Pa) during the aphelion season, but agree well with the data from towards the end of the perihelion season. The 2D filtered pressures agree better with the Insight data for the aphelion season as a whole, but appear to be underestimating pressure towards the end of the available Insight data in this season.

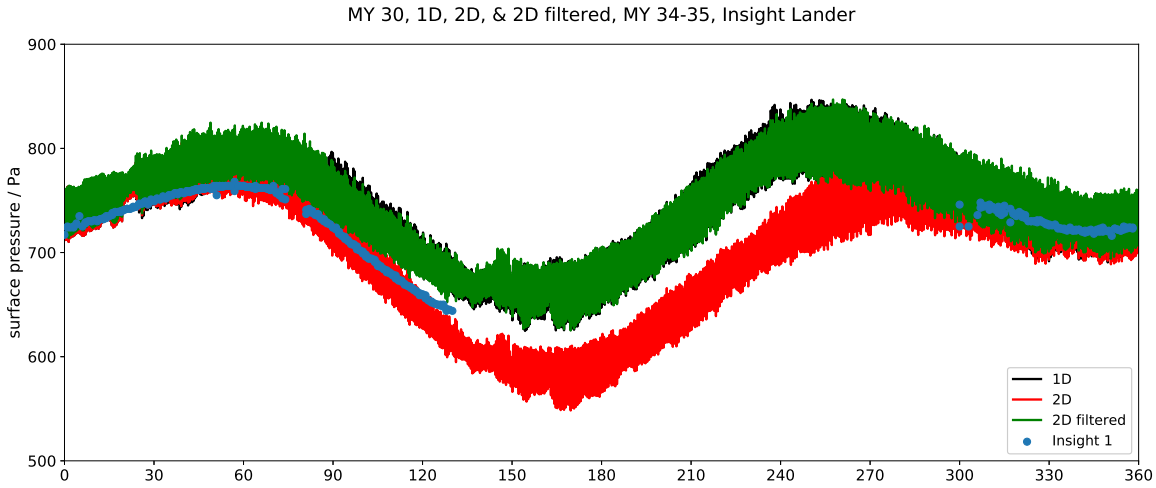

Fig. 6.25 Surface pressure at the Insight lander location for the martian years specified, from the 1D, 2D, and 2D filtered reanalyses and the Insight lander itself. No running mean has been implemented in order to show the range of diurnal variability.

Meanwhile, 2D filtered reanalysis wind speeds during the perihelion season are slightly higher (up to 1 m/s) than in the 1D case but significantly lower (up to 8 m/s) than in the 2D case. This is consistent with the fact that global surface pressures are almost identical to those in the 1D case.

There is little difference between the modelled southern ice caps in the 1D and 2D filtered cases at either aphelion or perihelion (Fig. 6.27). Both reproduce the degree of longitudinal asymmetry in ice coverage around the same locations as in the MCS observations, showing better agreement with the observed CO_2 ice coverage than the unfiltered 2D reanalysis. The

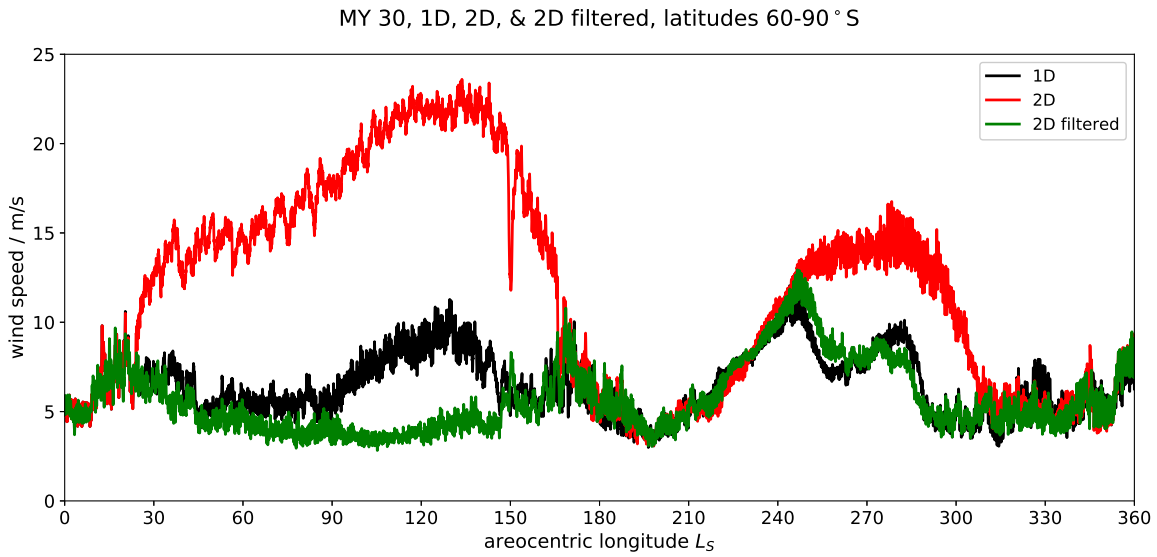

Fig. 6.26 MY 30 near-surface wind speeds as averaged between latitudes 60-90° S, for the 1D, 2D, and 2D filtered reanalyses.

2D filtered reanalysis does show slightly greater CO_2 ice mass than the 1D reanalysis over the southern pole at both aphelion and perihelion.

Finally, Fig. 6.28 compares the latitudinal extent of the seasonal caps throughout MY 30 for the 1D, 2D, and 2D filtered reanalyses to climatological data from MCS observations from Piqueux et al. (2015). The 2D reanalysis show increased (relative to the 1D and 2D filtered reanalyses) mass of the southern cap at high latitudes, poleward of 70-75° S, and reduced mass equatorward of that. It also shows reduced mass at the northern seasonal cap and, perhaps most interestingly, a permanent seasonal cap presence L_S=300-360°. This latter permanent coverage agrees with the climatological observations, which show surface CO_2 ice present at the south pole through the entire orbital cycle. While neither the 1D nor the 2D filtered reanalyses show a permanent CO_2 ice presence at the southern pole, there are differences between them. The 2D filtered reanalyses contains greater ice mass at the southern cap from L_S=90-270°, and less ice mass at the northern cap from L_S=270-90°. This mass distribution difference appears to balance out almost exactly, leading to identical surface pressure in both reanalyses.

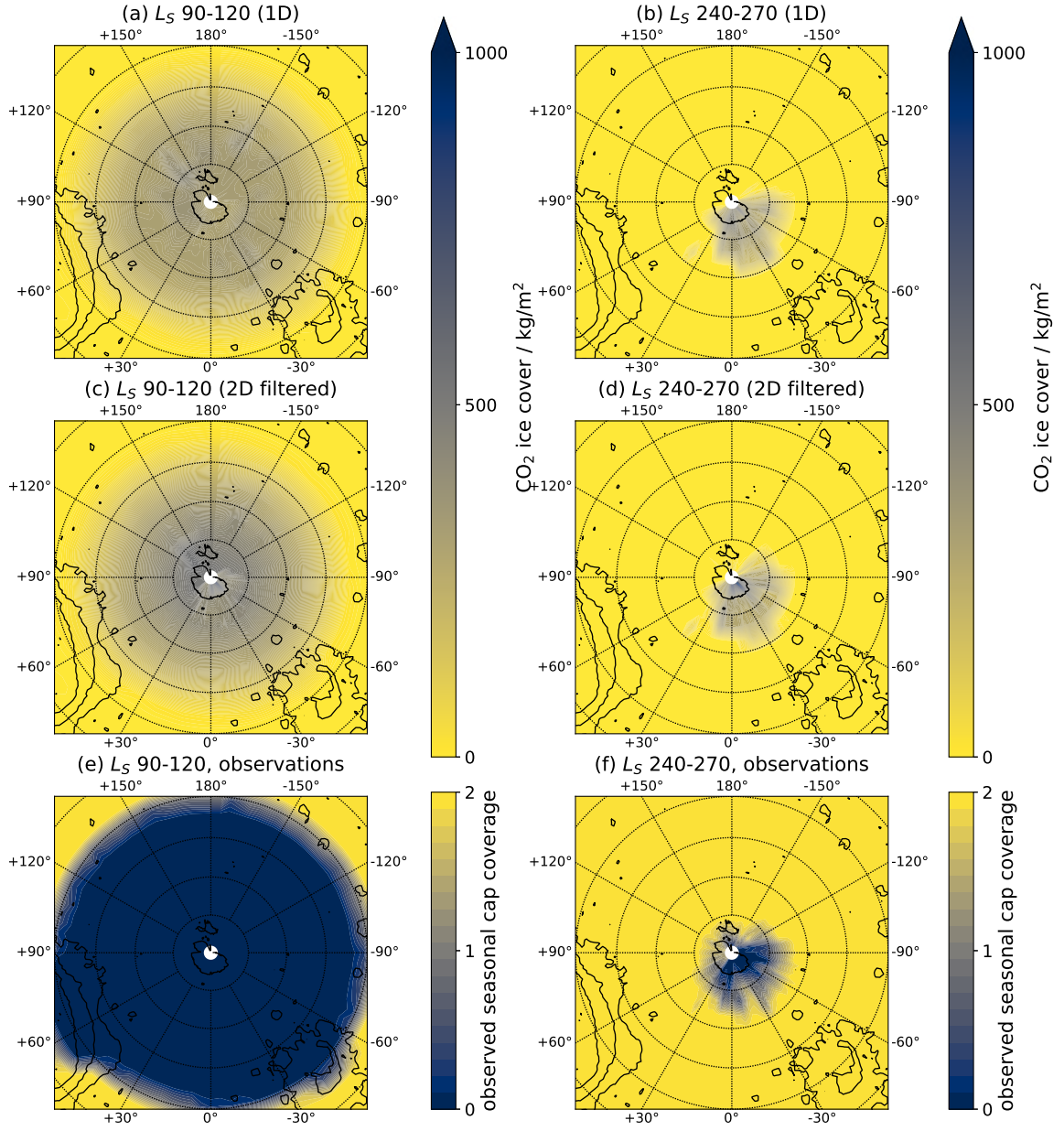

Fig. 6.27 MY 30 CO_2 surface ice mass at the SP (a,b,c,d) for the periods (left) L_S=90-120° and (right) L_S=240-270°, for the (top) 1D reanalysis and (middle) 2D filtered reanalysis; climatologically averaged seasonal CO_2 cap extent at the SP (e,f) for the same periods from Piqueux et al. (2015), as derived from MCS surface temperature data. In this notation, "2" signifies no CO_2 ice coverage during the relevant period, "1" indicates a boundary state, while "0" signifies the presence of surface CO_2 ice. See the Supplementary Information from Piqueux et al. (2015) for more information. Plots are stereographic projections where each latitude circle is 10° separate from its neighbours and the innermost circle represents the 80° latitude band.

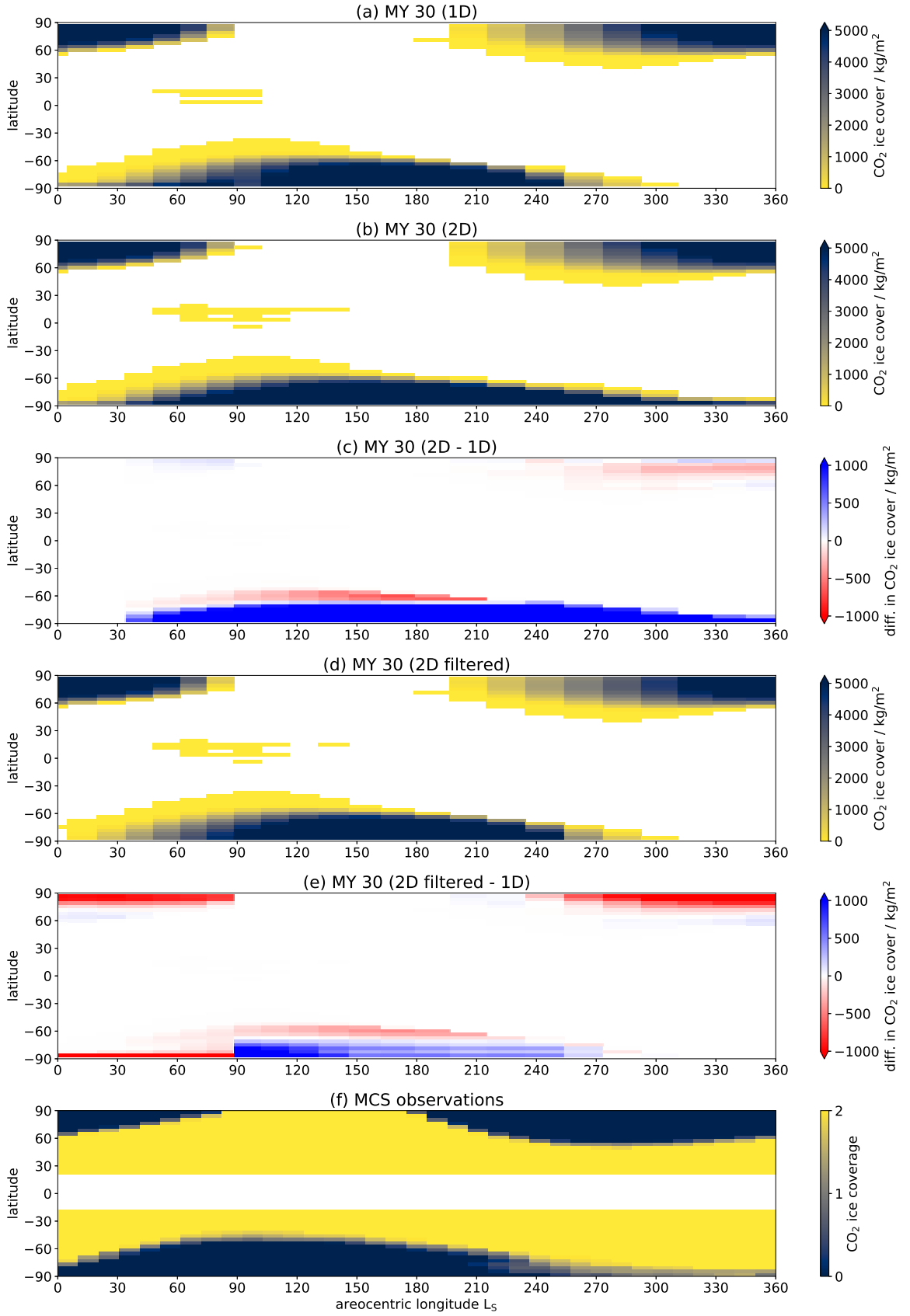

Fig. 6.28 a,b,d: zonally averaged surface CO_2 ice cover for MY 30 for the 1D, 2D, and 2D filtered reanalyses respectively. c,e: difference in such for MY 30 between the 2D and 1D reanalyses and the 2D filtered and 1D reanalyses, respectively. f: climatological surface CO_2 ice coverage observations, where "0" indicates seasonal cap presence; "1" indicates cap edge; "2" indicates no seasonal ice. The white space indicates lack of observations.

Consideration of the 2D filtered results requires a modification to the narrative explanation presented above. The 2D filtered reanalysis shows identical surface pressures to the 1D reanalysis and greater CO_2 mass locked up at high latitudes in the southern seasonal cap, and yet lower southern cap wind speeds. In other words, it appears to be the filter that is limiting condensation flow, despite there still being enhanced condensation occuring. There is a much reduced surface pressure gradient towards the pole, despite condensation to the surface still occurring; this implies that with the filter, the condensation process is a lot more stable, preventing a runaway condensation from drastically reducing surface pressures at southern high latitiudes and thus causing surface air from lower latitudes to rush in to equalise pressures. With the filter, condensation still occurs due to the cold polar night but there are fewer sudden condensations of large parts of the atmosphere and the process is more stable. However, the more massive southern cap (at latitudes $\geq$70° S) in the 2D filtered reanalysis is not sufficient to prevent its total recession during the perihelion season. In the unfiltered 2D reanalysis, by contrast, greater mass at the southern ice cap leads to reduced global surface pressures, a strong sublimation flow at perihelion, and a permanent southern high latitude CO_2 ice presence.

6.2.6 Conclusions and recommendations

It is clear that the particular temperature profiles used in the assimilated MGCM, and their processing pre-assimilation, have a huge impact on modelled near-surface wind speeds at southern high latitudes. Using the older 1D MCS retrievals, unfiltered, results in low wind speeds over the southern seasonal cap at aphelion and around the southern seasonal cap edge at perihelion. The southern seasonal cap recedes completely at around L_S=300°. Using the newer 2D retrievals, which show a significantly colder southern polar vortex, without filtering results in very high wind speeds over the southern seasonal cap at aphelion and around the southern seasonal cap edge at perihelion, these high near-surface winds being the

surface expression of intense barotropic jets which extend into the upper atmosphere. The southern seasonal cap is overall more massive with resultingly lower global surface pressures, and seasonal CO_2 ice is present at the southern pole throughout the entire orbital cycle. Filtering the newer 2D retrievals to set any sub-CO_2 condensation temperatures ($T < T_{CO_2}$) to T_{CO_2} results in lower wind speeds over the southern seasonal cap at aphelion than in the 1D case, and wind speeds similar to the 1D case around the southern seasonal cap edge at perihelion. As with the 1D case, there is not a permanent CO_2 ice presence over the southern pole throughout the whole orbital cycle. Surface pressures are higher than in the unfiltered 2D case, suggesting less mass locked in the southern seasonal cap. The 1D and 2D filtered reanalyses show a longitudinal asymmetry in CO_2 ice coverage at the southern cap during perihelion, as is present in MCS observations of the southern polar CO_2 cap. This asymmetry is not seen in the unfiltered 2D reanalysis.

The impact on near-surface southern high latitude wind speeds comes via the effect of atmospheric temperatures on condensation over the southern seasonal cap; condensation rates then affect the southern high latitude pressure gradient and surface pressures globally. Having constant atmospheric condensation and the resultingly lower surface pressures over the southern cap relative to lower latitudes leads to intense winds to compensate in the form of westerly barotropic jets, seen in the unfiltered 2D case. These jets have an associated shallow poleward meridional flow via the mechanism of Ekman flow. The more massive cap induces greater sublimation flow at perihelion, leading to the reverse situation than in the aphelion case: higher surface pressures at the south pole lead to easterly barotropic jets, with an associated shallow equatorward meridional flow. Reducing the constant and drastic atmospheric condensation in the MGCM parameterisation by filtering sub-T_{CO_2} temperatures still leads to a more massive southern cap at high latitudes, but eliminates the intense condensation flow seen without the filtering.

Direct observational comparison of the reanalysis wind speeds is currently impossible, but indirect comparison via surface pressure observations, seasonal cap extent observations, and other modelling work allows for an estimate of which reanalysis is closer to reality. The 1D/2D filtered and unfiltered 2D reanalyses respectively tend to overestimate and underestimate the surface pressures at the Viking Lander 1 and 2 locations throughout most of the period when the southern seasonal cap is at is greatest extent. However, there are strong caveats on using the Viking pressure data as a validation source due to the MGCM being tuned to match the Viking pressures under certain dust scenarios; future work should involve full retuning of the MGCM against both Viking and the newer surface pressure data from the MSL and Insight missions. At the Insight location, the 1D/2D filtered reanalyses overestimate surface pressures at aphelion, while the 2D unfiltered reanalysis shows better agreement with Insight data. All reanalyses agree reasonably with Insight surface pressures at perihelion. The 1D and 2D filtered reanalyses capture the longitudinal asymmetry of the southern seasonal cap at perihelion as seen in observations, while the unfiltered 2D reanalysis overestimates the latitudinal extent of CO_2 ice. However, the 2D unfiltered reanalysis does predict the presence of a permanent CO_2 ice presence at high southern latitudes in late perihelion, as present in in MCS observations, while the other reanalyses do not. Finally, other modelling work suggests the existence of a strong, shallow sublimation flow from the southern seasonal cap around perihelion; this agrees with all the reanalyses, but the 1D and filtered 2D appear to be closer in terms of magnitude while the unfiltered 2D would seem to overestimate wind speeds.

No one reanalysis therefore seems to provide the best fit to all observations, showing that further work is needed on this topic. Assimilation-based investigations which involve looking at the southern seasonal cap, its associated near-surface wind speeds, and global surface pressures generally would therefore be advised to consider carefully which MCS temperature dataset and which filtering method is optimal for the particular use case. The

2D unfiltered reanalysis fails to reproduce the observed longitudinal asymmetry in CO_2 ice coverage at perihelion; however, only the 2D unfiltered reanalysis correctly predicts the presence of a permanent southern CO_2 cap. This reanalysis also predicts higher near-surface wind speeds than those suggested by other modelling work. While the high wind speeds in the 2D unfiltered reanalysis are significantly higher than in the other reanalyses, the good agreement of the 2D unfiltered reanalysis pressure data with Insight and ice cap coverage with MCS means that the magnitude of these winds cannot be simply dismissed as an unphysical phenomenon.

In terms of future work, the disagreement in the longitudinal asymmetry and seasonal extent of the southern seasonal cap points to the need for further investigation of the causes of these features, and how to incorporate them into MGCM parameterisations. Assuming the trustworthiness of the 2D MCS temperature retrievals and their cold polar vortex, there is also a need to understand how to incorporate them into MGCMs without the need for filtering. This will involve looking at CO_2 supersaturation and CO_2 ice clouds (e.g. Audouard et al., 2017). For example, the current MGCM parameterisation used here assumes that air parcels below T_{CO_2} turn into snow and travel through the atmospheric layers below before being deposited onto the surface (Forget et al., 1998). The abundant presence of dust in the martian atmosphere and observations of tropospheric CO_2 ice clouds in the polar winter (e.g. Hayne et al., 2012; Hu et al., 2012) imply that cloud formation is another possibility in the polar night. How could cloud formation of this kind be parameterised? And what implications would this have for the surface energy budget? These are questions which bear addressing for future work on Mars' polar atmosphere and surface-atmosphere interactions. Importantly, as Insight continues to collect surface pressure data, it will provide a valuable and MGCM-independent source for comparison.

Finally, a key aim should be further comparison of reanalysis wind speeds with observations. As stated, there is currently a lack of orbital wind observations for the martian

atmosphere. The technique of cloud tracking has been used previously in the martian context to attempt to characterise wind speeds from orbit, by following recognisable cloud features using optical imagery (e.g. Kaydash et al., 2006; Wang and Ingersoll, 2003). This method could be used to compare against the wind speeds in the reanalyses described here, as the jets predicted by the 2D reanalysis extend into the upper atmosphere. Uncertainties in calculated velocity and cloud height make cloud tracking a difficult tool to use (Wang and Ingersoll, 2003), but the modelled differences of >30 m/s in zonal wind speeds between the 2D and 1D reanalyses may be sufficiently large that cloud tracking could provide a better idea of which reanalysis better represents southern high latitude winds.

Further in the future, orbital measurements of wind speeds would be an invaluable resource in characterising polar dynamics, including near-surface wind speeds, by allowing better constraints on modelled wind speeds via assimilation. The differences in model winds between the reanalyses discussed here extend >20 km above the surface, putting them well within the range of possible future orbital wind observations.

Chapter 7

Conclusions and future work

This chapter first presents a brief summary of the work undertaken in Chapters 4, 5, and 6 of this thesis, and the results from this work. Then, some general conclusions are drawn from the results and discussed in the context of the initial research questions posed in Chapter 1. Finally, avenues for future work are proposed, divided into the categories of work which could be feasibly done with the data and methods available at the time of writing and work which could be done with possible future observational datasets and modelling capabilities.

7.1 Summary of work presented

This section is intended as a high-level summary of the work undertaken in this thesis and the results presented. For more complete discussions of the results of this thesis, the reader is referred to the individual Conclusions sections of each results chapter (Chapters 4, 5, and 6), which provide more detailed summaries and comparisons with the existing literature.

The aim of this thesis was to investigate the radiative-dynamical impacts of suspended atmospheric dust and the cycle of dust in the atmosphere of Mars, via the assimilation of observational data into a Mars global climate model. The specific research questions (discussed in detail in the next section) focussed on the effects of the high dust loading caused

by the 2018 Global Dust Storm on surface and near-surface temperatures and on the polar vortices, and on the interannual patterns in surface dust lifting and deposition and their links to broader dynamical features and observed dust activity.

Previous modelling, observational, and assimilation work has demonstrated the crucial role of dust in martian meterology. Dust (and enhanced loading during storms) plays a causal role in modelled and observed large-scale dynamical features such as thermal tides (e.g. Guzewich et al., 2014; Lewis and Barker, 2005), polar warming (e.g. Wilson, 1997), the solsticial pause in baroclinic planetary wave activity (e.g. Lee et al., 2018; Mulholland et al., 2016), the mean meridional circulation (e.g. Haberle et al., 1982), and the structure of the polar vortices (e.g. Guzewich et al., 2016; Mitchell et al., 2015), as well as in controlling the surface energy budget (e.g. Read et al., 2016). At the same time, the lifting and transport of dust is in turn governed by large-scale dynamics: modelled dust lifting is controlled by near-surface wind speeds (e.g. Kahre et al., 2005; Montabone et al., 2005; Newman et al., 2002a), observed dust storms are frequently associated with baroclinic wave activity (e.g. Wang, 2018; Wang et al., 2013), and lofted dust is transported by the global circulation and redeposited (e.g. Newman et al., 2005; Szwast et al., 2006). However, outstanding questions still remain regarding both the atmospheric effects of dust and the spatiotemporal structure of the dust cycle. Some of these are the ones addressed in the research questions in Chapter 1: namely the radiative-dynamical effects of Global Dust Storms, such as the 2018 event, and the interannual pattern of lifting and deposition and its links to large-scale dynamical features and observed dust storm activity.

Chapter 3 described the methods used in these thesis to investigate the research questions: the Mars global climate model, the orbital observations of temperature and dust from the Mars Climate Sounder instrument, and the data assimilation scheme used to integrate the observations into the model. There are several advantages to this method over using either model or observations by themselves. Data assimilation helps overcome the inherent

limitations of observations from a single orbiter, namely their temporal and spatial sparsity, by using the model to fill the gaps and thereby provide a complete four-dimensional atmospheric state, including variables (such as wind speeds) which are not currently retrieved from orbit. Assimilation also has advantages over running the model by itself: by incorporating real observational data, it can produce more realistic dynamics and dust distributions, especially important for analysing specific dynamical features (such as the polar vortices) and real dust storms and their effects (such as the 2018 Global Dust Storm). Data assimilation is therefore a valuable tool for studying dust in the martian atmosphere, including its atmospheric impacts and how its cycle is governed by large-scale dynamics.

This thesis aims to advance our collective knowledge regarding these questions using the method of data assimilation. This technique combines the diagnostic power and full four-dimensional coverage of a global climate model with actual observations of the state of the martian atmosphere, making it ideally suited to tackling the research questions presented. Data assimilation was used study the dynamical and radiative changes caused by a real Global Dust Storm, and to examine how lifting and deposition varied over the course of six observed martian years.

Chapter 4 presented the results of an investigation into how the 2018 Global Dust Storm affected surface and near-surface air temperatures, using the assimilated MGCM and comparing with a relatively clear martian year. Observations have indicated that the presence of a Global Dust Storm generally reduces surface temperatures on the dayside of the planet and increased them on the nightside (e.g. Guzewich et al., 2019; Smith, 2004). This observational work has some limitations, however: orbital observations from the TES and MCS instruments are constrained to two local times, while surface-based observations show the full diurnal cycle but only at specific locations. Chapter 4 showed the results of the first-model based analysis of how a Global Dust Storm affects surface temperatures, giving results over all local times, and used a realistic dust distribution from the actual 2018

event. The results show that surprisingly the 2018 storm induced a net surface warming as averaged over the entire planet, while the spatial temperature difference map showed a high degree of heterogeneity in average surface warming or cooling depending on location, with low thermal inertia regions showing net warming. Whether a particular location warmed or cooled on average was controlled by two independent factors: the magnitude of dust loading at that location, and the surface thermal inertia. The former controlled the degree of dayside cooling by blocking of incident solar radiation, and the latter of nightside warming from backscattered surface infrared emission. The independence of these factors explained the heterogeneity of the surface warming/cooling map. The persistence of the nightside warming effect over the diurnal cycle explained why surface warming was the average result, despite the maximum dayside cooling and nightside warming values being very similar. Further free-running simulations were performed at different dust loadings to test the robustness of the results, and showed a consistent slight globally-averaged surface warming over most high dust loadings. Finally, results were compared to various observational datasets, including MCS surface temperature retrievals for the time of the Global Dust Storm, and showed generally good agreement, especially in the surface warming/cooling maps.

Chapter 5 showed the results of a multi-year analysis of patterns in modelled dust lifting and deposition with the assimilated MGCM, including the year of the 2018 Global Dust Storm. Previous studies of modelled dust lifting have used free-running simulations, which tend to show reasonable agreement with the observed dust distribution of a generic martian year but are currently incapable of replicating observed dust storms (e.g. Basu et al., 2004; Chapman, 2018; Kahre et al., 2006, 2005; Mulholland et al., 2013, 2015; Newman et al., 2002a,b). By using a model assimilated with six martian years worth of actual observations, this work aimed to provide an account of how lifting and deposition vary by season and geographical location between real martian years, including with the presence of observed storms such as recurring regional storms (Kass et al., 2016) and the 2018 Global Dust Storm.

Other literature has identified and characterised specific dynamical phenomena associated with winds at the martian surface, such as thermal tides (e.g. Lewis and Barker, 2005), the Hadley circulation and its associated flows (e.g. Joshi et al., 1997, 1995), baroclinic planetary waves (e.g. Wang et al., 2013), sublimation of the seasonal CO_2 caps (e.g. Chow et al., 2019), and the solsticial pause in wave activity (e.g. Lewis et al., 2016; Mulholland et al., 2016); this study aimed to comprehensively relate these features to modelled dust lifting.

The results showed a very high degree of interannual similarity in both modelled lifting and deposition of dust, in both seasonality and geographical location, with the exception of the period of the 2018 Global Dust Storm. The modelled geographical variation in lifting and deposition was shown to be almost entirely seasonal, with the higher wind speeds of the perihelion season leading to higher lifting. Lifting was generally greatest at high latitudes, due to the presence of baroclinic wave activity and cap-edge sublimation. The solsticial pause in baroclinic wave activity was detectable in high-latitude lifting at both hemispheres. There were also temporally limited bands of higher lifting associated with the subtropical jet caused by the Hadley circulation. The southern seasonal cap showed extremely high modelled lifting in early southern summer, apparently linked to high wind speeds driven by the sublimation of the southern seasonal cap. Regional and global-scale dust storms introduced some variability in lifting; the latter increased lifted dust flux by >1000%, while the former had more complex effects. The magnitude of regional storms at tropical latitudes appeared to be linked to the magnitude of southern seasonal cap-edge lifting, with more intense storms correlating to decreased lifting (and vice-versa) likely due to enhanced sublimation of the cap from the boosted meridional circulation. Meanwhile the 2018 Global Dust Storm had little discernible effect on southern cap edge lifting in early southern summer, but significantly enhanced lifting at tropical latitudes (particularly over areas of high topography) and at the southern cap edge later in southern summer. By contrast, lifting decreased at northern mid-high latitudes, due to an apparent decrease in baroclinic wave activity. The results were compared

to observed dust storm records. Interannually repeatable lifting features in the perihelion season appeared to be linked to the regularity of large regional storms in that season. High latitude lifting corresponded well with frequent observed storm activity. Modelled high lifting features associated with the southern subtropical jet and southern seasonal cap sublimation (both at perihelion) appeared to correlate with an absence of dust storm activity. Comparison with records of martian surface dust cover implied that these regions may be frequently swept clean by the high-speed, regular winds, casting doubts on their adequacy as sites for dust storm formation. The modelled dust deposition correlated almost exactly with dust loading in the assimilated MGCM, but high wind speeds also had an effect in inhibiting deposition.

Finally, Chapter 6 was split into two sections, both looking at aspects of polar atmospheric dynamics. The first section presented results comparing the structure of Mars' polar vortices during the 2018 Global Dust Storm to the same period in the previous year, in order to investigate the effects of the GDS on the vortices. Previous work has examined the effects on the northern polar vortex of a regional storm in southern autumn/winter from an assimilated dataset (Mitchell et al., 2015) and an idealised global-scale dust loading at southern summer solstice (Guzewich et al., 2016), and the effects on the southern polar vortex of the 2018 storm from MCS observations (Kleinböhl et al., 2020). This study looked at the effects in an assimilated model of the 2018 event, which was an equinoctial storm, on both vortices. The use of assimilation allowed the comparison of potential vorticity, wind speeds, and the mean meridional circulation, none of which are directly observed fields. The results showed a slightly smaller and significantly more symmetric northern polar vortex in the Global Dust Storm case, compared to the usual elliptical shape (e.g. Mitchell et al., 2015). In the south, the vortex was also significantly more symmetric and centred on-pole rather than shifted off-pole; unlike in the north, it was almost completely destroyed by heating from the storm. The natural experiment provided by the storm also allowed investigation into the annular shape of the polar vortices, particularly the northern vortex. The storm significantly disrupted the

topographic stationary wave patterns at high latitudes in both hemispheres, which correlated to the changes in vortex morphology towards a more symmetrical shape. This appeared to show that the elliptical morphology of the polar vortices is tied to the stationary topographic wave structure at high latitudes, as previously speculated by others (Rostami et al., 2018). Lastly, the effects of the storm on the diurnal cycle were also examined. The complete displacement of the southern polar vortex onto the nightside due to enhancement of the meridional circulation, proposed by Kleinböhl et al. (2020), was confirmed, and the diurnal changes in the meridional circulation were shown to also apply in a non-GDS year. A similar but much smaller effect was modelled in the north.

The second section carried on work from Chapter 5, by examining in closer detail the noted high speed jets at southern high latitudes; one over the cap itself in the aphelion season, and one at the cap edge in southern summer. Previous studies have made no mention of such features (e.g. Chapman, 2018), and analysis of other assimilated datasets shows significantly lower wind speeds at those times/locations (e.g. Montabone et al., 2014). This made them worthy of further investigation. One differing factor from previous assimilation studies is the use of the v5.2 MCS dataset, which uses 2D geometry leading to improved temperature and dust retrievals over the polar regions (Kleinböhl et al., 2017). This study first characterised the two jets, which showed high meridional and zonal flows and wind speeds which could exceed 30 m/s near the surface. This was noteably higher than in an assimilated model using the 1D (v4.3) MCS data. The differing dust retrievals were ruled out as the cause for the discrepancy. The discrepancy was instead linked to the colder temperatures over the southern pole in the 2D MCS data, which when assimilated were linked to enhanced condensation onto the seasonal CO_2 ice cap and a more massive cap by result. This larger seasonal cap in the 2D case appeared to drive greater sublimation around perihelion, and therefore higher surface pressures and a corresponding powerful barotropic zonal jet; the resulting strong meridional flow away from the cap could be a case of Ekman flow, given the low altitude

of the winds, which has been previously modelled to occur on Mars in the presence of CO_2 condensation (Ogohara and Satomura, 2010). Another result was a permanent CO_2 ice presence at southern high latitudes, in contrast with the 1D case; here the 2D case agreed better with observations of the cap extent (Piqueux et al., 2015). In order to verify the impact of low temperature retrievals on enhancing condensation, another experiment was conducted where sub-CO_2 condensation temperatures were filtered. Wind speeds in this case were closer to those in the 1D case, suggesting that runaway CO_2 condensation was indeed causally linked to the high wind speeds in the unfiltered 2D case. Given the lack of direct wind observations, comparisons were performed with surface pressures from the Viking landers and the Insight lander. None of the reanalyses agreed completely with surface pressure data; the 1D and 2D filtered reanalyses tended to overestimate surface pressure, while the 2D unfiltered reanalysis tended to underestimate surface pressure but showed the best agreement with Insight. However, the Viking lander data was used to tune the MGCM originally, making it a poor source for a reasonable comparison; the Insight lander provides an independent data source. Further comparisons were made using the modelled seasonal ice cap extent against MCS data; the 2D unfiltered case agreed better with the observations of a permanent CO_2 presence at southern high latitudes, not seen in the other reanalyses. However, the 1D and filtered 2D reanalyses captured the MCS-observed longitudinal asymmetry in southern polar ice coverage at perihelion, while the unfiltered 2D reanalysis overestimated the longitudinal extent of CO_2 ice coverage. The failure of any single reanalysis to agree completely with observations and previous modelling work shows that further work is needed to understand the behaviour of the southern seasonal CO_2 ice cap in Mars GCMs, and their link to southern high-latitude winds.

7.2 Conclusions

This section revisits the research questions originally posed in Chapter 1, and assesses the degree to which they have been addressed in the results from this thesis. More comprehensive conclusions can be found at the end of each relevant chapter; this section is intended to contextualise the broad findings of this thesis in terms of the research questions and the overall themes of the dust cycle and the radiative-dynamical impacts of atmospheric dust.

7.2.1 RQ1. How do Global Dust Storms affect Mars' surface and near-surface temperature environment?

The 2018 Global Dust Storm had the surprising effect of causing a globally-averaged surface warming. While previous observational work had noted that Global Dust Storms cause surface cooling on the dayside and warming on the nightside, this study shows that for the 2018 GDS these two effects result in a net global warming. One advantage of this study over previous work is the fact that the assimilated MGCM is able to report surface temperatures over all local times, and is not constrained to two local times as the TES and MCS instruments are. Using two prescribed local times, one daytime and one night-time, from the assimilated MGCM shows a slight cooling from the 2018 storm, which is more in line with the previous state on knowledge based on observations alone. This demonstrates that capturing the full diurnal cycle of temperature is important for characterising the true diurnally averaged effect of the storm; in particular, nightside warming, being driven by surface emission and backscattering rather than the the presence or absence of solar insolation, has a more persistent effect over local times than dayside cooling, which is highly correlated with time of day. This study also helps demonstrate the highly significant impact of dust optical properties on modelled effects. Specifically, small changes in the single-scattering albedo can cause huge differences in modelled surface temperatures. This suggests that surface temperature

observations could potentially be useful for validating dust optical properties, in conjunction with global climate models.

Varying the global dust opacity showed that the slight warming effect is robust for CDOD of up to 11 when the spatial dust distribution is prescribed to be uniform. However, there were significant differences in temperature effects between the actual 2018 storm and the equivalent uniform opacity artificial storms. This implies that Global Dust Storm geographical structure is crucially important in determining its surface temperature effects. As average warming ($\sim$13 K) occurred over low thermal inertia regions and average cooling ($\sim$14 K) elsewhere, storms with higher opacities over low thermal inertia regions should result in greater globally-averaged warming, and vice-versa. This importance of storm spatial structure in governing radiative impacts shows that studies with idealised dust distributions may not always be suitable for judging the radiative and dynamical impacts of actual Global Dust Storms. The idealised distributions used here for the 2018 GDS disagreed with the globally-averaged temperature changes in the reanalysis by $\sim$3 K and $\sim$4 K for the surface and near-surface atmosphere respectively. It is therefore important to take storm structure into consideration; the use of data assimilation is preferable where possible, as even two similar GDS such as the 2001 and 2018 events can have different surface temperature effects depending on their opacity structure (up to a globally-averaged $\sim$2 K in this case).

7.2.2 RQ2. Where and when does dust lifting occur on the martian surface, how does this vary between martian years and during a Global Dust Storm, and what dynamical processes are responsible?

While the research conducted in this thesis shows good agreement with general seasonal and geographical dust lifting trends in previous work, there are several novel results. The use of

an assimilated MGCM for six martian years shows a high degree of interannual similarity in both geographical location and seasonality, further showing the general interannual similarity of the martian atmosphere as a whole. This trend of similarity, however, breaks down in the presence of large (regional- and global-scale) dust storms. The large regional dust storms regularly observed during the perihelion season (Kass et al., 2016) are linked to dust lifting at the southern seasonal cap edge, through their effects on the meridional circulation. More intense storms cause a boosted circulation, leading to increased transport of warmer air to high latitudes and an enhanced sublimation of the southern cap, correlating with reduced dust lifting. Noteably, while every martian year without a Global Dust Storm follows this pattern, the year of the storm does not; there is no discernible pattern in the southern seasonal cap effects induced by the storm in early southern summer, though dust lifting increases relative to other years later in the summer. This suggests that there is a tipping point in storm intensity and/or size, after which other effects can counteract the enhanced southern seasonal cap recession seen in the non-Global Dust Storm years. The storm itself also led to an increase in dust lifting over tropical high-topography regions, suggesting that when wind speeds are sufficiently increased over these areas they can overcome the low surface pressures which makes dust lifting difficult there. Lastly, the Global Dust Storm also caused reduced dust lifting at northern mid-high latitudes, low topography areas which generally have high dust lifting due to the presence of baroclinic wave activity. This suppression of baroclinic wave-related dust lifting, together with increased dust deposition in the northern hemisphere, resulted in increased net dust deposition in the northern hemisphere. The results lend credence to the theory that these events help distribute dust from the southern to northern hemisphere (e.g. Haberle, 1986).

Regions of high dust lifting were present which did not appear to correlate with any observed storm activity. Most notably, these included the region corresponding to the location of the southern subtropical jet and the region around the southern cap edge. An

explanation for this lack of storm activity is that the constant and coherent (one-directional) flow associated with the dynamical features of the subtropical jet and sublimation flow act to keep these regions clear of dust, preventing storm formation. Orbital data shows that these regions do indeed have low surface dust content (e.g. Szwast et al., 2006). This suggests that dust lifting studies which incorporate observations of dust content from remote sensing may be the most promising avenue for future research, as in this case the simple application of the modelled dynamics and implied assumption of an infinite dust reservoir do not agree with the record of observed storms. However, the spatiotemporal location of high dust lifting zones during perihelion - at northern and southern high latitudes and in the southern subtropics - do appear to correlate with the regular presence of three large regional storms (Kass et al., 2016). In which case, either these large regional storms must originate in the northern dust lifting zones; or the southern dust lifting zones are capable of inciting large regional storms but not regular smaller storms; or the general atmospheric dynamics during the perihelion season are more important for the development and growth of large regional storms than the presence of the described dust lifting zones.

The results in Chapter 6 focus on dust lifting around the southern seasonal cap edge. This high dust lifting feature is a new finding, and a result of the assimilation of the 2D geometry MCS retrievals described by Kleinböhl et al. (2017). This study shows that the barotropic jets in the south are caused by the assimilation of this newer data, which displays colder polar temperatures than the previous retrieval version. These colder temperatures appear to induce greater southern CO_2 condensation of the MGCM, resulting in a more massive seasonal cap and a permanent CO_2 ice presence at southern high latitudes. Another result is the high wind speeds described, likely from zonal winds and meridional Ekman flow linked to the pressure changes caused by enhanced sublimation/condensation flow. Verifying the reality of these results is a difficult matter, and no strong conclusion can be drawn on this account given the lack of wind observations. Results assimilating temperature data where

sub-CO_2 condensation temperatures are filtered show a more massive southern ice cap as in the 2D unfiltered case, but surface pressures indentical to the 1D case. Comparison of the extent of the seasonal CO_2 cap in the assimilations to observations show better agreement in the 2D unfiltered case, which contains a permanent CO_2 ice presence at southern high latitudes. The 1D and filtered 2D reanalyses, though, were able to capture the MCS-observed longitudinal asymmetry of the southern seasonal cap at perihelion. Finally, comparison to previous modelling of the southern sublimation flow suggests that the 1D and 2D filtered cases provides the best fit, followed by the 2D filtered case. In conclusion, it is difficult to say for certain which assimilation provides the best representation of near-surface winds at southern high latitudes. Tentatively, the 2D unfiltered case has the best general match with Insight surface pressures, observations of the seasonal extent of the southern CO_2 cap, and previous modelling work, which implies that wind speeds at the southern cap could indeed be substantially higher than previously thought. Meanwhile, the 1D and 2D filtered cases agree better with Viking lander surface pressure data, and with MCS observations of the longitudinal structure of the southern CO_2 ice cap around perihelion. However, further comparisons are needed; the MGCM's atmospheric mass budget is based on specific dust scenarios and the Viking Lander pressure data, meaning that a full retuning of model parameters is necessary for a proper answer on how best to assimilate MCS temperature data around the southern seasonal cap and consequently the likely reality of these high near-surface wind speed features.

7.2.3 RQ3. How do Global Dust Storms affect Mars' polar vortices?

This is the first study to use an assimilated model of a real Global Dust Storm to investigate the impact on the polar vortices, the first study to investigate how both polar vortices were affected by the 2018 event, and the first study to investigate the effects of an equinoctal rather than solsticial (e.g. Guzewich et al., 2016) such event on both vortices. As it turns out, the

season at which the Global Dust Storm occurs appears to have a significant effect on its modelled impacts. Guzewich et al. (2016) modelled the effect of high dust loading at southern summer solstice, and found that it caused significant dynamical disruption to the northern polar vortex for tens of sols; an equally high loading at northern summer solstice caused far less disruption to the southern summer solstice. This study shows that the equinoctal dust storm of 2018 altered the morphology of the northern polar vortex, making it smaller in area and more symmetrical, but did not destroy potential vorticity to a significant extent. By contrast, the southern polar vortex was not only made more symmetrical but had much of its potential vorticity destroyed. Two factors may help provide an explanation here; first, the 2018 Global Dust Storm had a greater southern than northern latitudinal extent, reaching 70° S but only 40-50° N, allowing greater diabatic heating in the south (and therefore destruction of potential vorticity). Second, the time of year at which the storm occurred (starting at equinox) is a time at which the northern polar vortex is growing in strength as the southern vortex declines, due to the subsolar latitude moving south. This meant that in the south the storm accelerated a decline which was already in process; in the north, it was acting against the larger trend of the growth of the polar vortex.

The storm also provided a natural experiment: by causing the polar vortices to become more symmetrical, it allowed the identification and study of atmospheric processes in order to allow diagnosis of why the clear-case polar vortices are elliptical in shape. While of course many atmospheric properties were altered, the structure of high-latitude stationary planetary waves appeared to be changed in a manner equivalent to the alteration of the polar vortex morphology. This implies that the peculiar elliptical shape of Mars' polar vortices is linked to the presence of topographic stationary wave activity, with poleward-flow features of the planetary wave structure corresponding to a latidudinally narrower polar vortex and vice versa. Lastly, these results confirm the findings of Kleinböhl et al. (2020) that the southern polar vortex was entirely shifted to the nightside of the planet during the 2018 Global Dust

Storm, by way of comparison of the meridional circulation between the storm year and the previous clear year. This study shows that this effect appears to occur in all martian years, but was significantly boosted during the 2018 event by the enhanced circulation. Some diurnal variation was also visible in the northern case, but it is difficult to draw any conclusions given the small magnitude of the changes and the lack of clear correlation with local time.

7.3 Future work

The process of conducting the work related in this thesis has revealed many avenues of potential future work. This section describes a few of these, both work which is technically possible as of the time of writing, with currently available data and modelling resources, and work which may be possible in the future contingent on planned, proposed, and possible future observational and modelling resources.

The assimilation scheme and its associated elements offer several future projects. As noted in Chapter 6 and the corresponding discussions, the choice of which version of MCS temperature data to assimilate and how the data is processed before assimilation have significant effects on modelled near-surface dynamics. The reason that a proper validation of the MGCM as it is currently tuned is impossible against Viking Lander data is that the model was originally tuned to match this data (Hourdin et al., 1995), using specific dust scenarios. There are now newer sources of both dust and pressure data than were available when the MGCM was tuned, such as the Insight lander, allowing the possibilty of a new tuning of ice albedo parameters and the atmospheric mass budget, which may be closer to the true state of the martian atmosphere. This would by no means be a modest task; the tuning of GCMs is difficult and fraught with questions of causality and model sensitivity, to name but a few (e.g. Hourdin et al., 2016). But it is currently feasible, and may be valuable.

This thesis has presented work done assimilating dust column data; as mentioned in Chapter 3, there are currently ongoing efforts to assimilate dust profile data, such as those

directly retrieved by MCS (e.g. Navarro, 2016; Ruan, 2015), including by the author (e.g. Streeter et al., 2018). There would be two main advantages to having such a scheme. The first is in representing the radiative and dynamical effects of a realistic vertical dust distribution, which as MCS has shown differs from the monotonic distribution present in most Mars GCMs (e.g. McCleese et al., 2010); having such a distribution, with peaks in opacity at both the near-surface and at the location of detached dust layers (e.g. Heavens et al., 2011a), has been shown to have noticeable impacts on the modelled circulation (e.g. Guzewich et al., 2013b). This may be significant in determining how, for example, the polar vortices are represented in the assimilated MGCM. Once again, this is work which is technically difficult but feasible and possibly rewarding.

The TES and MCS instruments provide much of the data which has been used for assimilated studies to date due to their excellent global coverage; however, one limitation which has been mentioned in this thesis is the constrained local times of their spacecraft. Both instruments are only able to report observations at two fixed local times, excluding much of the martian diurnal cycle. The ExoMars Trace Gas Orbiter is currently active and carries two spectrometer suites, NOMAD (Vandaele et al., 2015) and ACS (Korablev et al., 2015). The instruments on this spacecraft measure at variable local times, allowing it to cover the full diurnal cycle and making it an exciting source of data for assimilation, particularly if coupled with data from MCS. Data from NOMAD and ACS is now (as of writing) beginning to flow and should therefore provide valuable insights into the diurnal cycle of dust, the polar vortices, and the temperature structure, among many others.

Perhaps the most uncertain of all future possibilities are the fates of proposed space exploration missions; nonetheless, one such is discussed here. The most pertinent to the work presented in this thesis is the proposed COMPASS mission (Byrne et al., 2020). While sadly not selected in the last NASA Discovery funding round, this mission would have carried not only a higher resolution version of the MCS instrument but an instrument able to remotely

sense winds. The potential uses for orbital wind data for Mars are numerous and exciting. The availability of such data would enable constraining and validation of many key modelled martian dynamical phenomena, including but not limited to the meridional circulation, the polar jets, and even simply modelled wind speeds themselves. In addition, assimilation of wind data is possible and already regularly performed on the Earth (e.g. Yu and Mcpherson, 1984). Application of such techniques for martian data assimilation should improve our understanding of the global circulation, and may even aid in future forecasting efforts.

7.4 Final words

The results in this thesis have shown the value of data assimilation in tackling questions regarding the contemporary meteorology of Mars, and in particular the radiative-dynamical impacts of dust and the dust cycle itself. By combining a robust martian global climate model with a high-volume dataset of temperature and dust observations, data assimilation enables better understanding of what the martian climate is really like today and how dust interacts with other elements of the atmosphere.

Suspended atmospheric dust is the most important radiative driver present in the martian atmosphere, and has numerous and complex effects on dynamical processes and the energy budget. The 2018 Global Dust Storm, the most-observed such event in history, was surprisingly shown to actually warm the surface on average, due to the greenhouse-like warming effect of the high dust loading. This warming, and its highly heterogeneous distribution across the planet, has implications for surface processes in general, from wind speeds to surface ice. The surface temperature changes were tightly linked to the structure of the GDS, showing how important dust spatial distribution is for understanding its radiative and dynamical effects.

The 2018 event also had important effects on Mars' polar vortices. These effects were not symmetric; the southern vortex was almost completely destroyed, while the northern vortex

remained coherent. Both vortices though had their morphologies significantly impacted, as the Global Dust Storm reduced their usual latitudinal asymmetry. This revealed the importance of high-latitude stationary planetary wave activity in maintaining the usual elliptical shape of the vortices. These findings are valuable additions to the existing literature on martian polar dynamics, which has before now not examined the effects of equinoctial Global Dust Storms. The time of year in which high dust loading occurs is indeed critical in determining its effects on Mars' polar atmosphere, and equinoctial events should not regarded as having the same effects as solsticial storms.

Global Dust Storms, along with regional storms, also have impacts on the dust cycle of lifting and deposition. The 2018 Global Dust Storm altered not only the amount of lifted dust, but the locations of dust lifting. Even smaller regional storms have indirect effects on lifting at the southern seasonal cap edge via their impacts to the large-scale meridional flow. Here, the exact way in which temperature data is assimilated has a huge effect on calculated dust lifting in the southern hemisphere: this is an interesting area for future research on near-surface winds on Mars.

There still remain many mysteries around Mars and its dusty atmosphere. Data assimilation will continue to provide a valuable tool in helping to resolve these mysteries and uncover even more of them. The author hopes that our knowledge of martian meteorology continues to grow and that we may one day regard Mars as our sibling planet not only due to its similarity to our own, but because of our collective ambition and achievement in understanding and exploring its secrets.

References

Acker, E. V. d., Hoolst, T. V., Viron, O. d., Defraigne, P., Forget, F., Hourdin, F., and Dehant, V. (2002). Influence of the seasonal winds and the CO2 mass exchange between atmosphere and polar caps on Mars' rotation. *Journal of Geophysical Research: Planets*, 107(E7):9–1–9–8.

Almeida, M. P., Parteli, E. J. R., Andrade, J. S., and Herrmann, H. J. (2008). Giant saltation on Mars. *Proceedings of the National Academy of Sciences*, 105(17):6222–6226.

Andrews, D. G., Holton, J. R., and Leovy, C. B. (1987). *Middle atmosphere dynamics.*

Antoniadi, E. M. (1975). *The planet Mars*. K. Reid, Shaldon.

Aoki, S., Vandaele, A. C., Daerden, F., Villanueva, G. L., Liuzzi, G., Thomas, I. R., Erwin, J. T., Trompet, L., Robert, S., Neary, L., Viscardy, S., Clancy, R. T., Smith, M. D., Lopez-Valverde, M. A., Hill, B., Ristic, B., Patel, M. R., Bellucci, G., and Lopez-Moreno, J.-J. (2019). Water Vapor Vertical Profiles on Mars in Dust Storms Observed by TGO/NOMAD. *Journal of Geophysical Research: Planets*, 124(12):3482–3497. _eprint: https://agupubs.onlinelibrary.wiley.com/doi/pdf/10.1029/2019JE006109.

Audouard, J., Määttänen, A., Listowski, C., Forget, F., Spiga, A., and Millour, E. (2017). A complete CO_2 ice clouds model for GCMs and mesoscale models.

Aye, K. M., Schwamb, M. E., Portyankina, G., Hansen, C. J., McMaster, A., Miller, G. R. M., Carstensen, B., Snyder, C., Parrish, M., Lynn, S., Mai, C., Miller, D., Simpson, R. J., and Smith, A. M. (2019). Planet Four: Probing springtime winds on Mars by mapping the southern polar CO2 jet deposits. *Icarus*, 319:558–598.

Bagnold, R. A. and Taylor, G. I. (1937). The size-garding of sand by wind. *Proceedings of the Royal Society of London. Series A - Mathematical and Physical Sciences*, 163(913):250–264.

Baines, P. G. and Palmer, T. N. (1990). Rationale for a new physically-based parameterization of subgridscale orographic effects.

Banfield, D., Ingersoll, A. P., and Keppene, C. L. (1995). A steady-state Kalman filter for assimilating data from a single polar orbiting satellite. *Journal of the atmospheric sciences*, 52(6):737–753.

Banfield, D., Spiga, A., Newman, C., Forget, F., Lemmon, M., Lorenz, R., Murdoch, N., Viudez-Moreiras, D., Pla-Garcia, J., Garcia, R. F., Lognonné, P., Karatekin, Ö., Perrin, C., Martire, L., Teanby, N., Hove, B. V., Maki, J. N., Kenda, B., Mueller, N. T., Rodriguez, S.,

Kawamura, T., McClean, J. B., Stott, A. E., Charalambous, C., Millour, E., Johnson, C. L., Mittelholz, A., Määttänen, A., Lewis, S. R., Clinton, J., Stähler, S. C., Ceylan, S., Giardini, D., Warren, T., Pike, W. T., Daubar, I., Golombek, M., Rolland, L., Widmer-Schnidrig, R., Mimoun, D., Beucler, É., Jacob, A., Lucas, A., Baker, M., Ansan, V., Hurst, K., Mora-Sotomayor, L., Navarro, S., Torres, J., Lepinette, A., Molina, A., Marin-Jimenez, M., Gomez-Elvira, J., Peinado, V., Rodriguez-Manfredi, J.-A., Carcich, B. T., Sackett, S., Russell, C. T., Spohn, T., Smrekar, S. E., and Banerdt, W. B. (2020). The atmosphere of Mars as observed by InSight. *Nature Geoscience*, 13(3):190–198. Number: 3 Publisher: Nature Publishing Group.

Barnes, J. R. (1984). Linear baroclinic instability in the Martian atmosphere. *Journal of the Atmospheric Sciences*, pages 1536–155.

Barnes, J. R., Haberle, R. M., Wilson, R. J., Lewis, S. R., Murphy, J. R., and Read, P. L. (2017). The Global Circulation.

Barnes, J. R., Pollack, J. B., Haberle, R. M., Leovy, C. B., Zurek, R. W., Lee, H., and Schaeffer, J. (1993). Mars atmospheric dynamics as simulated by the NASA AMES General Circulation Model. II - Transient baroclinic eddies. *Journal of Geophysical Research*, 98:3125–3148.

Barnes, J. R., Walsh, T. D., and Murphy, J. R. (1996). Transport timescales in the Martian atmosphere: General circulation model simulations. *Journal of Geophysical Research: Planets*, 101(E7):16881–16889.

Barnes, S. L. (1964). A Technique for Maximizing Details in Numerical Weather Map Analysis. *Journal of Applied Meteorology*, 3(4):396–409.

Basu, S., Richardson, M. I., and Wilson, R. J. (2004). Simulation of the Martian dust cycle with the GFDL Mars GCM. *Journal of Geophysical Research (Planets)*, 109:E11006.

Basu, S., Wilson, J., Richardson, M., and Ingersoll, A. (2006). Simulation of spontaneous and variable global dust storms with the GFDL Mars GCM. *Journal of Geophysical Research: Planets*, 111(E9):E09004.

Battalio, J. M. and Wang, H. (2019). The Mars Dust Activity Database (MDAD). type: dataset.

Battalio, M., Szunyogh, I., and Lemmon, M. (2016). Energetics of the martian atmosphere using the Mars Analysis Correction Data Assimilation (MACDA) dataset. *Icarus*, 276:1–20.

Bergthörsson, P. and Döös, B. R. (1955). Numerical Weather Map Analysis. *Tellus*, 7(3):329–340.

Bingham, S. J., Lewis, S. R., Newman, C. E., and Read, P. L. (2004). Environmental predictions for the Beagle 2 lander, based on GCM climate simulations. *Planetary and Space Science*, 52(4):259–269.

Bougher, S. W., Murphy, J., and Haberle, R. M. (1997). Dust storm impacts on the Mars upper atmosphere. *Advances in Space Research*, 19(8):1255–1260.

Burk, S. D. (1976). Diurnal Winds Near the Martian Polar Caps. *Journal of the Atmospheric Sciences*, 33(6):923–939.

Byrne, S., Hayne, P. O., Calvin, W. M., Tamppari, L. K., Kleinböhl, A., Smith, I. B., and Becerra, P. (2020). Climate Orbiter for Mars Polar Atmospheric and Subsurface Science (COMPASS). *LPI Contributions*, 2099:6013.

Böttger, H. M., Lewis, S. R., Read, P. L., and Forget, F. (2004). The effect of a global dust storm on simulations of the Martian water cycle. *Geophysical Research Letters*, 31(22):L22702.

Calvin, W. M., Cantor, B. A., and James, P. B. (2017). Interannual and seasonal changes in the south seasonal polar cap of Mars: Observations from MY 28-31 using MARCI. *Icarus*, 292:144–153.

Cantor, B., Malin, M., and Edgett, K. S. (2002). Multiyear Mars Orbiter Camera (MOC) observations of repeated Martian weather phenomena during the northern summer season. *Journal of Geophysical Research (Planets)*, 107:5014–1.

Cantor, B. A. (2007). MOC observations of the 2001 Mars planet-encircling dust storm. *Icarus*, 186(1):60–96.

Cantor, B. A., James, P. B., and Calvin, W. M. (2010). MARCI and MOC observations of the atmosphere and surface cap in the north polar region of Mars. *Icarus*, 208:61–81.

Cantor, B. A., James, P. B., Caplinger, M., and Wolff, M. J. (2001). Martian dust storms: 1999 Mars Orbiter Camera observations. *Journal of Geophysical Research: Planets*, 106(E10):23653–23687.

Chapman, R. (2018). *Temporal and Geographical Variation in Martian Surface Dust Lifting Processes*. phd, The Open University.

Chapman, R., Lewis, S., Balme, M., and Steele, L. (2017). Diurnal variation in martian dust devil activity. *Icarus*, 292:154–167.

Chow, K.-C., Xiao, J., Chan, K. L., and Wong, C.-F. (2019). Flow Associated With the Condensation and Sublimation of Polar Ice Caps on Mars. *Journal of Geophysical Research: Planets*, 124(6):1570–1580.

Clancy, R. T., Sandor, B. J., Wolff, M. J., Christensen, P. R., Smith, M. D., Pearl, J. C., Conrath, B. J., and Wilson, R. J. (2000). An intercomparison of ground-based millimeter, MGS TES, and Viking atmospheric temperature measurements: Seasonal and interannual variability of temperatures and dust loading in the global Mars atmosphere. *Journal of Geophysical Research: Planets*, 105(E4):9553–9571.

Clancy, R. T., Wolff, M. J., Whitney, B. A., Cantor, B. A., Smith, M. D., and McConnochie, T. H. (2010). Extension of atmospheric dust loading to high altitudes during the 2001 Mars dust storm: MGS TES limb observations. *Icarus*, 207:98–109.

Claudin, P. and Andreotti, B. (2006). A scaling law for aeolian dunes on Mars, Venus, Earth, and for subaqueous ripples. *Earth and Planetary Science Letters*, 252(1):30–44.

Colaprete, A., Barnes, J. R., Haberle, R. M., Hollingsworth, J. L., Kieffer, H. H., and Titus, T. N. (2005). Albedo of the south pole on Mars determined by topographic forcing of atmosphere dynamics. *Nature*, 435(7039):184–188.

Colaïtis, A., Spiga, A., Hourdin, F., Rio, C., Forget, F., and Millour, E. (2013). A thermal plume model for the Martian convective boundary layer. *Journal of Geophysical Research: Planets*, 118(7):1468–1487.

Colburn, D. S., Pollack, J. B., and Haberle, R. M. (1989). Diurnal variations in optical depth at Mars. *Icarus*, 79(1):159–189.

Collins, M., Lewis, S. R., and Read, P. L. (1995). Regular and irregular baroclinic waves in a Martian general circulation model: A role for diurnal forcing. *Advances in Space Research*, 16.

Collins, M., Lewis, S. R., and Read, P. L. (1997). Gravity wave drag in a global circulation model of the Martian atmosphere: Parameterisation and validation. *Advances in Space Research*, 19(8):1245–1254.

Collins, M., Lewis, S. R., Read, P. L., and Hourdin, F. (1996). Baroclinic Wave Transitions in the Martian Atmosphere. *Icarus*, 120(2):344–357.

Conrath, B. J. (1975). Thermal structure of the Martian atmosphere during the dissipation of the dust storm of 1971. *Icarus*, 24(1):36–46.

Conrath, B. J., Pearl, J. C., Smith, M. D., Maguire, W. C., Christensen, P. R., Dason, S., and Kaelberer, M. S. (2000). Mars Global Surveyor Thermal Emission Spectrometer (TES) observations: Atmospheric temperatures during aerobraking and science phasing. *Journal of Geophysical Research: Planets*, 105(E4):9509–9519.

Cressman, G. P. (1959). AN OPERATIONAL OBJECTIVE ANALYSIS SYSTEM. *Monthly Weather Review*, 87(10):367–374.

Daerden, F., Whiteway, J. A., Neary, L., Komguem, L., Lemmon, M. T., Heavens, N. G., Cantor, B. A., Hébrard, E., and Smith, M. D. (2015). A solar escalator on Mars: Self-lifting of dust layers by radiative heating. *Geophysical Research Letters*, 42(18):2015GL064892.

Edwards, C. S., Bennett, K. A., Vasavada, A. R., Piqueux, S., Hamilton, V. E., Fraeman, A., and Horgan, B. H. N. (2018). The Thermophysical Variability of the Vera Rubin Ridge as Explored by the Mars Science Laboratory. *AGU Fall Meeting Abstracts*, 21.

Evensen, G. (1994). Sequential data assimilation with a nonlinear quasi-geostrophic model using Monte Carlo methods to forecast error statistics. *Journal of Geophysical Research: Oceans*, 99(C5):10143–10162.

Fedorova, A. A., Montmessin, F., Korablev, O., Luginin, M., Trokhimovskiy, A., Belyaev, D. A., Ignatiev, N. I., Lefèvre, F., Alday, J., Irwin, P. G. J., Olsen, K. S., Bertaux, J.-L., Millour, E., Määttänen, A., Shakun, A., Grigoriev, A. V., Patrakeev, A., Korsa, S., Kokonkov, N., Baggio, L., Forget, F., and Wilson, C. F. (2020). Stormy water on Mars: The distribution and saturation of atmospheric water during the dusty season. *Science*, 367(6475):297–300. Publisher: American Association for the Advancement of Science Section: Report.

Fenton, L., Reiss, D., Lemmon, M., Marticorena, B., Lewis, S., and Cantor, B. (2016). Orbital Observations of Dust Lofted by Daytime Convective Turbulence. *Space Science Reviews*, 203(1-4):89–142.

Fenton, L. K., Geissler, P. E., and Haberle, R. M. (2007). Global warming and climate forcing by recent albedo changes on Mars. *Nature*, 446(7136):646–649.

Fenton, L. K., Pearl, J. C., and Martin, T. Z. (1997). Mapping Mariner 9 Dust Opacities. *Icarus*, 130(1):115–124.

Fernández, W. (1997). Martian Dust Storms: A Review. *Earth Moon and Planets*, 77:19–46.

Fonseca, R. M., Zorzano-Mier, M.-P., and Martín-Torres, J. (2018). Planetary boundary layer and circulation dynamics at Gale Crater, Mars. *Icarus*, 302:537–559.

Forget, F. (1998). Improved optical properties of the Martian atmospheric dust for radiative transfer calculations in the infrared. *Geophysical Research Letters*, 25:1105–1108.

Forget, F., Hourdin, F., Fournier, R., Hourdin, C., Talagrand, O., Collins, M., Lewis, S. R., Read, P. L., and Huot, J.-P. (1999). Improved general circulation models of the Martian atmosphere from the surface to above 80 km. *Journal of Geophysical Research: Planets*, 104(E10):24155–24175.

Forget, F., Hourdin, F., and Talagrand, O. (1998). CO2Snowfall on Mars: Simulation with a General Circulation Model. *Icarus*, 131(2):302–316.

Friedlander, S. K. (2000). *Smoke, dust, and haze: Fundamentals of aerosol dynamics*, volume 198. Oxford University Press New York.

Fuerstenau, S. D. (2006). Solar heating of suspended particles and the dynamics of Martian dust devils. *Geophysical Research Letters*, 33(19):L19S03.

Gandin, L. S. (1963). Objective analysis of meteorological fields. *Gidrometerologicheskoe Izdatelstvo*. English translation by Israeli Program for Scientific Translations, Jerusalem, 1965.

Gierasch, P. J. (1974). Martian dust storms. *Reviews of Geophysics and Space Physics*, 12:730–734.

Gierasch, P. J. and Goody, R. M. (1972). The Effect of Dust on the Temperature of the Martian Atmosphere. *Journal of the Atmospheric Sciences*, 29(2):400–402.

Greeley, R. and Iversen, J. D. (1985). *Wind as a geological process on Earth, Mars, Venus and Titan.*

Greybush, S. J., Gillespie, H. E., and Wilson, R. J. (2018). Transient Eddies in the TES/MCS Ensemble Mars Atmosphere Reanalysis System (EMARS). *Icarus*.

Greybush, S. J., Gillespie, H. E., and Wilson, R. J. (2019). Transient eddies in the TES/MCS Ensemble Mars Atmosphere Reanalysis System (EMARS). *Icarus*, 317:158–181.

Greybush, S. J., Wilson, R. J., Gillespie, H., Kalnay, E., Wespetal, M., Nehrkorn, T., Leidner, S. M., and Hoffman, R. (2017). Traveling Weather Systems in the Ensemble Mars Atmosphere Reanalysis System (EMARS). page 1305.

Greybush, S. J., Wilson, R. J., Hoffman, R. N., Hoffman, M. J., Miyoshi, T., Ide, K., McConnochie, T., and Kalnay, E. (2012). Ensemble Kalman filter data assimilation of Thermal Emission Spectrometer temperature retrievals into a Mars GCM. *Journal of Geophysical Research: Planets*, 117(E11):E11008.

Gurwell, M. A., Bergin, E. A., Melnick, G. J., and Tolls, V. (2005). Mars surface and atmospheric temperature during the 2001 global dust storm. *Icarus*, 175(1):23–31.

Guzewich, S. D., Lemmon, M., Smith, C. L., Martínez, G., Vicente-Retortillo, Á. d., Newman, C. E., Baker, M., Campbell, C., Cooper, B., Gómez-Elvira, J., Harri, A.-M., Hassler, D., Martin-Torres, F. J., McConnochie, T., Moores, J. E., Kahanpää, H., Khayat, A., Richardson, M. I., Smith, M. D., Sullivan, R., Juarez, M. d. l. T., Vasavada, A. R., Viúdez-Moreiras, D., Zeitlin, C., and Mier, M.-P. Z. (2019). Mars Science Laboratory Observations of the 2018/Mars Year 34 Global Dust Storm. *Geophysical Research Letters*, 46(1):71–79.

Guzewich, S. D., Talaat, E. R., Toigo, A. D., Waugh, D. W., and McConnochie, T. H. (2013a). High-altitude dust layers on Mars: Observations with the Thermal Emission Spectrometer. *Journal of Geophysical Research: Planets*, 118(6):1177–1194.

Guzewich, S. D., Toigo, A. D., Kulowski, L., and Wang, H. (2015). Mars Orbiter Camera climatology of textured dust storms. *Icarus*, 258:1–13.

Guzewich, S. D., Toigo, A. D., Richardson, M. I., Newman, C. E., Talaat, E. R., Waugh, D. W., and McConnochie, T. H. (2013b). The impact of a realistic vertical dust distribution on the simulation of the Martian General Circulation. *Journal of Geophysical Research: Planets*, 118(5):980–993.

Guzewich, S. D., Toigo, A. D., and Wang, H. (2017). An investigation of dust storms observed with the Mars Color Imager. *Icarus*, 289:199–213.

Guzewich, S. D., Toigo, A. D., and Waugh, D. W. (2016). The effect of dust on the martian polar vortices. *Icarus*, 278(Supplement C):100–118.

Guzewich, S. D., Wilson, R. J., McConnochie, T. H., Toigo, A. D., Banfield, D. J., and Smith, M. D. (2014). Thermal tides during the 2001 Martian global-scale dust storm. *Journal of Geophysical Research: Planets*, 119(3):2013JE004502.

Haberle, R. M. (1986). Interannual variability of global dust storms on Mars. *Science*, 234:459–461.

Haberle, R. M., Juárez, M. d. l. T., Kahre, M. A., Kass, D. M., Barnes, J. R., Hollingsworth, J. L., Harri, A.-M., and Kahanpää, H. (2018). Detection of Northern Hemisphere transient eddies at Gale Crater Mars. *Icarus*, 307:150–160.

Haberle, R. M., Kahre, M. A., Barnes, J. R., Hollingsworth, J. L., and Wolff, M. J. (2019). MARCI observations of a wavenumber-2 large-scale feature in the north polar hood of Mars: Interpretation with the NASA/Ames Legacy Global Climate Model. *Icarus*.

Haberle, R. M., Leovy, C. B., and Pollack, J. B. (1982). Some effects of global dust storms on the atmospheric circulation of Mars. *Icarus*, 50(2):322–367.

Haberle, R. M., McKay, C. P., Schaeffer, J., Cabrol, N. A., Grin, E. A., Zent, A. P., and Quinn, R. (2001). On the possibility of liquid water on present-day Mars. *Journal of Geophysical Research: Planets*, 106(E10):23317–23326.

Haberle, R. M., Murphy, J. R., and Schaeffer, J. (2003). Orbital change experiments with a Mars general circulation model. *Icarus*, 161(1):66–89.

Haberle, R. M., Pollack, J. B., Barnes, J. R., Zurek, R. W., Leovy, C. B., Murphy, J. R., Lee, H., and Schaeffer, J. (1993). Mars atmospheric dynamics as simulated by the NASA Ames General Circulation Model: 1. The zonal-mean circulation. *Journal of Geophysical Research: Planets*, 98(E2):3093–3123.

Hanel, R., Conrath, B., Hovis, W., Kunde, V., Lowman, P., Maguire, W., Pearl, J., Pirraglia, J., Prabhakara, C., Schlachman, B., Levin, G., Straat, P., and Burke, T. (1972). Investigation of the Martian environment by infrared spectroscopy on Mariner 9. *Icarus*, 17(2):423–442.

Haslam, S. (1888). *A General History of Labyrinths*. Vienna.

Hayne, P. O., Paige, D. A., Schofield, J. T., Kass, D. M., Kleinböhl, A., Heavens, N. G., and McCleese, D. J. (2012). Carbon dioxide snow clouds on Mars: South polar winter observations by the Mars Climate Sounder. *Journal of Geophysical Research: Planets*, 117(E8).

Heavens, N. G., Cantor, B. A., Hayne, P. O., Kass, D. M., Kleinböhl, A., McCleese, D. J., Piqueux, S., Schofield, J. T., and Shirley, J. H. (2015). Extreme detached dust layers near Martian volcanoes: Evidence for dust transport by mesoscale circulations forced by high topography. *Geophysical Research Letters*, 42(10):2015GL064004.

Heavens, N. G., Johnson, M. S., Abdou, W. A., Kass, D. M., Kleinböhl, A., McCleese, D. J., Shirley, J. H., and Wilson, R. J. (2014). Seasonal and diurnal variability of detached dust layers in the tropical Martian atmosphere. *Journal of Geophysical Research: Planets*, 119(8):2014JE004619.

Heavens, N. G., Kass, D. M., Kleinböhl, A., and Schofield, J. T. (2020). A multiannual record of gravity wave activity in Mars's lower atmosphere from on-planet observations by the Mars Climate Sounder. *Icarus*, 341:113630.

Heavens, N. G., Kass, D. M., and Shirley, J. H. (2019). Dusty Deep Convection in the Mars Year 34 Planet-Encircling Dust Event. *Journal of Geophysical Research: Planets*, 124(11):2863–2892.

Heavens, N. G., Kleinböhl, A., Chaffin, M. S., Halekas, J. S., Kass, D. M., Hayne, P. O., McCleese, D. J., Piqueux, S., Shirley, J. H., and Schofield, J. T. (2018). Hydrogen escape from Mars enhanced by deep convection in dust storms. *Nature Astronomy*, 2(2):126–132.

Heavens, N. G., Richardson, M. I., Kleinböhl, A., Kass, D. M., McCleese, D. J., Abdou, W., Benson, J. L., Schofield, J. T., Shirley, J. H., and Wolkenberg, P. M. (2011a). Vertical

distribution of dust in the Martian atmosphere during northern spring and summer: High-altitude tropical dust maximum at northern summer solstice. *Journal of Geophysical Research: Planets*, 116(E1):E01007.

Heavens, N. G., Richardson, M. I., Kleinböhl, A., Kass, D. M., McCleese, D. J., Abdou, W., Benson, J. L., Schofield, J. T., Shirley, J. H., and Wolkenberg, P. M. (2011b). The vertical distribution of dust in the Martian atmosphere during northern spring and summer: Observations by the Mars Climate Sounder and analysis of zonal average vertical dust profiles. *Journal of Geophysical Research: Planets*, 116(E4):E04003.

Held, I. M. and Hou, A. Y. (1980). Nonlinear Axially Symmetric Circulations in a Nearly Inviscid Atmosphere. *Journal of the Atmospheric Sciences*, 37(3):515–533.

Hernández-Bernal, J., Sánchez-Lavega, A., Río-Gaztelurrutia, T. d., Hueso, R., Cardesín-Moinelo, A., Ravanis, E. M., Burgos-Sierra, A. d., Titov, D., and Wood, S. (2019). The 2018 Martian Global Dust Storm Over the South Polar Region Studied With MEx/VMC. *Geophysical Research Letters*, 46(17-18):10330–10337.

Herschel, W. (1784). XIX. On the remarkable appearances at the polar regions of the planet Mars, and its spheroidical figure; with a few hints relating to its real diameter and atmosphere. *Philosophical Transactions of the Royal Society of London*, 74:233–273. Publisher: Royal Society.

Hinson, D. P. and Wang, H. (2010). Further observations of regional dust storms and baroclinic eddies in the northern hemisphere of Mars. *Icarus*, 206(1):290–305.

Hinson, D. P., Wang, H., and Smith, M. D. (2012). A multi-year survey of dynamics near the surface in the northern hemisphere of Mars: Short-period baroclinic waves and dust storms. *Icarus*, 219(1):307–320.

Hoffman, R. N. and Kalnay, E. (1983). Lagged average forecasting, an alternative to Monte Carlo forecasting. *Tellus A*, 35A(2):100–118.

Holben, B. N., Tanré, D., Smirnov, A., Eck, T. F., Slutsker, I., Abuhassan, N., Newcomb, W. W., Schafer, J. S., Chatenet, B., Lavenu, F., Kaufman, Y. J., Castle, J. V., Setzer, A., Markham, B., Clark, D., Frouin, R., Halthore, R., Karneli, A., O'Neill, N. T., Pietras, C., Pinker, R. T., Voss, K., and Zibordi, G. (2001). An emerging ground-based aerosol climatology: Aerosol optical depth from AERONET. *Journal of Geophysical Research: Atmospheres*, 106(D11):12067–12097.

Hollingsworth, J. L. and Barnes, J. R. (1996). Forced stationary planetary waves in Mars's winter atmosphere. *Journal of Atmospheric Sciences*, 53:428–448.

Hollingsworth, J. L., Haberle, R. M., and Schaeffer, J. (1997). Seasonal variations of storm zones on Mars. *Advances in Space Research*, 19:1237–1240.

Hollingsworth, J. L. and Kahre, M. A. (2010). Extratropical cyclones, frontal waves, and Mars dust: Modeling and considerations. *Geophysical Research Letters*, 37(22):L22202.

Holmes, J., Lewis, S., and Patel, M. (2019a). OpenMARS MY24-27 standard database (Version 1).

Holmes, J. A., Lewis, S. R., and Patel, M. R. (2015). Analysing the consistency of martian methane observations by investigation of global methane transport. *Icarus*, 257:23–32.

Holmes, J. A., Lewis, S. R., and Patel, M. R. (2017). On the link between martian total ozone and potential vorticity. *Icarus*, 282:104–117.

Holmes, J. A., Lewis, S. R., and Patel, M. R. (2020). OpenMARS: A global record of martian weather from 1999 2015. *Planetary and Space Science*, 188:104962.

Holmes, J. A., Lewis, S. R., Patel, M. R., and Smith, M. D. (2019b). Global analysis and forecasts of carbon monoxide on Mars. *Icarus*, 328:232–245.

Holton, J. R. (2004a). Chapter 10 The general circulation. In *An Introduction to Dynamic Meteorology*, volume 88 of *International Geophysics*, pages 313–369. Elsevier.

Holton, J. R. (2004b). Chapter 2 Basic conservation laws. In *An Introduction to Dynamic Meteorology*, volume 88 of *International Geophysics*, pages 28–56. Elsevier.

Holton, J. R. (2004c). Chapter 3 Elementary applications of the basic equations. In *An Introduction to Dynamic Meteorology*, volume 88 of *International Geophysics*, pages 57–85. Elsevier.

Holton, J. R. (2004d). Chapter 5 The planetary boundary layer. In *An Introduction to Dynamic Meteorology*, volume 88 of *International Geophysics*, pages 115–138. Elsevier.

Holton, J. R. (2004e). Chapter 8 Synoptic-scale motions II: Baroclinic instability. In *An Introduction to Dynamic Meteorology*, volume 88 of *International Geophysics*, pages 228–267. Elsevier.

Hoskins, B. J. and Simmons, A. J. (1975). A multi-layer spectral model and the semi-implicit method. *Quarterly Journal of the Royal Meteorological Society*, 101(429):637–655.

Houben, H. (1999). Assimilation of Mars global surveyor meteorological data. *Advances in Space Research*, 23:1899–1902.

Hourdin, F. (1992). A new representation of the absorption by the CO2 15-μm band for a Martian general circulation model. *Journal of Geophysical Research: Planets*, 97(E11):18319–18335.

Hourdin, F. and Armengaud, A. (1999). The Use of Finite-Volume Methods for Atmospheric Advection of Trace Species. Part I: Test of Various Formulations in a General Circulation Model. *Monthly Weather Review*, 127(5):822–837.

Hourdin, F., Forget, F., and Talagrand, O. (1995). The sensitivity of the Martian surface pressure and atmospheric mass budget to various parameters: A comparison between numerical simulations and Viking observations. *Journal of Geophysical Research: Planets*, 100(E3):5501–5523.

Hourdin, F., Le Van, P., Forget, F., and Talagrand, O. (1993). Meteorological Variability and the Annual Surface Pressure Cycle on Mars. *Journal of the Atmospheric Sciences*, 50(21):3625–3640.

Hourdin, F., Mauritsen, T., Gettelman, A., Golaz, J.-C., Balaji, V., Duan, Q., Folini, D., Ji, D., Klocke, D., Qian, Y., Rauser, F., Rio, C., Tomassini, L., Watanabe, M., and Williamson, D. (2016). The Art and Science of Climate Model Tuning. *Bulletin of the American Meteorological Society*, 98(3):589–602. Publisher: American Meteorological Society.

Hu, R., Cahoy, K., and Zuber, M. T. (2012). Mars atmospheric CO2 condensation above the north and south poles as revealed by radio occultation, climate sounder, and laser ranging observations. *Journal of Geophysical Research: Planets*, 117(E7).

Hébrard, E., Listowski, C., Coll, P., Marticorena, B., Bergametti, G., Määttänen, A., Montmessin, F., and Forget, F. (2012). An aerodynamic roughness length map derived from extended Martian rock abundance data. *Journal of Geophysical Research: Planets*, 117(E4).

Ingersoll, A. P. and Lyons, J. R. (1993). Mars Dust Storms: Interannual Variability and Chaos. *Journal of Geophysical Research E*, 98(E6):10951–10961.

James, P. B., Hollingsworth, J. L., Wolff, M. J., and Lee, S. W. (1999). North Polar Dust Storms in Early Spring on Mars. *Icarus*, 138:64–73.

Joshi, M. M., Haberle, R. M., Barnes, J. R., Murphy, J. R., and Schaeffer, J. (1997). Low-level jets in the NASA Ames Mars general circulation model. *Journal of Geophysical Research: Planets*, 102(E3):6511–6523.

Joshi, M. M., Lewis, S. R., Read, P. L., and Catling, D. C. (1994). Western boundary currents in the atmosphere of Mars. *Nature*, 367(6463):548–552.

Joshi, M. M., Lewis, S. R., Read, P. L., and Catling, D. C. (1995). Western boundary currents in the Martian atmosphere: Numerical simulations and observational evidence. *Journal of Geophysical Research: Planets*, 100(E3):5485–5500.

Juarez, M. d. l. T., Piqueux, S., Kass, D. M., Newman, C., and Guzewich, S. D. (2019). Pressure Deficit in Gale Crater and a Larger Northern Polar Cap after the Mars Year 34 Global Dust Storm. AGU.

Kahre, M. A. and Haberle, R. M. (2010). Mars CO2 cycle: Effects of airborne dust and polar cap ice emissivity. *Icarus*, 207(2):648–653.

Kahre, M. A., Hollingsworth, J. L., Haberle, R. M., and Murphy, J. R. (2008). Investigations of the variability of dust particle sizes in the martian atmosphere using the NASA Ames General Circulation Model. *Icarus*, 195(2):576–597.

Kahre, M. A., Hollingsworth, J. L., Haberle, R. M., and Wilson, R. J. (2015). Coupling the Mars dust and water cycles: The importance of radiative-dynamic feedbacks during northern hemisphere summer. *Icarus*, 260:477–480.

Kahre, M. A., Murphy, J. R., and Haberle, R. M. (2006). Modeling the Martian dust cycle and surface dust reservoirs with the NASA Ames general circulation model. *Journal of Geophysical Research: Planets*, 111(E6):E06008.

Kahre, M. A., Murphy, J. R., Haberle, R. M., Montmessin, F., and Schaeffer, J. (2005). Simulating the Martian dust cycle with a finite surface dust reservoir. *Geophysical Research Letters*, 32(20):n/a–n/a.

Kahre, M. A., Murphy, J. R., Newman, C. E., Wilson, R. J., Cantor, B. A., Lemmon, M. T., and Wolff, M. J. (2017). The Mars Dust Cycle.

Kahre, M. A., Vines, S. K., Haberle, R. M., and Hollingsworth, J. L. (2013). The early Martian atmosphere: Investigating the role of the dust cycle in the possible maintenance of two stable climate states. *Journal of Geophysical Research: Planets*, 118(6):1388–1396.

Kalnay, E. (2012). *Atmospheric modeling, data assimilation and predictability*. Cambridge University Press, Cambridge [u.a.].

Kass, D. M. (1999). *Change in the martian atmosphere*. phd, California Institute of Technology.

Kass, D. M., Kleinböhl, A., McCleese, D. J., Schofield, J. T., and Smith, M. D. (2016). Interannual similarity in the Martian atmosphere during the dust storm season. *Geophysical Research Letters*, 43(12):2016GL068978.

Kass, D. M., Schofield, J. T., Kleinböhl, A., McCleese, D. J., Heavens, N. G., Shirley, J. H., and Steele, L. J. (2019). Mars Climate Sounder observation of Mars' 2018 global dust storm. *Geophysical Research Letters*, n/a(n/a).

Kaydash, V. G., Kreslavsky, M. A., Shkuratov, Y. G., Videen, G., Bell, J. F., and Wolff, M. (2006). Measurements of winds on Mars with Hubble Space Telescope images in 2003 opposition. *Icarus*, 185(1):97–101.

Kleinböhl, A., Friedson, A. J., and Schofield, J. T. (2017). Two-dimensional radiative transfer for the retrieval of limb emission measurements in the martian atmosphere. *Journal of Quantitative Spectroscopy and Radiative Transfer*, 187:511–522.

Kleinböhl, A., John Wilson, R., Kass, D., Schofield, J. T., and McCleese, D. J. (2013). The semidiurnal tide in the middle atmosphere of Mars. *Geophysical Research Letters*, 40(10):1952–1959.

Kleinböhl, A., Schofield, J. T., Abdou, W. A., Irwin, P. G. J., and de Kok, R. J. (2011). A single-scattering approximation for infrared radiative transfer in limb geometry in the Martian atmosphere. *Journal of Quantitative Spectroscopy and Radiative Transfer*, 112:1568–1580.

Kleinböhl, A., Schofield, J. T., Kass, D. M., Abdou, W. A., Backus, C. R., Sen, B., Shirley, J. H., Lawson, W. G., Richardson, M. I., Taylor, F. W., Teanby, N. A., and McCleese, D. J. (2009). Mars Climate Sounder limb profile retrieval of atmospheric temperature, pressure, and dust and water ice opacity. *Journal of Geophysical Research: Planets*, 114(E10):E10006.

Kleinböhl, A., Spiga, A., Kass, D. M., Shirley, J. H., Millour, E., Montabone, L., and Forget, F. (2020). Diurnal Variations of Dust During the 2018 Global Dust Storm Observed by the Mars Climate Sounder. *Journal of Geophysical Research: Planets*, 125(1):e2019JE006115.

Kok, J. F., Parteli, E. J. R., Michaels, T. I., and Karam, D. B. (2012). The physics of wind-blown sand and dust. *Reports on Progress in Physics*, 75(10):106901.

Kok, J. F. and Renno, N. O. (2008). Electrostatics in Wind-Blown Sand. *Physical Review Letters*, 100(1):014501. Publisher: American Physical Society.

Korablev, O., Montmessin, F., Trokhimovskiy, A., Fedorova, A. A., Shakun, A. V., Grigoriev, A. V., Moshkin, B. E., Ignatiev, N. I., Forget, F., Lefèvre, F., Anufreychik, K., Dzuban, I., Ivanov, Y. S., Kalinnikov, Y. K., Kozlova, T. O., Kungurov, A., Makarov, V., Martynovich, F., Maslov, I., Merzlyakov, D., Moiseev, P. P., Nikolskiy, Y., Patrakeev, A., Patsaev, D., Santos-Skripko, A., Sazonov, O., Semena, N., Semenov, A., Shashkin, V., Sidorov, A., Stepanov, A. V., Stupin, I., Timonin, D., Titov, A. Y., Viktorov, A., Zharkov, A., Altieri, F., Arnold, G., Belyaev, D. A., Bertaux, J. L., Betsis, D. S., Duxbury, N., Encrenaz, T., Fouchet, T., Gérard, J.-C., Grassi, D., Guerlet, S., Hartogh, P., Kasaba, Y., Khatuntsev, I., Krasnopolsky, V. A., Kuzmin, R. O., Lellouch, E., Lopez-Valverde, M. A., Luginin, M., Määttänen, A., Marcq, E., Martin Torres, J., Medvedev, A. S., Millour, E., Olsen, K. S., Patel, M. R., Quantin-Nataf, C., Rodin, A. V., Shematovich, V. I., Thomas, I., Thomas, N., Vazquez, L., Vincendon, M., Wilquet, V., Wilson, C. F., Zasova, L. V., Zelenyi, L. M., and Zorzano, M. P. (2017). The Atmospheric Chemistry Suite (ACS) of Three Spectrometers for the ExoMars 2016 Trace Gas Orbiter. *Space Science Reviews*, 214(1):7.

Korablev, O. I., Montmessin, F., Fedorova, A. A., Ignatiev, N. I., Shakun, A. V., Trokhimovskiy, A. V., Grigoriev, A. V., Anufreichik, K. A., and Kozlova, T. O. (2015). ACS experiment for atmospheric studies on "ExoMars-2016" Orbiter. *Solar System Research*, 49(7):529–537.

Kreslavsky, M. A. and Head, J. W. (2000). Kilometer-scale roughness of Mars: Results from MOLA data analysis. *Journal of Geophysical Research: Planets*, 105(E11):26695–26711.

Kuroda, T., Hashimoto, N., Sakai, D., and Takahashi, M. (2005). Simulation of the Martian Atmosphere Using a CCSR/NIES AGCM. *Journal of the Meteorological Society of Japan. Ser. II*, 83(1):1–19.

Lahoz, W., Khattatov, B., and Menard, R., editors (2010). *Data Assimilation*. Springer Berlin Heidelberg, Berlin, Heidelberg.

Lee, C., Lawson, W. G., Richardson, M. I., Anderson, J. L., Collins, N., Hoar, T., and Mischna, M. (2011). Demonstration of ensemble data assimilation for Mars using DART, MarsWRF, and radiance observations from MGS TES. *Journal of Geophysical Research: Planets*, 116(E11):E11011.

Lee, C., Richardson, M. I., Newman, C. E., and Mischna, M. A. (2018). The sensitivity of solsticial pauses to atmospheric ice and dust in the MarsWRF General Circulation Model. *Icarus*, 311:23–34.

Leighton, R. B. and Murray, B. C. (1966). Behavior of Carbon Dioxide and Other Volatiles on Mars. *Science*, 153(3732):136–144.

Lemmon, M. T., Guzewich, S. D., McConnochie, T., Vicente-Retortillo, A. d., Martínez, G., Smith, M. D., Bell, J. F., Wellington, D., and Jacob, S. (2019). Large Dust Aerosol Sizes Seen During the 2018 Martian Global Dust Event by the Curiosity Rover. *Geophysical Research Letters*, 46(16):9448–9456.

Lemmon, M. T., Wolff, M. J., Bell III, J. F., Smith, M. D., Cantor, B. A., and Smith, P. H. (2015). Dust aerosol, clouds, and the atmospheric optical depth record over 5 Mars years of the Mars Exploration Rover mission. *Icarus*, 251:96–111.

Leovy, C. and Mintz, Y. (1969). Numerical Simulation of the Atmospheric Circulation and Climate of Mars. *Journal of the Atmospheric Sciences*, 26(6):1167–1190.

Leovy, C. B. and Zurek, R. W. (1979). Thermal tides and Martian dust storms: Direct evidence for coupling. *Journal of Geophysical Research: Solid Earth*, 84(B6):2956–2968.

Leovy, C. B., Zurek, R. W., and Pollack, J. B. (1973). Mechanisms for Mars dust storms.

Lewis, S. R. (2010). Data assimilation for other planets. In Lahoz, W., Khattatov, B., and Menard, R., editors, *Data Assimilation: Making Sense of Observations*, pages 681–699. Springer.

Lewis, S. R. and Barker, P. R. (2005). Atmospheric tides in a Mars general circulation model with data assimilation. *Advances in Space Research*, 36(11):2162–2168.

Lewis, S. R., Collins, M., and Forget, F. (2001). Mars Climate Database v3.0 Detailed Design Document. European Space Agency Technical Report.

Lewis, S. R., Collins, M., and Read, P. L. (1997). Data assimilation with a martian atmospheric GCM: an example using thermal data. *Advances in Space Research*, 19:1267–1270.

Lewis, S. R., Collins, M., Read, P. L., Forget, F., Hourdin, F., Fournier, R., Hourdin, C., Talagrand, O., and Huot, J.-P. (1999). A climate database for Mars. *Journal of Geophysical Research: Planets*, 104(E10):24177–24194.

Lewis, S. R., Mulholland, D. P., Read, P. L., Montabone, L., Wilson, R. J., and Smith, M. D. (2016). The solsticial pause on Mars: 1. A planetary wave reanalysis. *Icarus*, 264:456–464.

Lewis, S. R. and Read, P. L. (1995). An operational data assimilation scheme for the Martian atmosphere. *Advances in Space Research*, 16.

Lewis, S. R. and Read, P. L. (2003). Equatorial jets in the dusty Martian atmosphere. *Journal of Geophysical Research: Planets*, 108(E4):5034.

Lewis, S. R., Read, P. L., and Collins, M. (1996). Martian atmospheric data assimilation with a simplified general circulation model: Orbiter and lander networks. *Planetary and Space Science*, 44(11 SPEC. ISS.):1395–1409.

Lewis, S. R., Read, P. L., Conrath, B. J., Pearl, J. C., and Smith, M. D. (2007). Assimilation of thermal emission spectrometer atmospheric data during the Mars Global Surveyor aerobraking period. *Icarus*, 192(2):327–347.

Listowski, C., Määttänen, A., Montmessin, F., Spiga, A., and Lefèvre, F. (2014). Modeling the microphysics of CO2 ice clouds within wave-induced cold pockets in the martian mesosphere. *Icarus*, 237:239–261.

Lopéz-Valverde, M. and López-Puertas, M. (2001). CO2 non-LTE cooling rate at 15-um and its parameterization for the Mars atmosphere. Martian Environment Models.

Lorenc, A. C., Bell, R. S., and Macpherson, B. (1991). The Meteorological Office analysis correction data assimilation scheme. *Quarterly Journal of the Royal Meteorological Society*, 117(497):59–89.

Lott, F. and Miller, M. J. (1997). A new subgrid-scale orographic drag parametrization: Its formulation and testing. *Quarterly Journal of the Royal Meteorological Society*, 123(537):101–127.

Madeleine, J.-B., Forget, F., Millour, E., Montabone, L., and Wolff, M. J. (2011). Revisiting the radiative impact of dust on Mars using the LMD Global Climate Model. *Journal of Geophysical Research: Planets*, 116(E11):E11010.

Martin, L. J. (1984). Clearing the Martian air - The troubled history of dust storms. *Icarus*, pages 317–321.

Martin, L. J. and Zurek, R. W. (1993). An analysis of the history of dust activity on Mars. *Journal of Geophysical Research: Planets*, 98(E2):3221–3246.

Martin, T. Z. (1986). Thermal infrared opacity of the Mars atmosphere. *Icarus*, 66(1):2–21.

Martin, T. Z. and Richardson, M. I. (1993). New dust opacity mapping from Viking infrared thermal mapper data. *Journal of Geophysical Research: Planets*, 98(E6):10941–10949.

Martínez, G. M., Newman, C. N., De Vicente-Retortillo, A., Fischer, E., Renno, N. O., Richardson, M. I., Fairén, A. G., Genzer, M., Guzewich, S. D., Haberle, R. M., Harri, A.-M., Kemppinen, O., Lemmon, M. T., Smith, M. D., de la Torre-Juárez, M., and Vasavada, A. R. (2017). The Modern Near-Surface Martian Climate: A Review of In-situ Meteorological Data from Viking to Curiosity. *Space Science Reviews*, 212(1):295–338.

McCleese, D. J., Heavens, N. G., Schofield, J. T., Abdou, W. A., Bandfield, J. L., Calcutt, S. B., Irwin, P. G. J., Kass, D. M., Kleinböhl, A., Lewis, S. R., Paige, D. A., Read, P. L., Richardson, M. I., Shirley, J. H., Taylor, F. W., Teanby, N., and Zurek, R. W. (2010). Structure and dynamics of the Martian lower and middle atmosphere as observed by the Mars Climate Sounder: Seasonal variations in zonal mean temperature, dust, and water ice aerosols. *Journal of Geophysical Research: Planets*, 115(E12):E12016.

McCleese, D. J., Kleinböhl, A., Kass, D. M., Schofield, J. T., Wilson, R. J., and Greybush, S. (2017). Comparisons of Observations and Simulations of the Mars Polar Atmosphere. page 1104.

McCleese, D. J., Schofield, J. T., Taylor, F. W., Calcutt, S. B., Foote, M. C., Kass, D. M., Leovy, C. B., Paige, D. A., Read, P. L., and Zurek, R. W. (2007). Mars Climate Sounder: An investigation of thermal and water vapor structure, dust and condensate distributions in the atmosphere, and energy balance of the polar regions. *Journal of Geophysical Research: Planets*, 112(E5):E05S06.

McDunn, T., Bougher, S., Murphy, J., Kleinböhl, A., Forget, F., and Smith, M. (2013). Characterization of middle-atmosphere polar warming at Mars. *Journal of Geophysical Research: Planets*, 118(2):161–178.

McKim, R. J. (1996). The dust storms of Mars. *Journal of the British Astronomical Association*, 106:185–200.

Medvedev, A. S. and Hartogh, P. (2007). Winter polar warmings and the meridional transport on Mars simulated with a general circulation model. *Icarus*, 186(1):97–110.

Medvedev, A. S., Kuroda, T., and Hartogh, P. (2011). Influence of dust on the dynamics of the martian atmosphere above the first scale height. *Aeolian Research*, 3(2):145–156.

Miller, M. J., Palmer, T. N., and Swinbank, R. (1989). Parametrization and influence of subgridscale orography in general circulation and numerical weather prediction models. *Meteorology and Atmospheric Physics*, 40(1):84–109.

Mitchell, D. M., Montabone, L., Thomson, S., and Read, P. L. (2015). Polar vortices on Earth and Mars: A comparative study of the climatology and variability from reanalyses. *Quarterly Journal of the Royal Meteorological Society*, 141(687):550–562.

Montabone, L., Forget, F., Millour, E., Wilson, R. J., Lewis, S. R., Cantor, B., Kass, D., Kleinböhl, A., Lemmon, M. T., Smith, M. D., and Wolff, M. J. (2015). Eight-year climatology of dust optical depth on Mars. *Icarus*, 251:65–95.

Montabone, L., Lewis, S. R., and Read, P. L. (2005). Interannual variability of Martian dust storms in assimilation of several years of Mars global surveyor observations. *Advances in Space Research*, 36(11):2146–2155.

Montabone, L., Marsh, K., Lewis, S. R., Read, P. L., Smith, M. D., Holmes, J., Spiga, A., Lowe, D., and Pamment, A. (2014). The Mars Analysis Correction Data Assimilation (MACDA) Dataset V1.0. *Geoscience Data Journal*, 1(2):129–139.

Montabone, L., Spiga, A., Kass, D. M., Kleinböhl, A., Forget, F., and Millour, E. (2020). Martian Year 34 Column Dust Climatology from Mars Climate Sounder Observations: Reconstructed Maps and Model Simulations. *Journal of Geophysical Research: Planets*, n/a(n/a):e2019JE006111.

Montmessin, F., Forget, F., Rannou, P., Cabane, M., and Haberle, R. M. (2004). Origin and role of water ice clouds in the Martian water cycle as inferred from a general circulation model. *Journal of Geophysical Research: Planets*, 109(E10):E10004.

Mulholland, D. P. (2012). *Martian dust lifting, transport and associated processes*. PhD Thesis, University of Oxford.

Mulholland, D. P., Lewis, S. R., Read, P. L., Madeleine, J.-B., and Forget, F. (2016). The solsticial pause on Mars: 2 modelling and investigation of causes. *Icarus*, 264:465–477.

Mulholland, D. P., Read, P. L., and Lewis, S. R. (2013). Simulating the interannual variability of major dust storms on Mars using variable lifting thresholds. *Icarus*, 223(1):344–358.

Mulholland, D. P., Spiga, A., Listowski, C., and Read, P. L. (2015). An assessment of the impact of local processes on dust lifting in martian climate models. *Icarus*, 252:212–227.

Murphy, J. R., Pollack, J. B., Haberle, R. M., Leovy, C. B., Toon, O. B., and Schaeffer, J. (1995). Three-dimensional numerical simulation of Martian global dust storms. *Journal of Geophysical Research: Planets*, 100(E12):26357–26376.

Murphy, J. R., Toon, O. B., Haberle, R. M., and Pollack, J. B. (1990). Numerical simulations of the decay of Martian global dust storms. *Journal of Geophysical Research*, pages 14629–14.

Musiolik, G., Kruss, M., Demirci, T., Schrinski, B., Teiser, J., Daerden, F., Smith, M. D., Neary, L., and Wurm, G. (2018). Saltation under Martian gravity and its influence on the global dust distribution. *Icarus*, 306:25–31.

Navarro, T. (2016). *Etude de la météorologie de la planète Mars par assimilation de données satellite et modélisation*. phdthesis, Université Pierre et Marie Curie - Paris VI.

Navarro, T., Forget, F., Millour, E., and Greybush, S. J. (2014). Detection of detached dust layers in the Martian atmosphere from their thermal signature using assimilation. *Geophysical Research Letters*, 41(19):6620–6626.

Navarro, T., Forget, F., Millour, E., Greybush, S. J., Kalnay, E., and Miyoshi, T. (2017). The Challenge of Atmospheric Data Assimilation on Mars. *Earth and Space Science*, 4(12):2017ea000274.

Nayvelt, L., Gierasch, P. J., and Cook, K. H. (1997). Modeling and Observations of Martian Stationary Waves. *Journal of the Atmospheric Sciences*, 54(8):986–1013.

Neary, L. and Daerden, F. (2018). The GEM-Mars general circulation model for Mars: Description and evaluation. *Icarus*, 300:458–476.

Neary, L., Daerden, F., Aoki, S., Whiteway, J., Clancy, R. T., Smith, M., Viscardy, S., Erwin, J. T., Thomas, I. R., Villanueva, G., Liuzzi, G., Crismani, M., Wolff, M., Lewis, S. R., Holmes, J. A., Patel, M. R., Giuranna, M., Depiesse, C., Piccialli, A., Robert, S., Trompet, L., Willame, Y., Ristic, B., and Vandaele, A. C. (2020). Explanation for the Increase in High-Altitude Water on Mars Observed by NOMAD During the 2018 Global Dust Storm. *Geophysical Research Letters*, 47(7):e2019GL084354.

Newman, C. E., Lewis, S. R., and Read, P. L. (2005). The atmospheric circulation and dust activity in different orbital epochs on Mars. *Icarus*, 174(1):135–160.

Newman, C. E., Lewis, S. R., Read, P. L., and Forget, F. (2002a). Modeling the Martian dust cycle, 1. Representations of dust transport processes. *Journal of Geophysical Research: Planets*, 107(E12):5123.

Newman, C. E., Lewis, S. R., Read, P. L., and Forget, F. (2002b). Modeling the Martian dust cycle 2. Multiannual radiatively active dust transport simulations. *Journal of Geophysical Research: Planets*, 107(E12):5124.

Newman, C. E., Read, P. L., and Lewis, S. R. (2003). Breeding vectors and predictability in the Oxford Mars GCM. Granada, Spain.

Newman, C. E., Read, P. L., and Lewis, S. R. (2004). Investigating atmospheric predictability on Mars using breeding vectors in a general-circulation model. *Quarterly Journal of the Royal Meteorological Society*, 130(603):2971–2989.

Newman, C. E. and Richardson, M. I. (2015). The impact of surface dust source exhaustion on the martian dust cycle, dust storms and interannual variability, as simulated by the MarsWRF General Circulation Model. *Icarus*, 257:47–87.

Ockert-Bell, M. E., Bell, J. F., Pollack, J. B., McKay, C. P., and Forget, F. (1997). Absorption and scattering properties of the Martian dust in the solar wavelengths. *Journal of Geophysical Research: Planets*, 102(E4):9039–9050.

Ogohara, K. and Satomura, T. (2010). Changes in mass flow caused by co2 condensation in the martian atmosphere. In *Advances in Geosciences*, volume Volume 19 of *Advances in Geosciences*, pages 195–205. World Scientific Publishing Company.

Ojha, L., Lewis, K., Karunatillake, S., and Schmidt, M. (2018). The Medusae Fossae Formation as the single largest source of dust on Mars. *Nature Communications*, 9(1):2867.

Pankine, A. A. and Ingersoll, A. P. (2002). Interannual Variability of Martian Global Dust Storms - Simulations with a Low-Order Model of the General Circulation. *Icarus*, 155(2):299–323.

Pankine, A. A. and Ingersoll, A. P. (2004). Interannual variability of Mars global dust storms: an example of self-organized criticality? *Icarus*, 170(2):514–518.

Patel, M. R., Antoine, P., Mason, J., Leese, M., Hathi, B., Stevens, A. H., Dawson, D., Gow, J., Ringrose, T., Holmes, J., Lewis, S. R., Beghuin, D., van Donink, P., Ligot, R., Dewandel, J.-L., Hu, D., Bates, D., Cole, R., Drummond, R., Thomas, I. R., Depiesse, C., Neefs, E., Equeter, E., Ristic, B., Berkenbosch, S., Bolsée, D., Willame, Y., Vandaele, A. C., Lesschaeve, S., De Vos, L., Van Vooren, N., Thibert, T., Mazy, E., Rodriguez-Gomez, J., Morales, R., Candini, G. P., Pastor-Morales, M. C., Sanz, R., Aparicio del Moral, B., Jeronimo-Zafra, J.-M., Gómez-López, J. M., Alonso-Rodrigo, G., Pérez-Grande, I., Cubas, J., Gomez-Sanjuan, A. M., Navarro-Medina, F., BenMoussa, A., Giordanengo, B., Gissot, S., Bellucci, G., and Lopez-Moreno, J. J. (2017). NOMAD spectrometer on the ExoMars trace gas orbiter mission: part 2—design, manufacturing, and testing of the ultraviolet and visible channel. *Applied Optics*, 56(10):2771–2782.

Petrova, E. V. (1999). Mars aerosol optical thickness retrieved from measurements of the polarization inversion angle and the shape of dust particles. *Journal of Quantitative Spectroscopy and Radiative Transfer*, 63(2):667–676.

Petty, G. W. (2006). *A first course in atmospheric radiation*. Sundog Pub., Madison, Wisconsin. OCLC: 932561283.

Philpotts, A. and Ague, J. (2009). *Principles of Igneous and Metamorphic Petrology*. Cambridge University Press. Google-Books-ID: aAnxRS363lIC.

Piqueux, S., Kleinböhl, A., Hayne, P. O., Kass, D. M., Schofield, J. T., and McCleese, D. J. (2015). Variability of the martian seasonal CO2 cap extent over eight Mars Years. *Icarus*, 251:164–180.

Pollack, J. B., Colburn, D. S., Flasar, F. M., Kahn, R., Carlston, C. E., and Pidek, D. (1979). Properties and effects of dust particles suspended in the Martian atmosphere. *Journal of Geophysical Research: Solid Earth*, 84(B6):2929–2945.

Pollack, J. B., Haberle, R. M., Schaeffer, J., and Lee, H. (1990). Simulations of the general circulation of the Martian atmosphere: 1. Polar processes. *Journal of Geophysical Research: Solid Earth*, 95(B2):1447–1473.

Pollack, J. B., Leovy, C. B., Greiman, P. W., and Mintz, Y. (1981). A Martian General Circulation Experiment with Large Topography. *Journal of the Atmospheric Sciences*, 38(1):3–29.

Priestley, A. (1993). A Quasi-Conservative Version of the Semi-Lagrangian Advection Scheme. *Monthly Weather Review*, 121(2):621–629.

Putzig, N. E. and Mellon, M. T. (2007). Apparent thermal inertia and the surface heterogeneity of Mars. *Icarus*, 191(1):68–94.

Putzig, N. E., Mellon, M. T., Kretke, K. A., and Arvidson, R. E. (2005). Global thermal inertia and surface properties of Mars from the MGS mapping mission. *Icarus*, 173(2):325–341.

Qi, L. and Sun, J. (2006). Application of ATOVS microwave radiance assimilation to rainfall prediction in Summer 2004. *Advances in Atmospheric Sciences*, 23(5):815–830.

Rafkin, S. C. R. (2012). The potential importance of non-local, deep transport on the energetics, momentum, chemistry, and aerosol distributions in the atmospheres of Earth, Mars, and Titan. *Planetary and Space Science*, 60(1):147–154.

Rafkin, S. C. R., Maria, M. R. V. S., and Michaels, T. I. (2002). Simulation of the atmospheric thermal circulation of a martian volcano using a mesoscale numerical model. *Nature*, 419(6908):697–699.

Read, P. L., Barstow, J., Charnay, B., Chelvaniththilan, S., Irwin, P. G. J., Knight, S., Lebonnois, S., Lewis, S. R., Mendonça, J., and Montabone, L. (2016). Global energy budgets and 'Trenberth diagrams' for the climates of terrestrial and gas giant planets. *Quarterly Journal of the Royal Meteorological Society*, 142(695):703–720.

Read, P. L. and Lewis, S. R. (2004). *The Martian climate revisited: atmosphere and environment of a desert planet*, volume 26. Springer.

Read, P. L., Lewis, S. R., and Mulholland, D. P. (2015). The physics of Martian weather and climate: a review. *Reports on Progress in Physics*, 78(12):125901.

Read, P. L., Tabataba-Vakili, F., Valeanu, A., Wang, Y., and Young, R. M. B. (2017). Mars in Context: Comparative Atmospheric Circulation of Terrestrial Planets. page 1301.

Richardson, M. I. and Wilson, R. J. (2002). A topographically forced asymmetry in the martian circulation and climate. *Nature*, 416(6878):298–301.

Robert, A. J. (1966). The Integration of a Low Order Spectral Form of the Primitive Meteorological Equations. *Journal of the Meteorological Society of Japan. Ser. II*, 44(5):237–245.

Robock, A., Oman, L., and Stenchikov, G. L. (2007). Nuclear winter revisited with a modern climate model and current nuclear arsenals: Still catastrophic consequences. *Journal of Geophysical Research: Atmospheres*, 112(D13).

Rogberg, P., Read, P. L., Lewis, S. R., and Montabone, L. (2010). Assessing atmospheric predictability on Mars using numerical weather prediction and data assimilation. *Quarterly Journal of the Royal Meteorological Society*, 136(651):1614–1635.

Rossow, W. B. (1978). Cloud microphysics: Analysis of the clouds of Earth, Venus, Mars and Jupiter. *Icarus*, 36(1):1–50.

Rostami, M., Zeitlin, V., and Montabone, L. (2018). On the role of spatially inhomogeneous diabatic effects upon the evolution of Mars' annular polar vortex. *Icarus*, 314:376–388.

Ruan, T. (2015). *The climate of Mars from assimilations of spacecraft data*. Ph.D., University of Oxford.

Ruff, S. W. and Christensen, P. R. (2002). Bright and dark regions on Mars: Particle size and mineralogical characteristics based on Thermal Emission Spectrometer data. *Journal of Geophysical Research: Planets*, 107(E12):2–1–2–22.

Ryan, J. A. and Henry, R. M. (1979). Mars atmospheric phenomena during major dust storms, as measured at surface. *Journal of Geophysical Research: Solid Earth*, 84(B6):2821–2829.

Sagan, C., Toon, O. B., and Gierasch, P. J. (1973). Climatic Change on Mars. *Science*, 181(4104):1045–1049.

Salby, M. L. (2011). Physics of the Atmosphere and Climate.

Seu, R., Phillips, R. J., Biccari, D., Orosei, R., Masdea, A., Picardi, G., Safaeinili, A., Campbell, B. A., Plaut, J. J., Marinangeli, L., Smrekar, S. E., and Nunes, D. C. (2018). SHARAD sounding radar on the Mars Reconnaissance Orbiter. *Journal of Geophysical Research: Planets*.

Seviour, W. J. M., Waugh, D. W., and Scott, R. K. (2017). The Stability of Mars's Annular Polar Vortex. *Journal of the Atmospheric Sciences*, 74(5):1533–1547.

Shao, Y. (2008). *Physics and Modelling of Wind Erosion*. Springer Science & Business Media. Google-Books-ID: XSwwVeraxjcC.

Shao, Y. and Lu, H. (2000). A simple expression for wind erosion threshold friction velocity. *Journal of Geophysical Research: Atmospheres*, 105(D17):22437–22443.

Shell, K. M. and Somerville, R. C. J. (2007). Direct radiative effect of mineral dust and volcanic aerosols in a simple aerosol climate model. *Journal of Geophysical Research: Atmospheres*, 112(D3).

Shirley, J. H., Kleinböhl, A., Kass, D. M., Steele, L. J., Heavens, N. G., Suzuki, S., Piqueux, S., Schofield, J. T., and McCleese, D. J. (2019). Rapid expansion and evolution of a regional dust storm in the Acidalia Corridor during the initial growth phase of the Martian global dust storm of 2018. *Geophysical Research Letters*, n/a(n/a).

Siili, T., Haberle, R. M., and Murphy, J. R. (1997). Sensitivity of Martian Southern polar cap edge winds and surface stresses to dust optical thickness and to the large-scale sublimation flow. *Advances in Space Research*, 19(8):1241–1244.

Siili, T., Haberle, R. M., Murphy, J. R., and Savijarvi, H. (1999). Modelling of the combined late-winter ice cap edge and slope winds in Mars Hellas and Argyre regions. *Planetary and Space Science*, 47(8–9):951–970.

Smith, D. E., Zuber, M. T., Solomon, S. C., Phillips, R. J., Head, J. W., Garvin, J. B., Banerdt, W. B., Muhleman, D. O., Pettengill, G. H., Neumann, G. A., Lemoine, F. G., Abshire, J. B., Aharonson, O., David, C., Brown, Hauck, S. A., Ivanov, A. B., McGovern, P. J., Zwally, H. J., and Duxbury, T. C. (1999a). The Global Topography of Mars and Implications for Surface Evolution. *Science*, 284(5419):1495–1503. Publisher: American Association for the Advancement of Science Section: Research Article.

Smith, I. B., Diniega, S., Beaty, D. W., Thorsteinsson, T., Becerra, P., Bramson, A. M., Clifford, S. M., Hvidberg, C. S., Portyankina, G., Piqueux, S., Spiga, A., and Titus, T. N. (2017). 6th international conference on Mars polar science and exploration: Conference summary and five top questions. *Icarus*.

Smith, M. D. (2004). Interannual variability in TES atmospheric observations of Mars during 1999–2003. *Icarus*, 167(1):148–165.

Smith, M. D. (2008). Spacecraft Observations of the Martian Atmosphere. *Annual Review of Earth and Planetary Sciences*, 36:191–219.

Smith, M. D., Conrath, B. J., Pearl, J. C., and Christensen, P. R. (2002). Thermal Emission Spectrometer Observations of Martian Planet-Encircling Dust Storm 2001A. *Icarus*, 157(1):259–263.

Smith, M. D., Pearl, J. C., Conrath, B. J., and Christensen, P. R. (1999b). Mars Global Surveyor Thermal Emission Spectrometer (TES) Observations of Dust Opacity During Aerobraking and Science Phasing.

Smith, M. D., Pearl, J. C., Conrath, B. J., and Christensen, P. R. (2001). Thermal Emission Spectrometer results: Mars atmospheric thermal structure and aerosol distribution. *Journal of Geophysical Research: Planets*, 106(E10):23929–23945.

Smith, M. D. and Wolff, M. J. (2014). Dust Aerosol Particle Size and Shape using MER NAVCAM and PANCAM Sky Imaging. page 2101.

Smith, M. D., Wolff, M. J., Clancy, R. T., Kleinböhl, A., and Murchie, S. L. (2013). Vertical distribution of dust and water ice aerosols from CRISM limb-geometry observations. *Journal of Geophysical Research: Planets*, 118(2):321–334.

Smith, M. D., Wolff, M. J., Spanovich, N., Ghosh, A., Banfield, D., Christensen, P. R., Landis, G. A., and Squyres, S. W. (2006). One Martian year of atmospheric observations using MER Mini-TES. *Journal of Geophysical Research: Planets*, 111(E12). _eprint: https://agupubs.onlinelibrary.wiley.com/doi/pdf/10.1029/2006JE002770.

Souness, C. and Hubbard, B. (2012). Mid-latitude glaciation on Mars. *Progress in Physical Geography: Earth and Environment*, 36(2):238–261.

Spiga, A., Faure, J., Madeleine, J.-B., Määttänen, A., and Forget, F. (2013). Rocket dust storms and detached dust layers in the Martian atmosphere. *Journal of Geophysical Research: Planets*, 118(4):746–767.

Spiga, A., Hinson, D. P., Madeleine, J.-B., Navarro, T., Millour, E., Forget, F., and Montmessin, F. (2017). Snow precipitation on Mars driven by cloud-induced night-time convection. *Nature Geoscience*, 10(9):652–657.

Steele, L. J. (2014). *A study of the martian water cycle and cloud radiative effects using data assimilation*. PhD thesis, The Open University.

Steele, L. J., Lewis, S. R., and Patel, M. R. (2014a). The radiative impact of water ice clouds from a reanalysis of Mars Climate Sounder data. *Geophysical Research Letters*, 41(13):4471–4478.

Steele, L. J., Lewis, S. R., Patel, M. R., Montmessin, F., Forget, F., and Smith, M. D. (2014b). The seasonal cycle of water vapour on Mars from assimilation of Thermal Emission Spectrometer data. *Icarus*, 237:97–115.

Streeter, P., Lewis, S., Patel, M., and Holmes, J. (2018). Assimilation of Mars Climate Sounder Dust Observations: Challenges and Ways Forward. Savoie Technolac, Le Bourget-du-Lac, France.

Streeter, P. M., Lewis, S. R., Patel, M. R., Holmes, J. A., and Kass, D. M. (2020). Surface Warming During the 2018/Mars Year 34 Global Dust Storm. *Geophysical Research Letters*, 47(9):e2019GL083936. _eprint: https://agupubs.onlinelibrary.wiley.com/doi/pdf/10.1029/2019GL083936.

Szwast, M. A., Richardson, M. I., and Vasavada, A. R. (2006). Surface dust redistribution on Mars as observed by the Mars Global Surveyor and Viking orbiters. *Journal of Geophysical Research: Planets*, 111(E11):E11008.

Tabataba-Vakili, F., Read, P. L., Lewis, S. R., Montabone, L., Ruan, T., Wang, Y., Valeanu, A., and Young, R. M. B. (2015). A Lorenz/Boer energy budget for the atmosphere of Mars from a "reanalysis" of spacecraft observations. *Geophysical Research Letters*, 42(20):2015GL065659.

Talagrand, O. (1997). Assimilation of Observations, an Introduction (gtSpecial IssueltData Assimilation in Meteology and Oceanography: Theory and Practice). *Journal of the Meteorological Society of Japan. Ser. II*, 75(1B):191–209.

Thomas, I. R., Vandaele, A. C., Robert, S., Neefs, E., Drummond, R., Daerden, F., Delanoye, S., Ristic, B., Berkenbosch, S., Clairquin, R., Maes, J., Bonnewijn, S., Depiesse, C., Mahieux, A., Trompet, L., Neary, L., Willame, Y., Wilquet, V., Nevejans, D., Aballea, L., Moelans, W., Vos, L. D., Lesschaeve, S., Vooren, N. V., Lopez-Moreno, J.-J., Patel, M. R., Bellucci, G., and Team, t. N. (2016). Optical and radiometric models of the NOMAD instrument part II: the infrared channels - SO and LNO. *Optics Express*, 24(4):3790–3805.

Toigo, A. D., Lee, C., Newman, C. E., and Richardson, M. I. (2012). The impact of resolution on the dynamics of the martian global atmosphere: Varying resolution studies with the MarsWRF GCM. *Icarus*, 221(1):276–288.

Toigo, A. D., Richardson, M. I., Wang, H., Guzewich, S. D., and Newman, C. E. (2018). The cascade from local to global dust storms on Mars: Temporal and spatial thresholds on thermal and dynamical feedback. *Icarus*, 302:514–536.

Toigo, A. D., Richardson, M. I., Wilson, R. J., Wang, H., and Ingersoll, A. P. (2002). A first look at dust lifting and dust storms near the south pole of Mars with a mesoscale model. *Journal of Geophysical Research: Planets*, 107(E7):4–1–4–13.

Toigo, A. D., Waugh, D. W., and Guzewich, S. D. (2017). What causes Mars' annular polar vortices? *Geophysical Research Letters*, 44(1):71–78.

Tomasko, M. G., Doose, L. R., Lemmon, M., Smith, P. H., and Wegryn, E. (1999). Properties of dust in the Martian atmosphere from the Imager on Mars Pathfinder. *Journal of Geophysical Research: Planets*, 104(E4):8987–9007.

Toon, O. B., B. Pollack, J., and Sagan, C. (1977). Physical properties of the particles composing the Martian dust storm of 1971–1972. *Icarus*, 30(4):663–696.

Toon, O. B., McKay, C. P., Ackerman, T. P., and Santhanam, K. (1989). Rapid calculation of radiative heating rates and photodissociation rates in inhomogeneous multiple scattering atmospheres. *Journal of Geophysical Research: Atmospheres*, 94(D13):16287–16301.

Turco, R. P., Toon, O. B., Ackerman, T. P., Pollack, J. B., and Sagan, C. (1983). Nuclear Winter: Global Consequences of Multple Nuclear Explosions. *Science*, 222(4630):1283–1292.

Turco, R. P., Toon, O. B., Ackerman, T. P., Pollack, J. B., and Sagan, C. (1984). The Climatic Effects of Nuclear War. *Scientific American*, 251(2):33–43.

Urban, J., Dassas, K., Forget, F., and Ricaud, P. (2005). Retrieval of vertical constituents and temperature profiles from passive submillimeter wave limb observations of the Martian atmosphere: a feasibility study. *Applied Optics*, 44(12):2438–2455. Publisher: Optical Society of America.

Vals, M., Forget, F., Spiga, A., Millour, E., Wang, C., Bertrand, T., and Bardet, D. (2019). Modeling of Detached Dust Layers: Parametrization of the Dust Entrainment by Slope Winds at the Top of Sub-Grid Scale Topography. *LPI Contributions*, 2089:6220.

Vandaele, A. C., Neefs, E., Drummond, R., Thomas, I. R., Daerden, F., Lopez-Moreno, J. J., Rodriguez, J., Patel, M. R., Bellucci, G., Allen, M., Altieri, F., Bolsée, D., Clancy, T., Delanoye, S., Depiesse, C., Cloutis, E., Fedorova, A., Formisano, V., Funke, B., Fussen, D., Geminale, A., Gérard, J. C., Giuranna, M., Ignatiev, N., Kaminski, J., Karatekin, O., Lefèvre, F., López-Puertas, M., López-Valverde, M., Mahieux, A., McConnell, J., Mumma, M., Neary, L., Renotte, E., Ristic, B., Robert, S., Smith, M., Trokhimovsky, S., Vander Auwera, J., Villanueva, G., Whiteway, J., Wilquet, V., and Wolff, M. (2015). Science objectives and performances of NOMAD, a spectrometer suite for the ExoMars TGO mission. *Planetary and Space Science*, 119:233–249.

Wang, C., Forget, F., Bertrand, T., Spiga, A., Millour, E., and Navarro, T. (2018). Parameterization of Rocket Dust Storms on Mars in the LMD Martian GCM: Modeling Details and Validation. *Journal of Geophysical Research: Planets*, 123(4):982–1000.

Wang, H. (2007). Dust storms originating in the northern hemisphere during the third mapping year of Mars Global Surveyor. *Icarus*, 189(2):325–343.

Wang, H. (2018). Cross-Equatorial Flushing Dust Storms and Northern Hemisphere Transient Eddies: An Analysis for Mars Year 24. *Journal of Geophysical Research: Planets*, 123(7):1732–1745.

Wang, H. and Fisher, J. A. (2009). North polar frontal clouds and dust storms on Mars during spring and summer. *Icarus*, 204(1):103–113.

Wang, H. and Ingersoll, A. P. (2003). Cloud-tracked winds for the first Mars Global Surveyor mapping year. *Journal of Geophysical Research: Planets*, 108(E9). _eprint: https://agupubs.onlinelibrary.wiley.com/doi/pdf/10.1029/2003JE002107.

Wang, H. and Richardson, M. I. (2015). The origin, evolution, and trajectory of large dust storms on Mars during Mars years 24–30 (1999–2011). *Icarus*, 251:112–127.

Wang, H., Richardson, M. I., Toigo, A. D., and Newman, C. E. (2013). Zonal wavenumber three traveling waves in the northern hemisphere of Mars simulated with a general circulation model. *Icarus*, 223(2):654–676.

Wang, H., Richardson, M. I., Wilson, R. J., Ingersoll, A. P., Toigo, A. D., and Zurek, R. W. (2003). Cyclones, tides, and the origin of a cross-equatorial dust storm on Mars. *Geophysical Research Letters*, 30(9):1488.

Wang, H., Zurek, R. W., and Richardson, M. I. (2005). Relationship between frontal dust storms and transient eddy activity in the northern hemisphere of Mars as observed by Mars Global Surveyor. *Journal of Geophysical Research: Planets*, 110(E7):E07005.

Waugh, D. W., Toigo, A. D., and Guzewich, S. D. (2018). Age of Martian Air: Time scales for Martian atmospheric transport. *Icarus*.

Waugh, D. W., Toigo, A. D., Guzewich, S. D., Greybush, S. J., Wilson, R. J., and Montabone, L. (2016). Martian polar vortices: Comparison of reanalyses. *Journal of Geophysical Research: Planets*, 121(9):2016JE005093.

Wilson, R. J. (1997). A general circulation model simulation of the Martian polar warming. *Geophysical Research Letters*, 24(2):123–126.

Wilson, R. J. and Hamilton, K. (1996). Comprehensive model simulation of thermal tides in the Martian atmosphere. *Journal of Atmospheric Sciences*, 53:1290–1326.

Wolff, M. J., Lopéz-Valverde, M., Madeleine, J.-B., Wilson, R. J., Smith, M. D., Fouchet, T., and Delory, G. T. (2017). Radiative Process: Techniques and Applications.

Wolff, M. J., Smith, M. D., Clancy, R. T., Arvidson, R., Kahre, M., Seelos, F., Murchie, S., and Savijärvi, H. (2009). Wavelength dependence of dust aerosol single scattering albedo as observed by the Compact Reconnaissance Imaging Spectrometer. *Journal of Geophysical Research (Planets)*, 114:E00D04.

Wolff, M. J., Smith, M. D., Clancy, R. T., Spanovich, N., Whitney, B. A., Lemmon, M. T., Bandfield, J. L., Banfield, D., Ghosh, A., Landis, G., Christensen, P. R., Bell, J. F., and Squyres, S. W. (2006). Constraints on dust aerosols from the Mars Exploration Rovers using MGS overflights and Mini-TES. *Journal of Geophysical Research: Planets*, 111(E12):n/a–n/a.

Xiao, J., Chow, K.-C., and Chan, K.-l. (2019). Dynamical processes of dust lifting in the northern mid-latitude region of Mars during the dust storm season. *Icarus*, 317:94–103.

Yu, T.-W. and Mcpherson, R. D. (1984). Global Data Assimilation Experiments with Scatterometer Winds from SEASAT-A. *Monthly Weather Review*, 112(2):368–376. Publisher: American Meteorological Society.

Zhang, K. Q., Ingersoll, A. P., Kass, D. M., Pearl, J. C., Smith, M. D., Conrath, B. J., and Haberle, R. M. (2001). Assimilation of Mars Global Surveyor atmospheric temperature data into a general circulation model. *Journal of Geophysical Research E*, 106(E12):32863–32877.

Zurek, R. W. (1982). Martian great dust storms - An update.

Zurek, R. W., Barnes, J. R., Haberle, R. M., Pollack, J. B., Tillman, J. E., and Leovy, C. B. (1992). Dynamics of the atmosphere of Mars. In *Mars*, pages 835–933.

Zurek, R. W. and Haberle, R. M. (1988). Zonally Symmetric Response to Atmospheric Tidal Forcing in the Dusty Martian Atmosphere. *Journal of the Atmospheric Sciences*, 45(18):2469–2485.

Zurek, R. W. and Martin, L. J. (1993). Interannual variability of planet-encircling dust storms on Mars. *Journal of Geophysical Research: Planets*, 98(E2):3247–3259.

Appendix A

List of publications

Journal Publications

Streeter, P. M., Lewis, S. R., Patel, M. R., Holmes, J. A., and Kass, D. M. (2020). **Surface warming during the 2018/Mars Year 34 Global Dust Storm.** *Geophysical Research Letters*, 47, DOI: 10.1029/2019GL083936.

Conference Items

Streeter, Paul; Lewis, Stephen; Patel, Manish and Holmes, James (2020). **Martian Polar Vortex Dynamics and the 2018 Global Dust Storm**. In: *Seventh International Conference on Mars Polar Science and Exploration*, 13-17 Jan 2020, Ushuaia, Argentina.

Streeter, Paul; Lewis, Stephen; Patel, Manish; Holmes, James and Kass, David (2019). **Surface Warming During the 2018/MY 34 Mars Global Dust Storm**. In: *Ninth International Conference on Mars*, 22-25 Jul 2019, Pasadena, California, USA. (Talk)

Streeter, Paul; Lewis, Stephen; Patel, Manish and Holmes, James (2018). **Assimilation of Mars Climate Sounder Dust Observations: Challenges and Ways Forward**. In: *Mars*

Atmosphere Data Assimilation (MADA) workshop, 29-31 Aug 2018, Savoie Technolac, Le Bourget-du-Lac, France. (Talk)

Streeter, P. M.; Lewis, S. R.; Patel, M. R. and Holmes, J. A. (2018). **The circulatory impact of dust from dust profile assimilation**. In: *Mars Science Workshop "From Mars Express to ExoMars"*, 27-28 Feb 2018, ESAC, Madrid, Spain. (Poster)

Streeter, Paul; Lewis, Stephen; Patel, Manish and Holmes, James (2017). **Analysing martian polar dust transport using data assimilation**. In: *1st British Planetary Science Congress*, 3-5 Dec 2017, Glasgow, UK. (Talk)

Streeter, P. M.; Lewis, S. R.; Patel, M. R. and Steele, L. J. (2017). **Investigating the Role of Advection Processes in Improved Martian Dust Assimilation Techniques for ExoMars**. In: *Sixth International Workshop on the Mars Atmosphere*: Modelling and Observations, 17-20 Jan 2017, Granada, Spain. (Poster)